Simulation and Modeling Techniques for Signal Integrity and Electromagnetic Interference on High Frequency Electronic Systems.

by

Luca Daniel

Laurea (University of Padua, Italy) 1996

A dissertation submitted in partial satisfaction of the
requirements for the degree of
Doctor of Philosophy

in

Engineering - Electrical Engineering and Computer Sciences

in the

GRADUATE DIVISION
of the
UNIVERSITY of CALIFORNIA at BERKELEY

Committee in charge:

Professor Alberto L Sangiovanni-Vincentelli, Chair
Professor Jacob K White
Professor Robert K Brayton
Professor Ole H Hald

Spring 2003

The dissertation of Luca Daniel is approved:

Chair	Date
	Date
	Date
	Date

University of California at Berkeley

Spring 2003

Simulation and Modeling Techniques for Signal Integrity and Electromagnetic Interference on High Frequency Electronic Systems.

Abstract

Simulation and Modeling Techniques for Signal Integrity and Electromagnetic Interference on High Frequency Electronic Systems.

by

Luca Daniel
Doctor of Philosophy in Engineering - Electrical Engineering and Computer Sciences
University of California at Berkeley
Professor Alberto L Sangiovanni-Vincentelli, Chair

Many future electronic systems will consist of several significantly heterogeneous modules such as Opto-Electronic and analog RF links, mixed-signal analog to digital converters (ADC), digital signal processors (DSP), Central Processor Units (CPU), Memory modules, Microfabricated Electro-Mechanical (MEM) resonators, sensors and actuators with power electronics converters. When assembling such an heterogeneous set of modules on a single package (Systems on Package: SoP) or integrated circuit substrate (Systems on Chip: SoC), compatibility issues are soon to arise from many possible point of views. In this thesis, we will address the physical electromagnetic point of view. We aim to encompass phenomena that range from the well known electric field capacitive cross-talk, to the more challenging magnetic field inductive coupling, and even full-wave propagating electromagnetic field couplings. We find the standard approach to Electro-Magnetic Compatibility (EMC) used on Systems on Board (SoB) quite inappropriate for Systems on Chip (SoC) where prototyping, metal shielding and ground planes are often expensive, and sometimes completely impractical. In the first part of the thesis we propose instead an accurate and efficient three dimensional electromagnetic field solver as a valuable tool for verifying the design against all sorts of electromagnetic interference before fabrication. In the second part, we propose modeling techniques as a valuable tool for characterizing each module with respect to its electromagnetic properties, so that higher level circuit simulators can be used effectively to check the compatibility of different blocks. In the third part of the thesis we argue that compatibility should be achieved through an automatic interconnect synthesis process, enabled by our newly developed parameterized modeling technique.

The new generation of fast electromagnetic analysis programs, based on accelerated integral equation methods, has reduced the time required to analyze thousands of simultaneously interacting conductors from days to minutes. However such solvers are either inappropriate for, or are very inefficient at, analyzing interconnect exhibiting *high frequency effects*. With processor clock speeds exceeding two gigahertz and harmonics exceeding twenty gigahertz, high frequency effects cannot be ignored. The effects that are most troublesome for fast solvers are skin and proximity effects. Such phenomena can significantly affect interconnect performance and should not be neglected, in particular when either wire width or thickness is greater than two "skin-depths." Interconnect performance on Printed Circuit Boards (PCB) and on IC Packages has suffered from such effects for many years. Even some Integrated Circuits are now starting to be affected at the global interconnect level (power, ground and clock distribution networks). For instance skin-depth in aluminum interconnect at the tenth harmonic of a two gigahertz clock is around a half micron. Skin and proximity effects are troublesome for current fast solvers because they generate an exponentially varying current distribution inside each conductor. Trying to represent that current variation using the standard piecewise constant basis functions commonly available in fast solvers requires a large number of unknowns. Since the computation time for fast solvers is supposed to increase only linearly (more precisely $O(n\log(n))$) with the total number n of basis functions used in the problem, it may seem that the increase in unknowns to represent current variation is not that problematic. However, when many basis functions are used to represent

the current variation in a cross-section of a conductor, those basis functions interact densely in a way that can not be reduced by the algorithms used on most fast solvers. Thus, the computation time for modeling high frequency effects increases with the *square* of the number of unknowns required to model the current variation within conductors even for fast solvers. Two contributions of this specific Ph.D. work concentrate on addressing this issue by generating specialized basis functions, which more efficiently capture the exponential variation in the conductor current. Specifically we use the Helmholtz equation for the interior of the conductors to generate analytic solutions in one case (the ***conduction modes basis functions***) and numerical solutions in the other case (the ***proximity templates basis functions***). Both basis functions can be employed to discretize the Mixed Potential Integral Equation (MPIE) with a Galerkin technique. Both new sets of basis functions result in simulation times and memory requirements 400 times smaller than with piecewise constant basis functions. The analytical basis functions are more flexible when combined with model order reduction algorithm. The numerical basis functions are more flexible when handling general wire cross-sections.

Electromagnetic analysis of a collection of interconnect is an essential tool for the verification of modern electronic circuits. However, of possibly greater importance, is the ability to capture such detailed, accurate and typically time consuming electromagnetic analysis into a small model. Quick evaluation of the model is essential for an acceptable time domain simulation speed in a circuit simulator. At the same time, parasitic extractor accuracy is essential for providing to the circuit designer the confidence that the actual fabricated electronic circuit will perform as predicted by the circuit simulation. Finally, producing models that preserve important system properties such as stability, passivity, and causality is crucial for a numerically stable behavior of the models when used in any time domain simulator. The problem of preserving passivity has been partially address only recently by an algorithm (PRIMA). PRIMA can be applied only when the system to be modeled can be formulated in a very specific form. A way to formulate systems in such form has been given in literature for a general collection of conductors. No approach to ***preserve passivity*** is available instead when ***dielectrics*** or an ***IC substrate*** are present, or when ***full-wave*** analysis is needed to model systems whose dimensions are not small compared to wavelength (such as on todays' PCB and packages, and in future IC power network grids). Two contributions in this thesis address exactly such points providing passivity preserving reduced order modeling algorithms for such applications.

Model order reduction is typically a two-step procedure. In a first step one would typically apply the algorithms mentioned above since they can handle extremely large collection of interconnect and they can reduce them to an intermediate model. In a second step, better reductions are typically obtained employing the more optimal but also more computationally demanding Truncated Balance Realization (TBR) algorithm. Unfortunately this algorithm, in the form available in literature, does not necessarily preserve the passivity of the models it reduces. In another contribution, we developed a technique that has the same compression capabilities as ***TBR***, but in addition it is also guaranteed to ***preserve passivity.*** Furthermore, our algorithm does not require the system to be in any special form.

All interconnect models mentioned so far are intended for a higher level circuit simulator for verification of a given design. In a third part of this thesis we begin to address the "synthesis" problem. We develop a ***parameterized model order reduction*** technique that produces models that feature field solver accuracy when some pre-identified geometrical parameters (such as wire widths or wire spacing) are allowed to vary in a design exploration space. Our models are small enough to be used within an optimization loop by for example an interconnect router. Furthermore, the presented model generation approach is automatic. It is based on a very fast multi-parameter moment matching model-reduction algorithm. Thus parameterized reduced models can be constructed "on the fly", and can account for any possible interconnect or circuit block already committed to layout, e.g. when designing and optimizing an interconnect bus or power and clock distribution networks.

Professor Alberto L Sangiovanni-Vincentelli
Dissertation Committee Chair

To my family

Contents

Acknowledgements

Undoubtedly I owe to both my advisers, Prof. Alberto Sangiovanni-Vincentelli (UC Berkeley), and Prof. Jacob White (MIT) a great deal. They have greatly supported me under every possible aspect of this long and difficult journey. They have been continuous source of motivation, and inspiration. They have provided guidance, technical criticism, valuable feedback. And at times they have been even fathers and friends when a few personal problems attempted to mine the success of this journey.

There is a third person, Dr. Joel Phillips (Cadence Berkeley Labs), that I truly feel I can address as co-adviser for this work. Two important contributions of this thesis have originated from a summer internship at Cadence Berkeley Labs under his supervision. Most importantly, the still ongoing interactions with Dr. Phillips subsequent to that internship have brought to my work both deep theoretical understanding as well as attention to practical implications and industry needs.

I would also like to thank the other two members of my committee: Prof. Hald (UC Berkeley), who has provided valuable feedback during my qualifying exam and during my dissertation talk, and Prof. Robert Brayton (UC Berkeley), who has reviewed with overwhelming attention and criticism my thesis. I feel I learned quite a lot about technical writing by studying his many comments.

Many people have contributed to this work with interactions and technical discussions, or by providing code I could build upon. Among them I would like to mention: Prof. Luis Miguel Silveira (Tech. Univ. of Lisbon, Portugal) for collaborating on the passive truncated balance model order reduction project; Prof. Andreas Cangellaris (University of Illinois, Urbana-Champaign) for many discussions and feedback on transmission liner solvers and on different 3D field solvers, as well as on model order reduction techniques; Jung Hoon Lee (MIT) for reading so carefully this thesis pointing out not only many typos but also for providing very useful feedback and comments, Jung Hoon Lee together with Prof. Alexandre Megretski have also contributed with discussion on model order reduction using FFT methods; Xin Hu (MIT) for further developing the idea of the "conduction modes"; Zhen Hai Zhu (MIT) for daily discussions on electromagnetic formulations; Thomas Klemas (MIT) for discussions on passive model order reduction of structures with dielectrics; Carlos Coelho (MIT), for providing preprints of some relevant publications; Alessandra Nardi (UC Berkeley) for collaborating on the current injection spectrum estimation project; Dr. Matt Kamon (Coventor), and Dr. Nuno Marques (Alcatel) for providing "fastpep" code and examples; Prof. Paolo Tenti (Universita degli Studi di Padova, Italy) Prof. Seth Sanders (UC Berkeley), Prof. Charles Sullivan (Dartmouth College), and Prof. Mauro Feliziani (Universita degli Studi dell'Aquila, Italy), for discussion on power electronics applications and electromagnetic compatibility; Prof. Flavio Canavero (Politecnico di Torino, Italy) and Dr. Carla Giacchino (HDT Italia) for discussion on electromagnetic field solvers; Dr. Michael Tsuk (HP), Dr. Marco Sabatini (Barcelona Design), Dr. Norman Chang (Apache Design Solutions), Dr. Shen Lin (Apache Design Solutions), Dr. Diego Lasagna (Magneti Marelli), Dr. Piero De la Pierre (Magneti Marelli), Dr. Damiano (Magneti Marelli), Dr. Saverio Pezzini (STMicroelectronics), Dr. Montagnana (STMicroelectronics), Dr. Sekine Kazutoyo (Sony) for discussion on industrial electromagnetic compatibility problems.

Over the years this research has been in part founded by the Hewlett Packard Company, Conexant, the MICRO California program and the Semiconductor Research Corporation (SRC). In particular the SRC during the past three years has provided a significant International Graduate Fellowship. I really enjoyed being part of the SRC family. Participating to their many conferences, workshops and reviews allowed me to meet many people from industry and I feel this has steered my research toward the most pressing problems of today and tomorrow IC design industry.

Finally I would like to spend a special word of appreciation for my parents and for my grandmother. Leaving my country and my family has been difficult for me, but I recognize it must have been even harder on them. Nevertheless they have always supported and encouraged me: Thanks!

And now in Italian for them: Infine vorrei dedicare un speciale ringraziamento ai miei genitori e mia nonna. Lasciare il mio paese e la mia famiglia e' stato difficile per me, ma mi rendo conto di come debba essere stato ancor piu duro per loro. Cio' nonostante mi hanno sempre sostenuto e incoraggiato: Grazie!

Berkeley, June 18, 2003 *Luca Daniel*

Chapter 1

Introduction

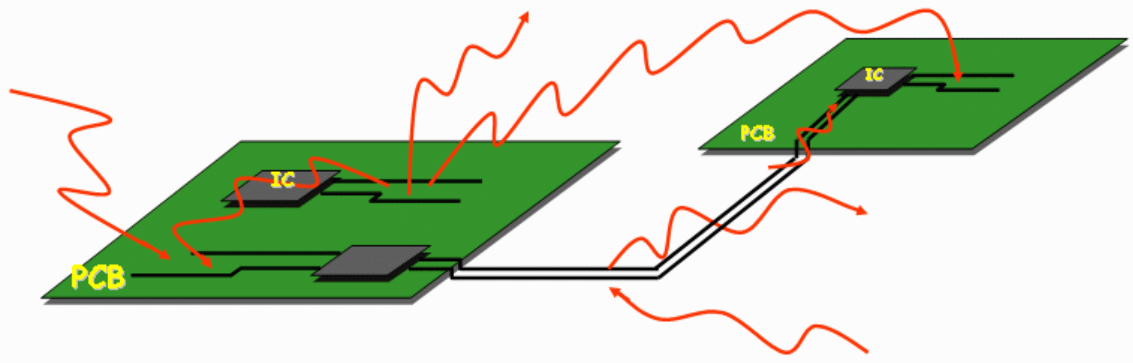

Figure 1.1: *Electro-Magnetic Interference (EMI). Arrows indicate static, quasi-static electric or magnetic fields, and propagating electromagnetic fields that are produced by electronic circuits and can cause their malfunction or the malfunction of other nearby circuits.*

Many future electronic systems will consist of several significantly heterogeneous modules such as Opto-Electronic and analog RF links, mixed-signal analog to digital converters (ADC), digital signal processors (DSP), Central Processor Units (CPU), Memory modules, Microfabricated Electro-Mechanical (MEM) resonators, sensors and actuators with power electronics converters. When assembling such an heterogeneous set of modules on a single package (Systems-on-Package: SoP) or integrated circuit substrate (Systems-on-Chip: SoC), compatibility issues are soon to arise from many possible point of views. In this thesis we will address the physical electromagnetic point of view.

Electronic circuits inevitably produce both static and quasi-static electric and magnetic fields, as well as also propagating electromagnetic fields. At the same time, similar fields present in the environment where an electronic circuit is supposed to operate, could potentially cause its malfunction. Such phenomenon is identified with the general term *Electro-Magnetic Interference (EMI)*. Ensuring *Electro-Magnetic Compatibility (EMC)* of an electronic system means ensuring its correct operation with respect to all possible electromagnetic interference phenomena.

A way to achieve EMC consists of finding a compromise between the levels of emissions from a device and the levels of susceptibility of other adjacent devices. For this purpose, standards have been introduced to specify maximum emission levels, and, in some cases, to specify susceptibility levels. Designing for EMC, according to the classical methodology, means ensuring that each device satisfies the predefined standards.

Traditionally, electromagnetic interference is classified as *conducted* and *radiated*, according to the method of transmission of the disturbances. Fig. 1.1 illustrates some of the EMI phenomena. Conducted interference

refers to any transmission of disturbances by means of conductors. In power electronics, such disturbances are induced into the power delivery network by for example electric motors, or switching power supplies. In integrated circuits (ICs), conducted interference would include substrate currents, or the current spikes induced into the chip power supply network by the switching activity of the digital gates. In a broader definition, interference transmitted a short distance by a simple electric field (capacitive cross-talk coupling) or by a simple magnetic field (inductive coupling), could also be considered as conducted interference. *Quasi-static* circuit modeling theory is applicable for their analysis. For example, coupled inductors can model the magnetic coupling between two close pins of a package. Capacitors could model the cross-talk due to electric field coupling between two long and close conductors. Conducted interference has been studied and extensively characterized in the literature at the Printed Circuit Board level (PCB). At that level, many methods to control its effects are known at that level. For example, in power electronics and electric motors, filters have been designed to suppress such interference into the power delivery network. In contrast, in ICs or IC packages, only a few problems concerning conducted interference have been addressed. For instance, substrate noise on ICs has been characterized [91, 22], and design techniques to control cross-talk effects have been developed [75]. However, much research work is still needed, in particular with respect to conducted emissions produced by the switching activity of digital IC's onto the power and ground system.

Radiated interference is concerned with transmission of disturbances by means of propagating electromagnetic waves. In this case, distances between source and victim are usually not negligible compared to the wavelength. The electric and magnetic fields are interdependent. Simple quasi-static circuit models cannot be used to model this type of transmission. Efficient and accurate analysis and modeling techniques for radiated interference are not available for any type of electronic system (ICs, packages or even PCBs).

In this research, we have developed a design methodology for EMC consisting of a simulation tool and of a set of modeling and design techniques considering both conducted and radiated emissions in PCBs and in ICs. In this introduction we first show the emerging trend toward component-based design styles such as Systems-on-Chip (SoC)[60]. We then describe the classical approaches to EMC and analyze if they can be employed also for SoC. To handle complexity, we formalize the compatibility problem using a hierarchical abstraction of the electronic systems. We conclude by suggesting a design methodology working on the principles of our hierarchical model. In the reminder of this thesis subsequent chapters will be geared toward supporting our methodology by providing a collection of tools and techniques both for the EMI analysis, modeling, and the EMI-aware synthesis of electronic circuits. In particular, the remaining chapters are grouped into three *"Parts"*:

- Chapters 2 to 6 in Part I describe the design of our EMI simulator. Chapters 2 and 3 review existing techniques, while Chapters 4 and 5 provide two contributions aimed at enabling full-board or full-chip EMI analysis by speeding up simulator runtime and reducing memory requirements by factors of 400.
- Chapters 7 to 13 in Part II describe techniques for constructing small and accurate electromagnetic models of interconnect that can be used in higher level circuit simulators. Introductory Chapters 7 to 10 describe the state of the art in this new field. Chapters 11 to 13 provide the details of three contributions, aimed at preserving crucial properties such as passivity for the generated interconnect models.
- Chapters 14 to 16 in Part III describe some modeling techniques supporting automatic and optimized synthesis, such as constructing geometrically parameterized interconnect models (in Chapter 15), and optimally sizing decoupling capacitors (in Chapter 16).

1.1 The high frequency electronic system design scenario

1.1.1 Systems-on-Board (SoB)

Electronic systems consist nowadays of one or more Printed Circuit Boards (PCB), on which different components (e.g. ICs and discrete elements as shown in Fig. 1.2), are placed and interconnected. The system

designer chooses from different available integrated circuit providers. The ICs are mounted on the board and connected using planar interconnect wires (sometimes referred to as traces).

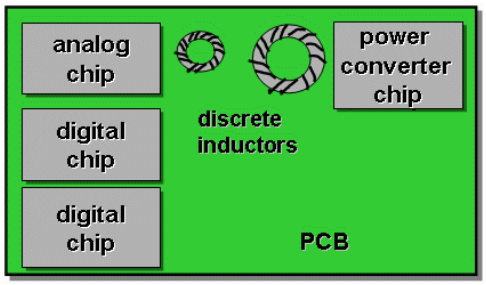

Figure 1.2: *System-on-Board (SoB).*

1.1.2 Systems-on-Chip (SoC)

With the advent of Deep Sub-Micron (DSM) technologies, an entire system can be embedded on a single integrated circuit, including programmable components, memory and peripheral units [44, 1, 60, 70] as sketched in Fig. 1.3.

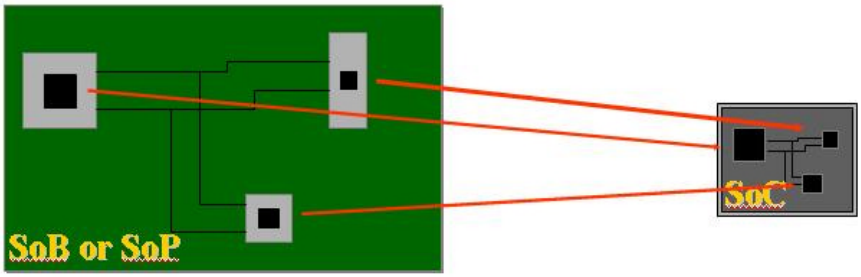

Figure 1.3: *Complete electronic systems, once assembled as Systems on Board (SoB) are beginning to be assembled as Systems on Package (SoP) or Systems on Chip (SoC).*

Electronic systems will then consist of a single package or a single chip as shown in Fig. 1.4, on which different components are placed and interconnected, e.g. digital, analog and power electronics Intellectual Property (IP) circuit blocks, integrated inductors and Micro-Electro-Mechanical (MEM) devices both for RF signal filtering and for power electronics energy storage and conversion. The system designer chooses from different available IP component providers. The IP circuit blocks or microfabricated passive components are then realized on a common integrated circuit and interconnected, using on chip wires.

Because of the enormous complexity of these ICs, few companies will be able to design the entire set of components for SoC. Hence, system companies will create pressure on semiconductor manufacturers to incorporate components designed by other design companies. A new market of IPs will come of age, where designs will be produced and traded as chips are today. To make this evolution possible, IP blocks will have to be easily mixed and matched with other IP's coming from many sources. This requires each component to be somewhat insensitive with respect to its environment, both at the functional and the physical level.

1.1.3 Main EMI problems for system design

To support the emerging design style described above, increasing attention needs to be devoted to ensure proper component encapsulation. Encapsulation is relative to a particular phenomenon of interest. While

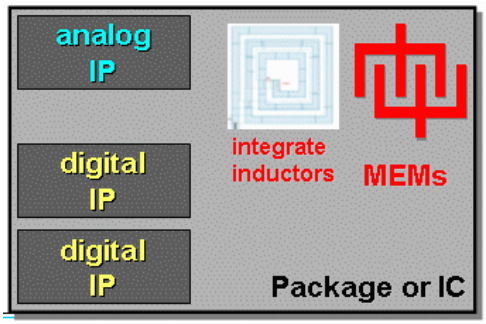

Figure 1.4: *System-on-Package (SoP) or System-on-Chip (SoC)*

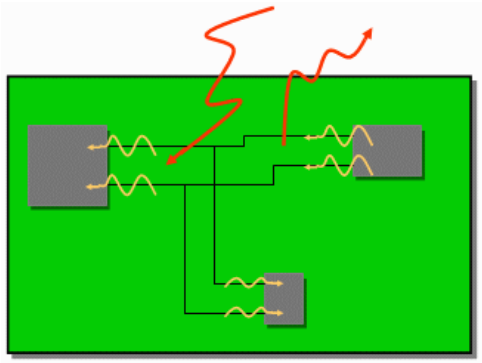

Figure 1.5: *Spikes of current produced by the internal switching activity of the digital components employed in a SoB, SoP or SoC can escape as conducted emissions and contaminate the global power distribution system. There, they can find long enough wires to be irradiated as propagating electromagnetic fields. On the other hand, significant electromagnetic fields can induce noise currents and voltages in long interconnect wires that will result in component malfunctions.*

electric cross-talk, impedance matching, electro-migration have all been considered in a way, all other conducted and radiated EMI phenomena have not been properly addressed this far. Since EMI emissions and susceptibility are of growing importance, as frequencies keep increasing in the GHz region, this encapsulation aspect needs to be addressed as well, in order to ensure the design quality and design time expected by this new SoC design style.

We further recognize that EMI problems are mainly due to two mechanisms: EMI emissions due to the components' switching activity, and emissions and susceptibility of the communication wires interconnecting the components.

EMI emissions due to the switching activity of digital components

Most of the components used to assemble SoB, SoP or SoC, typically contain fast switching digital circuit blocks. Thousands to millions of gates may switch at the same time producing large spikes of currents in the power and ground connections of the block. Such currents are very-high-frequency conducted emissions that escape from the component, "polluting" the entire power and ground system. Flowing on the much longer wires of the power and ground grid, they can easily find favorable "dimension to wavelength" ratios and radiate. This phenomenon, depicted in Fig 1.5, can be responsible for the largest portion of EMI emissions.

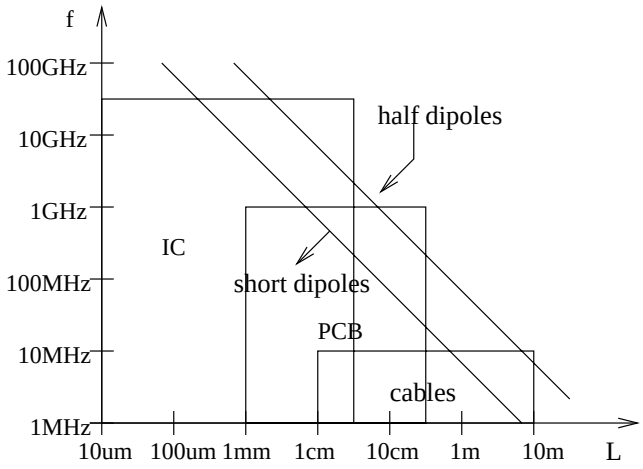

Figure 1.6: *Typical harmonic contents and wire lengths on present and future electronic systems.*

Emissions and susceptibility of communication wires among system components

Components are connected by wires to provide the necessary functionality. I/O communication wires represent a second very important issue, both for EMI emissions, and for susceptibility.

Such wires carry high frequency communication signals between blocks and can be long compared to the wavelengths of the harmonics of the signals they carry. EMI emissions in this situation are very likely unless a close return path is provided.

Such wires can be very susceptible to radiation present in the environment, or coming from nearby systems. Incident electromagnetic fields can induce currents and voltages on such wires as shown in Fig. 1.5. These are mixed with the signals on the wires, and act as noise to the receiving input buffers. Severe and apparently inexplicable faults can result when this noise exceeds than the noise margins of the receiver.

1.1.4 Is EMI a problem for System-on-Package or System-on-Chip?

The problems described in the previous section are already a major concern in the design of today's SoB while they have not been a concern at package and IC levels yet. We believe that EMI due to communication wires connecting components will become a problem for SoP where dimensions will be comparable to signal wavelengths. This specific problem is not instead expected for SoC since on-chip communication wires between distant circuit blocks will always be "segmented" by buffers (repeaters), latches, registers or even "*relay stations [17]*".

However, EMI emissions due to digital switching activity, will represent a major concern both for future SoP's *and for SoC's*. We outline our arguments in the following.

1. ICs dimensions have been too small compared to the signal frequencies and their harmonics. However, there is a steady trend toward higher frequencies, meaning smaller wavelengths. Soon SoC power and distribution networks will have the same wire-lengths to wavelengths ratios observed in present SoB as shown in Fig. 1.6 and 1.7. Power and ground wires of length comparable to the wavelength can pose a severe risk on EMI emissions and susceptibility in IC's. Fig 1.7 shows the wire dimension ranges of electronic systems compared to their ranges of frequencies; signal harmonics are included in the plot. For example, consider a typical today's system-on-PCB. Wire dimensions can be on the order of 10 cm, clock frequencies on the order of 100 MHz, with harmonics on the order of 1 GHz and wavelengths on the order of 30 cm. Such systems can be quite susceptible to EMI problems. This happens mainly because the wire dimensions are as long as wavelengths. The same ratio between wire dimensions and

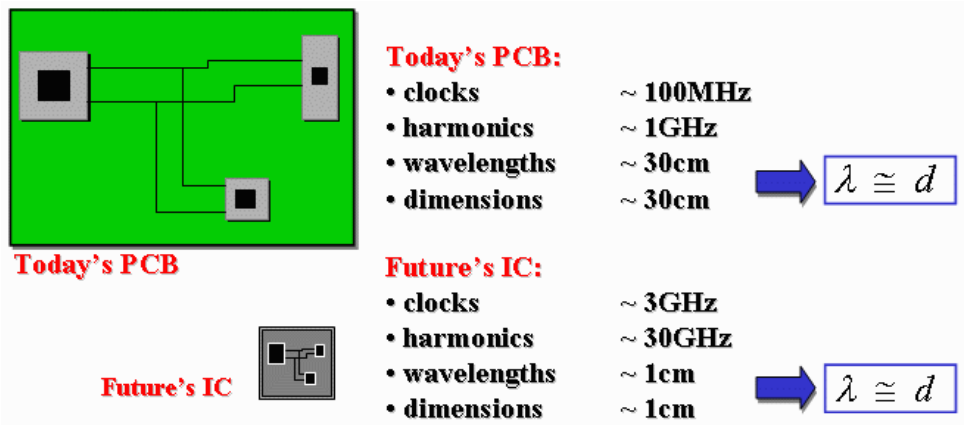

Figure 1.7: *Future IC's power and ground wires will have the same wire-length over wavelength ratios observed in todays PCB, responsible for most EMI problems.*

Figure 1.8: *Trend of interconnect behavior for global on-chip interconnect (ground, supply and clock distribution networks). Power distribution networks on global interconnect are not so resistive as local interconnect and may be then affected by resonances.*

wavelength can be found in future Systems-on-Chip. For example, consider a chip with power and ground wires on the order of 1 cm, clock frequencies on the order of 3 GHz, harmonics on the order of 30 GHz, and wavelengths on the order of 1 cm. These systems would have the same ratio, about 1, and could possibly have EMI problems similar to the today's PCB systems.

2. One objection to the argument above might be that wires on chips are quite resistive, and tend to behave like RC lines, rather than transmission lines and therefore cannot resonate. This has been true so far, but there is a trend toward the use of lower resistivity materials such as copper in place of aluminum. Inductance is already becoming a problem for global on-chip interconnect. Such interconnects behave now very much as RLC lines, rather than RC lines as shown in Fig 1.8. This suggests a behavior similar to PCB, where one can observe both RLC resonances, as well as resonances related to wire wavelengths. Such resonances could cause large oscillations on IC power networks resulting in the same EMI problems observed on todays' PCBs.

3. In today's SoB the highly inductive pins or wire bonding often provide a natural physical isolation for digital components (ICs) by blocking their high frequency conducted emissions due to their internal switching activity. This isolation is slowly disappearing in SoP where less inductive solder balls are used. Low inductive connections are desirable for a circuit block because they increase the speed of I/O communication with other blocks, and they increase the internal switching speed providing faster di/dt. However that fast di/dt becomes a problem for the environment by leaking very high frequency harmonics to the power and ground networks. This phenomenon will be particularly relevant in SoC where each digital circuit block does not have any inductive isolation from the rest of the on-chip global ground and supply network as shown in Fig. 1.9.

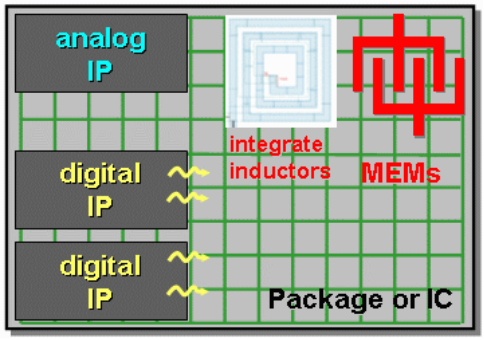

Figure 1.9: *Some issues in high frequency SoC Design: digital IP circuit blocks, because of their internal switching activity, can leak high frequency currents and contaminate in this way the power and ground distribution grid of the entire package of IC.*

4. One might argue that on-chip nearby metal interconnects would provide enough return current paths to eliminate any radiation or susceptibility problem. This would be true if every single interconnect would be close enough to the power or ground grid. However, today's digital designers do not address this condition; thus return current paths are typically very complicated as illustrated in Fig. 1.10. The

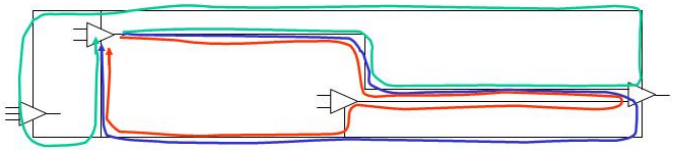

Figure 1.10: *Return current paths.*

layers above and below a wire usually carry orthogonal wires. Although for capacitive purposes such orthogonal wires look like an almost uniform metal plane, they often cannot provide a useful return path for inductive or radiation purposes. In some designs, tens of layers are available, e.g. relatively expensive modern and fast microprocessors, and one or more layers are used as complete metal planes. However, many ICs cannot afford such waste in routing area.

1.2 The present approaches to EMC for System-on-Board

1.2.1 The "Build, Test and Hope!" design methodology

In many electronic design companies, the following approach to EMC is used. A prototype of the circuit is built, usually with very little, or no regard for EMI issues. Emissions, and sometimes susceptibility, of the prototype are then measured in a semi-anechoic chamber. If the prototype does not pass the test allowed by the compatibility standard in use, an EMC expert is employed. who tries to guess what the problem is, mainly based on previous experience with somewhat similar problems. Once problems are identified, the EMC expert tries to suppress them using a broad range of techniques and tricks, e.g. adding components (such as decoupling capacitors), metal shields, suggesting a re-routing of some wires, or the addition of ground planes. Even worse, the re-layout of the whole circuit might become necessary!

This approach, in almost all cases, leads to the solution of the problem at PCB level. However, it has potentially for high costs in terms of added components and metal shields. Furthermore, if the whole circuit needs to be re-designed, design time and cost could double, causing the company to miss the tightly budgeted market window for insertion of the product.

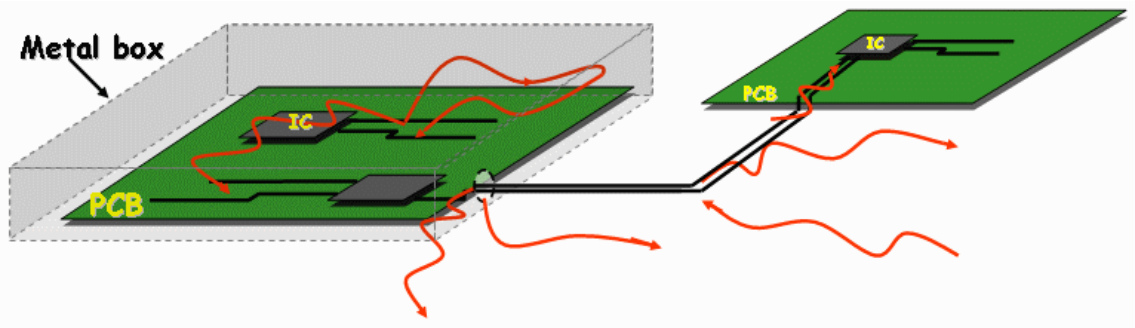

Figure 1.11: *Metal shielding around an electronic circuit. Some disadvantages are here shown: internal interference is not blocked, the shield may cause reflections toward the circuit itself, and the emissions from apertures and cables still persist.*

1.2.2 Shielding

As mentioned, shielding, shown in Fig. 1.11, is a common technique for obtaining compatibility. A metal shield can block electromagnetic waves. Even though shielding might seem the solution to all EMI problems, it has several important disadvantages. For instance, shielding can be very *expensive*, specially for "cheap systems." Using metal shields for relatively expensive equipment such as desktop computers, servers etc. might not affect the overall cost of the product very much. However, shields in portable computers, cellular phones, pagers, embedded systems, etc. where cost and weight are a major concern, might not be feasible.

Furthermore, a metal shield can block interference between the circuit and the surrounding environment, but it cannot block interference between components *within* the circuit itself as depicted in Fig. 1.11. As a matter of fact, a metal shield acts as a mirror, thereby blocking electromagnetic waves from propagating further. The incident field induces currents on the metal surface of the shield. Such currents *radiate back* toward the circuit inside the shield (Fig. 1.11). Thus the circuit inside the shield can be affected by its own radiation emissions.

A completely closed shield would be an effective way to block almost all emissions. Unfortunately, *apertures* on the shield are needed for communication and power cables, or for cooling. Such apertures interrupt the flow of the previously mentioned currents. Electric fields can then develop across the apertures, acting as emitting antennas toward the exterior of the shield. In some cases, emissions from apertures can be as large as the emissions without a shield.

Communication and power *cables* can carry high frequency currents, such as common mode currents. Such currents can easily radiate, but the shield would not be able to block such emissions. Cables can also pick up external fields, and conduct the disturbance to the circuit. Once again the shield cannot block such interference.

1.2.3 Ground planes

Insertion of a uniform metal plane as a layer of a PCB is a very effective and commonly adopted technique to control EMI. A uniform metal plane presents a very small impedance return path for all wires of the layers above and below. Thus very close current loops are achieved, and small emissions and susceptibility are possible. This is a very good solution for all electronic systems that can afford it, i.e. reasonably large and expensive systems, but many other electronic systems cannot afford this. Often a PCB designer is constrained to work with 2 or 4-layer boards; thus routing area cannot be wasted in a uniform metal plane. Examples of such applications are small portable devices (pagers, cellular phones, etc.), printers, embedded systems, ignition circuits for the automotive industry. Surprisingly, even a system running at relatively low frequencies can present large EMI problems. While large and fast servers and computers can benefit from all kinds of

ground planes and metal shielding, the slower embedded system circuitry cannot afford such amenities and often has EMI problems not easy to solve.

1.3 Motivations for an EMI simulator and an EMC design methodology

In the previous sections discussed how the present approach to EMC at the board level is both costly and time consuming, especially for cheap systems where shielding and ground planes are not an option. A key problem of the present approach, is that EMC is addressed only *after* the design stage. Often the EMI problem becomes evident only after a prototype has been built and tested. To address these concerns, simulation tools and a design methodology that *addresses the problem at the design stage* are needed.

Among the advantages of simulation we note that it can cut the cost and time needed to build and test a physical prototype. A simulator could, in fact, check if a circuit will pass measurement tests in the early stages of the design. It can help isolate the problems. Measurements of quantities at points otherwise unreachable by physical instruments become possible. It can provide fast exploration of alternative solutions. "What if" analysis can be performed and an optimal solution with small cost can be achieved in short time.

In addition to simulation, we propose a new "correct by construction" design style, where each action is taken and verified as part of a budgeting plan that ensures EMC during the design process. Prototyping should stop being an iterative process. We hope that, with some of the techniques presented and others developed in the future, prototyping will eventually become simply the *one time* and final certifying step of the design cycle.

1.4 Our design methodology for EMC

We propose a design methodology to help ensure EMC at the design stage. This consists of a collection of EMI-aware tools and techniques that can be used according to a hierarchical budgeting/verification strategy early in the design and assembly of today's Systems-on-PCB or tomorrow's Systems-on-Chip. First, we present a hierarchical abstraction of an electronic circuit from the EMC prospective. This model leads to a formal definition of the compatibility problem. Finally, we describe the suggested procedure step by step.

1.4.1 A hierarchical abstraction of an electronic circuit from the EMC prospective

Considering a system under different abstracted points of view is a useful design technique. For example, timing issues are usually analyzed separately from functionality issues. In this section, a system abstraction of an electronic circuit from the EMC prospective is given, which decouples the EMC problem from other design issues such as timing and functionality.

Every wire on a circuit can potentially interact with every other wire. Considering all such interactions during the design stage would be too complex for a large circuit. To handle complexity and to facilitate design re-usability, a hierarchical structure is proposed. As illustrated in Fig. 1.12, at each level of the hierarchy the following components are considered: circuit block components, the wires connecting them, and the surrounding environment.

Component characterization

Each of these elements is regarded as a "system component". A system component can be characterized from the EMC point of view specifying:

- ***Radiated emission spectrum,*** i.e. the field $|R(d_0)|$ radiated from the component at, for example, a standard distance d_0 as shown in Fig. 1.13.

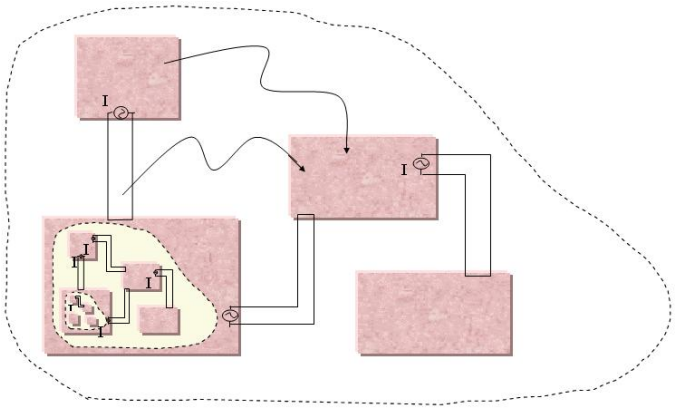

Figure 1.12: *Hierarchical abstraction of an electronic circuit from the EMC prospective*

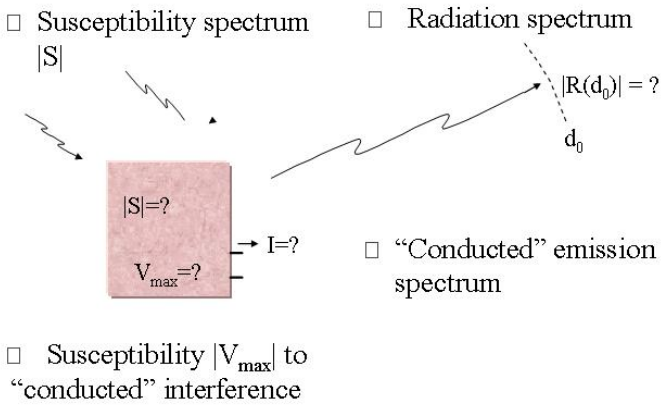

Figure 1.13: *Component characterization from the EMC point of view.*

- ***Radiated susceptibility spectrum,*** i.e. the maximum field $|S|$ that does not cause malfunctions in the component
- ***Conducted emission spectrum.*** Radiation from wires attached to component terminals depends on which currents excite them. For each pair of terminals, equivalent current or voltage sources and impedances should be specified in order to derive the actual currents exciting the attached wires.
- ***Conducted susceptibility spectrum,*** i.e. the maximum tolerable noise level for each pair of terminals that does not cause malfunctions.

A similar characterization is required in part by the several EMC standards imposed by the governments of many countries. Our proposed characterization approach is different from the existing EMC standards since such standards typically specify only emission requirements. Susceptibility requirements are usually imposed only by military standards, or by some specific markets such as the automotive electronics. However, susceptibility characterization might become necessary for any product, if a top-down design approach is used. Susceptibility characterization might also be useful for re-usability issues, or when subcomponents are bought from other providers in a system-assembly design style.

Furthermore, EMC standards usually impose limits on conducted emissions by specifying the voltage levels developed on a standard impedance load for frequencies up to 30MHz. However, for the abstracted

model presented in this methodology, also conducted characterization should be specified in the range of frequencies associated with radiation (typically up to 30GHz).

1.4.2 Formal definition of Compatibility

Definition 1 *Electromagnetic compatibility, with respect to radiated EMI in a system abstracted as in the previous section, exists if for each level of the system hierarchy, for each component j, and each frequency f:*

$$\sum_i R_i(f,\mathbf{x}_j) \leq S_j(f), \tag{1.1}$$

where $R_i(f,\mathbf{x}_j)$ is the field produced by component i at position $\mathbf{x}_j$ and frequency f, while $S_j(f)$ is the susceptibility level of component j at frequency f, i.e. the maximum field at frequency f that component j can tolerate without malfunctioning.

This definition, simply states that the total field at position $\mathbf{x}_j$, where component j is located, and due to the contributions R_i of all the other components, should not exceed the maximum field S_j that it can tolerate. A similar definition is given in [134].

A simplifying assumption

A further simplification can be used if directions are neglected and only distances are used in the characterization of every component. Values R_i and S_i corresponding to the directions of *maximum* radiation and susceptibility should be used in this case. Using such an assumption, the definition of compatibility becomes

$$\sum_i R_i(f,d_{ij}) \leq S_j(f) \tag{1.2}$$

where d_{ij} is the distance between component i and component j.

To evaluate the compatibility constraint in the previous equation, the radiation $R_i(f,d_{ij})$ of component i at the general distance d_{ij} can be related through a function $T(f,d_{ij})$ to the available information on its radiation $R_i(f,d_0)$ at its characterization distance d_0, as illustrated in Fig. 1.14,

$$R_i(f,d_{ij}) \leq T(f,d_{ij})\,R_i(f,d_0), \tag{1.3}$$

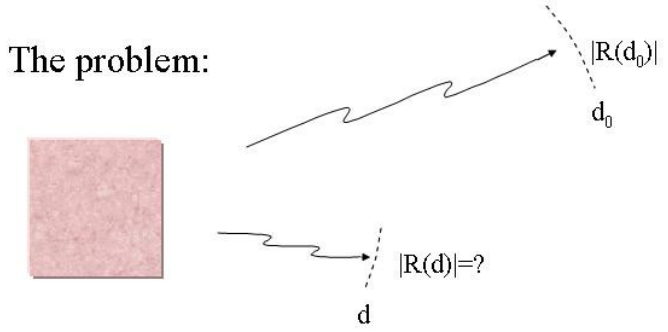

Figure 1.14: *Field at a general distance d can be related to the field at the characterization distance d_0.*

A matrix formulation for the compatibility problem

Assume the radiation and susceptibility spectra are specified over a finite set of frequencies $\{f_1, f_2, ..., f_M\}$, typically the clock and its first twenty harmonics. Define the radiation vector as

$$\begin{aligned}\mathbf{R} \quad = \quad & [R_1(f_1,d_0), R_2(f_1,d_0), ..., R_N(f_1,d_0),\\ & R_1(f_2,d_0), R_2(f_2,d_0), ..., R_N(f_2,d_0),\\ & ...,\\ & R_1(f_M,d_0), R_2(f_M,d_0), ..., R_N(f_M,d_0)].\end{aligned}$$

where N is the number of components. Define the susceptibility vector as

$$\begin{aligned}\mathbf{S} \quad = \quad & [S_1(f_1), S_2(f_1), ..., S_N(f_1),\\ & S_1(f_2), S_2(f_2), ..., S_N(f_2),\\ & ...,\\ & S_1(f_M), S_2(f_M), ..., S_N(f_M)]\end{aligned}$$

Now construct the matrix $\mathbf{T}$ evaluating the function $T(f_n, d_{ij})$ for every frequency f_n and distance d_{ij}. The general entry in position $[j, (n-1)N+i]$ of the matrix $\mathbf{T}$ is given by the evaluation of the function $T(f_n, d_{ij})$ where f_n is the n^{th} frequency in the considered set of frequencies and d_{ij} is the distance between component i and component j.

With the previous definitions, the compatibility problem can be reformulated in matrix form

$$\mathbf{TR} \leq \mathbf{S}. \tag{1.4}$$

1.4.3 A top-down Constraint-driven design methodology to ensure EMC

In this section, a top-down constraint driven design methodology is proposed, to ensure the EMC of an electronic system. This methodology has been used for other design problems such as analog IC design [20]. A somewhat similar methodology has been suggested for EMC design in [134].

The design methodology is summarized with the following steps:

1. Some of the components could be already available. For example a component library could be available, or components could be acquired from external providers. Such available components are assumed completely characterized. Their radiation and susceptibility spectra are known and just inserted in the vectors **R** and **S**.

2. Radiation and susceptibility levels of the components to be designed are budgeted according to the constraints stated by Eq. (1.4).

3. Once individual budget levels are known, the design of each component proceeds independently and hierarchically. Constraints are "down propagated". The radiation and susceptibility budgets of a component become its environmental constraints. Down propagation continues until "leaves", i.e. wires, are encountered.

4. Down propagation of budgeted radiation and susceptibility levels to wires can be achieved using the parameterized models presented in the Chapter 15. For example, radiation and susceptibility constraints easily translate into physical layout constraints on the maximum length of the wires, and in particular on the maximum allowed separation between a current and its return path. In case of emissions from the Vdd and Gnd systems due to the switching activity of a digital block, constraints can be down propagated to the sizing of decoupling capacitors as proposed in more detail in Section 16.2.

5. A "bottom-up" accurate verification phase is then required to check the actual radiation and susceptibility levels of the designed component against the assigned budget level. Chapters 2- 6 in Part I describe our design and implementation of such a tool.

6. If a large positive margin is found at the end of a component design and verification, a “re-budgeting” phase could redistribute this margin to other components where, for example, constraints were more difficult, or could not be met at all.

The main contribution in this thesis, described in the following chapters, is the development of a collection of tools and techniques both for the EMI analysis, modeling, and the EMI-aware synthesis of electronic circuits in order to support our methodology or similar design methodologies.

Part I

ANALYSIS

Chapter 2

Background: analysis tools

Examining the Signal Integrity (SI) and EMI simulation literature and market, one can distinguish, two general types of techniques: transmission lines based simulators, and three dimensional (3D) electromagnetic field solvers.

2.1 Transmission line simulators

The main steps of the Transmission-line (T-line) based simulators can be summarized as follows. Each wire is referred to its closest metal plane or planes (above and below) and modeled using a transmission line. Two nearby parallel wires carrying a fully differential signal can also be modeled with a transmission line, and group of nearby parallel wires can be treated as multiconductor transmission lines. Characteristic parameters of the line are calculated from the interconnect geometry by a parameter extractor, The extractor is typically a two dimensional electric field solver that calculates per-unit-length capacitance and inductance matrices C and L, as well as a series per-unit-length resistance matrix R accounting for conduction losses, and a a parallel per-unit-length conductance matrix G, accounting for dielectric losses,

$$\frac{dV}{dz} = -(R + j\omega L)I \tag{2.1}$$

$$\frac{dI}{dz} = -(G + j\omega C)V. \tag{2.2}$$

V and I are vectors with the voltages and currents along direction z of the conductors lines. Such model can be integrated in different ways with a SPICE like circuit simulator. For instance a a subcircuit model of the multiconductor T-line can be generated and included directly with the rest of the circuit for a SPICE like simulator analysis. Or one can use a specialized solver to handle the multiconductor transmission lines, and run a SPICE like simulator in parallel handling the rest the circuit. Electromagnetic radiation can be calculated once all currents on the lines are known, using superposition and Green Function integrals [103].

2.1.1 Advantages and disadvantages of T-line based simulators

As described above, the main and almost only disadvantage of T-line based simulators is the need for a clear and well defined return path for the current such as a parallel ground wire nearby or a metal reference plane. Without such a reference, the transmission line propagation hypothesis fails, and T-line based simulators cannot be used. In particular, we would like to underline that by metal reference plane we mean a *complete and uniform* metal plane. A layer divided into some islands of ground and Vdd partial planes does NOT satisfy this hypothesis. All wires crossing the intersection from a ground plane region to a Vdd plane region will not be in general simulated correctly. Holes on the plane and gaps can produce severe radiation that

would not be captured by T-line simulators. For these reasons T-line simulators may not be the appropriate choice for handling for instance two-layers PCB or 4-layers PCB without at metal plane reference.

Assuming a good reference is present, any T-line based simulator becomes a wonderful tool for Signal Integrity and maybe even for EMI analysis. Speed is for instance among the main advantages of the T-line based simulators. Such simulators can usually handle entire PCB systems. Their computation speed is as fast as a SPICE like circuit simulator. T-line simulators can also account naturally for reflections from unmatched loads or terminations. Because they work in the time domain, they can also easily account for non-linear devices and loads. Reflections from wire bends could be included without much effort, even though not many available simulators implement this feature yet.

2.2 Three dimensional field solvers

We have seen in the previous section how Transmission line simulator can be the tools of choice for all systems with a uniform metal plane or for those interconnect in a system that are fully differential. However, we have also discussed how such simulators are completely inadequate for systems with a partial and segmented metal plane or with no plane at all. For these systems, one cannot make any assumption on the type of propagation (e.g TEM transmission line modes). The best approach for this situation at the moment is solving numerically the Maxwell equations. There exist many different numerical methods. Each method has its own peculiar characteristics that makes it suitable for one particular application rather than another. It seems that so far no one single method is suitable for all types of application and simulation analysis. In this section, we try to give a brief summary of the main characteristics of the most important numerical methods in computational electromagnetics. Our focus will be in trying to underlying the advantages and disadvantages of each method rather than on giving any technical description of the method itself. We will point out what we think are the best applications for each method, and in the process, we will select an approach for our specific application: EMI simulation in electronic circuits.

Before we show the differences among the methods, let us present some common features. In particular, almost all numerical methods are characterized by the following three phases:

1. **Discretization of the simulation domain.** Numerical methods cannot generally work with continuous quantities. The simulation domain is therefore subdivided into elementary cells. The main idea for most methods is that such cells are so small that field or charge and current quantities within such cells can be considered uniform. Some methods need to use the same size cell for the entire domain. This usually leads to waste of memory. Others can discretize with smaller cell sizes regions of space where fields or other quantities vary more rapidly in space. Some methods need to discretize the entire domain of simulation. This also can lead to waste of memory and computation power. Other methods can discretize only the parts of the simulation domain that are of interest for the particular application (for example only conductors, or only the surface of conductors).

2. **Setup of a linear system of equations.** The main purpose of the discretization is to be able, in a second phase, to convert some forms of the Maxwell equations into a linear system of algebraic equations.

3. **Solution of the linear system.** Finally the system is solved using algebraic techniques that in some cases can exploit the underline physical structure of the problem.

3D solvers all discretize some form of Maxwell equations. We can distinguish four main classes based on the the domain of the operator (giving differential equation methods or integral equation methods); and the domain of the variable (giving time domain methods or frequency domain methods).

2.2.1 Differential methods vs. Integral equation methods.

The natural form of Maxwell equation is a system of differential equations. We call *differential methods* those methods that directly discretize such system. Examples are the Finite Difference Time Domain

(FDTD) method and the Finite Element Method (FEM). Differential equations methods discretize the entire domain. Hence they usually end up with huge linear systems to be solved (tens to hundreds of millions of unknowns). Fortunately, the matrices are very sparse because each cell in the discretization only interacts with its neighbor. Hence, they massively exploit sparse matrix algorithms for the solution of their system. Because they discretize the entire domain, they can easily handle very inhomogeneous problems, for example when material properties vary quite rapidly in space. However, modeling of open boundary problems can be problematic because of numerical reflections at the boundaries.

Maxwell differential equations can also be rewritten in an integral equation formulation as we show later the next Chapter 3. Tools that discretize such formulation are called *integral equation methods*. Examples are for instance the Method of Moments (MoM), or the Partial Element Equivalent Circuit (PEEC) method. Integral methods need to discretize only the "active" regions, for example the conductors, or the surface of the conductors. Hence, they usually end up with much smaller systems than the differential methods (hundred thousands to millions of unknowns). Unfortunately, the resulting linear system has a very dense matrix because each element in the discretization interacts to all other elements. Highly inhomogeneous media are difficult to model with these methods. On the other hand, open boundary conditions and thin wire-like geometries such as in circuits can be modeled easily.

We summarize in Table 2.1 the main characteristic of both integral and differential methods.

Table 2.1: *Comparison of differential vs. integral equation methods.*

Differential methods	Integral Methods
discretize entire domain	discretize only "active" regions
lead to huge but sparse linear systems	lead to small but dense linear systems
good for inhomogeneous materials	problems with inhomogeneous materials
problems with open boundary conditions	good for open boundary conditions

2.2.2 Time domain vs. Frequency domain methods

A second important classification of numerical methods can be done based on the domain of the variables. Time-domain methods can easily handle non-linearities, furthermore they can produce very educational and intuitive animations of the wave propagation phenomena. Among the main disadvantages, in order to produce a spectrum result they need to run a very long time simulation in which all the significant modes need to be exited and need to be given enough time to develop and eventually decay. Finally, a Fast Fourier Transform of the resulting time waveforms gives the desired spectrum. The most important example of a time domain method is the Finite Difference Time Domain (FDTD) method. Another example of a time domain method is the Partial Element Equivalent Circuit (PEEC) method [121].

Frequency-domain methods consider harmonic solutions of Maxwell equations, simulating the system only at specified frequency points, Among the advantages, they naturally provide the frequency response at the specified frequency with a reasonably short simulation time, so that if only a small frequency range is required, much computation can be saved. They produce dynamical linear systems on which it is possible to apply the *Reduced Order Modeling* techniques described in Part II to get very accurate broad range frequency responses without having to evaluate every single frequency point. Non linearities are problematic

for frequency domain methods. Usually the system needs to be separated into a non linear part and a linear part. The frequency domain method only handles the linear part. Examples of frequency domain methods are the Finite Element Method (FEM), and the Method of Moments (MoM). The Partial Element Equivalent Circuit (PEEC) method can be modified and used not only in the time domain but also in the frequency domain [68, 67].

We summarize in Table 2.2 the main characteristic of both time and frequency domain methods.

Table 2.2: *Comparison of time vs. frequency domain methods.*

Time-domain methods	Frequency-domain methods
can handle non-linearities	problems with non-linearities
run a long simulation exciting all significant modes and then take an FFT	solve for specific frequency points
can produce insightful animations	can exploit new techniques for fast calculation of the dominant eigenvalues

2.2.3 Examples of 3D field solver methods

Table 2.3 identifies according to the previous type of classifications some of the most popular electromagnetic field solvers.

Table 2.3: *Classification of some of the most popular numerical methods.*

	Differential Methods	**Integral Methods**
Time-domain Methods	**FDTD**	**PEEC**
Frequency-domain Methods	**FEM**	**MoM, PEEC**

FDTD: Finite-Difference Time-Domain. It is a differential, time domain method. For most of its implementations the entire simulation domain needs to be discretize in uniform cells. Maxwell differential equations are approximated by difference equations. One very simple and intuitive (although not optimal) example of such an approximation is illustrated in Fig. 2.1. As initial conditions one needs to specify the fields in every cell at the initial simulation time. Then, as shown in Fig. 2.1 cell fields are calculated for the next time step. The smallest feature of interest and the smallest wavelength of interest determine the cell size. The cell size and the desired accuracy, together with stability requirements, decide the size of the time step. This usually leads to large memory requirements to store fields on all cells, and very long simulation times to analyze significantly long system responses to excitations. This method is becoming appealing only recently

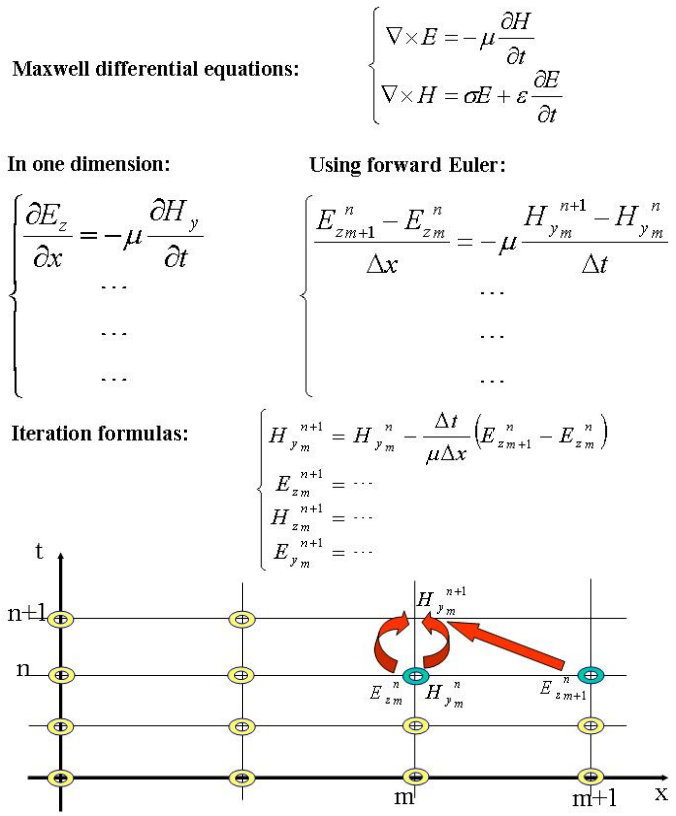

Figure 2.1: *One very simple and intuitive (although not optimal) example of a finite-difference time-domain (FDTD) numerical method.*

thanks to the availability of large computer memory and speed. FDTD can produce very nice movie-type animations of the wave propagation, facilitating very good understandings of the electromagnetic phenomena. FDTD can easily handle non-linearities being a time domain method. Furthermore it can also handle non homogeneous materials. The most critical disadvantage is the simulation of open field environment. In fact, field reflections due to numerical errors can be produced at the boundaries of the discretized domain. To overcome this problem, absorbing boundary conditions have been developed [117], but are still problematic in some applications. The simulation of the effectiveness of metal shields is one of the applications most suited for this method. The closed simulation environment of a shield is ideal for this method. Small apertures and attenuation across thick metals can also be modeled quite easily.

FEM: Finite Element Method. FEM is a differential method working in the frequency domain. The entire domain is discretized into cells. Cell sizes can be chosen according to the fast or slow variations of fields around some parts of the simulation domain. In particular, much larger cells can be used far away from sources or conductors or non-homogeneous media. Because the entire domain is discretized and non uniform cell sizes can be used, this method is ideal for highly inhomogeneous materials. Because of the non uniform cell sizes, the method has smaller memory requirements than FDTD for storing computed fields. However additional memory is required when storing explicit matrices for the computation. Because it works in the frequency domain, it naturally provides frequency responses but cannot handle non-linearities. The method has the similar problems of FDTD when dealing with open field environment.

MoM: Method of Moments. An integral equation method working in the frequency domain. Only the surface of the conductors are discretized. The method accounts for the interactions between all surface currents using for instance the Electric Field Integral Equation (EFIE) (eq. 3.14) formulations of Maxwell differential equations. The linear system resulting from the discretization is much smaller than in FDTD and FEM. This implies smaller memory requirements when using fast methods [152] that do not require explicit storage of the system matrix. The system is unfortunately very dense, because every surface element interacts with every other surface element. This method is ideal for open field environment simulations and can handle very efficiently antenna design application. In fact, in intentional antennae, frequencies are so high that currents mainly flows only on the surface of the conductors.

PEEC: Partial Element Equivalent Circuit. This is an integral equation method originally developed in the time domain [121]. A similar type of discretization based on the same integral equation can also be used in the frequency domain [67]. Conductor surfaces are discretize to capture charge accumulation or displacement currents. Conductor volumes are discretize to capture skin effects and proximity effects. This volume integral equation discretization seems suitable for the mixed simulation of electromagnetic and circuit phenomena. In this thesis we develop techniques for improving the frequency domain volume integral equation method which we describe in details in Chapter 3. Using such volume integral equation formulation in combination with fast methods requires a smaller amount of memory than FDTD and FEM for many electronic systems applications. The surface integral formulation of the MoM when combined with the same fast methods would have required an even smaller amount of memory. However, the MoM, in its original formulation [54], does not capture accurately current distributions inside the conductors that are important for the range of EMI frequencies and geometries. However new surface integral equation formulations are very recently being developed with good accuracy on wide frequency bands [152] and memory requirements smaller than the volume integral equation formulations.

Chapter 3

Background: a frequency domain integral equation 3D solver

In this Chapter we describe in details a frequency domain integral equation 3D field solver. In Section 3.1 we formulate Maxwell equation in a Mixed Potential Differential Equation form (MPDE). In Section 3.2 we show the correspondent Mixed Potential Integral Equation form (MPIE). In Section 3.3 we identify the main unknowns of the problem (charges on the surface of conductors and currents in the interior) and we show how to discretize them with a classical choice of piece-wise constant basis functions. In Section 3.4 we show how to generate from the MPIE a system of linear equations. Sections 3.5 and 3.6 show how to solve efficiently such system. Finally in Section 3.7 we show what kind of simulation outputs can be produced for Signal Integrity and EMI analysis.

3.1 The Mixed Potential Differential Equation formulation (MPDE)

Maxwell differential equations expressed in the frequency domain with respect to the the magnetic field **H**, and the electric field **E** are [62],

$$\nabla \times \mathbf{H} = j\omega\varepsilon\mathbf{E} + \mathbf{J} \tag{3.1}$$

$$\nabla \times \mathbf{E} = -j\omega\mu\mathbf{H}. \tag{3.2}$$

$$\nabla \cdot \mu\mathbf{H} = 0 \tag{3.3}$$

$$\nabla \cdot \varepsilon\mathbf{E} = \rho \tag{3.4}$$

The charge density is indicated with ρ and the current density with **J**. The frequency is $\omega = 2\pi f$, while μ is the magnetic permeability, and ε is the dielectric constant in free space.
From (3.3) we can define a vector **A** (the magnetic vector potential), such that

$$\mathbf{B} = \mu\mathbf{H} = \nabla \times \mathbf{A}. \tag{3.5}$$

Substituting (3.5) into (3.2) we obtain

$$\nabla \times (\mathbf{E} + j\omega\mathbf{A}) = 0. \tag{3.6}$$

Hence we can define a scalar potential ϕ such that

$$\mathbf{E} + j\omega\mathbf{A} = -\nabla\phi. \tag{3.7}$$

This equation expresses the electric field **E** in terms or the basic potential quantities **A** and ϕ. We will now express **A** and ϕ in terms, respectively, of the current density **J**, and in terms of the charge density ρ. First calculate **A** in terms on **J**. After substituting (3.5) and (3.7) into (3.1) we obtain

$$\nabla \times \nabla \times \mathbf{A} = j\omega\mu\varepsilon(-j\omega\mathbf{A} - \nabla\phi) - \mu\mathbf{J} \tag{3.8}$$

Using the Laplacian identity

$$\nabla \times \nabla \times \mathbf{A} = \nabla(\nabla \cdot \mathbf{A}) - \nabla^2 \mathbf{A} \tag{3.9}$$

and choosing the Lorenz gauge

$$\nabla \cdot \mathbf{A} = -j\omega\mu\varepsilon\phi \tag{3.10}$$

equation (3.8) becomes an Helmholtz equation for the magnetic vector potential (3.11).
Taking the divergence of (3.7), substituting (3.4) and using the Lorenz gauge (3.10), we can express the potential $\phi(\mathbf{r})$ in terms of the charge density ρ using the Helmholtz equation (3.12).
In summary the Maxwell equations in Mixed Potential Differential Equation (MPDE) form are

$$\nabla^2 \mathbf{A} + \omega^2 \mu\varepsilon \mathbf{A} = -\mu \mathbf{J} \tag{3.11}$$

$$\nabla^2 \phi + \omega^2 \mu\varepsilon\phi = -\frac{\rho}{\varepsilon} \tag{3.12}$$

3.2 The Mixed Potential Integral Equation formulation (MPIE)

In an homogeneous medium, the solution of (3.11) for the magnetic vector potential $\mathbf{A}$ in position $\mathbf{r}$ due to a current distribution in the volume V is given by [62]

$$\mathbf{A}(\mathbf{r}) = \frac{\mu}{4\pi} \int_V \mathbf{J}(\mathbf{r}') \frac{e^{j\frac{\omega}{c}|\mathbf{r}-\mathbf{r}'|}}{|\mathbf{r}-\mathbf{r}'|} d\mathbf{r}'. \tag{3.13}$$

where $c = 1/\sqrt{\mu\varepsilon}$ is the speed of light. If the medium is not uniformly homogeneous because of layered dielectric materials present for example between PCB layers, the solution can be modified using the appropriate Green functions. Using the constitutive relation for the electric field $\mathbf{E} = \sigma\mathbf{J}$, where σ is the conductors' conductivity, and substituting equation (3.13) into the electric field equation (3.7), we obtain the electric field integral equation (3.14).
In a homogeneous medium the solution of the Helmholtz equation for the scalar potential $\phi(\mathbf{r})$ is given by (3.15). If the medium is not uniformly homogeneous because of some layered dielectrics, once again the expression can be modified using the appropriate Green functions.
In summary, as described also in [121, 67], the following set of integral equations can be used for the solution of the conductor current distribution, $\mathbf{J}$, and of the conductor surface charge, ρ,

$$\frac{\mathbf{J}(\mathbf{r})}{\sigma} + j\omega\frac{\mu}{4\pi} \int_V \mathbf{J}(\mathbf{r}') \frac{e^{j\frac{\omega}{c}|\mathbf{r}-\mathbf{r}'|}}{|\mathbf{r}-\mathbf{r}'|} d\mathbf{r}' = -\nabla\phi(\mathbf{r}), \tag{3.14}$$

$$\frac{1}{4\pi\varepsilon} \int_S \rho(\mathbf{r}') \frac{e^{j\frac{\omega}{c}|\mathbf{r}-\mathbf{r}'|}}{|\mathbf{r}-\mathbf{r}'|} d\mathbf{r}' = \phi(\mathbf{r}), \tag{3.15}$$

$$\nabla \cdot \mathbf{J}(\mathbf{r}) = 0, \tag{3.16}$$

$$\hat{\mathbf{n}} \cdot \mathbf{J}(\mathbf{r}) = j\omega\rho(\mathbf{r}), \tag{3.17}$$

where V and S are the union of the conductor volumes and surfaces, ϕ is the scalar potential on the conductor surfaces. Equations (3.16) and (3.17) are added to the system to ensure current conservation in the interior of the conductors and charge conservation on the surface of the conductors respectively.

As boundary conditions, given a collection of interconnect, i.e. conductors, in a SI or EMI analysis one would often identify some "ports", i.e. conductor contact areas, where some voltage excitation source is applied and the resulting current is calculated solving the MPIE. In this way one can calculate the port impedance matrix. Other desirable outputs of the simulation are, as illustrated in Section 3.7, for a given excitation, the current distributions in all the conductors or the field intensity on a sphere at 3 or 10 meters from the circuit.

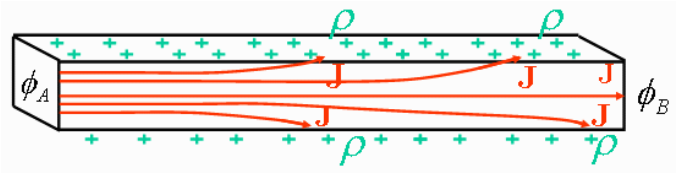

Figure 3.1: *In the Mixed Potential Integral Equation formulation (MPIE) one solves Maxwell Equations once expressed in terms of conductor current distribution,* **J**, *and of the conductor surface charge,* ρ
.

3.3 Discretization

To compute accurate conductor current and charge distributions, or terminal input and coupling impedances, it is necessary to solve the system of integro-differential equations given by (3.14)-(3.17). The main unknowns of such equations are the current density J in the interior of the conductors and the charge density ρ on the surface of the conductors as illustrated in Fig. 3.1. One standard numerical procedure for solving (3.14)-(3.17) begins with approximating the volume currents and surface charges by a weighted sum of a finite set of basis functions $\mathbf{w}_j \in C^3$ and $v_j \in C^1$ as in

$$\mathbf{J}(\mathbf{r}) \approx \sum_j \mathbf{w}_j(\mathbf{r}) I_j \tag{3.18}$$

$$\rho(\mathbf{r_s}) \approx \sum_m v_m(\mathbf{r_s}) q_m, \tag{3.19}$$

where I_j and q_m are the basis function weights.

A Galerkin procedure [54] can be used to generate a system of equations for the weights. The procedure is to substitute the representations (3.18) and (3.19) for **J** and ρ, into (3.14) and (3.15), and then insist that the equation residuals are orthogonal to the basis functions. That is,

$$\left\langle \frac{\sum_j \mathbf{w}_j(\mathbf{r}) I_j}{\sigma} + \frac{j\omega\mu}{4\pi} \int_V \sum_j \mathbf{w}_j(\mathbf{r}') I_j \frac{e^{j\frac{\omega}{c}|\mathbf{r}-\mathbf{r}'|}}{|\mathbf{r}-\mathbf{r}'|} d\mathbf{r}' + \nabla\phi \ , \ \mathbf{w_i} \right\rangle = 0$$

$$\left\langle \frac{1}{4\pi\varepsilon} \int_S \sum_m v_m(\mathbf{r}'_\mathbf{s}) q_m \frac{e^{j\frac{\omega}{c}|\mathbf{r_s}-\mathbf{r}'_\mathbf{s}|}}{|\mathbf{r_s}-\mathbf{r}'_\mathbf{s}|} d\mathbf{r}'_\mathbf{s} - \phi(\mathbf{r_s}) \ , \ v_l \right\rangle = 0,$$

where the inner products are defined as

$$\langle \mathbf{f}(\mathbf{r}) \, , \, \mathbf{w_i}(\mathbf{r}) \rangle = \int_V \mathbf{w_i}^*(\mathbf{r}) \cdot \mathbf{f}(\mathbf{r}) \, d\mathbf{r} \tag{3.20}$$

$$\langle g(\mathbf{r_s}) \, , \, v_l(\mathbf{r_s}) \rangle = \int_S v_l^*(\mathbf{r_s}) \, g(\mathbf{r_s}) \, d\mathbf{r_s}. \tag{3.21}$$

The result, as in [67], is a matrix equation of the form

$$\begin{bmatrix} R + j\omega L & 0 \\ 0 & P \end{bmatrix} \begin{bmatrix} I \\ q \end{bmatrix} = \begin{bmatrix} V_\phi \\ \phi \end{bmatrix} \tag{3.22}$$

where I and q are vectors of current and charge basis function weights, respectively, and ϕ and V_ϕ are the vectors generated by inner products of the surface potential or the volume potential gradient with the basis

functions. The matrices R, L and P are derived directly from the Galerkin condition and are given by

$$R_{ij} = \frac{1}{\sigma}\int_V \mathbf{w}_i^*(\mathbf{r})\cdot\mathbf{w}_j(\mathbf{r})\,d\mathbf{r} \tag{3.23}$$

$$L_{ij} = \frac{\mu}{4\pi}\int_V\int_V \mathbf{w}_i^*(\mathbf{r})\cdot\mathbf{w}_j(\mathbf{r}')\frac{e^{j\frac{w}{c}|\mathbf{r}-\mathbf{r}'|}}{|\mathbf{r}-\mathbf{r}'|}d\mathbf{r}'d\mathbf{r} \tag{3.24}$$

$$P_{lm} = \frac{1}{4\pi\varepsilon}\int_S\int_S v_l^*(\mathbf{r_s})\,v_m(\mathbf{r}'_\mathbf{s})\frac{e^{j\frac{w}{c}|\mathbf{r_s}-\mathbf{r}'_\mathbf{s}|}}{|\mathbf{r_s}-\mathbf{r}'_\mathbf{s}|}d\mathbf{r}'_\mathbf{s}d\mathbf{r_s}. \tag{3.25}$$

3.3.1 Piecewise Constant Basis Functions

Several basis function sets are present in literature (piecewise constant, piecewise linear, RWG [6]). In the remainder of this section we will develop the mathematical details of a particularly simple yet powerful choice of basis functions: piecewise constant. These basis functions are the classical standard choice because of their great flexibility in representing any shape of solution. However it is possible to tune the discretization to a given class of problems by selecting basis functions which accurately represent expected charge densities and current flows. In this way solution times and memory requirements can be greatly decreased. As a matter of fact, in two of the main contributions of this work presented in Chapters 4 and 5 we develop two different choices of basis functions tuned to the particular class of interconnect problems reducing solution time and memory by a factor of 400.

Piecewise constant basis functions for the conductor surfaces

We now show the mathematical details of the discretization. We begin here with the discretization of the conductors surfaces referring to eq. (3.15). Let S be the union of all conductor surfaces. Subdivide S into small panels of area S_m, as shown in Fig. 3.2, such that we can associate them with a constant charge

$$q_m = \int_{S_m}\rho(\mathbf{r})d\mathbf{r} \tag{3.26}$$

We can express the charge density on all surfaces as a collection of such panels charges

$$\rho(\mathbf{r}) = \sum_m v_m(\mathbf{r})q_m \tag{3.27}$$

where $v_m(\mathbf{r})$ are the surface discretizing basis functions

$$v_m(\mathbf{r}) = \begin{cases} \frac{1}{S_m} & \text{if } \mathbf{r}\in S_m \\ 0 & \text{otherwise} \end{cases} \tag{3.28}$$

After the discretization equation (3.15) becomes

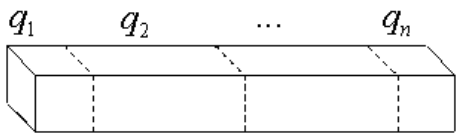

Figure 3.2: *Discretization of the surface of conductors into small panels to model charge accumulation or displacement currents.*

$$\phi(\mathbf{r}) = \frac{1}{4\pi\varepsilon}\int_S\sum_m v_m(\mathbf{r}')q_m\frac{e^{j\frac{\omega}{c}|\mathbf{r}-\mathbf{r}'|}}{|\mathbf{r}-\mathbf{r}'|}d\mathbf{r}' \tag{3.29}$$

$$= \sum_m\left[\frac{1}{4\pi\varepsilon}\frac{1}{S_m}\int_{S_m}\frac{e^{j\frac{\omega}{c}|\mathbf{r}-\mathbf{r}'|}}{|\mathbf{r}-\mathbf{r}'|}d\mathbf{r}'\right]q_m \tag{3.30}$$

In order to generate a system of equations for the unknowns q_m one choice is to enforce eq. (3.30) on each of the discretization panels S_l. The most simple way, is to enforce the equation in a point r_l in the center of each panel S_l. Such scheme is called *collocation*:

$$\phi_l = \phi(\mathbf{r_l}) \tag{3.31}$$

$$= \sum_m \left[\frac{1}{4\pi\varepsilon} \frac{1}{S_m} \int_{S_m} \frac{e^{j\frac{\omega}{c}|\mathbf{r_l}-\mathbf{r}'|}}{|\mathbf{r_l}-\mathbf{r}'|} d\mathbf{r}' \right] q_m \tag{3.32}$$

$$= \sum_m p_{lm} q_m \tag{3.33}$$

p_{lm} are called coefficients of potential, and can be calculated directly from the geometry. Their interpretation is in equation (3.33): assuming we are given the n charges q_m on the n panels S_m, the coefficients of potentials give a way to calculate the n potentials ϕ_l on the same n panels.

For better accuracy, a *Galerkin* scheme could be used to calculate the coefficient of potential. In collocation, the n potentials are evaluated only at one single point on the panel, typically the center point r_l. In a Galerkin scheme, instead, we enforce eq. (3.30) loosely speaking as an average over the entire surface of the panel. In more precise terms, we apply the following inner product (3.21) to both sides of eq. (3.30) obtaining

$$\frac{1}{S_l} \int_{S_l} \phi(\mathbf{r}) d\mathbf{r} = \sum_m \left[\frac{1}{4\pi\varepsilon} \frac{1}{S_l S_m} \int_{S_l} \int_{S_m} \frac{e^{j\frac{\omega}{c}|\mathbf{r}-\mathbf{r}'|}}{|\mathbf{r}-\mathbf{r}'|} d\mathbf{r}' d\mathbf{r} \right] q_m \tag{3.34}$$

$$\phi_l = \sum_m p_{lm} q_m \tag{3.35}$$

Finally, we introduce a convenient matrix notation for the rest of the chapter. The coefficient of potentials p_{lm}, calculated with collocation or with Galerkin, can be collected into a matrix P. Equation (3.33) or (3.35) can be expressed with:

$$Pq = \phi \tag{3.36}$$

where q is the vector with the n charges on the n panels, and ϕ is the vector of the n potentials on the same panels. Note that the coefficient of potentials in matrix P are frequency dependent due to our "full-wave" type of analysis.

Piecewise Constant Basis Functions for conductor volumes

When discretizing relatively long and thin conductors, piecewise-constant basis functions are typically used [121, 143, 68]. The functions are generated by first chopping the long wires into a large number of sections (Fig. 3.3) that are short compared to the wavelength of the highest frequency of interest. Conduction currents inside conductors, are affected by skin effects and proximity effects. For this reason we discretize the interior of the conductors into small and short filaments of current as in Fig. 3.3. Let V be the union of

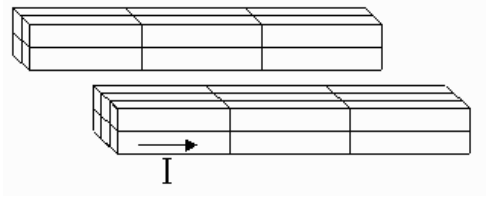

Figure 3.3: *Discretization of the conductor volume into piecewise constant basis functions (i.e. short thin filaments) to model the internal current distribution (skin effects, proximity effects).*

all conductor volumes. Subdivide V into small filaments of volume V_j and cross section A_j, such that we can

associate them with a constant current along each filament

$$I_j = \frac{1}{l_j}\int_{l_j}\int_{A_j} \mathbf{J}(\mathbf{r}) dA_j dl_j \tag{3.37}$$

We can express the current density on all filaments as a collection of such filaments currents

$$\mathbf{J}(\mathbf{r}) = \sum_j \mathbf{w}_j(\mathbf{r}) I_j \tag{3.38}$$

where $\mathbf{w}_j(\mathbf{r})$ are the volume discretizing basis functions

$$\mathbf{w}_j(\mathbf{r}) = \begin{cases} \frac{\hat{\mathbf{dl}}}{A_j} & \text{if } \mathbf{r} \in V_j \\ 0 & \text{otherwise} \end{cases} \tag{3.39}$$

where $\hat{\mathbf{dl}}$ is simply a unit vector indicating the orientation of the filament. After the discretization, equation (3.14) becomes

$$\frac{\sum_j \mathbf{w}_j(\mathbf{r}) I_j}{\sigma} + j\omega\frac{\mu}{4\pi}\int_V \sum_j \mathbf{w}_j(\mathbf{r}') I_j \frac{e^{j\frac{\omega}{c}|\mathbf{r}-\mathbf{r}'|}}{|\mathbf{r}-\mathbf{r}'|} d\mathbf{r}' = -\nabla\phi(\mathbf{r}) \tag{3.40}$$

In order to generate a system of equations we can enforce eq. (3.40) on each of the discretization filaments V_i. The collocation scheme would just enforce it on a single point $\mathbf{r_i}$ in the center of each filament

$$\left[\frac{l_i}{\sigma A_i}\right] I_i + \sum_j j\omega \left[\frac{\mu}{4\pi}\frac{1}{A_j}\int_{V_j} \frac{e^{j\frac{\omega}{c}|\mathbf{r_i}-\mathbf{r}'|}}{|\mathbf{r_i}-\mathbf{r}'|} d\mathbf{r}'\right] I_j \quad = \quad \phi_A(\mathbf{r_i}) - \phi_B(\mathbf{r_i}) \tag{3.41}$$

$$R_i I_i + \sum_j j\omega L_{ij} I_j = \phi_A(\mathbf{r_i}) - \phi_B(\mathbf{r_i}) \tag{3.42}$$

where R_i is the resistance of filament i and L_{ij} are the partial inductances between filament i and any other filament j. Both R_i and L_{ij} can be calculated directly from the geometry. No numerical solution is needed. Potentials ϕ_A and ϕ_B are the potentials at the extremes of the filament.

For better accuracy, one can use a *Galerkin* scheme. Instead of enforcing equation (3.40) only in the center points of each filament, loosely speaking we enforce it on average over the entire length of each filament. In more precise terms we apply the inner product (3.20) to both sides of eq. (3.40) an we obtain

$$\left[\frac{l_i}{\sigma A_i}\right] I_i + \sum_j j\omega \left[\frac{\mu}{4\pi}\frac{1}{A_i A_j}\int_{V_i}\int_{V_j} \mathbf{dl_i}\cdot\mathbf{dl_j} \frac{e^{j\frac{\omega}{c}|\mathbf{r}-\mathbf{r}'|}}{|\mathbf{r}-\mathbf{r}'|} d\mathbf{r}' d\mathbf{r}\right] I_j \quad = \quad \phi_A - \phi_B$$

$$R_i I_i + \sum_j j\omega L_{ij} I_j = \phi_A - \phi_B \tag{3.43}$$

Finally, we introduce a convenient matrix notation for the rest of the chapter. The resistances R_i are collected into a diagonal matrix R. The partial inductances L_{ij}, calculated with a Galerkin scheme, are collected into a matrix L. Equation (3.43) can then be expressed with:

$$[R + j\omega L] I = V_\phi \tag{3.44}$$

where I is the vector of the n currents on the n filaments, and V_ϕ is the vector of the n voltages across the same filaments. Note that the partial inductances in matrix L are frequency dependent due to our "full-wave" type of analysis.

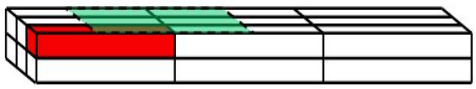

Figure 3.4: *Surface panels are centered at the filaments partition points.*

Interpretation as an equivalent circuit

We have shown so far how piecewise constant basis functions can be used to discretize both the interior of the conductors into filaments and the surface of conductors into panels. The panels discretization corresponds to filaments discretization as shown in Fig. 3.4.
We can see in Figure 3.4 how panels are centered at the filaments partition points. In the PEEC method given in [121], it is described how how this type of discretization can be interpreted with a circuit equivalent. Equation (3.43) can be viewed as a branch equation for filament i. Basically, it states that we can model filament i with a resistance R_i in series with many coupled inductors driven by the currents I_j of all the other filaments. A wire is divided in pieces along its length which will appear in series in the equivalent circuit. The wire is also divided into filaments across its cross section. In our equivalent circuit, all such filaments will appear in parallel. The resulting model is shown in Fig. 3.5. Equation (3.35) corresponds to coupled

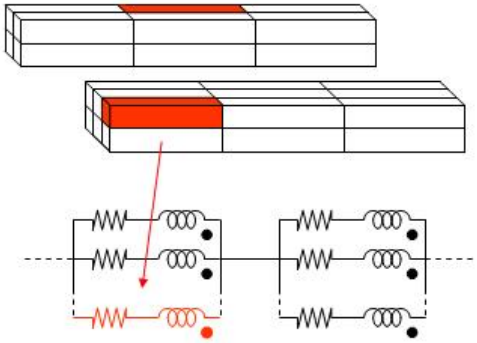

Figure 3.5: *Equivalent circuit model of a wire after the interior has been discretize into filaments. Each filament is modeled by a resistance and many partial inductors in series. Each of the filament of a wire cross-section are connected in parallel in the circuit model. Finally, many such groups of filaments are connected in series to model the entire length of the wire.*

capacitors inserted at the break points between filaments. For conductors much thinner than a wavelength it is safe to assume that all filament cross-sections at a break point have the same potential as the panels on the surface near such break point. This can be modeled as in the final circuit equivalent in Fig. 3.6.

3.4 Problem set up as a linear system of equations

The discretized equations (3.44) and (3.36) can be collected into a more compact block matrix form

$$\begin{bmatrix} R+j\omega L & 0 \\ 0 & P \end{bmatrix} \begin{bmatrix} I \\ q \end{bmatrix} = \begin{bmatrix} V_\phi \\ \phi \end{bmatrix} \tag{3.45}$$

If we introduce the currents $I_p = j\omega q$ to represent the displacement current from panels we can rewrite equation (3.45) as

$$\begin{bmatrix} R+j\omega L & 0 \\ 0 & \frac{P}{j\omega} \end{bmatrix} \begin{bmatrix} I \\ I_p \end{bmatrix} = \begin{bmatrix} V_\phi \\ \phi \end{bmatrix} \tag{3.46}$$

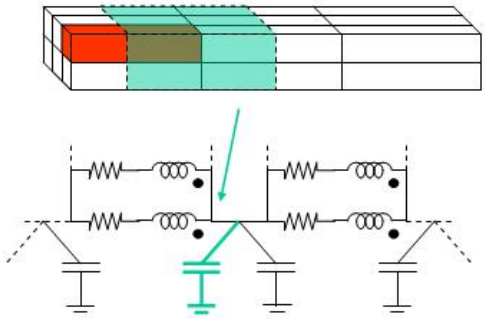

Figure 3.6: *Equivalent circuit model from the PEEC-type discretization. Inductances and capacitances are frequency dependent in a full-wave analysis. The panels are centered at the filament break points such that we can insert capacitors modeling such panels between groups of parallel filaments.*

where vector

$$I_b = \begin{bmatrix} I \\ I_p \end{bmatrix} \tag{3.47}$$

is now containing all branch currents of the equivalent circuit network in Fig. 3.6. Vector

$$V_b = \begin{bmatrix} V_\phi \\ \phi \end{bmatrix} \tag{3.48}$$

contains all the branch voltages of the network. Defining as Z_{EM} the branch equation impedance matrix of the equivalent circuit network in eq. (3.46) we can rewrite (3.46) as

$$Z_{EM} I_b = V_b \tag{3.49}$$

3.4.1 The classical approach: Nodal analysis

So far we have seen how the first two equations (3.14) and (3.15) in the MPIE formulation can produce, once discretized, a set of algebraic and linear branch equations. The remaining two equations (3.16) and 3.17) in the MPIE can then be used to set up an algebraic linear system. Specifically, imposing such current and charge conservation on the MPIE corresponds in the equivalent circuit interpretation to imposing Kirchoff Currents Laws (KCL) to each node of the circuit. The PEEC method in [121] and almost all circuit simulators such as SPICE, solve circuit networks using such *nodal analysis* method [56]. Substituting the branch equations (3.49) into such KCL's, we obtain a linear system where the unknowns are the nodal potentials.

3.4.2 An alternative approach: Mesh analysis

An alternative way to impose current and charge conservations in both the MPIE or in its equivalent circuit is to use a *mesh analysis* formulation as in [68] and in [67]. In fact, using loop currents as main unknowns directly guarantees current conservation. This also guarantees directly charge conservation when charge accumulation on the surface of the conductors are modeled as displacement current and mesh current loops include both conductor currents and displacement currents. Fig. 3.7 shows such mesh loop currents. As shown in [68, 67, 65], mesh analysis is to be preferred to nodal analysis since it produces better conditioned systems and hence it gives better convergence behavior in the iterative methods we present later in this chapter. A mixed mesh-nodal approach has also been presented in [86].

We describe here the details of a pure mesh analysis approach. Practically speaking using mesh analysis means writing as many Kirchoff Voltage Laws (KVL) as independent meshes in the network as shown in Fig. 3.7. In matrix form we have

$$M V_b = V_{ms} \tag{3.50}$$

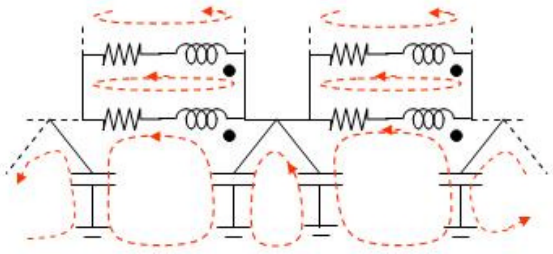

Figure 3.7: *Current and charge conservation can be imposed using as unknowns a set of independent mesh or loop currents. Such currents may include displacement currents modeling charge accumulation on the surface of the conductors.*

where V_b is the vector of branch voltages, V_{ms} is the vector of mesh voltages sources, mostly zero. M is the very sparse mesh matrix. Each row represents one KVL. Substituting the branch equations (3.49) we obtain

$$MZ_{EM}I_b = V_{ms} \tag{3.51}$$

Finally we observe from circuit network theory [77] that the mesh currents I_m are related to the branch currents I_b by

$$I_b = M^T I_m \tag{3.52}$$

Substituting we get

$$[MZ_{EM}M^T]I_m = V_{ms} \tag{3.53}$$

which is a linear system of equations in the unknowns mesh currents, I_m. Solving the system we get I_m and from those we can get any other quantity in the circuit

$$I_b = M^T I_m \tag{3.54}$$
$$V_b = Z_{EM}I_b \tag{3.55}$$

To summarize, we have so far showed how to convert a linear system of partial differential-integral equations (3.14) and (3.15) into a linear system of equations (3.53). We observe that the system matrix $MZ_{EM}M^T$ is very dense. The matrix dimension is the number of meshes in the equivalent circuit network, hence on the order of the number of filaments and number of panels in the discretization.

3.5 Solution of a large and dense linear system

Almost all the computation time of the simulator is spent in solving the large and dense system of equations (3.53). For this reason it is crucial to select the proper solution technique and to try and improve its simulation time and memory requirements.

3.5.1 Classical approach: LU decomposition or Gaussian elimination

Assume we are suppose to solve the linear system

$$Ax = b \tag{3.56}$$

where A is a known nonsingular matrix, b is a known vector and x is the vector of unknowns. The most common way to solve such system is a fancy implementation of the trivial Gaussian elimination algorithm: LU decomposition. In LU decomposition the system matrix A is first factored into a lower triangular matrix L and an upper triangular matrix U such that

$$A = LU \tag{3.57}$$

The system is then solved by solving two easier subsystems using forward elimination and back substitution respectively

$$Ly = b \tag{3.58}$$
$$Ux = y \tag{3.59}$$

The advantage of first decomposing A is evident when the system needs to be solved for many different right-hand-sides b. This method is the method of choice when solving large and *sparse* systems for which the computational complexity with respect to the dimension n of the matrix can be as low as $O(n^{1.2})$. However it is not practical for solving large and *dense* linear systems for which the computational complexity is $O(n^3)$ and it is dominated by the factorization step. Such high order of complexity implies an explosion in the computation times when a large matrix is to be solved.

3.5.2 Krylov subspace iterative methods

When solving large and dense linear systems it is more convenient to employ Krylov subspace iterative methods. The main structure of this family of algorithms is as follows:

1. *Pick and initial guess for the solution vector x_0*
2. *REPEAT*
   (a) *calculate the residue $r_i = Ax_i - b$ representing the distance between x_i and the exact solution of the problem $\hat{x}$.*
   (b) *Choose the next vector x_{i+1} that minimizes the next residue r_{i+1} searching in the Krylov subspace generated from the history of the previous iterations*
   $K_i(A, r_0) = x_0 + \text{span}(r_0, Ar_0, A^2r_0, \ldots, A^{i-1}r_0)$.
3. *UNTIL the desired accuracy (measured by r_i) is achieved.*

Many implementation variants are available of this Krylov subspace iterative strategy. GMRES for instance is a common choice is described for example in [41]. Krylov subspace iterative methods perform much better than LU decomposition in terms of speed for two main reasons:

- EMI measurements are usually not extremely precise (on the order of few percent), while LU decomposition calculates the solution with as many digits as the precision available from the computer hardware (typically 15 digits with the IEEE standard). This means in most cases a large waste of computation power that we can instead save using an iterative method. In fact, an iterative method can stop the computation immediately when the desired accuracy is achieved, (for example after 4-5 digits).

- The computational complexity of the Krylov subspace iterative method is dominated by the matrix vector product Ax_i, that must be evaluated at each iteration to calculate the residue and to update the Krylov subspace. Such matrix-vector product has a complexity of order $O(n^2)$. Many implementations (for example GMRES that we use) are guaranteed to converge to the desired accuracy in no more than n iterations. At a first glance this would imply an overall complexity of order $O(n^3)$. Fortunately, it is possible to obtain a convergence in an almost constant and very small number of iterations if a good *pre-conditioner* is used. For example we observed a convergence in about 20 iterations to 3-4 digits precision also for systems as big as $n = 100,000$ unknowns. The final complexity of the algorithm is therefore only $O(n^2)$ much smaller compared to the LU decomposition $O(n^3)$.

3.5.3 Preconditioning

In the previous section, we mentioned that in order to guarantee the convergence of the iterative methods, we need to use a good preconditioner. Preconditioning the systems means manipulating the system $Ax = b$ with a matrix N in order to obtain a new system, for instance

$$NAx = Nb \tag{3.60}$$

that shows a faster convergence in the iterative method. An example of a good preconditioner is any *easy to calculate approximation of* A^{-1}. The perfect preconditioner in terms of convergence rate would be of course the inverse itself: $N = A^{-1}$. In fact, in that case, $NA = I$ is just the identity and the convergence is immediate. However, if we need to invert A, we would have already solved the system without any need for iterative methods! A good preconditioner is therefore a matrix that is as close as we can get to the inverse *without doing much calculations!* Note that, if N is a good approximation for A^{-1}, and $NA \approx I$. Hence, we have also just found a good initial guess for the iterations

$$x_0 = Nb \tag{3.61}$$

Looking for approximations of A that are easy to invert, a practical choice for many systems is for example the diagonal of A. The preconditioner is then

$$N = [\text{diag}(A)]^{-1} \tag{3.62}$$

This is called Jacoby preconditioner and works very well especially when the matrix is diagonally dominant. The matrix in our system is $A = MZ_{EM}M^T$. We can observe that while Z_{EM} might have some reasonable diagonal dominance, it is very unlikely that $MZ_{EM}M^T$ preserves such property. Therefore the preconditioner will not perform well in this case. A better preconditioner for this case is instead:

$$N = [M\text{diag}(Z_{EM})M^T]^{-1} \tag{3.63}$$

Inverting $M\text{diag}(Z_{EM})M^T$ is not expensive because M is extremely sparse and so is $\text{diag}(Z_{EM})$. Also, note that $M\text{diag}(Z_{EM})M^T$ is a good approximation of $MZ_{EM}M^T$. This preconditioner shows very good performance in terms of convergence rate of Krylov subspace iterative methods as shown in Fig. 3.8. In such Figure, we compare the convergence rate of GMRES without preconditioner, GMRES with the diagonal-of-A preconditioner and GMRES with diagonal-of-Z_{EM} preconditioner.

Even though the diagonal-of-Z_{EM} preconditioner is already very good, more improvement is possible. For example, reconsider the matrix Z_{EM}. We are approximating it with its diagonal. This implies that we neglect all the mutual coupling terms. This is probably not a good idea for example for the tightly coupled filaments in parallel on the same wire section. Looking at the structure of the partial inductance matrix L inside Z_{EM}, we can recognize blocks of tightly coupled filaments and include them with the diagonal elements in the preconditioner [65]. This of course increases the computation required to invert the matrix $M\text{diag}(Z_{EM})M^T$, which is anyway still quite sparse. The preconditioner will have better performance in terms of GMRES convergence rate, but it gives more overhead. One can continue in this search for better preconditioners (for further details see for instance [65]) until the overhead imposed by their inversion becomes larger than the speed up they provide in the GMRES convergence rate.

3.6 Matrix-vector product acceleration: precorrected-FFT

While describing the Krylov subspace iterative methods, we have seen how the dominant factor in the computational complexity is the matrix-vector product Ax_i which is of order $O(n^2)$ in the size of the matrix. In our case $A = MZ_{EM}M^T$ and $x_i = I_{m_i}$. However, exploiting the physical structure of the problem it is possible to calculate this matrix-vector product in just order $O(nlog(n))$. The method is called *precorrected-FFT*. The

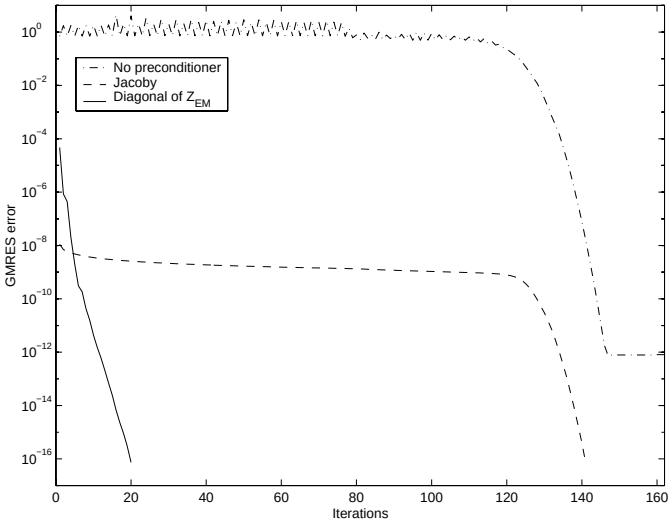

Figure 3.8: *Convergence rate of GMRES with and without preconditioners. The size of the system is 162. Without preconditioner, GMRES is as slow as Gaussian elimination. The Jacoby preconditioner is simply the diagonal of the system matrix* $[MZ_{EM}M^T]^{-1}$ *and it gives a poor performance. A much better preconditioner is instead* $[M\mathrm{diag}(Z_{EM})M^T]^{-1}$*, which brings GMRES to convergence in 20 to 30 iterations even for systems of hundreds of thousands of unknowns.*

theoretical principles of the method have been originally developed by Joel Phillips in [110]. Precorrected-FFT has been already applied to the acceleration of other field solvers such as [152], and it can be applied in particular to our EMI simulation problem.

Consider our matrix-vector product $[MZ_{EM}M^T]I_{m_i}$. First the product $I_b = M^T I_{m_i}$ can be calculated directly. M^T is extremely sparse and contains only $+1$ and -1 elements. Hence, this product is not expensive at all. The next product is instead quite expensive $Z_{EM}I_b$. Subdivide it in its components:

$$Z_{EM}I_b = \begin{bmatrix} R + j\omega L & 0 \\ 0 & \frac{P}{j\omega} \end{bmatrix} \begin{bmatrix} I \\ I_p \end{bmatrix} = \begin{bmatrix} RI + j\omega LI \\ Pq \end{bmatrix} \tag{3.64}$$

, where $q = I_p/j\omega$. Note that R is a diagonal matrix. Hence the product RI takes no time. The expensive matrix-vector products are LI and Pq. In order to evaluate them as fast as possible let us exploit what we know about the physics of the problem. From the section on the conductor surface discretization we know that the product Pq simply corresponds to calculating the n potentials ϕ on the n surface panels due to the n charges in vector q on the same panels. An approximation to this physical problem can be used instead of simply treating it as an algebraic problem of $O(n^2)$. In the same way, from the section on the conductor volume discretization into filaments, we know that the product LI simply corresponds to calculating the m magnetic potentials A on the m filaments due to the m currents in vector I on the same filaments. Again, the algebraic problem is $O(m^2)$, however precorrected-FFT offers a good and less expensive approximation to the physics problem.

Consider for example the first physics problem: calculate n potentials on n panels due to n charges on the same panels. The main idea of the precorrect-FFT algorithm is depicted in Fig. 3.9 and is summarized here:

1. First superimpose an imaginary three-dimensional grid to the entire volume. Fig. 3.9 only shows a two-dimensional grid. Project the panel charges onto the nearby grid points. The projection is done such that the potential produced by the new charges on the other further away grid points is the same as the potential originally produced by the old charges on the panels.

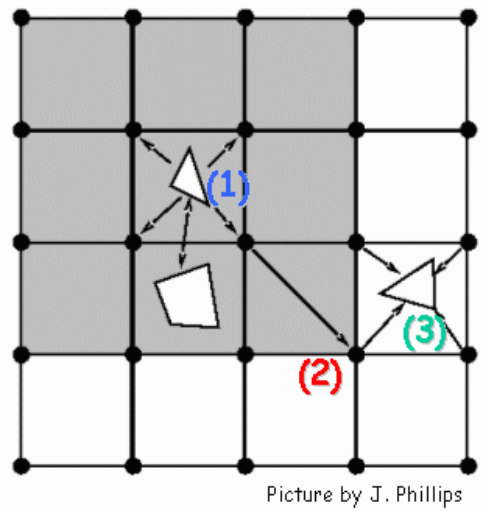

Figure 3.9: *Precorrected-FFT: an algorithm for the fast evaluation of the matrix-vector product in order* $O(n\log(n))$. *Phase 1. Projection of the panel charges to the grid points. Phase 2. Calculation of the potentials on the grid points due to the charges on the grid points. Phase 3. Interpolation of the potentials from the grid points to the panels. (Picture by Joel Phillips, Cadence Berkeley Labs)*

2. Now, let us calculate the potentials on all the grid points due to the charges on the same grid points. Given the regular structure of the operation, it basically turns out to be a convolution operation in the space domain The convolution in the space domain can be easily calculated in the "spatial frequency domain" using a *Fast-Fourier-Transform* (FFT).

3. As a final step, after we have the potentials on the grid points, we can easily interpolate the potentials on the panels.

Note that this algorithm does not work if two or more panels are very close to each other. The projection step is valid only at far enough distance. Therefore we need to calculate the contributions of nearby panels directly. The other contributions can be calculated with the algorithm above. A *precorrection* step will take care of making sure that contributions of closely interacting panels are not included twice.

The computational complexity of the entire algorithm is dominated by the FFT which takes $O(N\log(N))$ in the number of grid points N. In most practical applications the number of grid points N is about the same as the number of panels ($N \approx n$). This is a significant improvement with respect to the classical algebraic approach that gives $O(n^2)$.

In the same way we can evaluate the magnetic vector potentials due to the currents on the filaments.

1. Instead of projecting charges we project currents to the grid points.

2. We then evaluate with an FFT the magnetic vector potentials on the grid points due to the currents on the grid points.

3. Finally, we interpolate the magnetic vector potentials from the grid points to the filaments.

The contributions from close filaments are calculated directly and a precorrection step avoids we count them twice in the algorithm.

3.6.1 Comparing solution methods for large and dense linear systems

As a summary of this section we compare in Table 3.1 several methods for the solution of large and dense linear systems with respect to solution time and memory requirements. The combination of Krylov subspace

iterative methods with a the Precorrected-FFT fast matrix vector product gives in most cases an almost linear complexity both in the time and in the memory requirements.

Table 3.1: *Comparing solution methods for large and dense linear systems.*

Algorithms:	Complexity:	Storage:
Gaussian elimination	$O(N^3)$	$O(N^2)$
Krylov subspace iterative methods	$O(N^2)$	$O(N^2)$
Our approach: Krylov iter. + Precorrected-FFT	O(N log(N))	O(N log(N))

3.7 Examples of types of field solver analysis

3.7.1 Return current path analysis at any frequency

We have implemented the techniques described so far in this Chapter in a field solver prototype which we then used for developing our contributions presented in the next Chapters 4 and 5. Typical analysis outputs of an EMI fields solvers are for instance the capability for current distribution display.

Consider for instance a very small but intuitive example presented in Fig. 3.10. In such figure we show three conductors. A simple small resistive load is driven through the shown conductors by an ideal voltage generator. The two conductors on the left are shorted together on both sides and provide the ground return for the conductor on the right carrying the main signal.

Figure 3.10: *Simple example to describe high frequency effects such as skin and proximity effects. Conductors are 6 mm long, 1mm wide and 1mm far apart from each other. The two conductors on top are two possible return paths for the current on the conductor on the bottom.*

We can verify in Fig. 3.11 the expected behavior of such system:

- perfect path sharing at very small frequencies in Fig. 3.11.a;
- increased current density on the closer conductor with smaller loop are when, at larger frequencies, inductance becomes the dominant factor in the impedance of the return path (Fig. 3.11.b);
- skin effect and proximity effect at even larger frequencies in Fig. 3.11.c;

- finally current propagation in waves, with standing waves phenomena, when the conductors length becomes comparable to the wavelength in Fig. 3.11.d.

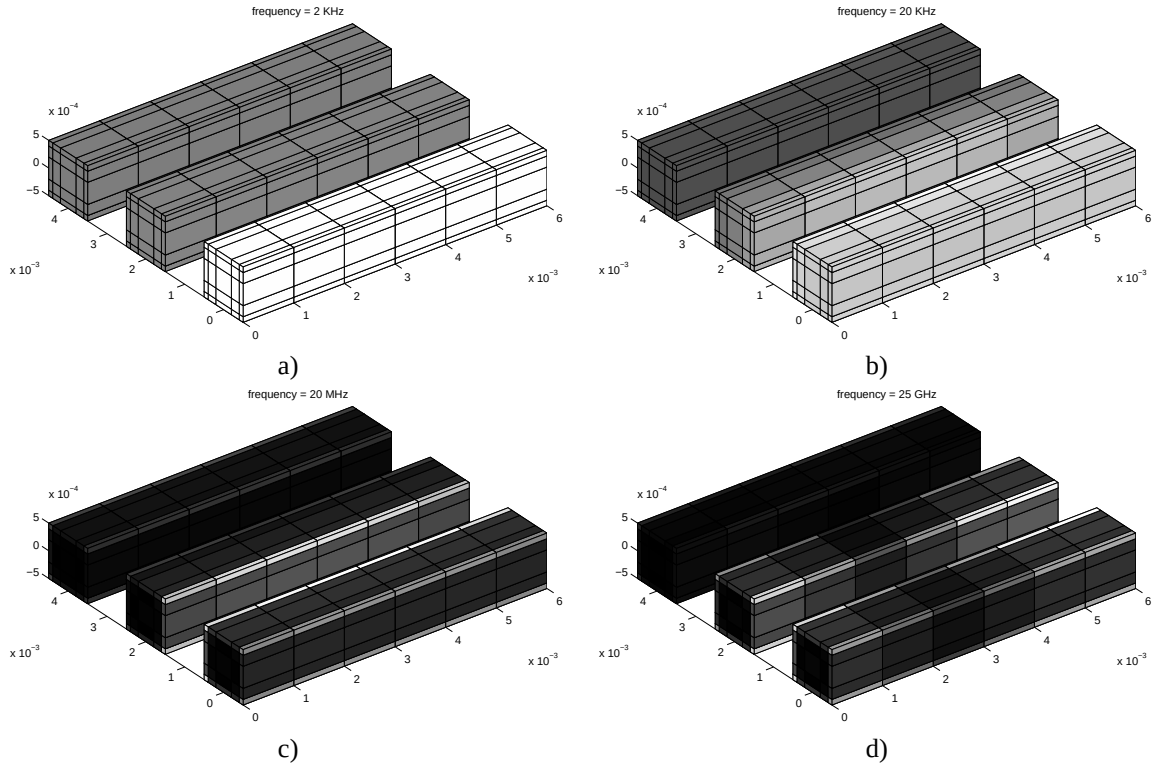

Figure 3.11: *Example of current distribution analysis of the very simple geometry in Fig. 3.10. Dark grays mean small current density, lighter grays mean larger current density. a) At this small, 2 KHz, the current is shared equally by the two returns. b) As frequency increases (20 KHz), inductance becomes the dominant factor in the impedance of the return paths. More and more current chooses the closer return with smaller loop area and therefore smaller inductance. c) At 20MHz current flows only near the surface of the conductors (skin effect), in particular it flows on the side facing other nearby conductors (proximity effect). d) Finally at very high frequencies (25GHz) the conductor length becomes comparable to the wavelength. Current propagates in waves and is reflected by unmatched loads. We can observe here standing waves maxima and minima along the conductors.*

3.7.2 Radiation and susceptibility patterns at any frequency

From the current distribution we can generate for example emission and susceptibility patters at any specified frequency adding the contributions from each of the conductor discretization filaments as sketched in Fig. 3.12

As an example we show in Fig. 3.13 the radiation patterns of the simple example in Fig. 3.10 when excited at its quarter wavelength and at its half wavelength resonance frequencies.

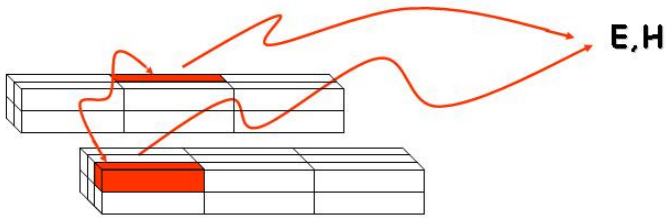

Figure 3.12: *Radiated fields can be easily calculated by a post-processing step once current distribution are available on all discretization filaments. Note that interference between filaments has already been taken when solving for the current distributions.*

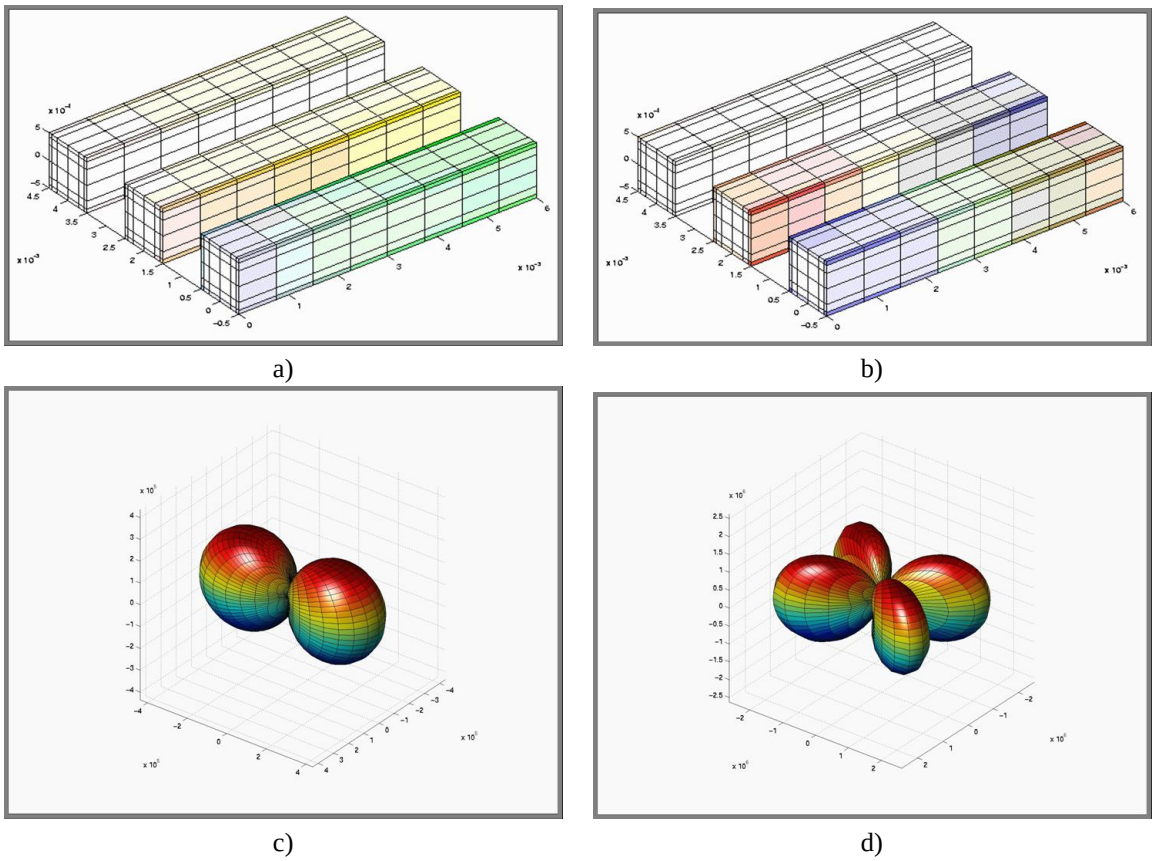

Figure 3.13: *Current distributions and radiation patterns for the simple circuit in Fig. 3.10 are shown in a) and c) for its quarter wavelength resonance and in b) and d) for its half wavelength resonance.*

Chapter 4

Conduction modes basis functions

This chapter describes the first contribution presented in this thesis. The work in this chapter has been done in collaboration also with Prof. Jacob White, Massachusetts Institute of Technology, and it has first appeared in [35, 37, 39].

The new generation of fast electromagnetic analysis programs, based on accelerated integral equation methods described in the previous Chapter 3, has reduced *from days to minutes* the time required to analyze thousands of simultaneously interacting conductors [94, 68, 110, 136, 71]. As good as these fast solvers are, they are either inappropriate for, or are very inefficient at, analyzing interconnect exhibiting *high frequency effects*. With processor clock speeds now exceeding two gigahertz and harmonics exceeding twenty gigahertz, it is no longer possible to ignore these high frequency effects.

The high frequency effects that are most troublesome for fast solvers are skin and proximity effects. Nevertheless such phenomena can significantly affect interconnect performance and should not be neglected, in particular when either wire width or thickness are equal to, or larger than two "skindepths." [1] In order to describe such phenomena let us consider the very simple example already introduced in Section 3.7 and shown in Fig. 3.10. At low frequencies, those for which both wire with and thickness are much smaller than two skindepths, the cross-sectional current density can be considered with a good approximation constant as shown in Fig. 4.1. When either wire width or thickness are equal to, or larger than two "skindepths" the

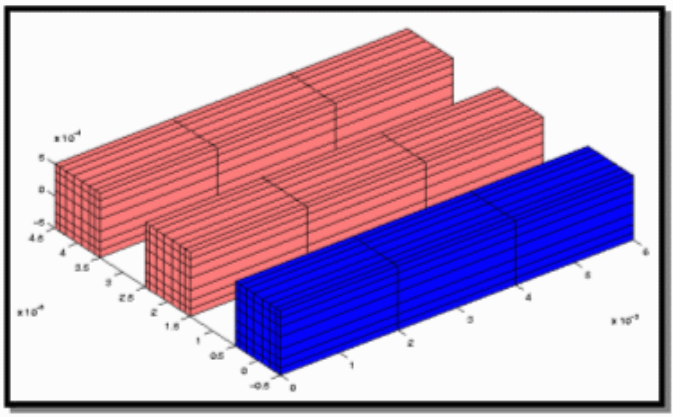

Figure 4.1: *Current distributions at low frequencies.*

current begins to crowd toward edges and corners of the wire cross-section (skindepth effect). Furthermore,

[1] The skin depth for a signal at a certain frequency f is defined as $\delta = 1/\sqrt{\pi f \mu \sigma}$, where μ is the permeability and σ is the conductivity of the conductor.

opposite currents in adjacent conductors tend to be as close as possible (proximity effect). Both such effects are visible in Fig. 4.2 obtained with our simulation tool.

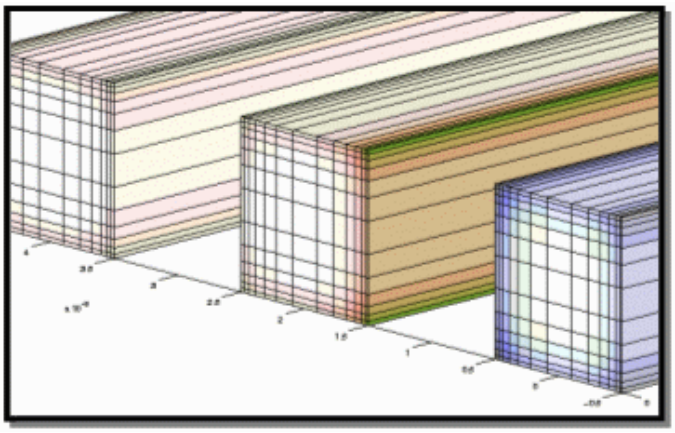

Figure 4.2: *Cross-sectional current distributions at high frequency. Skin and proximity effects are visible.*

Interconnect performance on Printed Circuit Boards (PCB) and on IC Packages have been suffering for many years from such effects. Even some Integrated Circuit are now beginning to be affected at the global interconnect level (power and ground distribution network or clock distribution network). For instance skindepth in Aluminum interconnect at the tenth harmonic of a two gigahertz clock is around a half micron.

Skin and proximity effects are troublesome for present fast solvers because they generate an exponentially varying current distribution inside each conductor. Trying to represent that current variation using the piecewise constant basis functions described in Section 3.3.1 and in [121, 143] commonly available in fast solvers [68] requires a large number of unknowns. Since the computation time for fast solvers is supposed to increase only linearly (more precisely $O(n\log(n))$) with the total number n of basis functions used in the problem, it may seem that the increase in unknowns to represent current variation is not that problematic. However, when many basis functions are used to represent the current variation in a cross-section of a conductor, those basis functions densely interact in a way that can not be reduced by the algorithms used in most fast solvers. For this reason, the computation time for modeling high frequency effects increases with the square of the number of unknowns required to model the current variation within conductors even for fast solvers.

Some research efforts have been previously concentrated on solving this issue by avoiding representing currents in conductor interiors

- $2\frac{1}{2}$-D approximations using surface impedances has been used for instance in [141, 139, 140],
- alternatively it has been recognized that the many conductor interiors can be decoupled into separate Helmholtz problems, which can then be combined with a global exterior Helmholtz problem [138, 30, 142, 151]. The many Helmholtz equations can then be solved either by integral or by differential methods.
- Finally Silvester proposed to expand the current in a flat conductor into a series or orthogonal eigenmodes [133].

Two contributions of this specific Ph.D. work concentrate on addressing the same issue by generating specialized basis functions which more easily capture the exponential variation of the conductor current:

1. We will develop in this same Chapter the *"conduction modes basis functions"* In such method we take a different approach from the previous [133, 140, 138, 30, 142, 151] and use the interior Helmholtz equation to generate basis functions for use in the standard Galerkin technique [54] for solving the Mixed Potential Integral Equation (MPIE).

2. We will be present in the following Chapter 5.1. the *"proximity templates basis functions"* approach [38]. In such method we demonstrate that it is also possible to generate numerically a set of basis functions which efficiently represent conductor current variation. Similar performance is achieved as with the conduction modes basis functions, but unlike the conduction mode approach, the template approach is easily extended to general shape cross-sections (e.g. trapezoidal).

The remainder of this Chapter is organized as follows: in 4.1, we derive the "conduction modes" from the solution of the electric field Helmholtz equation for the interior of the conductors. Based on such modes, we define cross-section basis functions and we show how to use our new basis functions for the discretization of the Mixed Potential Integral Equations (MPIE) presented in Section 3.2. Several examples are finally shown in 4.2 to verify the capabilities of our method and its computational attractiveness. In particular, we show how our new approach can successfully and efficiently capture skin effects, proximity effects, multiple return current paths distributions, and transmission line resonances.

4.1 Using conduction modes as basis functions for the conductor currents

4.1.1 Conduction modes

Combining the two Maxwell differential equations,

$$\nabla \times E = -j\omega\mu H \tag{4.1}$$
$$\nabla \times H = (j\omega\varepsilon + \sigma)E, \tag{4.2}$$

and using the "good conductor hypothesis", $\sigma \gg j\omega\varepsilon$, we obtain the governing Helmholtz diffusion equation for the region *inside* each conductor:

$$\nabla \times \nabla \times \mathbf{E} + j\omega\mu\sigma\mathbf{E} = 0. \tag{4.3}$$

In terms of the current density, $\mathbf{J} = \sigma\mathbf{E}$, and the skin depth, $\delta = \sqrt{2/(\omega\mu\sigma)}$, (4.3) can be rewritten as

$$\nabla \times \nabla \times \mathbf{J} + \left(\frac{1+j}{\delta}\right)^2 \mathbf{J} = 0. \tag{4.4}$$

Assuming the current in each conductor section flows primarily lengthwise (as shown in Fig. 4.3), $\mathbf{J}$ can be approximated by $\mathbf{J} = J_z\hat{\mathbf{a}}_z$, where $\hat{a}_z$ points along the conductor length. The scalar J_z then satisfies

$$\frac{\partial^2 J_z}{\partial x^2} + \frac{\partial^2 J_z}{\partial y^2} - \left(\frac{1+j}{\delta}\right)^2 J_z = 0. \tag{4.5}$$

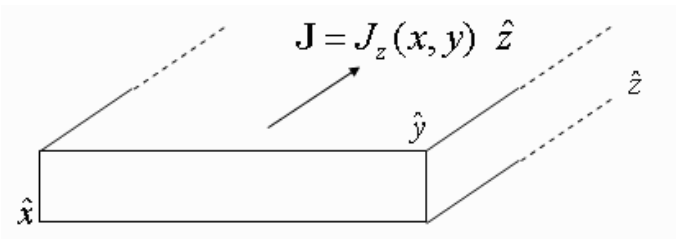

Figure 4.3: *We assume the current flows primarily along the length of the conductors: the z axis in this picture.*

The general solution of (4.5) is the infinite series:

$$J_z(x,y) = \sum_{\nu} C_\nu e^{-\psi_\nu x} e^{-\eta_\nu y}, \tag{4.6}$$

where C_ν are free coefficients and ψ_ν and η_ν satisfy [40]

$$\psi_\nu^2 + \eta_\nu^2 = \left(\frac{1+j}{\delta}\right)^2. \tag{4.7}$$

Each term in the previous series is referred to as a "conduction mode". As an illustrative example of a very simple conduction mode, let

$$\psi_\nu = \frac{1+j}{\delta} \tag{4.8}$$

$$\eta_\nu = 0. \tag{4.9}$$

This mode can account for cross-sectional current distributions decaying exponentially, with spatial constant δ, from one edge of the conductor cross-section. The picture on the left in Fig. 4.4 shows a graphical representation of such a current distribution.

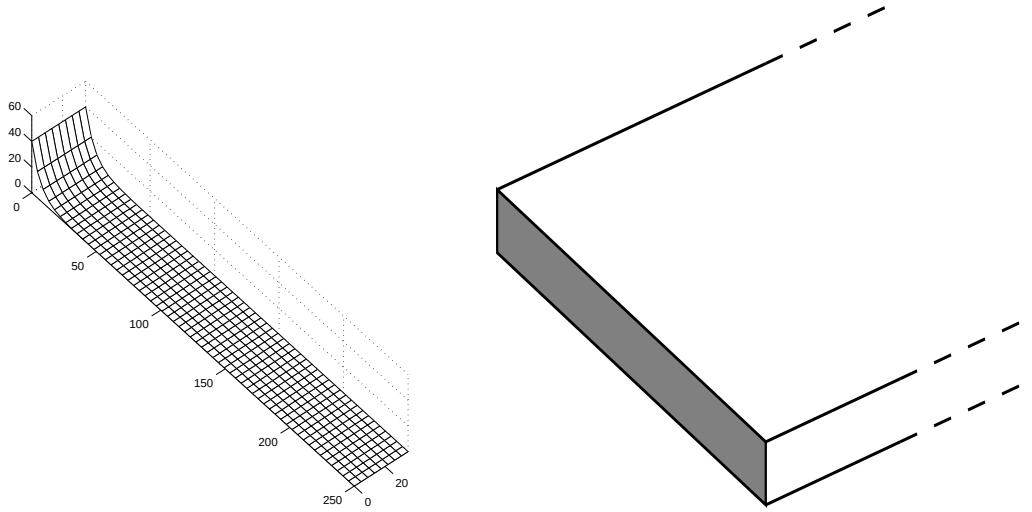

Figure 4.4: *Current density for an "edge mode" (on the left) associated with the shaded rectangular cross-section (on the right). In the figure on the left, axes x and y correspond to the width and length of the wire cross-section. Hence axis z is parallel to the direction of current flow, and shows the current density for each point of the cross-section. The conduction mode shown here is named "edge mode" since it represents current crowding at one of the four edges of the wire cross-section.*

For current distributions generated by interconnect problems, J_z can be accurately represented using only a few conduction modes. For example, a combination of four simple edge modes, one for each edge, can account for most of the high frequency cross-sectional conductor current distribution. At very high frequency, a few other modes might be needed to account for corner effects. The simplest example of corner mode is obtained by choosing

$$\psi_\nu = \eta_\nu = \frac{1}{\sqrt{2}}\left(\frac{1+j}{\delta}\right). \tag{4.10}$$

As it is shown in the picture on the left in Fig. 4.5, this mode can easily account for a cross-sectional current distribution decaying exponentially from the corner of the conductor cross-section.

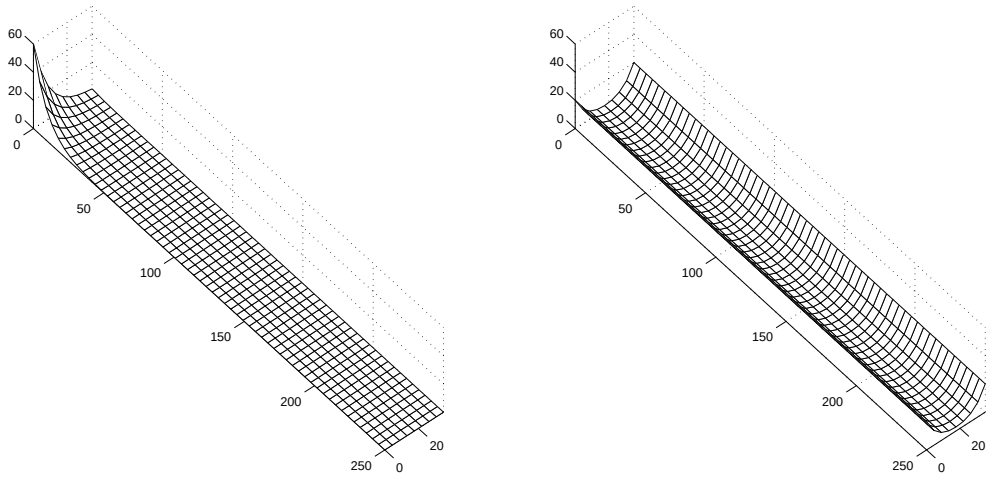

Figure 4.5: *On the left: "corner mode" for a rectangular cross-section. On the right: example of a single basis function obtained combining two horizontal edge modes.*

4.1.2 Discretization basis functions

Now construct a set of discretization basis functions for the conductor volumes. Long conductors are subdivided along their length into sections that are short compared to the smallest wavelength. The current density is represented by a collection of basis functions in each section,

$$\mathbf{J}(\mathbf{r}) = \sum_{j,k} I_{jk} \mathbf{w}_{jk}(\mathbf{r}), \tag{4.11}$$

where j is a summation index over all the sections of all the conductors, and k is a summation index over all the basis functions in a given section. The conduction modes in (4.6) represent a natural choice for the section basis functions:

$$\mathbf{w}_{jk}(\mathbf{r}) = \begin{cases} \frac{\hat{\mathbf{a}}_{z_j}}{A_{jk}} \sum_p e^{\pm\psi_{jkp}(x-x_{jkp})} e^{\pm\eta_{jkp}(y-y_{jkp})} & \text{if } \mathbf{r} \in V_j \\ 0 & \text{otherwise} \end{cases} \tag{4.12}$$

where V_j is the volume of section j, x and y are variables spanning the section j, and

$$\mathbf{r} = \mathbf{r}_{j_{\text{corner}}} + x\,\hat{\mathbf{a}}_{x_j} + y\,\hat{\mathbf{a}}_{y_j}. \tag{4.13}$$

Translation constants, x_{jkp} and y_{jkp}, as well as the "plus" signs in front of ψ_{jkp} and η_{jkp}, account for modes decaying from the other corners or edges. We have chosen to introduce a normalization constant A_{jk} defined such that parameter I_{jk} in (4.11) represents the total current in section j associated with basis function $\mathbf{w_{jk}}$. Therefore

$$A_{jk} = \int_{S_j} \sum_p e^{\pm\psi_{jkp}(x-x_{jkp})} e^{\pm\eta_{jkp}(y-y_{jkp})} dx\,dy, \tag{4.14}$$

where S_j is the cross-section of volume V_j.

To reduce the number of degrees of freedom for the discretization, it is possible to "pair-up" modes which are likely to have the same magnitude. One example where it is helpful to combine two modes into a single basis function occurs when modeling a PCB wire. In this case, one may wish to combine the lower horizontal edge mode with the upper horizontal edge mode, as shown in the picture on the right in Fig. 4.5. The large aspect ratio, and large layer separation, of the PCB cross-section wires, typically limits proximity effect

differences between lower and upper horizontal edge modes. Edge modes on opposite lateral sides (left to right) can not be combined as differences in left to right neighboring geometry will result in different left to right edge mode amplitudes, due to proximity effects. For this reason, the two lateral edge modes should instead be assigned to two separate basis functions.

4.1.3 Discretization of the MPIE

Substituting (4.11) into (3.14) and using a Galerkin method as described in Section 3.3 results in

$$\sum_k R_{ihik} I_{ik} + \sum_{j,k} j\omega L_{ihjk} I_{jk} = \phi_A - \phi_B \tag{4.15}$$

where one can recognize terms that could be interpreted as equivalent resistances and partial inductances of the conduction mode basis functions

$$R_{ihik} = \frac{1}{\sigma} \int_{V_i} \mathbf{w}^*_{ih}(\mathbf{r}) \cdot \mathbf{w}_{ik}(\mathbf{r})\, d\mathbf{r} \tag{4.16}$$

$$L_{ihjk} = \frac{\mu}{4\pi} \int_{V_i} \int_{V_j} \mathbf{w}^*_{ih}(\mathbf{r}) \cdot \mathbf{w}_{jk}(\mathbf{r}) \frac{e^{j\frac{w}{c}|\mathbf{r}-\mathbf{r}'|}}{|\mathbf{r}-\mathbf{r}'|} d\mathbf{r}' d\mathbf{r}. \tag{4.17}$$

The index h specifies the conduction mode basis function on the wire section i.

When using piecewise-constant, or filament basis functions for each section, the resulting resistance matrix is diagonal. This is because the filament basis functions are orthogonal, which follows from the fact that they have a non-overlapping support. The conduction modes generate non-orthogonal basis functions in each section, but basis functions in different sections still do not overlap. These facts imply that the resistance matrix generated from conduction mode basis functions will be block diagonal, where the block size is equal to the number of conduction modes in a section. A diagonal matrix R can be obtained by first using Gramm-Schmidt to orthogonalize the basis functions.

As in the PEEC method [121], an equivalent circuit interpretation can be given also to our method (Fig. 4.6), although we do not use this circuit interpretation in the solution of our system. In the conventional PEEC method, resistances and inductances refer to small cross-sectional filaments. In our case, instead, resistances and inductances refer to our conduction mode basis functions.

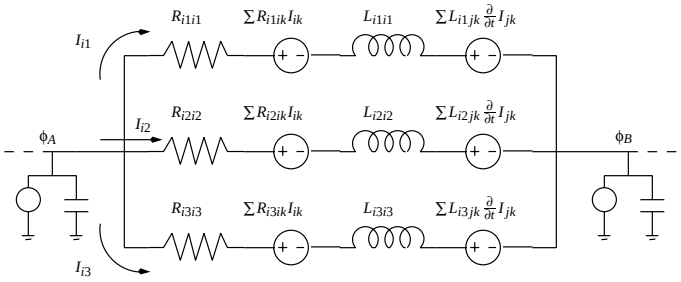

Figure 4.6: *An equivalent circuit interpretation can be given to this new cross-section basis function method as in the PEEC method. Every piece of conductor is modeled by the circuit shown here. Resistances and inductances refer to the conduction mode basis functions, rather than to small cross-sectional conductor filaments. In this particular model, we are showing 3 cross-section basis functions per piece of conductor.*

4.1.4 Numerical implementation considerations

The integral in (4.17) can be evaluated numerically using, for instance, a Gaussian quadrature algorithm. At first glance, one can observe that for the complete matrix setup, such integrals must be calculated $O(n^2 N_f)$

times, where n is the number of basis functions and N_f the number of frequency points. However, all this computation can be performed off-line before solving the resulting linear system.

Furthermore the amount of computation can be reduced by observing that for the purpose of evaluating the integral in (4.17), one can introduce a piecewise constant thin filaments discretization of each cross-section and approximate (4.17),

$$L_{ihjk} \approx \sum_{n_i=1}^{N_i} \sum_{n_j=1}^{N_j} \mathbf{w}^*_{ih}(\mathbf{r_{n_i}}) \cdot \mathbf{w}_{jk}(\mathbf{r_{n_j}})\, e^{j\frac{w}{c}|\mathbf{r_{n_i}} - \mathbf{r'_{n_j}}|}\, \hat{L}_{n_i n_j}, \tag{4.18}$$

where n_i, n_j, and r_{n_j}, r_{n_j} indicate the indexes and the centers of the integration thin filaments in conductor i and j respectively. $\hat{L}_{n_i n_j}$ is the well known quasi-static partial inductance Galerkin integral between two thin filaments V_{n_i} and V_{n_j}:

$$\hat{L}_{n_i n_j} = \frac{\mu}{4\pi} \int_{V_{n_i}} \int_{V_{n_j}} \frac{d\mathbf{r}' d\mathbf{r}}{|\mathbf{r} - \mathbf{r}'|}. \tag{4.19}$$

When the two conductors are parallel, there are formulas for (4.19) such as in [121]. Furthermore, the integral $\hat{L}_{n_i n_j}$ is not frequency dependent, and therefore can be evaluated only once and re-used at all frequency points. The order of computation for the complete system setup is now $O(N_{th})$ where N_{th} is the total number of thin filaments. Therefore in terms of *setup time*, the conduction modes method is no worse than the classical thin filament piece-wise constant method [121, 143, 68].

However, the most important contribution to the overall computation time and memory requirements is due to the subsequent linear system solution step, which is typically $O(n^2)$ even when using fast methods if skin effects and proximity effects need to be accounted for accurately. In Section 4.2 examples will be presented showing that for the same final accuracy the conduction mode basis functions method requires $1/20^{th}$ the number of basis functions used by the classical piece-wise constant method, and therefore reduces solution times and memory requirements by a factor of 400.

4.2 Implementation examples

Below are several example results from our implementation of the conduction modes approach. These examples verify that the method can successfully and efficiently capture skin effects, proximity effects, return current paths distributions, and transmission line resonances. These examples also verify that, for the same final accuracy, the method is much more efficient than the classical piece-wise constant thin filament method [121, 143, 68].

4.2.1 Capturing skin effects on two widely separated copper strips

Table 4.1: *Skin effect in copper strips (1.26cm x 0.1575cm x 32m) widely separated (60cm).*

Temperat. deg. cent.	Frequency [Hz]	R_{DC} [Ω] measured	R_{AC}/R_{DC} measured	R_{AC}/R_{DC} 3 cond. modes	Error %	R_{AC}/R_{DC} 48 thin filam.	Error %
+6.8	225	0.0563	1.004	1.003	0.1	1.003	0.1
-2.0	708	0.0539	1.038	1.029	0.9	1.030	0.8
-1.8	1188	0.0541	1.085	1.067	1.6	1.074	1.1
+6.0	1900	0.0554	1.161	1.131	2.6	1.145	1.4
-1.5	2980	0.0541	1.261	1.228	2.6	1.241	1.6
-5.0	3690	0.0534	1.326	1.289	2.8	1.296	2.2
-1.3	5169	0.0543	1.426	1.409	1.2	1.398	2.0

In this first example we reproduced in our field solver the experimental setup described in [72]. This example will show that the conduction modes method can capture skin effects, matching actual experimental

measurements. Two copper strips are placed parallel to each other at a distance of 60 cm, they are shorted at one end and the resistance is measured at the other end at different frequencies. As observed in [72] in this experiment a 60 cm separation is large enough that proximity effects are *not* significant on the two strips. The copper strips are 1.26 cm wide and 0.1575 cm thick. In [72] no explicit information is given on both their actual length and conductivity, although such information can be partially recovered using the data given on the measured DC resistance. In our computer model we chose strips of length 32 m which is consistent with a typical copper conductivity around $\sigma = 5.8x10^7(\Omega - m)^{-1}$. More precisely we fine tuned conductivities such that the DC resistance of the simulated strip matched the measured DC resistances in Table 4.1 at the different temperatures in each experiment.

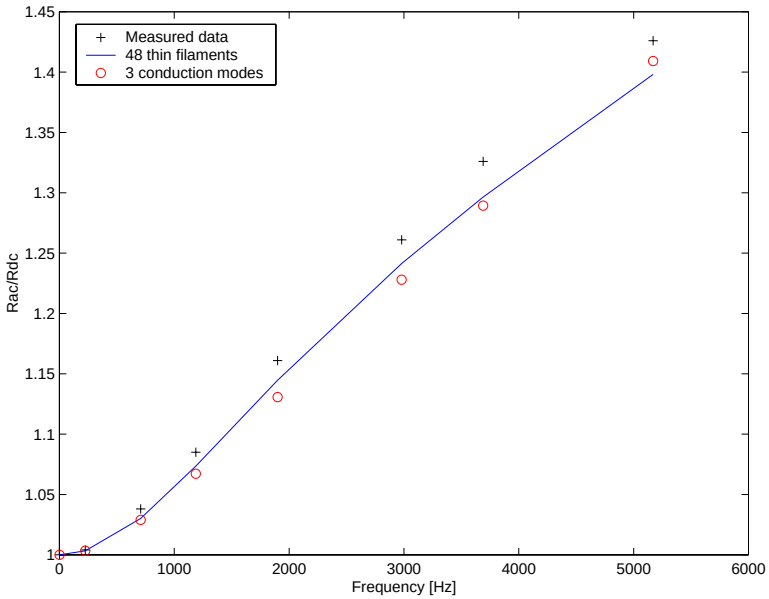

Figure 4.7: R_{AC}/R_{DC} *vs. frequency for two widely separated copper strips. The black crosses are measured data from a physical experiment. The continuous blue lines are obtained from a classical thin filaments discretization approach using 48 thin filaments per cross-section. Red circles indicate results from our new method using, in this particular example, only 3 cross-sectional basis functions.*

In this example, we have used a classical surface discretization with 32 small panels per wire to account for surface charge. We have used our conduction-mode cross-section basis functions to account for cross-sectional current density inside the conductors. In particular, we have used the following *three* basis functions:

- one for the left side edge-mode (on the left in Fig. 4.4);
- one for a similar right edge-mode;
- and one for the combined upper and lower conduction modes shown on the right in Fig. 4.5.

Using such basis functions we computed the terminal impedance, Z, versus frequency and considered its real part $R_{AC} = Re\{Z\}$ for comparison with the experimentally measured data from [72] as shown in Table 4.1 and Fig. 4.7.

In Table 4.1 and Fig. 4.7, we also compare our conduction mode method with one that uses the same discretization for the conductor surfaces, and a classical piece-wise constant thin filaments discretization. From Table 4.1, our method shows a worst case 2.8% error compared to measured data. In order to achieve a similar accuracy, the classical filament discretization method requires 12x4 = 48 thin filaments per cross-section, even when adopting the filaments to be thinner close to edges and corners. In particular, as we get

closer to edges and corners we kept decreasing the filament thickness by a factor of 1.5. For this example, maintaining comparable accuracies, our method produced a system with $1/16^{th}$ the number of unknowns, leading to a speed improvement factor of 256, when using iterative linear system solvers.

4.2.2 Capturing skin effects on a PCB wire example

A simple PCB wire example was used to test the ability of the conduction modes method to capture frequency variations of resistance and inductance due to skin effects. We computed the terminal impedance, Z, versus frequency for a a typical PCB wire (250μm wide, 35μm thick, and 5mm long). Fig. 4.9 and 4.10 shows the real part of the impedance ($Re\{Z\}$), and the imaginary part divided by ω ($L = Im\{Z\}/\omega$), as a function of frequency.

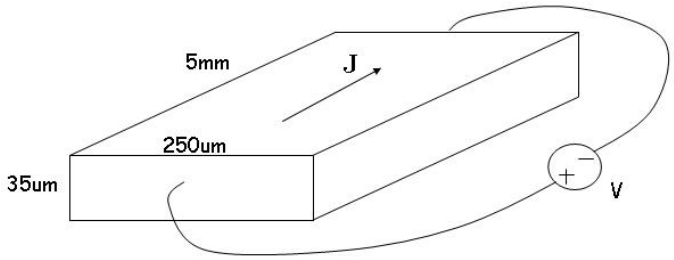

Figure 4.8: *PCB wire setup*

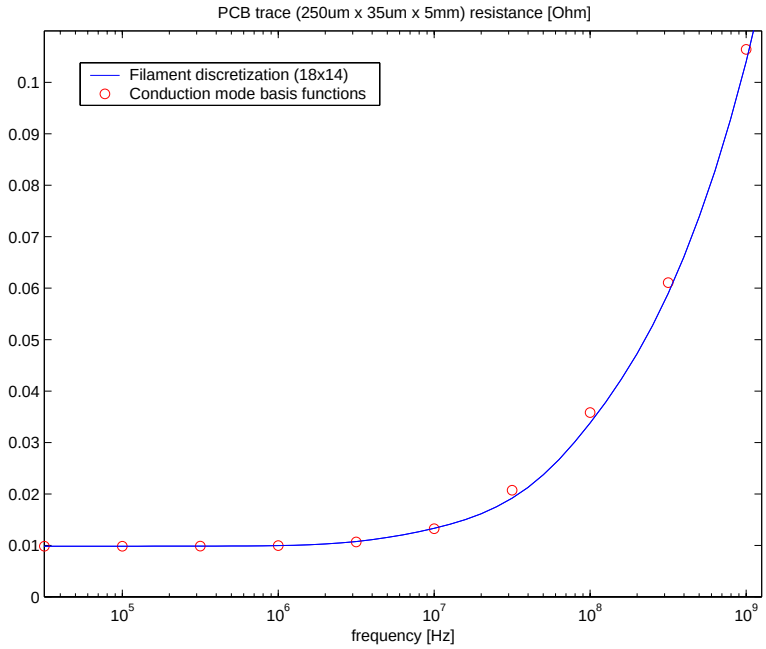

Figure 4.9: *$Re\{Z\}$ vs. frequency for a typical PCB wire. The continuous curves are obtained from a classical very accurate 18x14 filaments discretization approach. Circles indicate results from our new method using, in this particular example, only 3 cross-section basis functions.*

In this example, we have used a classical surface discretization into small panels to account for surface charge, while we have used our conduction-mode cross-section basis functions to account for cross-sectional

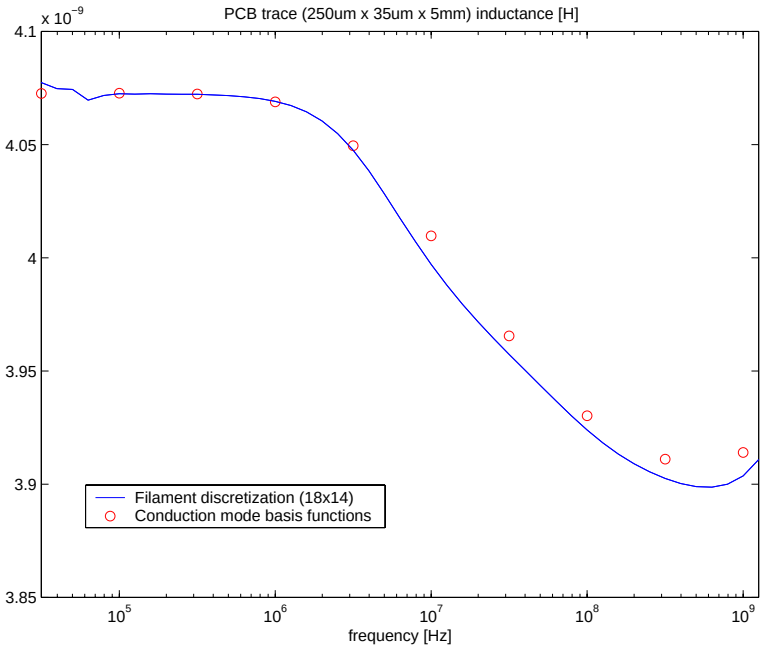

Figure 4.10: $L = Im\{Z\}/\omega$ *vs. frequency for a typical PCB wire. The continuous curves are obtained from a classical very accurate 18x14 filaments discretization approach. Circles indicate results from our new method using, in this particular example, only 3 cross-section basis functions.*

current density. In particular, we have used the following three basis functions:

- one for the left side edge-mode (on the left in Fig. 4.4);
- one for a similar right edge-mode;
- and one for the combined upper and lower conduction modes shown on the right in Fig. 4.5.

In Fig. 4.9 and 4.10 we compare our method with one that uses the same discretization for the conductor surfaces, and a very accurate classical piece-wise constant cross-sectional discretization using 18x14 small filaments. In the filament approach, we have used thinner filaments close to edges and corners as shown in Fig. 4.11. In particular, as we get closer to edges and corners we keep decreasing the filament thickness by a factor of 1.5.

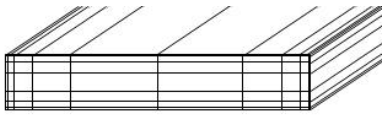

Figure 4.11: *The optimal way to implement the filament approach is to use a non-uniform discretization with thinner filaments close to edges and corners where the current density profile changes more rapidly.*

Compared to the accurate filaments solution, our method shows (in the worst case):

- a 5% error for the resistive part of the impedance $Re\{Z\}$,
- and a (very small) 0.2% error for the inductive part of the impedance, $L = Im\{Z\}/\omega$.

In a second experiment on the same example, we tested the convergence rate of the classical filaments discretization approach. In this experiment we have observed that, in order to achieve the same accuracy of our conduction modes method, the classical filament discretization method requires 10x7 small filaments per cross-section, with filaments thickness decreasing at a ratio of 5 at each step as we get closer to edges and corners. Hence in this example, for the same final accuracy, our method produced a system with 1/23 of the number of unknowns, leading to a linear system solve 500 times faster when using iterative methods.

4.2.3 Capturing proximity effects on an IC bus example

In this second example, we test the ability of our method to model proximity effects combined with skin effects on the IC bus example shown in Fig. 4.12. Six long interconnect wires are routed very close to each other (2μm). Each wire is 2μm wide and 2.5μm thick, and therefore has a very different cross-sectional

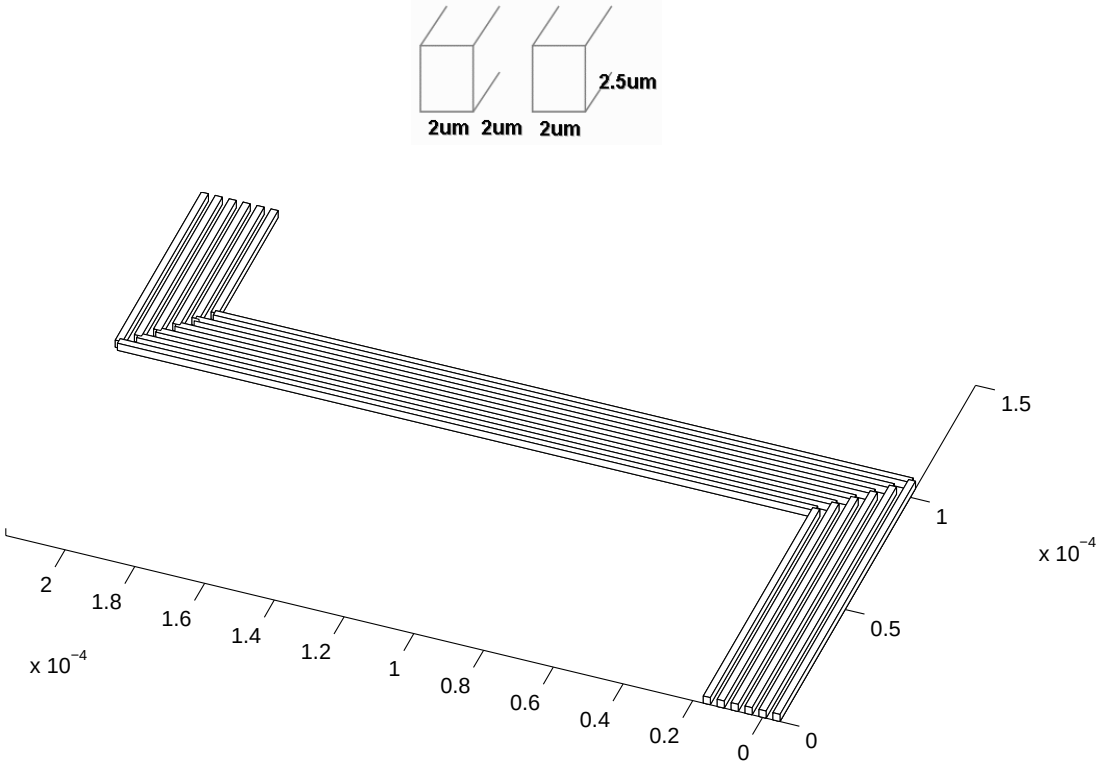

Figure 4.12: *IC bus: 4 signal wires between two ground return wires. In our simulation, the second wire from the right is shorted on one side of the bus to the lateral ground wires. The other side is driven by an ideal voltage source. All wires are 2µm wide, 2.5µm thick and 2µm far apart. The three legs of the bus are 100µm, 200µm and 50µm long respectively.*

aspect ratio from the previous example. The six wires are routed in a dog-leg bus configuration, where the three sections are 100μm, 200μm and 50μm long respectively. The four wires in the center of Fig. 4.12 are signal wires. The first and last wire are ground return wires. In our experiment, we grounded one side of the second wire from the right in Fig. 4.12, and we drove the other side with an ideal voltage source.

Fig. 4.13 shows the resistive part (above) of the impedance as a function of frequency, as well as $L = Im\{Z\}/\omega$, the "inductive" part of the impedance (below). The continuous lines are obtained using a very fine piece-wise constant thin filament discretization with 90 filaments per wire cross-section. These 90 filaments are sufficient to consider the continuous lines in Fig. 4.13 as the "exact" solution. Circles show the results

obtained using only three conduction modes. In the worst case, our three conduction modes give an error of 1.5% in the resistive part of the impedance, and 0.9% in the inductive part of the impedance. In Fig. 4.13, one can notice three frequency regimes:

- a low-frequency regime, with very small resistance since the current returns from both available ground wires.
- a mid-frequency regime, where the closer ground begins to be preferred to the farther away ground on the other side of the bus. The inductance begins to decrease since less current is now flowing on the largest loop. The resistance begins to increase.
- a high-frequency regime, where inductance keeps decreasing and resistance starts increasing exponentially. In this regime most of the current has crowded on only one side of the wire due to the proximity effect. The cross-sectional current distributions on the bus are shown in Fig. 4.15 for an excitation at 30 GHz. In Fig. 4.14, we compare the cross-sectional current density on the driven wire. On the left we show the result from the very fine thin filament discretization, and on the right we show the result obtained using only 3 conduction modes per cross-section. Comparing the figures makes it clear that our method captures accurately both skin effects and proximity effects.

We also observed that for the same final 1.5% accuracy, the classical method would require at least 49 thin filaments per cross-section even when adopting the filaments to be smaller near edges and corners. Therefore, in this example, we conclude that our approach requires 16 times fewer parameters than the classical method for the same final accuracy, leading to system solves 256 faster when using iterative methods.

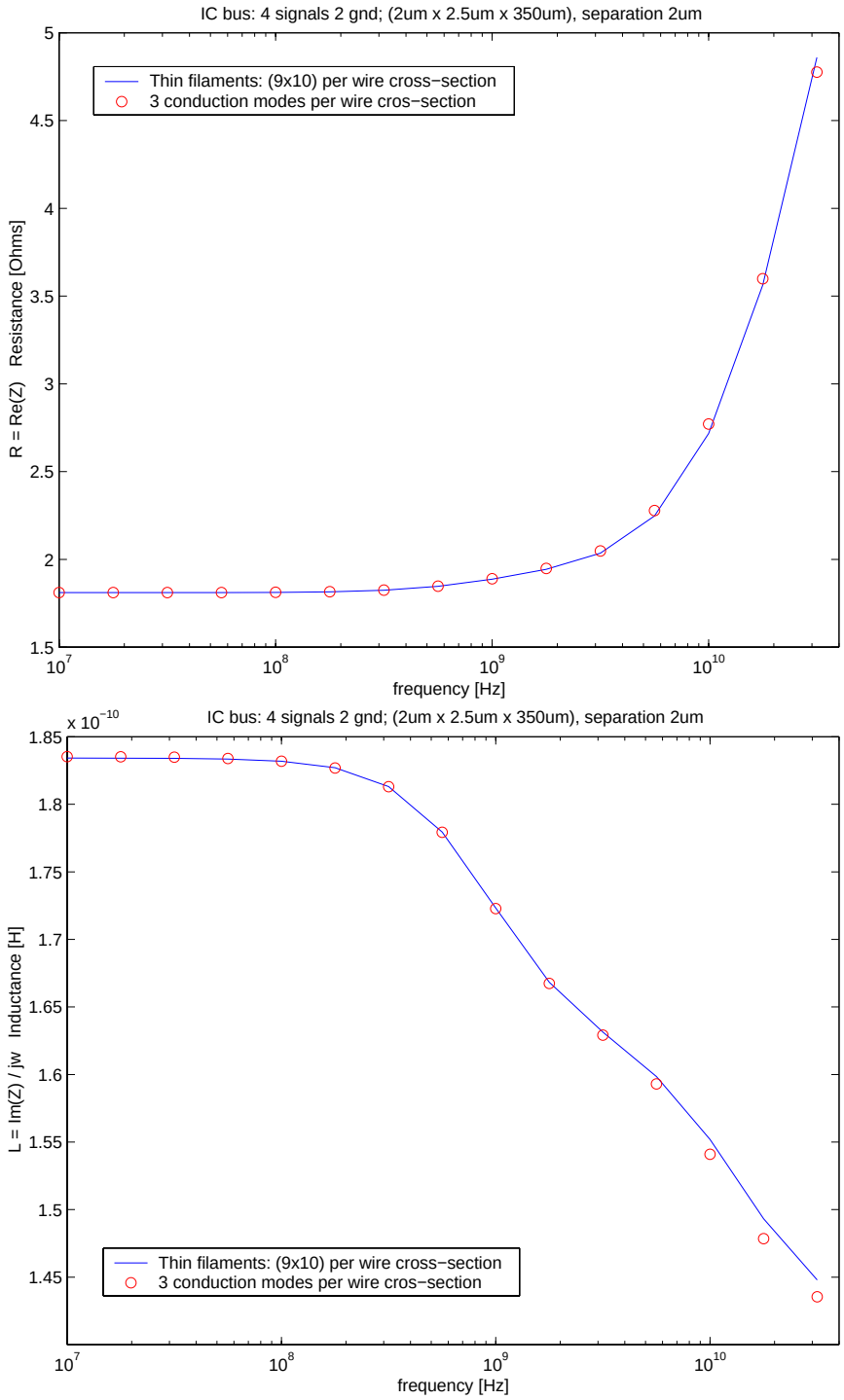

Figure 4.13: *$Re\{Z\}$ and $L = Im\{Z\}/\omega$ vs. frequency for bus in Fig 4.12. The continuous lines are obtained using a very fine thin filament discretization with 90 filaments per wire cross-section. Circles show the results obtained using only three conduction modes.*

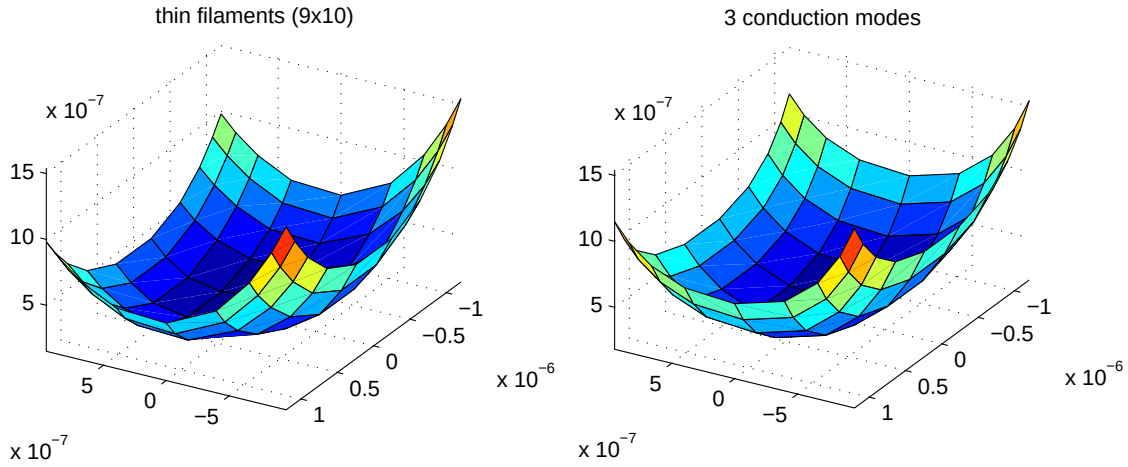

Figure 4.14: *Comparison for the cross-sectional current density on the driven second wire from the right of Fig 4.15. In the picture presented here on the left we show the result from a very fine thin filament discretization. On the right we show the result obtained using only 3 conduction modes per cross-section.*

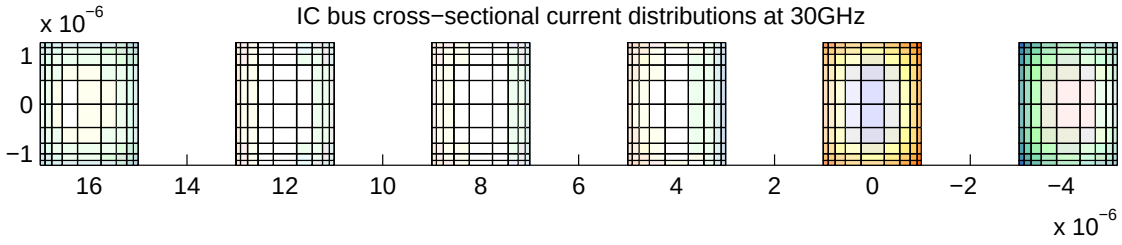

Figure 4.15: *Cross-sectional current distributions on the IC bus in Fig 4.12. The second wire from the right is driven by and ideal voltage source at 30 GHz. The first wire from the left and the first wire from the right are DC ground returns.*

4.2.4 Capturing resonances on a PCB transmission line example

In a third example, we test the ability of our method to capture wavelength related resonance phenomena. Characterization of resonance's positions and amplitudes is very important in applications such as signal integrity and electromagnetic interference. Unfortunately, such resonances are typically difficult to simulate with accuracy since their amplitude is very much influenced by the conductor's AC resistances due to internal current distributions. Although we present here a simple and intuitive geometry, our method can characterize such wavelength related resonances for any general 3D geometry even when a transmission line structure is not so well defined as in the following case.

We model here two coplanar PCB wires, 30cm long, very close together in a coplanar transmission line configuration shown in Fig. 4.16. Wires are 250μm wide, 35μm thick and 150μ far apart.

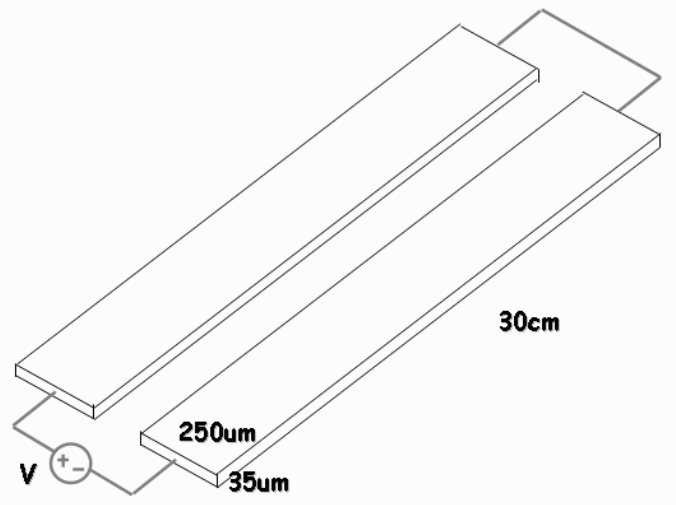

Figure 4.16: *Shorted coplanar T-line. Wires are 250µm wide, 35µm thick, 30cm long and 150µm far apart.*

Worst case high-Q resonances are obtained when the two wires are shorted at one end, and are excited on the other end at the resonance frequencies with an ideal voltage source. For instance, when the frequency is such that the transmission line length is close to a quarter of a wavelength or to half a wavelength, one can observe in Fig. 4.17 and 4.18 resonance peaks. Continuous lines in Fig. 4.17 and 4.18 are obtained using a classical piece-wise constant very fine cross-sectional discretization of 252 thin filaments per cross-section. This kind of discretization is sufficient to consider once again those continuous lines the "exact" solution. Circles are obtained instead using only three conduction modes per wire cross-section. Both in the thin filaments method and in our conduction modes method, we subdivided each wire along its length into pieces short compared to a wavelength. In Fig. 4.18, we measure that our three conduction modes method gives a worst case 1.3% error in the position of the second half-wavelength admittance resonance. A higher worst case error (9.6%) is measured on the amplitude of the same resonance. Fig. 4.19 compares at such resonance frequency the current distributions on the cross-section of one of the wires. On the left we show the result from the very fine 252 thin filaments discretization. On the right we show our three conduction modes solution. One can observe that the two current distributions are very much alike, except for the corners. At this frequency, currents begin to crowd more significantly on the corners of the cross-section, requiring the inclusion of a few "corner modes" in the set of the discretization basis functions, if higher accuracies are needed.

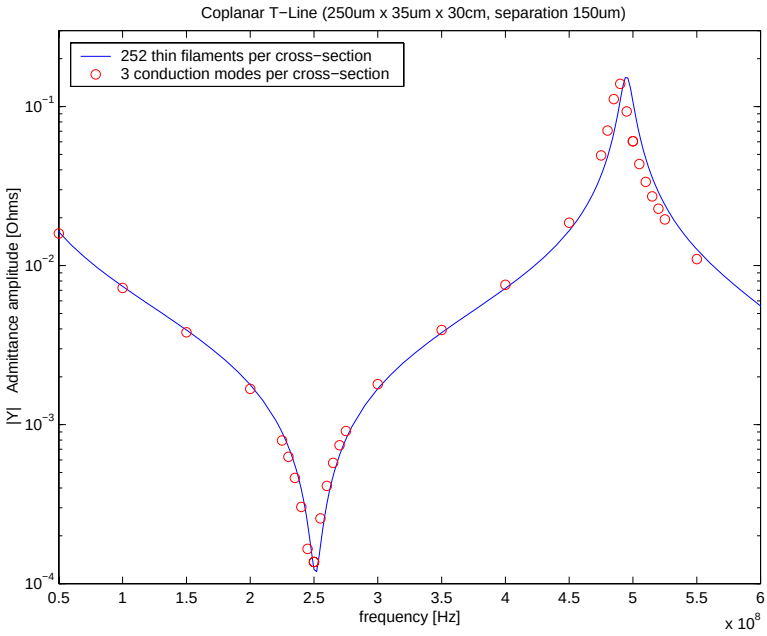

Figure 4.17: *Admittance amplitude vs. frequency for a shorted coplanar T-line. Wires are 250µm wide, 35µm thick, 30cm long and 150µm far apart. The continuous line is obtained using a very fine 252 thin filaments per cross-section discretization. The circles are the results obtained using only 3 conduction modes per cross-section. In both cases conductors lengths are subdivided into 10 pieces per wavelength along their length.*

4.3 Conclusions on the conduction modes basis functions

In this Chapter we have presented a new method for modeling internal conductor current distributions in a quasi-static or full-wave electromagnetic simulator. We have shown how to derive conduction modes for use in the discretization of the Mixed Potential Integral Equation. We have demonstrated the method on three examples, from both IC and PCB applications. We showed that skin effects, proximity effects and transmission line resonances can all be successfully and efficiently captured for different wire configurations and cross-sectional aspect ratios. In our examples, for the same final accuracies, using our conduction modes method, linear systems of equations are obtained on average 16 to 20 times smaller than when using the classical thin filament discretization methods. Hence solutions on average 256 to 400 times faster are possible when using iterative methods.

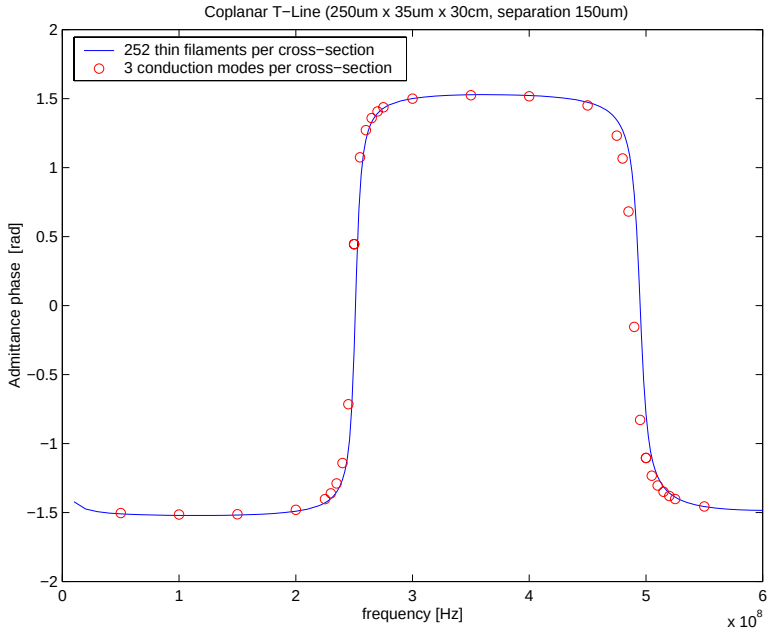

Figure 4.18: *Admittance phase vs. frequency for the same coplanar T-line as in Fig. 4.17.*

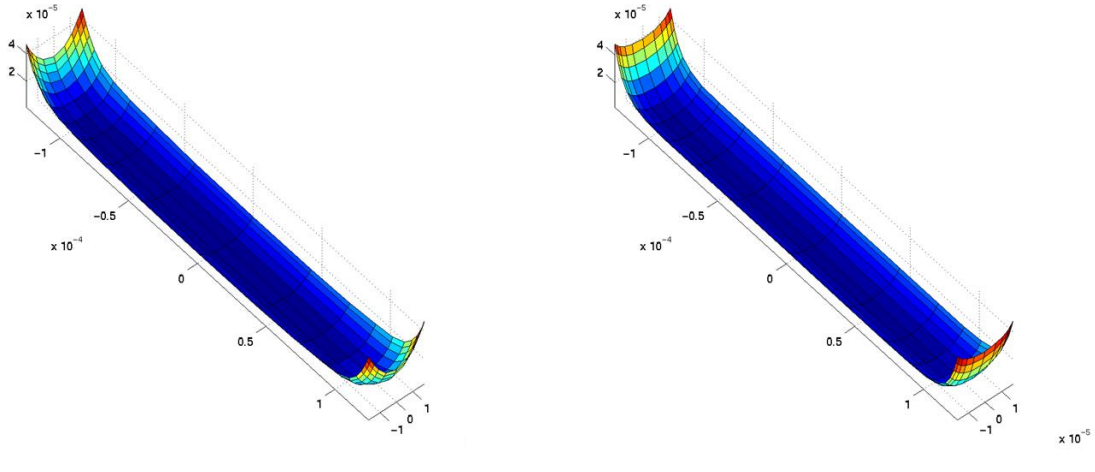

Figure 4.19: *Cross sectional current distributions at the half-wavelength resonance. On the left: result from a very fine cross-sectional discretization. On the right: result from the 3 "edge" conduction modes per cross-section method. Inclusion of corners modes can farther improve the fit if higher accuracies are needed.*

Chapter 5

Proximity template basis functions

In this Chapter we demonstrate that it is possible to generate numerically a set of basis functions which efficiently represent conductor current variation. The work in this Chapter has first appeared in [38]. Our method is based on solving a sequence of simple "template" problems for the typical geometries associated with a given interconnect technology. These template problem solutions are then used as replacement for the piece-wise constant basis functions in an integral equation method based on the Galerkin discretization of the Mixed-Potential Integral Equation (MPIE) presented in Section 3.3. As our results will demonstrate, the numerically computed basis functions require 7 to 20 times fewer unknowns than piece-wise constant basis functions. It should be noted that similar performance was achieved by generating basis functions using 2-D conduction modes [35, 37] in Chapter 4, but unlike the conduction mode approach, the template approach is easily extended to general shape cross-sections (e.g. trapezoidal).

In Section 5.1 we describe the steps for the pre-computation of our template basis functions. In Section 5.2 we show how to use the templates in the Galerkin integral equation method underlining some numerical implementation issues. Finally in Section 5.3 we present several example results on typical IC, package and PCB simple interconnect structures.

5.1 Pre-computation of the proximity template basis functions

In this section, we describe our procedure to construct a set of template basis functions for the discretization of the conductor volumes within the context of an integral equation electromagnetic field solver. As in the classical piece-wise constant approach [121, 143, 68] described in Section 3.3.1, or as in the conduction modes approach [35, 37], in Chapter 4, we assume that the current flows only along the length of the conductors, and that long conductors are subdivided into sections short compared to the smallest wavelength of interest. We then categorize and label each conductor section according to its cross-section "type". Each "type" is uniquely identified by its cross-section dimensions and shape. For instance, for wires with a trapezoidal cross-section: width, thickness and etching slope could be used as identifying parameters.

Often when performing an electromagnetic analysis, one is interested in the current (or fields) distribution at a particular excitation frequency, or in the impedance at some terminals for several excitation frequencies. *For each frequency of interest* and *for each wire cross-section "type"*, we pre-compute off-line a set of proximity template basis functions. Each basis function is constructed by solving a small simulation experiment:

1. Given a cross-section type, for the construction of the first template basis function we consider one wire not interacting with any other wire, and excited with a unity current source at the frequency of interest. For the solution of this simple problem we use a very fine piece-wise constant thin filament discretization method [121, 143, 68]. We then choose as basis function the current density profile derived on the entire cross-section by this analysis. We show on the left of Fig. 5.1 the thin filament discretization of the wire cross-section and to its right the resulting cross-section current density that

we use as first basis function. In Fig. 5.1 the wire cross-section is rectangular, *but general cross-section shapes can be handled in the same way by our procedure.* From an intuitive point of view, the template basis function described here is used to capture skin effect phenomena.

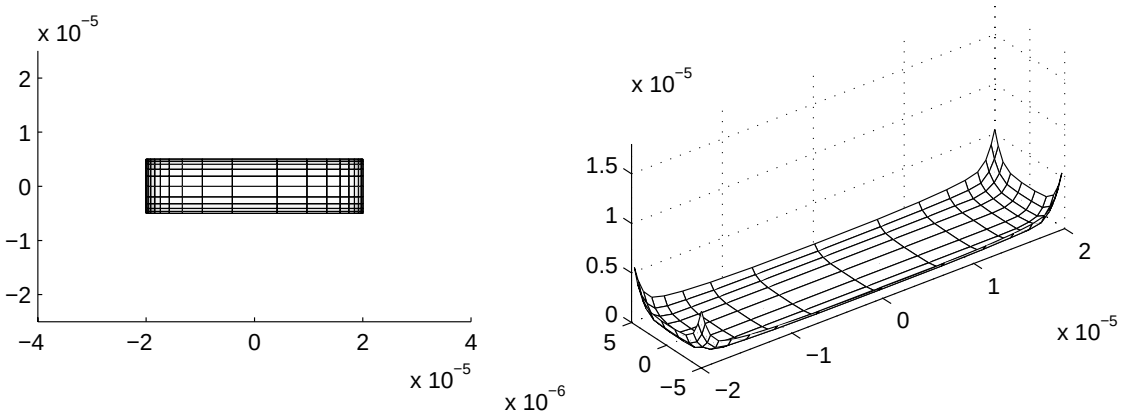

Figure 5.1: *Example of the first proximity template basis function. On the left, we show a cross-section of the simulation experiment setup used to pre-compute the basis function. The basis function is defined as the current density (shown on the right) resulting on the cross-section of the wire.*

2. Other basis functions are then constructed to capture proximity effect phenomena. In order to capture proximity effect phenomena due to wires on the side, we construct a second template basis function solving a second simple experiment. In this second experiment we consider two wires not interacting with any other wire. The cross-section of the "main" wire is chosen equal to the cross-section shape and dimensions for the "type" under consideration. A second auxiliary wire is located on one of the two sides of the main wire, as close to the "main" wire as the technology fabrication process would allow. The auxiliary wire is chosen with the minimum width and thickness allowed by the technology fabrication process. Fig. 5.2 shows on the left the cross-section configuration of the two wires. For the analysis of this problem we use a classical and very fine piece-wise constant discretization for both such wires. We short them together on one side, apply a unity current source at the remaining two terminals, and solve for the current density within the conductors. We finally define as second proximity template basis function the current density profile observed on the *main* wire. On the right in Fig. 5.2 we show the cross-sectional current density of the second basis function.

3. We proceed constructing additional proximity template basis functions using the procedure described in point 2 above, but every time moving the auxiliary wire in a different location around the main wire, always as close to the main wire as the technology fabrication process allows. Fig. 5.3 shows other two examples of template basis functions with their corresponding experiment setups for the same cross-section as in Fig. 5.1 and 5.2.

5.1.1 Choosing the number of template basis functions per wire cross-section

More specifically, the total number of template basic functions precomputed for each cross-section type can be decided according to the following considerations.

In some cases, one only needs to use a total of three proximity templates for each cross-section type: a "skin effect template" constructed as in Fig. 5.1, and two "side proximity templates", one for the right side as in Fig. 5.2 and one for the left side (typically symmetric to the one in Fig. 5.2). This choice is typically

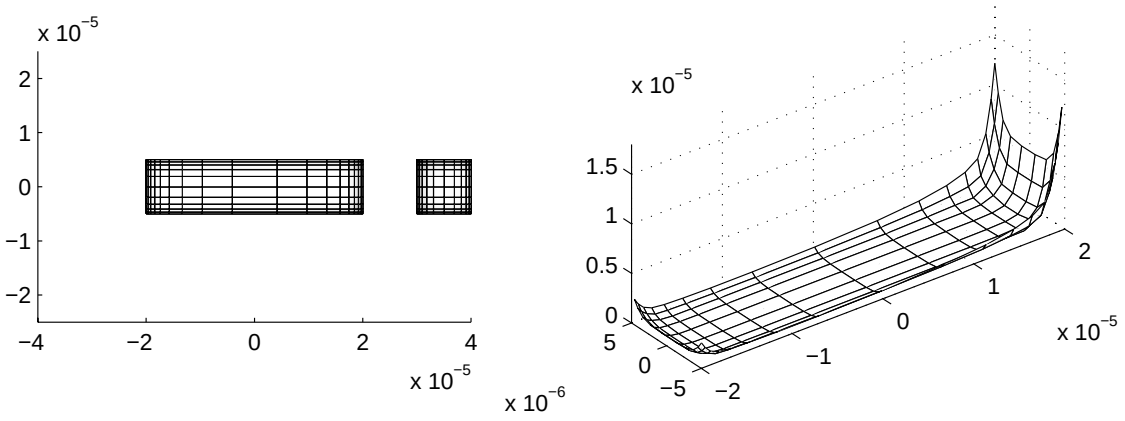

Figure 5.2: *Example of the second proximity template basis function. On the left, a cross-section of the simulation experiment setup used to pre-compute the basis function. On the right the basis function itself: i.e. the current density resulting on the* main *wire cross-section.*

appropriate for wires on most Printed Circuit Board (PCB) applications, where the separation between different layers is particularly large, and proximity effects are only observed in correspondence of "side by side" wires, and *not* in correspondence of wires on different layers.

When separation between metalization layers is small as in packages and in integrated circuits, one needs to be able to account for proximity effects due not only to wires "side by side" but also due to wires on upper and lower layers. In this case, for thin wires we use a total of nine templates: a "skin effect template", four proximity templates constructed using an auxiliary wire moved to each of the four sides of the main wire, and four proximity templates with the auxiliary wire moved to each of the corners around the main wire. Fig. 5.1, 5.2, and 5.3, show four out of nine of such templates. One can notice that in case of symmetric cross-sections the other five templates do not need to be computed.

Finally, in the case of considerably wide wires, in addition to the nine templates previously described, one needs to use a few more proximity templates to capture appropriately proximity effects due to thin wires in any location above or below such wide wire. In our implementation we precompute templates using an auxiliary wire that for each template is moved in different locations around the main wire. We remind the reader that the auxiliary wire width an thickness are chosen as the minimum allowed by the technology process, and that the auxiliary wire is located at the minimum distance from the main wire allowed by the technology process. For each template we then move the auxiliary wire to locations each separated by 4 times the auxiliary wire width.

5.1.2 Accuracy and basis function richness

The accuracy of the final solution is related to the ability of the chosen basis functions to "explain" most of the cross-sectional current density capturing current crowing in different parts of each cross-section due to the specific locations of nearby wires. More precisely, in linear algebra terms: when considering the cross-sectional current density as a vector, the accuracy of the final solution is related to the ability of the chosen basis functions to "span" most of the subspace generated by all practical current density vectors. In general the accuracy of the final solution can be arbitrarily improved if the set of all basis functions that one can choose from is sufficiently reach to span the entire subspace of all practical solutions. In our case, in theory the basis function set is quite reach since one could increase the accuracy of the final solution by simply adding more and more basis functions, one for each possible practical location of nearby wires. However we have observed experimentally (see Examples 5.3.2 and Example 5.3.1) that the procedure in 5.1 and 5.1.1

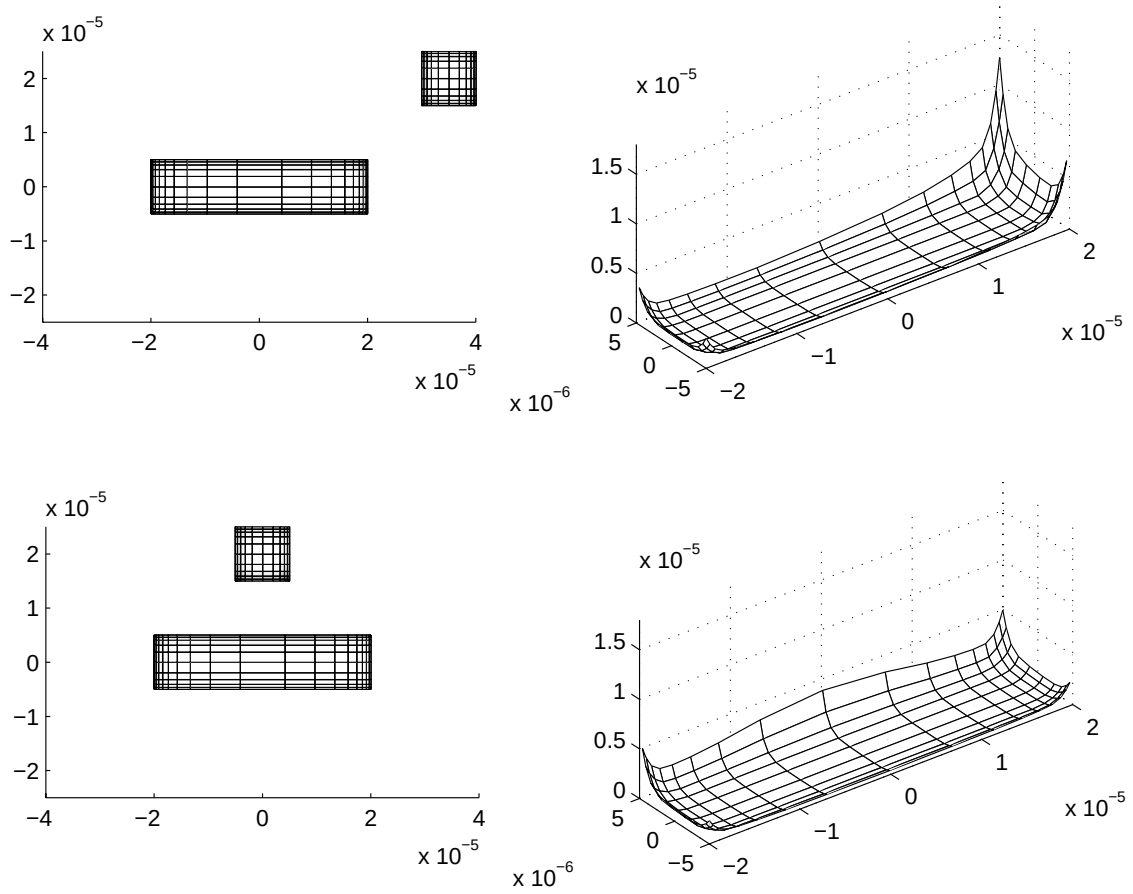

Figure 5.3: *Example of other two proximity template basis function. On the left, a cross-section of the simulation experiment setups used to pre-compute the basis functions. On the right the basis functions themselves: i.e. the current densities resulting on the* main *wire cross-sections.*

constructs a *much smaller* set of basis functions at the same time still allowing of a good final solution accuracy.

5.1.3 Advantages and disadvantages of the proximity template basis functions

From the construction procedure described above in 5.1 and 5.1.1 one can notice several advantages and disadvantages of our template basis functions in particular when compared to other higher order basis function choices such as the "conduction modes" described in [35, 37]. Among the advantages it can be noticed that:

- our template basis functions can handle any wire cross-section shape, i.e. the common trapezoidal cross-sections due to chemical etching slopes. In the conduction modes basis function approach [35, 37], instead, only cross-section shapes for which analytic solutions of the diffusion equation are available can be handled, i.e. mainly rectangular and cylindrical cross-sections.
- our template basis functions can capture proximity effects due to thin wires above very wide wires (as shown later in Example 5.3.2 and Fig. 5.5) that are not captured by the "conduction mode" approach.

Among the disadvantages of our template basis functions, we remind the reader that:

- a complete set of template basis functions need to be pre-computed *for each wire cross-section "type"* (i.e. shape and dimensions). Fortunately, one can further observe that often the actual number of wire cross-section types on a typical PCB, package or IC is quite limited. For instance the etching slope can be assumed constant for all cross-sections for a given process. The variability of the wire thickness is limited to the number of metalization layers in the design. Also the variability of the wire width parameter in practical designs is often limited to a finite and small set of admissible values by design rules or CAD tools. It is also worth noticing that once the template basis functions are computed they can be stored in a file and re-used for subsequent designs based on the same process technology.

- Another disadvantage of our proximity templates compared to the conduction modes is that a complete set of template basis functions need to be pre-computed *for each frequency of interest.* Typically one is not interested in a large number of frequencies. For instance in digital interconnect one is typically only interested in the clock frequency and its first 10 to 15 harmonics. Once again, one can further notice that once the template functions are calculated for a particular frequency, they can be stored and re-used in subsequent designs for analysis at that same frequency. However admittedly a significant advantage of the conduction mode basis functions over our proximity templates is the availability of the conduction modes in analytical form which can be exploited when performing model order reduction.

5.1.4 Representation of basis functions

As just observed in the previous section, we represent our basis functions with a piecewise constant values of the current density on each small cross-sectional filament. In this way for each basis function we only need to store some information on the discretization scheme from which one can easily derive filament geometries (e.g. width of corner filament and incremental ratio between nearby filaments), and a vector with the values of current density on each filament.

One could think of using more efficient representations in terms of some interpolation functions in order to save some storage memory and some computation time in the Galerkin integral computations. We expect however to obtain the most advantage by fitting our templates basis functions to interpolation function not only to represent their shape along the wire cross-section but also and above all to capture their dependency from frequency. In fact, this could allow us to perform model order reduction with our template basis functions as efficiently as with the conduction modes. However, we have not verified yet the practical feasibility of such procedure.

5.2 Parasitic extraction for a large collection of interconnect

Given a large collection of wires, for a given frequency of interest, each wire is associated with the set of pre-computed proximity template basis functions corresponding to its cross-section type. The basis functions chosen in this way, together with a standard Galerkin procedure [54], are used to discretize the Mixed Potential Integral Equation (MPIE) and calculate the overall resistance R and the partial inductance L matrices in eq. (3.23) and (3.24) as shown in Section 3.3. Accumulation of charge on the surfaces of the conductors can still be handled for example using the classical piece-wise constant discretization of such surface into small panels as described in Section 3.3.1. A mesh analysis technique [67] is then finally used to set up a linear system of equations that can be solved to find the weights $\mathbf{w}_j$ and $\mathbf{v}_m$ associated with each single basis function.

From a numerical implementation prospective one can observe that the proximity template basis functions as constructed in Section 5.1 are not orthogonal. The resistance matrix for instance is block diagonal. In general, when the basis functions are almost linearly dependent, their associated coefficients representing the final solution may result very large, similar in magnitude, and possibly of opposite phases partially canceling each others, which may produce errors when using a finite precision representation. One can avoid this problem and achieve better numerical stability by ortho-normalizing the basis functions before using them with for instance a "Modified Gramm-Schmidt" procedure [41]. Another advantage of orthonormalizing the

basis functions is that a completely diagonal resistance matrix is produced, which is convenient for instance when performing a subsequent model order reduction step that may require an inversion of such matrix. The orthogonalization procedure is quite fast and most importantly it is part of the "precomputation" phase, hence it does not affect the speed and memory performance during the analysis of a very large collection of interconnect.

As a final remark, it can be noticed that our proximity templates basis functions can be used in combination with fast matrix solvers [94, 68, 110, 136, 71].

5.3 Examples

5.3.1 Capturing proximity effect between two wires at arbitrary distance

In this section, we intend to show with an example that although our proximity templates are constructed using an auxiliary wire very close to the main wire, such template basis functions can successfully capture proximity effects due to wires at *any arbitrary* distance. Consider for instance a typical PCB wire 250μm wide, and 35μm thick. In this example we used a set of three template basis functions per cross-section. One template was constructed using one wire alone with a 250μm x 35μm cross-section. A second template was constructed using one main wire (cross-section: 250μm x 35μm) in the center and one auxiliary wire (250μm x 35μm) on one side at a separation distance of 100μm. A third template was constructed by moving the auxiliary wire to the other side at the same separation distance. For the construction of the basis functions, we discretized each wire into 24x14=344 thin filaments. After the three template basis functions have been constructed, we used them in the integral equation Galerkin procedure described in Section 3.3 to calculate the frequency response of two wires with the same cross-section at different separation distances: 100μm, 190μm, 305μm, 448μm, and 629μm. We compare in Fig. 5.4 the result obtained using our three proximity template basis functions per cross-section with the result obtained using 344 thin filaments basis functions per cross section. Of course one can expect a negligible error when the wires' separation is exactly equal to the separation used for the construction of the basis functions (100μm). However, we also observed an equally very small error (worst case 0.7% error for the real part of the impedance, and a 0.01% error for the imaginary part divided by ω) for the case in which the separation between the two wires increased to an arbitrary distance and did not coincide anymore with the separation used during the construction of the basis functions.

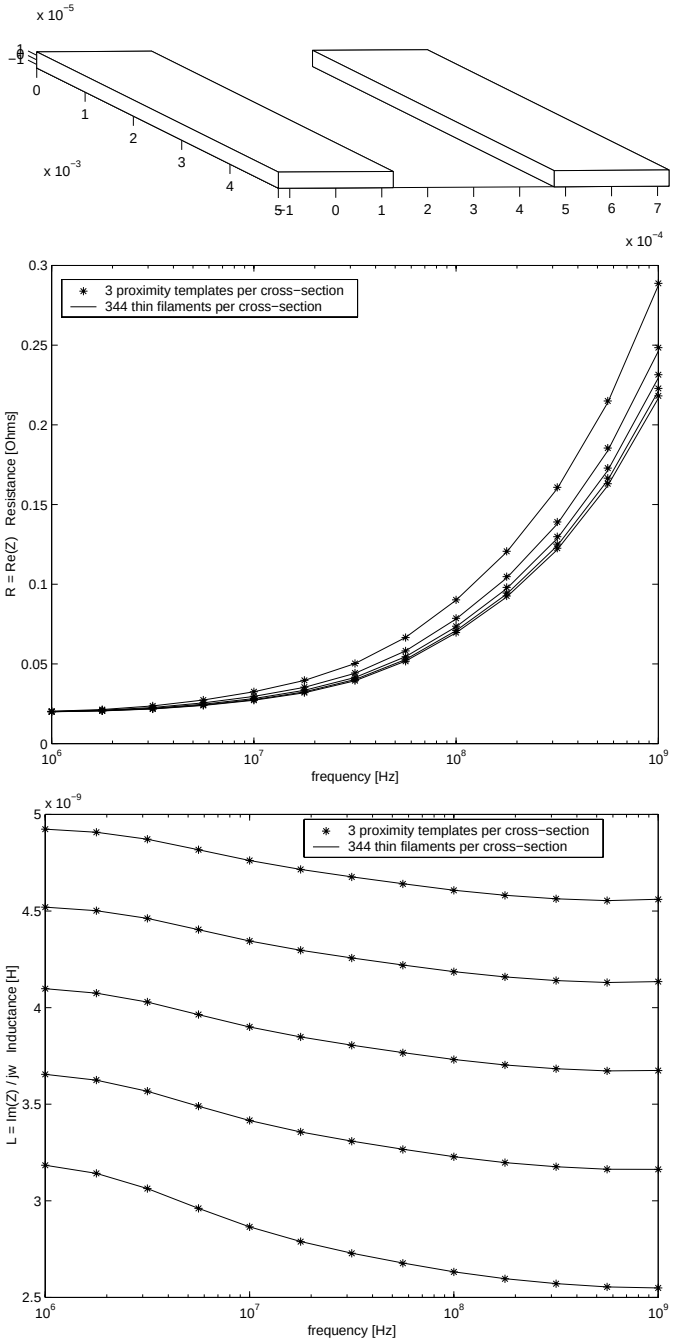

Figure 5.4: *Frequency response of two shorted PCB wires: real part of the impedance on the top, and imaginary part divided by* ω *on the bottom. The different curves represent different distances between the two wires: 100µm, 190µm, 305µm, 448µm, and 629µm (from top to bottom on the left and from bottom to top on the right). The continuous lines are the results obtained using the classical thin filament method. The small crosses are the results obtained using three template basis functions pre-computed for a minimum separation distance 100µm.*

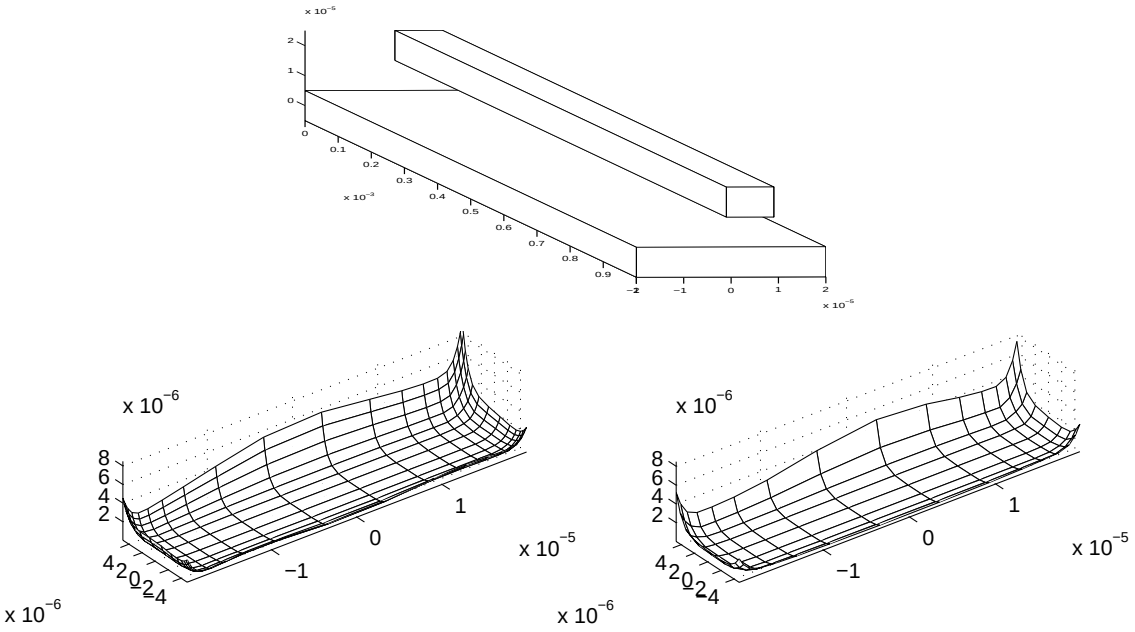

Figure 5.5: *Package wire cross sectional current density "reconstructed" from a set of nine pre-computed proximity template basis functions (picture on the left), compared to the current density (picture on the right) from using a set of 16x9 = 144 thin filaments basis functions. A larger current distribution can be noticed on one edge and on one corner of the cross-section due to the proximity of the small wire. Note that the location of the small wire is off center, hence it does not coincide with any of the locations used to pre-compute the nine template basis functions. One can notice that the current density is still captured accurately.*

5.3.2 Capturing proximity effect between a thin wire in an arbitrary location above a wide wire

From the previous example we have seen that the proximity templates is an approach at least as efficient as the conduction modes approach [35] in terms of used number of unknowns. In addition, we show in this example that the proximity templates can successfully capture one particular case not captured by the conduction modes approach: proximity effects between a thin wire *above and close to* a very wide wire. Consider for instance a package wire 40μm wide and 10μm thick. Pre-compute a set of nine proximity effects basis functions for this wire. Fig. 5.1, 5.2, and 5.3 show four of such nine basis functions for the cross-section type described in this example. The auxiliary wire is 10μm wide and is moved into several locations all around the main wire all at a distance of 10μm. After the computation of the basis functions, we have setup the experiment on top of Fig. 5.5. The small wire is 10μm x 10μm, the wider wire right below it is 40μm x 10μm at a 10μm separation. We can also notice that the small wire is off center by 4μm so that its location *does not* coincide with one of the locations used for the basis function construction (compare the cross-section in Fig. 5.3 with the cross-section of the geometry in Fig. 5.5). The two remaining pictures in Fig. 5.5 compare the cross sectional current density resulting from using our set of nine pre-computed proximity template basis functions (left), with the result (on the right) obtained using a set of 16x9 = 144 thin filaments basis functions. We conclude that the proximity templates provide accurate results not only for wires at an arbitrary distance as shown in Example 5.3.1, but also for wires located "in between" the original locations used for the basis functions construction.

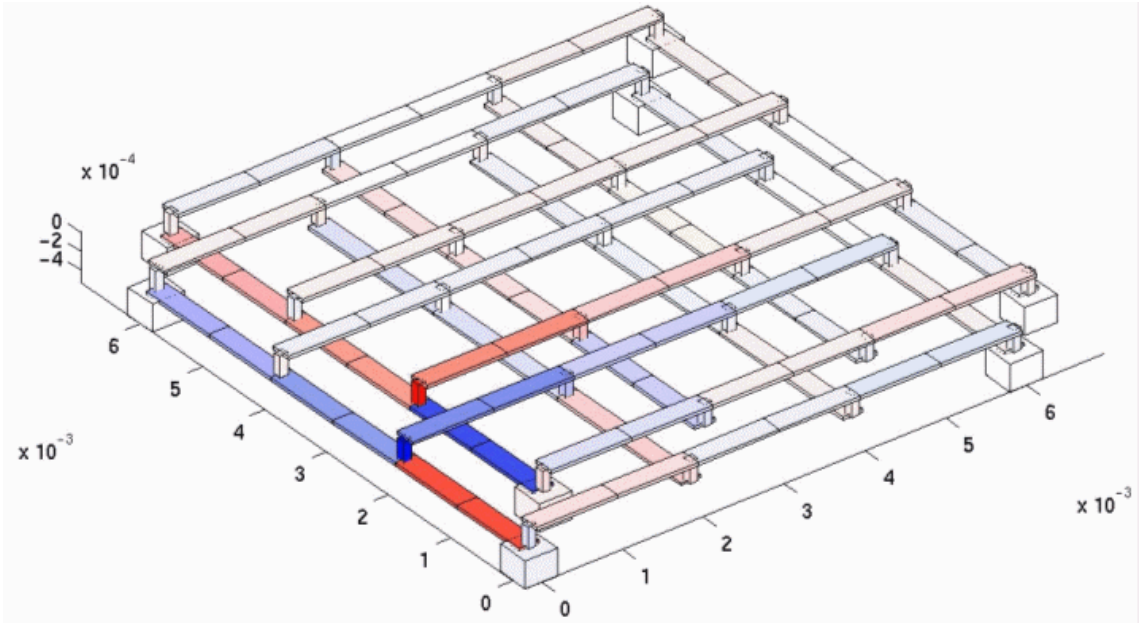

Figure 5.6: *A simplified representation of a power and ground grid of a package or of an integrated circuit. Gray shading on the the grid indicate current distributions calculated by our solver when a current source excites the grid node x = 4mm and y = 0mm. In this example we used three proximity template basis functions for each wire cross-section.*

5.3.3 A package power and ground distribution example

Finally we show here a package power and ground distribution grid Example (Fig. 5.7). Wires are 10μm wide and 5μm thick. Vertical separation between layers is 5μm. Side separation between Gnd and Vdd lines is 1mm. The total package size is 12mm x 12mm. We assumed bond wires connections shorting Gnd and Vdd wires to an underneath PCB on all 4 corners of the package. We can notice that only one type of cross-section is present in this design. For that cross-section type, we have pre-computed a set of three basis functions as in Example 5.3.1. We have then used our three basis functions per segment to discretize the entire geometry and find the frequency response at one particular node of the grid: the node at x = 4mm and y = 0 mm (see Fig. 5.7). In our simulations we have also included the effects of charge accumulation on the surface of the conductors using a piece-wise constant discretization into small panels. In Fig. 5.7 we compare the frequency response of the grid at the node indicated above according to our three proximity templates per wire versus the frequency response obtained using a thin filament discretization with 5x4 = 20 thin filaments per each wire segment of the grid. Our approach required a total of 48x3=144 unknowns for the conductor currents, while to get a similar accuracy with the thin filament approach we had to use a total of 48x20=960 unknowns. In particular, for our proximity templates approach we observed from the admittance phase vs. frequency curve in Fig. 5.7 a worst case error of 0.5% in the position of the resonances. We observed from the admittance amplitude vs. frequency curve a worst case 7% error in amplitude at the resonances, where the impedance is mainly determined by skin effects and proximity effects.

5.4 Conclusions on the proximity templates basis functions

In this Chapter we have described a procedure to construct a set of template basis functions for the discretization of conductor volumes in an integral equation method. The template basis functions are pre-computed off-line using small simulation experiments. The templates can capture successfully both skin

effect and proximity effects. Our examples show that compared to the thin filament methods they provide the same 7 to 20 improvement factors in terms of number of unknowns reported by the conduction modes approach presented in the previous Chapter 4. In addition the proximity templates can be employed in applications with wire cross-sections of arbitrary shape, and with proximity effects on wide wires due to above and close thin wires.

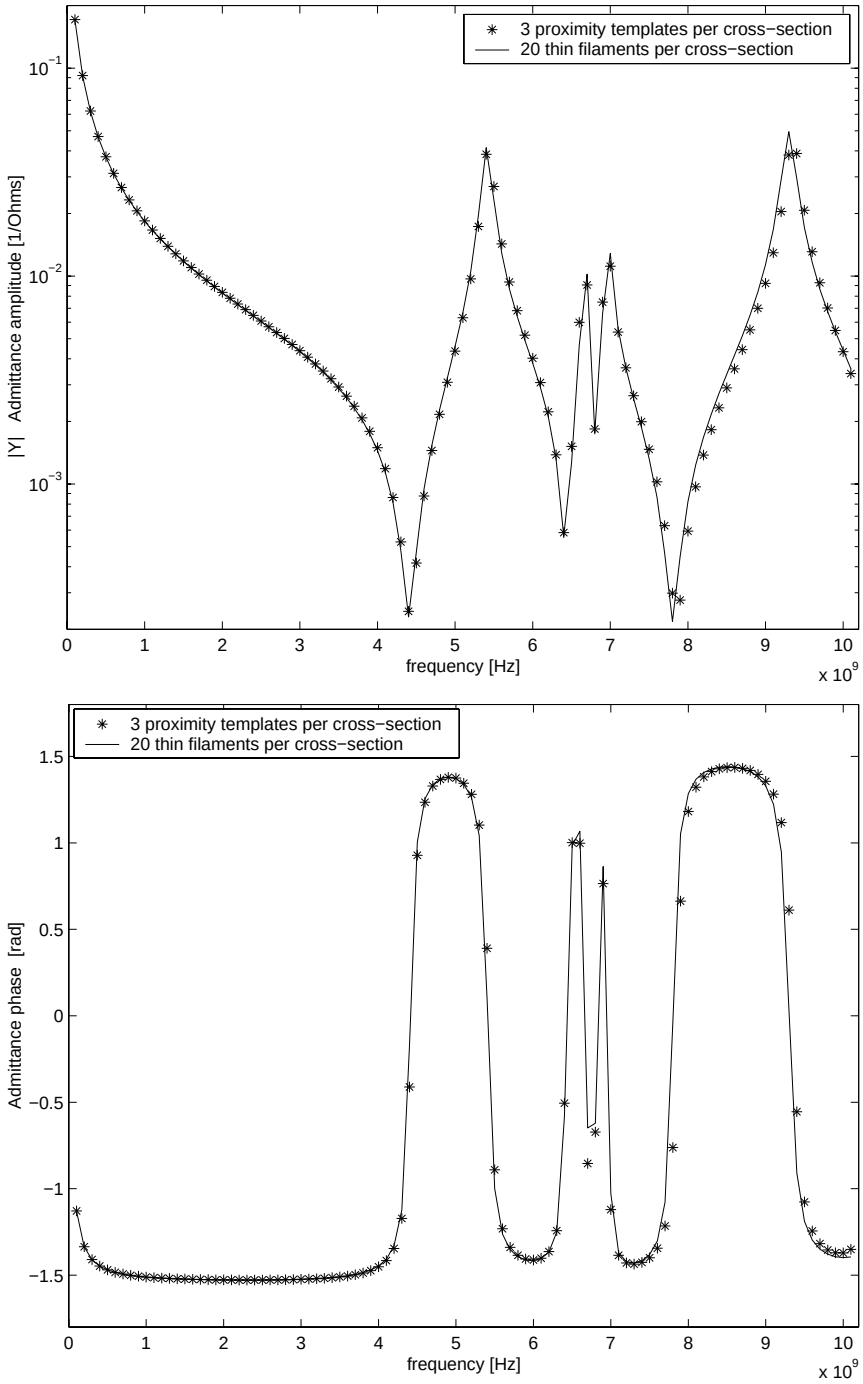

Figure 5.7: *On top we show the admittance amplitude, on the bottom the admittance phase vs. frequency observed at that same grid node in x = 4mm and y = 0mm of Fig. 5.6. In this example we used three proximity template basis functions for each wire cross-section.*

Chapter 6

Future work in analysis

6.1 Adjoint method for fast transfer functions calculation

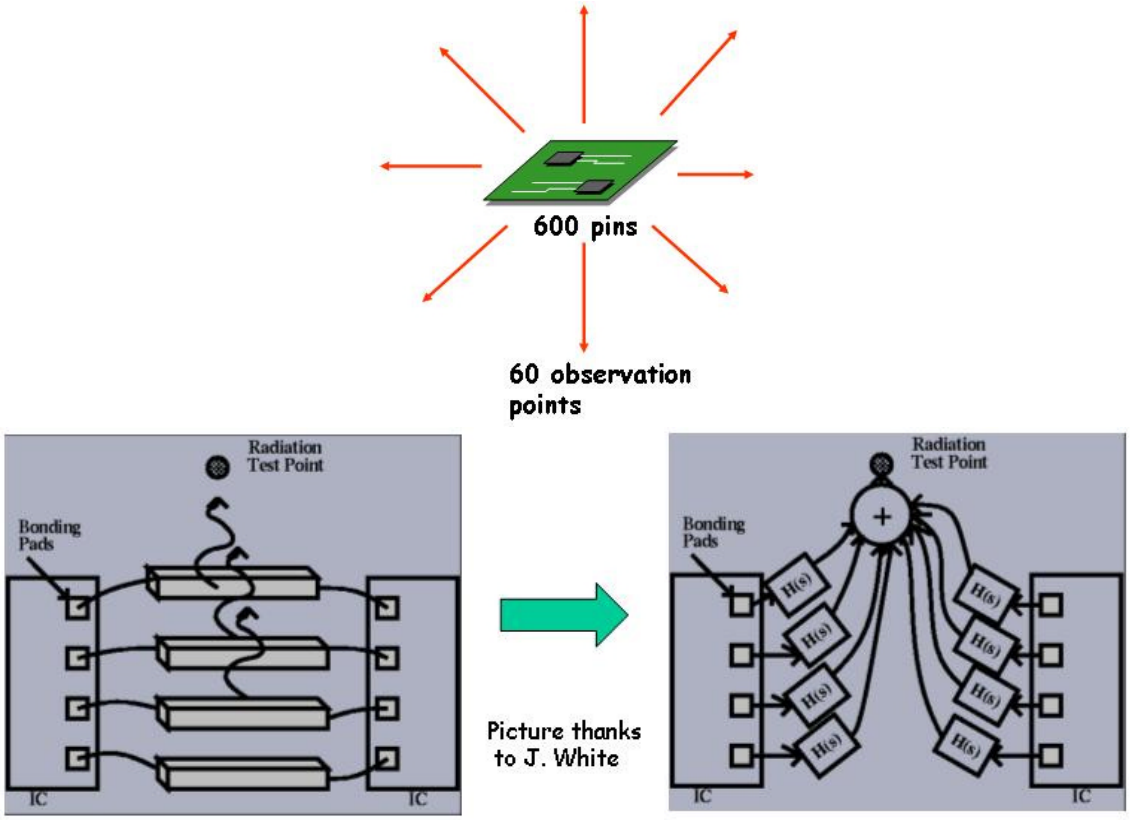

Figure 6.1: *Typical radiation problem: obtaining all the transfer functions from the sources (e.g. 600 IC pins on a PCB) to some observation points (e.g. 60 points) on a sphere the board at a 3 meters or 10 meters as specified by EMI standards.*

In order to quickly isolate the sources of EMI related problems a transfer function analysis capability could be used. For example, during a PCB analysis, one would specify as possible sources of EMI all the

pins of the chips mounted on the board. One would like also to measure the emitted fields all around the board at a 3 meters or 10 meters standard distance for semi-anechoic measurements. We have calculated that 60 observation points all around the board can give a good characterization of the radiation pattern for the frequencies of interest to EMI.

By transfer function analysis we mean providing the transfer functions from all the source pins (e.g. 600 pins) to all the observation points (e.g. 60) as illustrated in Fig. 6.1. Pins mostly responsible for emissions can in this way be easily isolated and design for EMC can be driven to the wires connecting those pins.

In the classical and natural transfer function calculation method, one would apply test sources one at the time to each of the pins and would then simulate the board to measure the emitted fields at all the observation points. This requires one system solve for each pin.

We observed, anyway, there can be thousands or more pins even on a simple PCB with a few IC's. This would lead to thousands of systems solve using the classical direct method. A better way is using an *adjoint method*. The main idea is that instead of obtaining from each system solve the transfer functions from one pin to all the observation points, we set up the system such that for each system solve we obtain the contributions from all pins to one single observation point. In this way we only perform as many system solves as observation points, i.e. only 60.

In mathematical terms, let E_R be the vector of fields measures at the 60 observation points. Let I_p be the vector of currents at the pins (or input terminals). Our objective is to calculate the transfer functions from all pins to all the observation points, that is, we want to calculate all the elements of the matrix Y.

$$E_R = Y I_p \tag{6.1}$$

Of course Y is frequency dependent so we need to calculate Y at all frequencies of interest (typically the clock frequency and its first few harmonics for digital circuits).

The direct method would calculate one column at the time of the thousands of columns of Y. We calculate instead one row at the time of the 60 rows of Y. Let Y_j^T be the j^{th} column of Y corresponding to the j^{th} observation point where we measure the field E_{R_j}

$$E_{R_j} = Y_j^T I_p \tag{6.2}$$

In order to calculate Y_j^T let us first show how to calculate the field E_{R_j}.

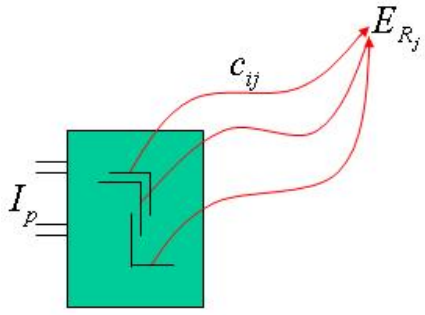

Figure 6.2: *Assuming the exact current distributions I_b in all filaments are known, in one system solve we can calculate and add up their contributions to field E_{R_j} in location R_j.*

Assuming the exact current distributions I_b in all filaments are known, one can simply add up their contributions in terms of field E_{R_j} (Fig. 6.2)

$$E_{R_j} = c^T I_b \tag{6.3}$$

where c^T are coefficients for the field produced by a short filament antenna. Basically they are simple trans-

lations and rotations of the formula for a short antenna along the $\hat{a}_z$ axis from [118]

$$c_i = \frac{l_i}{4j\pi\omega\varepsilon}\frac{e^{-jkr_i}}{r_i}\left[\left(-k^2+\frac{jk}{r_i}+\frac{1}{r_i^2}\right)\sin\theta\,\hat{a}_\theta+\left(\frac{2jk}{r_i}+\frac{2}{r_i^2}\right)\cos\theta\,\hat{a}_r\right] \tag{6.4}$$

where l_i is the length of filament i, r_i is the distance from the filament to the observation point, $k=2\pi/\lambda$ is the wave number.
Using some of the notation of the previous Chapter 3 on the equivalent circuit network set up we have

$$\begin{aligned} E_{R_j} &= c^T I_b && (6.5)\\ &= c^T M^T I_m && (6.6)\\ &= c^T M^T (MZ_{EM}M^T)^{-1} V_{ms} && (6.7)\\ &= c^T M^T (MZ_{EM}M^T)^{-1} Z_{th} I_p && (6.8)\\ & && (6.9)\end{aligned}$$

where Z_{th} is a Thevenin impedance matrix converting the terminal current sources I_p into mesh voltage sources V_{ms}. The column of transfer functions we are interested in is therefore

$$Y_j^T = c^T M^T (MZ_{EM}M^T)^{-1} Z_{th} \tag{6.10}$$

or

$$Y_j = Z_{th}^T \left[(MZ_{EM}M^T)^T\right]^{-1} Mc \tag{6.11}$$

as we can see most of the computation is still used when solving for matrix $(MZ_{EM}M^T)^T$ which is simply the transpose of the matrix we would solve in the direct method.

A physical intuitive interpretation is possible for this method. Basically instead of setting up a test current source for each pin and measuring the fields everywhere, we set up an imaginary current source in each observation point and then we measure the voltage induced on all the pins by such imaginary source as shown in Fig. 6.3. This suggests also a powerful method for calculating circuit susceptibility to external EMI as we show in the next section.

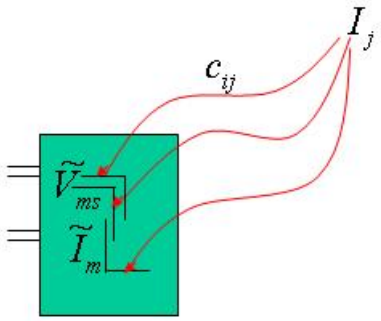

Figure 6.3: *A physical intuitive interpretation of the adjoint method: instead of setting up a test current source for each pin and measuring the fields everywhere, we set up an imaginary current source in each observation point and then we measure the voltage induced on all the pins by such imaginary source.*

6.2 Susceptibility analysis using reciprocity

The previous adjoint method suggests that emission and susceptibility analysis are intimately correlated. The main reason for this correlation is the Reciprocity Theorem. We show here how to apply such reciprocity theorem to obtaining susceptibility analysis results from emission analysis results.

Theorem 1 (The reciprocity theorem.) *Consider a current distribution in some region of the space* $\mathbf{J_a}$. *Let* $\mathbf{E_a}$ *be the field radiated by such source. Now remove the first current distribution and let us consider another current distribution* $\mathbf{J_b}$. *Let* $\mathbf{E_b}$ *be the field radiated by this second source. The reciprocity theorem states that*

$$\int_V \mathbf{J_a} \cdot \mathbf{E_b}\, dV = \int_V \mathbf{J_b} \cdot \mathbf{E_a}\, dV. \tag{6.12}$$

Now apply such theorem. For our purposes, we choose the first current distribution as a collection of current sources applied at the terminals ports of our board (i.e. the pins)

$$J_a(\mathbf{r}) = \sum_i \frac{I_{p_i}(\mathbf{r} - \mathbf{r_{p_i}})}{A_{p_i}} \tag{6.13}$$

where the summation is over all terminal ports, $\mathbf{r_{p_i}}$ is the position of the port i and A_{p_i} is its cross sectional area.
As our second distribution of currents let us choose a collection of small imaginary current sources placed at the observation points all around the board mentioned in the previous section.

$$J_b(\mathbf{r}) = \sum_j \frac{I_{s_j}(\mathbf{r} - \mathbf{r_{s_j}})}{A_{s_j}} \tag{6.14}$$

Applying Theorem 1:

$$\int_V \mathbf{J_a} \cdot \mathbf{E_b}\, dV = \int_V \mathbf{J_b} \cdot \mathbf{E_a}\, dV \tag{6.15}$$

$$\int_V (\mathbf{J_a} dS) \cdot (\mathbf{E_b} dl) = \int_V \mathbf{E_a} \cdot (\mathbf{J_b} dS) dl \tag{6.16}$$

$$\sum_i I_{p_i} V_{s_i} = \sum_j E_{R_j}[I_{s_j} dl] \tag{6.17}$$

$$I_p^T V_s = E_R^T [I_s dl] \tag{6.18}$$

where I_p is the vector of the port current sources, E_R is the vector of the fields produced by such sources in the observation points. I_s is the vector of imaginary current sources of small length dl that we have placed in a second experiment in the observation points. Finally, but most importantly V_s is a vector of voltages induced by the imaginary sources on the port terminals. V_s is exactly the answer of a susceptibility problem because it tells us what noise is induced on the port terminals due to some external field coming from the environment around (in this specific case some points on a sphere at 3 meters or 10 meters).

We now show how we can calculate susceptibility transfer functions from the observation points to the port terminals using a previous emission transfer function analysis. If we have already performed an emission transfer function analysis, we have basically calculated all the coefficients in the matrix Y

$$E_R = Y I_p \tag{6.19}$$

Substituting into (6.18) we get

$$I_p^T V_s = I_p^T Y^T [I_s dl] \tag{6.20}$$

$$V_s = Y^T [I_s dl] \tag{6.21}$$

Hence the same transfer functions we calculated for emissions are the transfer functions for susceptibility, and eq. (6.21) shows us how to use them to calculate induced noise voltages V_s on the circuit ports due to sources of interference from the environment I_s.

Part II

MODELING

Electromagnetic analysis of a collection of interconnect is an essential tool for the verification of modern electronic circuits. Such analyzes are of limited value unless the results can be combined with the circuit's transistors to simulate circuit performance. Typically, a designer would identify a few terminals for which a model of the interconnect "seen" at the selected terminals is to be constructed. Such a model should reproduce frequency and time domain behavior at the terminal of the original interconnect with an accuracy comparable to electromagnetic analysis. Then, this model would be combined with the transistors connected to the interconnect and simulated using a circuit simulator. Quick evaluation of the model is essential for an acceptable time domain simulation speed in the circuit simulator, but at the same time, parasitic extractor accuracy is essential for providing confidence to the circuit designer that the actual fabricated electronic circuit will perform as predicted by the circuit simulation.

In this chapter we will first describe a method for constructing electromagnetic models of interconnect using the discretization techniques of the Mixed Potential Integral Equation presented in the previous Chapters 3-5. Such models are based on a dynamical state space system representation. Unfortunately, the order of the resulting dynamical state space system is as large as the number of elements in the discretization. We will then describe techniques that can reduce the order of the dynamical linear system while preserving time and frequency domain behavior as well as other properties. In particular, we will illustrate the importance of producing *passive* reduced order models from originally *passive* interconnect structures. Finally, we will describe the main contributions of this thesis in the field of model order reduction. Specifically, we will describe our contributions consisting in model order reduction techniques that preserve passivity:

- when handling structures that include dielectrics using polarization currents and, in the context of Krylov subspace projection methods (Chapter 11);
- when handling structures that include dielectrics or integrated circuit substrates using special frequency dependent green functions, or when handling fullwave propagation kernels, in the contest of Krylov subspace projection methods (Chapter 12);
- when using the truncated balance realizations method (Chapter 13).

Chapter 7

Background: reduced order modeling of interconnect

7.1 Modeling of interconnect

Large electronic systems can be thought as a collection of analog, digital or mixed signal circuit blocks, connected by a collection of wires (interconnect). Such a simple representation can be observed in almost all electronic systems: Integrated Circuits (IC), package multi-chip modules (MCM), and printed circuit boards (PCBs). In this thesis we are interested in analyzing and modeling the interconnect. Typically, we are given a large collection of interconnect where some ports have been identified for the connection of some circuit blocks. It is our task to produce a model of the interconnect as "seen" from the ports identified for the connection to the circuit blocks (Fig. 7.1). The model should capture all the time and frequency behavior and properties of the interconnect that are relevant for the interaction with the circuit block.

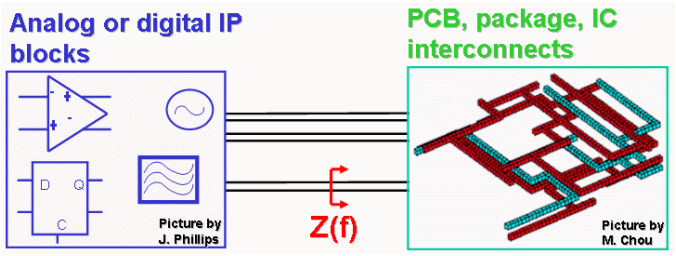

Figure 7.1: *Given a large collection of wires where some ports have been identified for the connection to circuit blocks, we are interested in producing a small but accurate model of the interconnect as "seen " from the ports.*

For simplicity, consider a single interconnect wire. The electromagnetic phenomena that describe the behavior of such a wire can be described as shown in Chapters 3-5 in Part I using the Mixed Potential Integral Equation formulation. The main unknowns in such formulation are the current density inside the conductors, and the charge density on the surface of the conductors. Typically, as seen in Section 3.3.1, one represents such unknowns using a collection of basis functions. For instance, one can represent the current inside the conductor using a collection of short thin filaments each carrying a constant current, and one can represent the charge on the surface of the conductors using a collection of small panels each carrying a constant charge as shown in Fig. 3.6. As described in our contributions in the previous Chapters 4 and 5 one can choose other basis functions for current (see for instance Fig. 4.6) and even for charges. However, regardless of the choice adopted, it is typically possible to use the coefficients (or unknowns) associated to each of such basis

functions as the coefficients of the *state vector x* describing the state of the wire in a dynamical linear system representation. A dynamical linear system is therefore one of the most natural choices that comes to mind when trying to produce an electromagnetic model of a wire. The state of the system is associated with the energy storing elements of the system. Since charge accumulation on the surface of the conductors can be thought as a capacitor, and since the electric energy storage on such capacitors is a function of the surface charge itself (or potential), one can see how the small panel charges (or potentials) are a good candidate for the state vector. Furthermore, since the current in the conductors is typically associated with magnetic energy storage, which is a function of the current itself, one can also realize how the state vector should also contain coefficients associated with discretization basis functions for the current. The Figure 7.2 gives a graphical representation of the relation between state vector and the equivalent circuit produced by the discretization of a wire shown in Fig. 3.6.

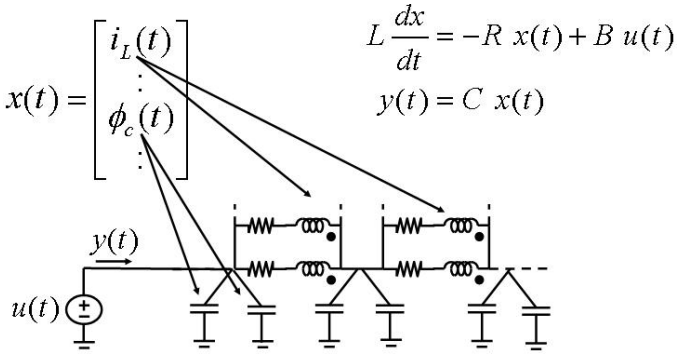

Figure 7.2: *A dynamical linear system can be used for electromagnetic modeling of an interconnect wire. The discretization of the Mixed Potential Integral Equation produces an equivalent circuit. The currents on the inductors and the potentials on the capacitors can be used as state vector coefficients for the dynamical linear system. If the input is chosen as a voltage source, and the output as the resulting current into the wire, the model represents the input admittance of the wire.*

As input $u(t)$ for the dynamical linear system one can choose for instance the voltage applied at one terminal of the wire. As output $y(t)$ one can choose the resulting current. In this way the dynamical linear system will represent the admittance of the wire seen at such terminal. Models with multiple input and multiple outputs can be used to model multiple terminals. The equations in the dynamical linear system are exactly the same equations (KCL/KVL sparse tableau analysis, or KCL nodal analysis, or KVL mesh analysis, or mixed nodal-mesh analysis) that one would write when setting up a linear system for solving the system as described in Section 3.4. Collecting terms that depend on the time derivative of the state, and terms that depend linearly on the state one can recognize matrices L and R respectively in Fig. 7.2. Matrices B and C relate input to the state equations and the state to the output respectively.

Although, as we will see later, it will be important to be able to work with matrices L and R separately and with multiple input and multiple outputs, in this first introductory stage assume for simplicity of exposition that we have only one input and one output, that matrix R is non-singular, and that the system in Fig. 7.2 is described in time domain as

$$E\frac{dx}{dt} = x(t) + bu(t) \quad y(t) = c^T x(t), \tag{7.1}$$

and in frequency domain,

$$sEx = x + bu \quad y = c^T x \tag{7.2}$$

where $E = R^{-1}L$ and $b = R^{-1}B$, and s is the Laplace frequency variable.

7.2 Model order reduction

The order of the dynamical linear systems produced by the discretized MPIE formulation is as large as the number of discretization elements ($n = 100,000$ to 500,000 for large interconnect systems). The cost of "evaluation" of a dynamical linear system model for a particular point in time or frequency is typically of the same complexity as solving a linear system with size as large as the order of the dynamical linear system. Therefore the model as shown in Fig. 7.2 is in most cases of little practical use.

During the past decade much research effort has been devoted to "reducing" the order n of a given very large dynamical linear system to a much smaller size q (typically $q < 100$) as illustrated in Fig. 7.3, while preserving the most relevant part of the time and frequency input/output behavior and properties of the original system.

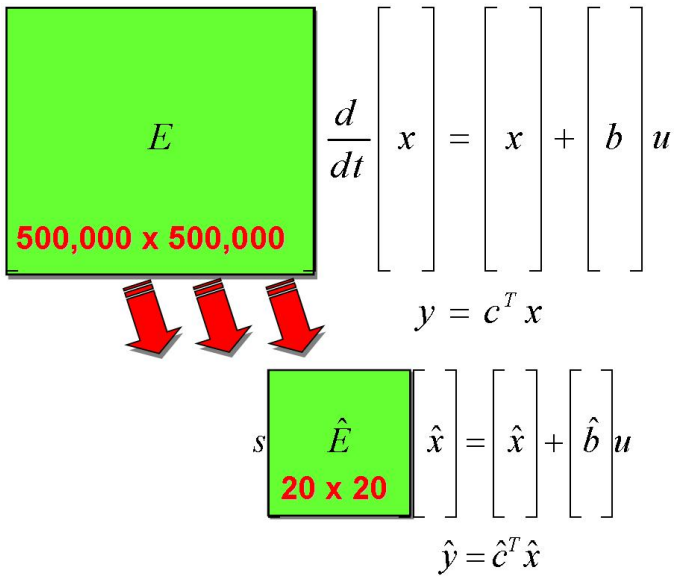

Figure 7.3: *Given a dynamical linear system with a large matrix descriptor E of size around $n = 500,000$, the objective of the "model order reduction" algorithms is to produce a dynamical linear system with a much smaller matrix $\hat{E}$ of size typically around $q = 20$, but with the same time and frequency domain behavior and properties.*

In an integrated circuits context, initial interest in model reduction techniques stemmed from efforts to accelerate analysis of circuit interconnect [111]. More recently, model reduction has come to be viewed as a method for generating compact models from all sorts of physical system modeling tools [69, 104, 120, 106, 105, 18, 19, 131, 119, 32].

In the remainder of this Chapter and in Chapters 8-9, we will review the main existing techniques for model order reduction. In Chapters 11-13 we then develop our new algorithms.

7.3 Model order reduction via eigenmode analysis

When the matrix E can be diagonalized, the transfer function of the dynamical linear system can be written in a pole-residue form. Specifically, if

$$E = S\Lambda S^{-1} \tag{7.3}$$

where Λ is a diagonal matrix containing the eigenvalues of E, then one can write the transfer function as

$$\begin{aligned} H(s) &= -c^T(I-sE)^{-1}b = && (7.4)\\ &= -c^T(SS^{-1}-sS\Lambda S^{-1})^{-1}b = && (7.5)\\ &= -c^TS(I-s\Lambda)^{-1}S^{-1}b = && (7.6)\\ &= -\tilde{c}^T(I-s\Lambda)^{-1}\tilde{b} = && (7.7)\\ &= -\sum_{i=1}^{n}\frac{\frac{1}{\lambda_i}\tilde{c}_i\tilde{b}_i}{s-\frac{1}{\lambda_i}} && (7.8)\\ &= \sum_{i=1}^{n}\frac{r_i}{s-p_i} && (7.9) \end{aligned}$$

where the residues are $r_i = \frac{1}{\lambda_i}\tilde{c}_i\tilde{b}_i$ and the poles are $p_i = \frac{1}{\lambda_i}$. The correspondent impulse response therefore decomposed into its "modes"

$$h(t) = \sum_{i=1}^{n} r_i e^{p_i t} \tag{7.10}$$

A first intuitive way to perform model order reduction consists in observing that one can:

- remove pole/zero near-cancellations (volume discretizations are well known for introducing many of such pole/zero near-cancellations that do not have any affect on the transfer function);
- drop all other modes with small residues;
- drop also modes decaying too "fast" for the signals of interest to the user (i.e. poles with large real parts);
- cluster poles that are very close.

Retaining in this way the dominant modes of the system is a familiar procedure to many circuit designers. However this procedure is not practical to solve our problem. First of all it is extremely expensive, since finding the poles has a non-practical computational complexity $O(n^3)$. Secondly, it is relatively inefficient, since for a given model size, many other approaches can provide better accuracy.

7.4 Model order reduction via truncated balanced realizations (TBR)

One of the approaches that can provide optimal accuracy for a given final order of the reduced model is the Truncated Balance Realization (TBR) algorithm. In this Section, primarily to conform to literature standards, we will assume the system to be reduced has been put in the form

$$sx = Ax + Bu \qquad y = Cx \tag{7.11}$$

The TBR procedure as first presented in [93] is centered around information obtained from the controllability Grammian W_c, which can be obtained from solving the Lyapunov equation

$$AW_c + W_cA^T = -BB^T \tag{7.12}$$

for W_c, and the observability Grammian W_o, which can be obtained from the dual Lyapunov equation

$$A^TW_o + W_oA = -C^TC \tag{7.13}$$

for W_o.

Under any similarity transformation of the state-space model,

$$A \to T^{-1}AT, \quad B \to T^{-1}B, \quad C \to CT \tag{7.14}$$

***Algorithm* 1 Truncated Balanced Realization (TBR)**

1. *Solve* $AW_c + W_cA^T = -BB^T$ *for* W_c
2. *Solve* $A^TW_o + W_oA = -C^TC$ *for* W_o
3. *Compute Cholesky factors* $W_c = L_cL_c^T$, $W_o = L_oL_o^T$,
4. *Compute SVD of Cholesky product* $U\Sigma V = L_o^TL_c$ *where* Σ *is diagonal positive and* U, V *have orthonormal columns*
5. *Compute the balancing transformations* $T = L_cV\Sigma^{-1/2}, \quad T^{-1} = \Sigma^{-1/2}U^TL_o^T$
6. *Form the balanced realization as* $\hat{A} = T^{-1}AT, \quad \hat{B} = T^{-1}B, \quad \hat{C} = CT$
7. *Select reduced model order and partition* $\hat{A}, \hat{B}, \hat{C}$ *conformally*
8. *Truncate* $\hat{A}, \hat{B}, \hat{C}$ *to form the reduced realization* $\tilde{A}, \tilde{B}, \tilde{C}$

the state-space model, and the transfer function, are invariant (only the internal variables are changed). The Grammians, however, vary under the rules

$$W_c \to T^{-1}W_cT^{-T}, \quad W_o \to T^TW_oT \tag{7.15}$$

and so are not invariant. The TBR procedure is based on two observations about W_o and W_c. First, the eigenvalues of the product W_cW_o are invariant. These eigenvalues, the Hankel singular values, contain useful information about the input-output behavior of the system. In particular, "small" eigenvalues of W_cW_o correspond to internal sub-systems that have a weak effect on the input-output behavior of the system and are therefore close to non-observable or non-controllable or both.

Second, since a similarity transformation on A induces a congruence transformation of the Grammians, and since any pair of symmetric matrices can be simultaneously diagonalized by an appropriate congruence transformation [57], it is possible to find a similarity transformation T that leaves the state-space system dynamics unchanged, but makes the (transformed) $\hat{W}_o$ and $\hat{W}_c$ equal and diagonal[1]. In these coordinates, with $\hat{W}_c = \hat{W}_o = \Sigma$, we may partition Σ into

$$\Sigma = \begin{bmatrix} \Sigma_1 & 0 \\ 0 & \Sigma_2 \end{bmatrix} \tag{7.16}$$

where Σ_1 describes the "strong" sub-systems to be retained and Σ_2 the "weak" sub-systems to be deleted. Conformally partitioning the transformed matrices as

$$\hat{A} = \begin{bmatrix} \hat{A}_{11} & \hat{A}_{12} \\ \hat{A}_{21} & \hat{A}_{22} \end{bmatrix}, \quad \hat{B} = \begin{bmatrix} \hat{B}_1 \\ \hat{B}_2 \end{bmatrix}, \quad \hat{C} = \begin{bmatrix} \hat{C}_1 & \hat{C}_2 \end{bmatrix}, \tag{7.17}$$

and truncating the model, retaining $\tilde{A} = \hat{A}_{11}, \tilde{B} = \hat{B}_1, \tilde{C} = \hat{C}_1$ as the reduced system, therefore has the effect of deleting the "weak" internal subsystems. A complete TBR algorithm [78] is shown in Algorithm 1. An approach with improved numerical properties may be found in [123].

[1] To see this it may help to note that W_c^{-1} and W_o transform according to the same congruence operation; but if W_c^{-1} is diagonalized, so is W_c.

One of the attractive aspects of TBR methods is that computable error bounds are available. If the ith diagonal entry of the matrix Σ in Algorithm 1 is given by σ_i, and the σ_i ordered $\sigma_1 \geq \sigma_2 \geq \cdots \sigma_N$, then the error in the transfer function of the order-q reduced model is bounded by [51]

$$||H(s) - \hat{H}_q(s)||_\infty \leq 2 \sum_{k=q+1}^{N} \sigma_k. \tag{7.18}$$

A similar algorithm (Hankel model order reduction [51] can provide an error bound twice as lower than TBR.

Although TBR and Hankel reduction algorithms provide one of the best compressions in terms of accuracy for a given final order, their computational complexity, $O(n^3)$, makes them impractical as a "first stage" reduction operating on our huge interconnect systems. However, they are often used as a "second reduction step" as described in Section 10.1.

7.4.1 Physical interpretation of the TBR procedure

In order to later contrast the physical significance of the passivity-preserving TBR methods developed in Chapter 13, here we review the physical interpretation of the method in Algorithm 1.

The observability Grammian W_o is related to the L_2 norm of the output produced in free evolution ($u(t) = 0, \forall t \geq 0$) from an initial state x_0 at time 0,

$$x_0^T W_o x_0 = \int_0^\infty y(t)^T y(t) dt, \quad x(0) = x_0,\ u(t) = 0, \forall t \geq 0. \tag{7.19}$$

The controllability Grammian W_c is related to the minimum L_2 norm of the input over all possible input that can control the system from state 0 to the state x_0 at time 0.

$$x_0^T W_c^{-1} x_0 = \inf \left\{ \int_{-\infty}^0 u(t)^T u(t) dt, \quad u(t) \text{ controlling to } x(0) = x_0 \right\}. \tag{7.20}$$

Noting that $\int_0^\infty y(t)^T y(t) dt$ and $\int_{-\infty}^0 u(t)^T u(t) dt$ are the L_2 norms of the system output (restricted to $t \geq 0$) and the system input (on $t \leq 0$) respectively, it is seen that small eigenvalues of the observability Grammian W_o are associated with state eigenvectors ("normal modes" [93]) that produce small free evolution L_2 output norms. These modes are therefore relatively unimportant for the system response. Small eigenvalues of the controllability Grammian W_c are associated with state eigenvectors (modes) that can be controlled only employing inputs with large L_2 norm (regardless of what trajectory we follow to reach them). Hence the system is not very likely to be driven into those states and they are not likely to be important for the system response. It can be noticed that some modes, although could produce large outputs, are difficult to be controlled by the input. Vice-versa there can be some modes that, although are controlled with small input norm, they produce small output norms. This is the reason for the balancing procedure that transforms to coordinates that "balance" the importance of past inputs and future outputs, the weighting revealed by the eigenvalues of the product of the observability and controllability Grammian. The algorithm will keep in the final reduced model all the modes that are

- either easily controllable, meaning they do not require a large input L_2 norm to reach, and
- easily easily observable, meaning that they produce free evolution outputs with large L_2 norms.

7.5 Model order reduction via rational function fitting (point matching)

The transfer function $H(s)$ of a dynamical system of form (7.2) and of order n is a rational function with $2n$ coefficients

$$H(s) = \frac{b_0 + b_1 s + \ldots + b_{n-1} s^{n-1}}{1 + a_1 s + \ldots + a_n s^n} \tag{7.21}$$

The transfer function $\hat{H}(s)$ of the system after the reduction to order $q << n$ must also be a rational function. In this case the free coefficients are $2q$.

$$\hat{H}(s) = \frac{\hat{b}_0 + \hat{b}_1 s + ... + \hat{b}_{q-1} s^{q-1}}{1 + \hat{a}_1 s + ... + \hat{a}_q s^q} \tag{7.22}$$

Hence, an idea to perform model order reduction is to choose those $2q$ coefficients in order to match "as much as possible" of the original transfer function. Perhaps the most intuitive way to achieve this is to match the original transfer function in exactly $2q$ points as shown in Fig. 7.4

$$H(s_i) = \frac{\hat{b}_0 + \hat{b}_1 s_i + ... + \hat{b}_{q-1} s_i^{q-1}}{1 + \hat{a}_1 s_i + ... + \hat{a}_q s_i^q}, \quad i = 1, ..., 2q. \tag{7.23}$$

Cross-multiplying the denominators of these $2q$ equations generates a linear system of equations

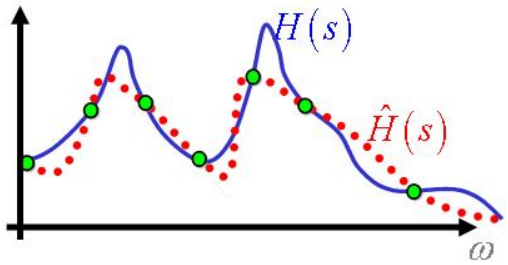

Figure 7.4: *One idea for model order reduction is to "fit" a rational function $\hat{H}(s)$ with very few coefficients ($2q << 2n$) by matching in exactly $2q$ points the original function $H(s)$ described by $2n$ coefficients.*

$$\begin{bmatrix} -s_1 H(s_1) & \dots & -s_1^q H(s_1) & 1 & s_1 & \dots & s_1^{q-1} \\ -s_2 H(s_2) & \dots & -s_2^q H(s_2) & 1 & s_2 & \dots & s_2^{q-1} \\ \dots & \dots & \dots & \dots & \dots & \dots & \dots \\ -s_{2q} H(s_{2q}) & \dots & -s_{2q}^q H(s_{2q}) & 1 & s_{2q} & \dots & s_{2q}^{q-1} \end{bmatrix} \begin{bmatrix} \hat{a}_1 \\ \dots \\ \hat{a}_q \\ \hat{b}_0 \\ \hat{b}_1 \\ \dots \\ \hat{b}_{q-1} \end{bmatrix} = \begin{bmatrix} H(s_1) \\ H(s_1) \\ \dots \\ H(s_{2q}) \end{bmatrix} \tag{7.24}$$

that can be solved for the coefficients $\hat{a}_1, ...\hat{a}_n, \hat{b}_0, ..., \hat{b}_{n-1}$.

Unfortunately this approach tends to generate a very ill-conditioned system due to the progressively higher powers k of the test frequencies s_i^k. Furthermore, the resulting transfer function is extremely sensitive to the position of the points chosen for the matching, and large errors are typically observed in the regions between matching points. This is of particular concern when the range of the frequency response that is required to be matched by the given application contains sharp resonance peaks. A better approach to overcome the second of these two issues is to use a moment matching approach instead of a point matching one.

7.6 Model order reduction via Pade' approximations (moment matching)

As an alternative to choosing the $2q$ coefficients so that the reduced order transfer function matches the original transfer function in $2q$ points, one can instead choose to match one point and the first $2q-1$ derivatives at that point. Fig 7.5 is an attempt to represent this concept pictorially, where we are representing derivatives with concentric circles around the matching point.

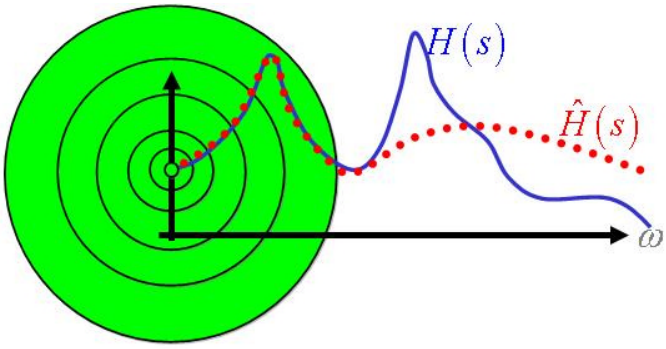

Figure 7.5: *Pictorial representation of the moment matching approach. The* $2q$ *coefficients of the reduced transfer function* $\hat{H}(s)$ *are chosen in order to match one point of the original transfer function* $H(s)$ *and* $2q-1$ *derivatives at that same point. Matching of derivatives is represented here pictorially by concentric circles around the matching point.*

This approach corresponds to expanding the transfer function in Taylor series,

$$H(s) = H(s)|_{s=0} + \left.\frac{dH}{ds}\right|_{s=0} s + \frac{1}{2!}\left.\frac{d^2H}{ds^2}\right|_{s=0} s^2 + \frac{1}{3!}\left.\frac{d^3H}{ds^3}\right|_{s=0} s^3 + \ldots \tag{7.25}$$

$$= m_0 + m_1 s + m_2 s^2 + m_3 s^3 + \ldots \tag{7.26}$$

and matching its first $2q$ coefficients m_k by imposing

$$\frac{\hat{b}_0 + \hat{b}_1 s + \ldots + \hat{b}_{q-1} s^{q-1}}{1 + \hat{a}_1 s + \ldots + \hat{a}_q s^q} = m_0 + m_1 s + m_2 s^2 + m_3 s^3 + \ldots m_{2q-1} s^{2q-1} \tag{7.27}$$

It can be further observed that the coefficients m_k of the Taylor series expansion of the transfer function are intimately related to the time domain moments $\tilde{m}_k$ of the impulse response,

$$\tilde{m}_k = \int_0^\infty t^k h(t) dt. \tag{7.28}$$

Specifically it can be easily be shown that

$$m_k = \frac{(-1)^k}{k!} \tilde{m}_k. \tag{7.29}$$

Hence, producing a reduced system which matches the first $2q$ Taylor series coefficients m_k of the original system, corresponds to matching its first $2q$ time domain moments $\tilde{m}_k$.

In order to produce the reduced system one can:

1. calculate the coefficients m_k of the Taylor series expansion up to order $2q-1$ observing that

$$H(s) = -c^T (I - sE)^{-1} b = \sum_{k=0}^{\infty} \left(-c^T E^k b\right) s^k = \sum_{k=0}^{\infty} m_k s^k \tag{7.30}$$

and hence concluding that

$$m_k = -c^T E^k b, \quad k = 0, 1, \ldots, 2q-1. \tag{7.31}$$

When applied to circuits, the method in this section is referred to as AWE since the moments can be calculated using Asymptotic Waveform Evaluations (AWE) [112];

2. cross-multiply the denominators in equation (7.27) and matching like powers of s, in order to assemble the following two linear systems

$$\begin{bmatrix} m_0 & m_1 & \dots & m_{q-1} \\ m_1 & \dots & & \vdots \\ \vdots & & & \\ m_{q-1} & \dots & & m_{2q-2} \end{bmatrix} \begin{bmatrix} \hat{a}_q \\ \hat{a}_{q-1} \\ \vdots \\ \hat{a}_1 \end{bmatrix} = - \begin{bmatrix} m_q \\ m_{q+1} \\ \vdots \\ m_{2q-1} \end{bmatrix} \tag{7.32}$$

$$\begin{bmatrix} m_0 & 0 & \dots & 0 \\ m_1 & m_0 & 0 & \vdots \\ \vdots & & & 0 \\ m_{q-1} & \dots & & m_0 \end{bmatrix} \begin{bmatrix} 1 \\ \hat{a}_1 \\ \vdots \\ \hat{a}_{q-1} \end{bmatrix} = \begin{bmatrix} \hat{b}_0 \\ \hat{b}_1 \\ \vdots \\ \hat{b}_{q-1} \end{bmatrix} \tag{7.33}$$

3. the first of the two systems can be solved to calculate coefficients $\hat{a}_1, \dots, \hat{a}_q$, subsequently the second system can be used to calculate coefficients $\hat{b}_0, \dots, \hat{b}_{q-1}$.

Since the moment matching approach illustrated above is based on calculating the (truncated) Taylor series expansion of the original function, it could potentially capture accurately most sharp resonance peaks relatively close to the expansion point, without having to know their exact location before the reduction procedure. However, the linear system (7.32) still becomes quickly ill-conditioned for large values of q (typically for $q > 20$). As a matter of fact the moments m_k in (7.31), contain a power series which tend to align the matrix vector product toward the dominant eigenvector of the matrix E corresponding to the dominant eigenvalue λ as illustrated in Fig. 7.6

$$m_k = c^T (E^k b) \approx c^T (\lambda^k b) \approx \lambda^k m_0, \quad \text{for large } k. \tag{7.34}$$

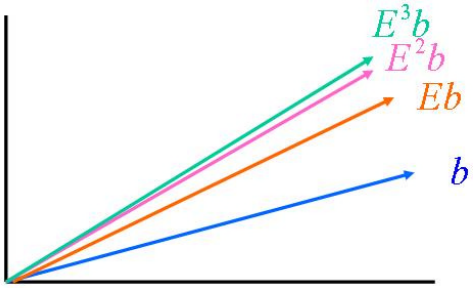

Figure 7.6: *Any vector b transformed by a large power of a matrix E_k tend to "align" toward the dominant eigenvector of the matrix.*

This implies that for large values of q the last columns (and the last rows) of the matrix in (7.32) tend to become linearly dependent and therefore the system almost singular.

$$\begin{bmatrix} m_0 & m_1 & \dots & m_{q-2} & m_{q-1} \\ m_1 & m_2 & \dots & m_{q-1} & m_q \\ \dots & \dots & \dots & \dots & \dots \\ m_{q-2} & m_{q-1} & \dots & m_{2q-4} & m_{2q-3} \\ m_{q-1} & m_q & \dots & m_{2q-3} & m_{2q-2} \end{bmatrix} \approx \begin{bmatrix} m_0 & m_1 & \dots & m_0\lambda^{q-2} & m_0\lambda^{q-1} \\ m_1 & m_2 & \dots & m_0\lambda^{q-1} & m_0\lambda^q \\ \dots & \dots & \dots & \dots & \dots \\ m_0\lambda^{q-2} & m_0\lambda^{q-1} & \dots & m_0\lambda^{2q-4} & m_0\lambda^{2q-3} \\ m_0\lambda^{q-1} & m_0\lambda^q & \dots & m_0\lambda^{2q-3} & m_0\lambda^{2q-2} \end{bmatrix} \tag{7.35}$$

Practically speaking, one would like to be able to increase the accuracy of the produce model by increasing its order q, however, since for larger values of q the system becomes ill-conditioned, coefficients $a_1, \dots, a_q$ cannot be calculated accurately and the actual accuracy of the reduced model does not improve. This result can be observed for instance in Fig. 7.7.

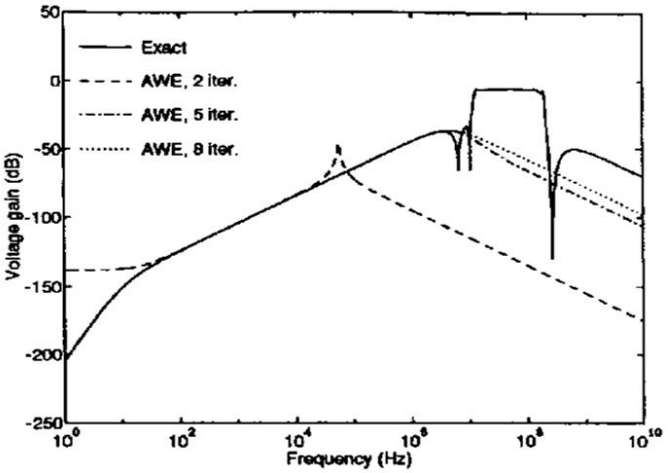

Figure 7.7: *Transfer functions calculated using AWE (Asymptotic Waveform Evaluation) or in other words using the Pade' approximations described in 7.6. At each iteration of the algorithm one can increase the order q of the produced system. Results for orders $q = 2, 5$ and 8 are compared to the original transfer function. One can observe that because of numerical ill-conditioning of the procedure the accuracy does not increase much when using larger values of q.[Picture by Feldmann and Freund [45]]*

Chapter 8

Background: the projection framework

In this section we will introduce a framework that can be used to develop many different model order reduction techniques. If we compare the two systems in Fig. 7.3 we observe that the state of the original system is a long vector of size n (with $n \approx 500,000$) "living" in an n-dimensional space. The state of the reduced system is a short vector of size q (with $q \approx 20$) living in a reduced subspace of size q. Assume that the large original state can be obtained from the reduced state using a linear transformation or "change of basis" as illustrated in Fig. 8.1. The transformation matrix U_q has size $n \times q$. Its columns are the vector basis for the "reduced subspace", or more specifically they contain the coefficients needed to represent the basis for the "reduced subspace" according to the basis for the original subspace.

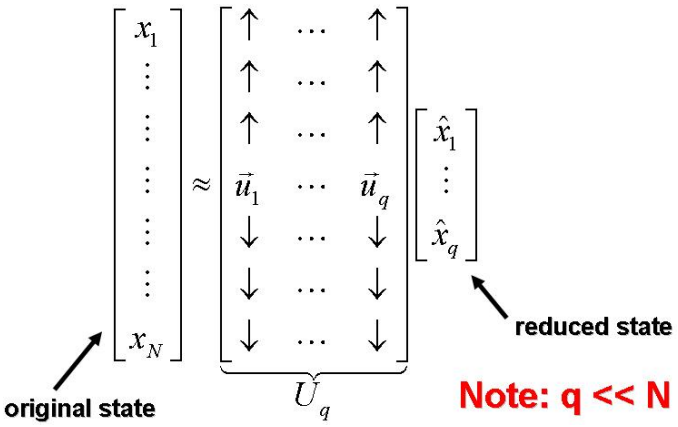

Figure 8.1: *Assume the original state can be obtained from the reduced one using a linear transformation. The change of basis matrix U_q is assembled using as columns the basis of the reduced subspace.*

Using the change of basis transformation $x = U_q \hat{x}$ in the original system

$$sEx = x + bu, \quad y = c^T x \tag{8.1}$$

one obtains a new dynamical linear system

$$sEU_q\hat{x} = U_q\hat{x} + bu, \quad \hat{y} = c^T U_q \hat{x} \tag{8.2}$$

In this new system of equations we still count n equations but we have only q variables with $q << n$. The system is therefore highly over-determined. One easy way to reduce the number of equations is to multiply the whole system by an "equation test matrix" V_q^T of size $q \times n$ obtaining the reduced system in Fig. 8.2. It is

convenient to use an equation test matrix bi-orthonormal to the change of basis matrix

$$V_q^T U_q = I \tag{8.3}$$

We illustrate pictorially in Fig.8.3 how the original matrix E is squashed by the equation test matrix and by the change of basis matrix.

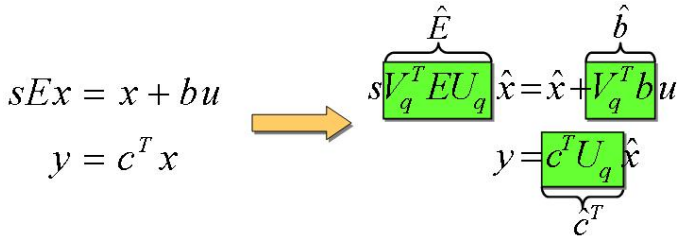

Figure 8.2: *According to the projection framework, the reduced system can be obtained from the original using a "change of basis matrix" U_q and by pre-multiplying by an "equation test matrix" V_q^T bi-orthonormal to U_q, i.e. $V_q^T U_q = I_q$.*

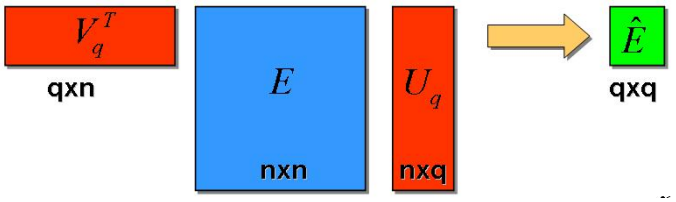

Figure 8.3: *Using the transformation in Fig.8.2 one can "squash" the dimensions of the original matrix E from $n \times n$ to the much smaller $q \times q$.*

8.1 Choosing the change of basis matrix U_q

So far we have assumed that the "*reduced subspace*" where the reduced state vector lives, is known and described in terms of a set of basis that can be used as columns of matrix U_q. However finding a good approximation for such subspace is actually the core of any of the model order reduction algorithms based on the projection framework.

Many choices are available to provide an approximation to such subspace. One way to think about our problem is to try to characterize somehow a subset of the original state space where the state vector "spends most of its evolution in a practical application of the model.

1. For instance, if available one could use as a basis for the reduced subspace a few "dominant" state eigenmodes, that is the eigenvectors of the system matrix corresponding to the eigenvalues selected as described before in 7.3. Reduced models of any order q could be constructed without extra effort. Unfortunately, as mentioned before, performing an eigenmode analysis of the original huge system requires an $O(n^3)$ diagonalization operation which is computationally not tractable.

2. An additional idea is to use dominant singular vectors of the System Grammians introduced in Section 7.4. The dominant singular vectors of the controllability and observability Grammians are associated to modes or state vectors of the system that are controllable by small inputs and produce large outputs respectively. The singular vectors corresponding to modes that are both easily controllable and

easily observable are more likely to contribute to the input/output response we want to capture, and we can use them a basis for the reduced subspace. Computationally this approach requires calculating the Grammians and then applying a Singular Value Decomposition for a total complexity $O(n^3)$ regardless of the order of the model produced. However in [81, 80, 79] more efficient methods are shown where the dominant eigenvectors of the controllability and observability Grammians are calculated by iteration.

3. Another simple way to characterize the subspace where the state vector is most likely to move around during its evolution for practical applications is to apply some practical inputs to the original system and calculate its evolution for some short time for all such inputs. This would produce a large collection of state vectors X = $\{x_{u_1}(t_1),...,x_{u_1}(t_k),...,x_{u_h}(t_1),...,x_{u_h}(t_k)\}$, which could represent a decent approximation to the subspace we are looking for. We could use such hk vectors as columns of U_q directly but that could be inefficient as many of the vectors will likely be linearly dependent. Using linearly dependent vectors would be possible but it would produce a low accuracy for a given order q of the reduced system. What determines the accuracy of the reduced model is the dimension of the space spanned by the columns of U_q, and not the number of vectors in the columns of U_q [53]. A more efficient basis of such subspace could then be obtained selecting the first $q << hk$ dominant singular vectors of the matrix constructed using the vectors in X as columns. One can notice that this algorithm is particularly expensive since it requires the simulation of the *original* system for different inputs and time points. Each of the hk vectors in X requires roughly the solution of a dense linear system of size $n \approx 500,000$. Each solve requires $O(n\ log(n))$, when using iterative methods with the fast matrix vector products described in 3.6. The total computational complexity for constructing a reduced model of order q would be $O(hk\ n\ log(n))$.

4. For most applications of interest in digital or mixed-signal integrated circuits the input signals are periodic and typically one is interest in the frequency response only up to a certain frequency. Therefore one could think of applying the same procedure illustrate above in the frequency domain. One could compute several state vectors at several frequency points X = $\{x_{u_1}(s_1),...,x_{u_1}(s_k),...,x_{u_h}(s_1),...,x_{u_h}(s_k)\}$, assemble then a matrix using such vectors as columns, calculate the first $q << hk$ dominant singular vectors of such matrix and use those as columns of the change of basis matrix U_q. The computational complexity of this frequency domain variant of the previous approach is the same $O(hk\ n\ log(n))$. However for those applications mentioned before one could expect slightly smaller values of k.

5. Finally, an effective approach from a computational point of view when reducing very large and dense systems is to construct the columns of U_q using vectors in the Krylov subspace generated by the input or output vectors b, c and the dynamic matrix E. Details of this method are described in the following section.

8.2 Moment matching reduction via Krylov subspace projection framework methods

We have already seen in 7.6 that one way to reduced the order of the system is through matching the first Taylor series coefficients (or moments) of its transfer functions. However, although computationally very efficient, the approach presented in 7.6 is still of little practical value because it suffers of noticeable numerical problems. Other approaches presented in 7.3,7.4, and in 8.1 use numerically very stable algorithms such as eigenvalue or singular value decomposition, however they are of little practical value because of their huge computational cost. We present here a family of algorithms based on the projection framework that exploit the computational efficiency of the moment matching approach and are at the same time numerically robust.

In order to approach the details of the algorithm first consider for simplicity a single input single output

dynamical linear system as in in (7.2), The transfer function from the input to the state is

$$x = -\left(I - sE\right)^{-1} bu. \tag{8.4}$$

Using a Taylor series expansion around the point $s = 0$ we can write the state x as a linear combination of a whole bunch of vectors $E^k b,\ \ k = 0, 1, \ldots$

$$x = -\sum_{k=0}^{\infty} s^k\, E^k b\, u. \tag{8.5}$$

In other words the state x lives in the space spanned by vectors

$$x \in \text{span}\{b, Eb, E^2 b, \ldots\}. \tag{8.6}$$

If we are interested in producing a reduced model where we only care about the first q coefficients of the Taylor series expansion of the transfer function around $s = 0$, then a natural choice for approximating the reduced state subspace is to use the one spanned by the first q vectors $E^k b,\ \ k = 0, 1, \ldots, q-1$. A more general version and proof of such conjecture will be proven later in this section by the Grimme's theorem [53]. We recall here that subspaces of this type are well known and studied in the linear algebra literature.

Definition 2 *The* **Krylov subspace** *of order q of a matrix E and a vector b is defined as the subspace spanned by the vectors*

$$K_q(E, b) = \text{span}\{b, Eb, E^2 b, \ldots, E^{q-1} b\}. \tag{8.7}$$

8.2.1 Grimme's theorem [53]

The most general version of a theorem proving the foundations of the Krylov subspace projection framework methods is given in [53]. We recall here the theorem and we highlight a few special cases.

Theorem 2 *Given a dynamical linear system as in (7.2),*
IF *the projection framework illustrated in Fig. 8.2 is used and matrices U_q and V_q are constructed such as*

$$\text{columnspan}\left(\mathrm{U_q}\right) \quad \subseteq \quad \bigcup_{j=1}^{J} K_{k_j^{(b)}}\left(\ \left(I - s_j E\right)^{-1} E,\ \ \left(I - s_j E\right)^{-1} b\ \right), \tag{8.8}$$

$$\text{columnspan}\left(\mathrm{V_q}\right) \quad \subseteq \quad \bigcup_{j=1}^{J} K_{k_j^{(c)}}\left(\ E^T \left(I - s_j E\right)^{-T},\ \ \left(I - s_j E\right)^{-T} c\ \right) \tag{8.9}$$

with $\sum_{j=1}^{J}\left[k_j^{(b)} + k_j^{(c)}\right] = 2q$,
THEN

$$H(s_j) \quad = \quad \hat{H}(s_j) \qquad \text{for } j = 1, 2, \ldots, J; \tag{8.10}$$

$$\frac{d^{l_j} H(s_j)}{ds^{l_j}} \quad = \quad \frac{d^{l_j} \hat{H}(s_j)}{ds^{l_j}} \qquad \text{for } j = 1, 2, \ldots, J; \quad l_j = 1, 2, \ldots, k_j^{(b)} + k_j^{(c)} - 1 \tag{8.11}$$

where $H(s)$ is the transfer function of the original system and $\hat{H}(s)$ is the transfer function of the reduced system.

In words, the theorems proves that if we include in the column span of U_q the first $k_j^{(b)}$ vectors from the Krylov subspace $K_{k_j^{(b)}}\left(\ \left(I - s_j E\right)^{-1} E,\ \ \left(I - s_j E\right)^{-1} b\ \right)$, then the reduced model transfer function matches the original for at least the first $k_j^{(b)}$ derivatives in s_j. Furthermore, if we include in the column span of V_q the

first $k_j^{(c)}$ vectors from the Krylov subspace $K_{k_j^{(c)}}\left(E^T(I-s_jE)^{-T},\ (I-s_jE)^{-T}\ c \right)$ then the reduced model transfer function matches the original for at least the first $k_j^{(b)}+k_j^{(c)}$ derivatives in s_j. Hence we can match as many derivatives as we want at any expansion point simply including either in the span of U_q or V_q some vectors from the appropriate Krylov subspace. Complete proof in the general case for the theorem is given in [53]. We recall here only two special cases that have a particular practical use.

8.2.2 Special simple case #1: reduction via Arnoldi

Corollary 1 *Given a dynamical linear system as in (7.2),*
IF *the projection framework illustrated in Fig. 8.2 is used and matrices U_q and V_q are constructed using the Arnoldi process in Fig. 8.4 such that*

$$\begin{aligned} \text{columnspan}(\text{U}_\text{q}) &= K_q(E,b) = \text{span}\{b, Eb, ..., E^{q-1}b\} && (8.12)\\ V_q &= U_q && (8.13)\\ U_q^T U_q &= I && (8.14) \end{aligned}$$

THEN

$$\begin{aligned} H(0) &= \hat{H}(0) && (8.15)\\ \frac{d^k H(0)}{ds^k} &= \frac{d^k \hat{H}(0)}{ds^k} \quad \text{for} \quad k = 1, 2, ..., \mathbf{q-1} && (8.16) \end{aligned}$$

and the procedure is numerically robust (i.e. high orders of derivatives can be matched even in finite precision arithmetic)

When constructing the change of basis matrix U_q one can use any basis of the reduced space subspace. Having chosen $K_q(E,b)$ as reduced subspace one could at a first glance consider using vectors $\{b, Eb, E^2b, ..., E^{q-1}b\}$ as columns of U_q. However that is not a convenient choice from a numerical point of view because, as seen in 7.6, vectors $E^k b$ tend to become linearly dependent in finite precision for values of k larger than 20. A numerically more robust base for the same Krylov subspace can instead be constructed using the Arnoldi orthonormalization process [53] described in Fig. 8.4. The Arnoldi process is an iterative one. At each iteration k for $k < n$, a new vector is generated which expands the Krylov subspace spanned by one order. The power series $E^k b$ still embedded in the algorithm is not allowed to align toward the dominant eigenvector since at each iteration k any component in the direction of all previously generated $k-1$ base vectors is immediately discarded by the orthogonalization step. Hence any convergence toward any previously generated direction is prevented.
Note that the orthonormal condition is a consequence of the Arnoldi process which provides the numerical robustness to the algorithm.

From a computational point of view, each iteration of the Arnoldi process requires a matrix-vector product with a dense matrix E of size $n \approx 500,000$ which require $O(n\,log(n)$ when using the fast-matrix vector products shown in 3.6. Hence the overall complexity to construct a reduced model of size q is simply $O(q\,n\log(n))$ which is tractable and scales with the accuracy needed for the model. One can notice that the cost to produce the entire reduced order model is the same cost that would be required to calculate q time points in the time domain response of the original system or q frequency points in the frequency response of the original systems.

8.2.3 Special simple case #2: Pade' Via Lanczos (PVL)

Corollary 2 *Given a dynamical linear system as in (7.2),*
IF *the projection framework illustrated in Fig. 8.2 is used and matrices U_q and V_q are constructed using a*

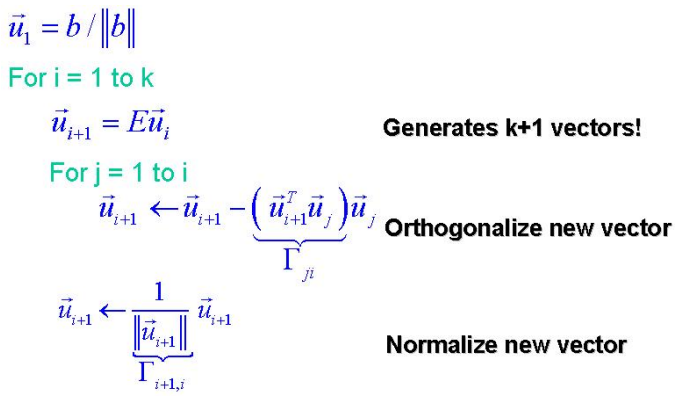

Figure 8.4: *Arnoldi orthonormalization process of the vectors in the Krylov subspace $K_q(E,b)$. This process generates a numerically robust orthonormal basis for the reduced state subspace for the construction of the change of basis matrix U_q.*

Lanczos bi-orthonormalization process [45] such as

$$\text{columnspan}(\text{U}_\text{q}) = K_q(E,b) = \text{span}\{b, Eb, \ldots, E^{q-1}b\} \tag{8.17}$$

$$\text{columnspan}(\text{V}_\text{q}) = K_q(E^T,c) = \text{span}\{c, E^Tc, \ldots, (E^T)^{q-1}c\} \tag{8.18}$$

$$V_q^T U_q = I \tag{8.19}$$

THEN

$$H(0) = \hat{H}(0) \tag{8.20}$$

$$\frac{d^k H(0)}{ds^k} = \frac{d^k \hat{H}(0)}{ds^k} \quad \text{for} \quad k = 1,2,\ldots, \mathbf{2q-1} \tag{8.21}$$

and the procedure is numerically robust (i.e. high orders of derivatives can be matched even in finite precision arithmetic)

Note that the orthonormal condition is a consequence of the Lanczos look-ahead bi-orthonormalization process which provides the numerical robustness to the algorithm. Case #2 is also known as *" PVL or Pade' via Lanczos"* [45]. Fig. 8.5 shows the results of a PVL algorithm when applied to the same problem used for the numerically unstable simple Pade approximation (or AWE) in Fig. 7.7.

From a computational point of view, each iteration of the Lanczos process requires a matrix-vector product with a dense matrix E of size $n \approx 500{,}000$ as for the Arnoldi process, hence the overall complexity to construct a reduced model of size q is $O(q\,n\log(n))$. Comparing case #1 with case #1 one observes that both cases produce a reduced model of same size q with the same amount of effort. However case #2 is twice as efficient than case #1 since in case #1 only *q moments are matched* while in case #2, 2*q moments are matched*. Intuitively case #1 was expected to be less efficient since no information from the output vector c is used in the reduction procedure. Note that in this section we have compared case #1 and case #2 strictly from a computational efficiency point of view. Such comparison however is not complete and we will extended it in subsequent Chapter 9 to include preservation of important system properties such as passivity. A comparison summary will be presented in Table 10 in Chapter 10.

8.2.4 "Multi-point" moment matching

Although the most important improvement of the Krylov subspace projection framework algorithms is their numerically stability, they also provide the ability to combine the techniques seen before of point match-

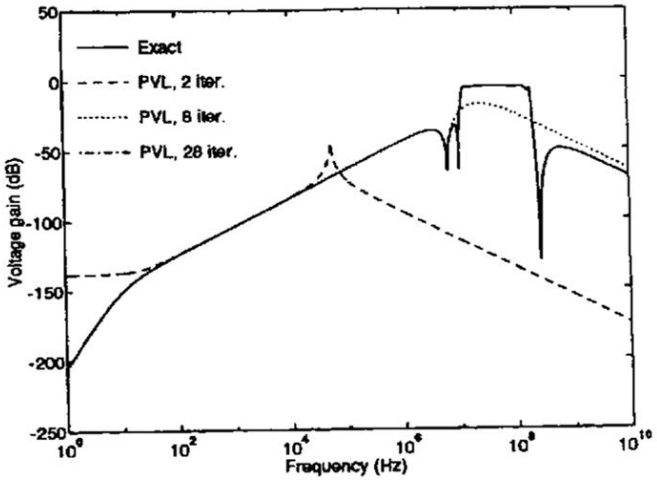

Figure 8.5: *Transfer functions calculated using PVL (Pade' via Lanczos described in Corollary 2. At each iteration of the algorithm one can increase the order q of the produced system. Results for orders* $q = 2, 8$ *and* 28 *are compared to the original transfer function. Comparing with Fig. 7.7 one can observe that arbitrary higher accuracy for the reduced model can be obtained simply using more iterations q. For instance using* $q = 28$ *the reduced transfer function has no appreciable error from the exact one. [Picture by Feldmann and Freund [45]]*

ing and moment matching in 7.5 and 7.6 respectively. Specifically, these algorithms allow to match an arbitrary number of derivatives (or moments) around *many distinct* Taylor series expansion points. Fig. 8.6 illustrates pictorially such concept, where once again derivative matching is illustrated by concentric circles around the expansion point.

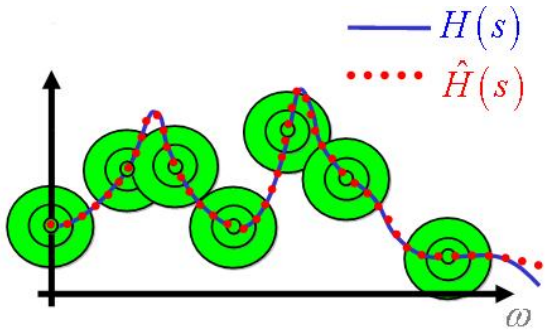

Figure 8.6: *The Krylov subspace projection framework methods allow to perform model reduction combining point matching and moment matching. Specifically in this figure we show with concentric circles the ability of matching derivatives (moments) around several distinct expansion points.*

We recall that the only thing we need to do is "identify" a reduced state subspace and some numerically robust set of vectors that span it. Some of such vectors can be generated from the first terms of a Taylor expansion around $s = 0$, but other vectors can be generated by the first terms of Taylor expansions around other points.

Lemma 1 *A Taylor series expansion around a generic point* $s = s_j$ *produces the following Krylov subspace*

$$x \in K_{k_j}\left((I - s_j E)^{-1} E,\ (I - s_j E)^{-1} b \right). \tag{8.22}$$

Proof. This can be derived for instance using a simple change of variables

$$s = \tilde{s} + s_j \tag{8.23}$$

which transform the system into

$$(\tilde{s} + s_j)Ex = x + bu \tag{8.24}$$

or

$$\tilde{s}(I - s_j E)^{-1} Ex = x + (I - s_j E)^{-1} bu \tag{8.25}$$

Finally we can use the procedure illustrated above for a Taylor series expansion around $\tilde{s} = 0$.

Chapter 9

Background: preserving passivity

Given a large dynamical linear system that models a collection of interconnect, so far we have only discussed how to produce a much smaller size system with a "similar" frequency response (at least in a band of frequencies of interest). Typically this is "good enough" in the case when the model will be used only for a fast evaluation of the frequency response, such as in "radar cross-section" (or field scattering) application problems. However in integrated circuit design, interconnect models are very often used in many other possible ways. Reduced order models (ROM) can be used to capture second order parasitic effects of interconnect wires between circuit blocks as shown in Fig. 9.1 and Fig. 9.2. Models are often connected to construct larger models of complicated structures (Fig. 9.1). In mixed-signal or in analog circuits it is often the case that the reduced order models of interconnect are closed in a feedback loop as shown in Fig. 9.2. All these previous systems are then typically analyzed in a time domain simulator.

All such applications require that the composition of reduced order models with other reduced order models or with circuit blocks is numerically "well-behaved" when we use it for instance in a time domain simulator. We observe that any collection of interconnect is a real, stable, passive, causal system. If we simply limit ourself to produce a reduced order model with a transfer function "similar" to the original, we might not necessarily preserve any of those crucial system properties. For instance, we might observe numerical instability (clearly illustrated in Fig. 9.2 or in Fig. 9.3 from [97]) when using in a time domain simulator an unstable reduced order model, or a stable but non-passive reduced order model connected in an external feedback loop, or many stable but non-passive reduced order models connected arbitrarily. We observe in particular that preserving passivity is far more important than preserving stability of the original model. That is because not only does passivity imply stability, but also because the arbitrary interconnection of many passive models as in Fig. 9.1 is also guaranteed to be passive (and hence stable), while the arbitrary interconnection of many stable (but not passive) models is not guaranteed to be stable (nor passive).

9.1 Passivity for systems modeling immittance

Let us now take a more formal approach, and recall some definitions and some useful linear system theory results. In this section we will be concerned with properties of an abstract system $H : X \to X$, transforming vector input signals u into vector output signals $y = Hu$ within a space of signals X. In the majority of the IC interconnect modeling problems, it is typical to assume that the system inputs, $u : \mathbf{R}^+ \to \mathbf{R}^p$ represent port voltages, and that the outputs $y : \mathbf{R}^+ \to \mathbf{R}^p$ represent port currents, or the converse (the inputs are currents and the outputs voltages). The Laplace-domain representation of the system H is then a matrix $H(s)$, such that

$$y(s) = H(s)u(s), \tag{9.1}$$

where $u(s)$ and $y(s)$ are the Laplace-domain representations of inputs $u(t)$ and outputs $y(t)$. Hence, $H(s)$ is an immittance function: either an admittance matrix $\mathbf{Y}(s)$, or an impedance matrix $Z(s)$. Introduce two inner

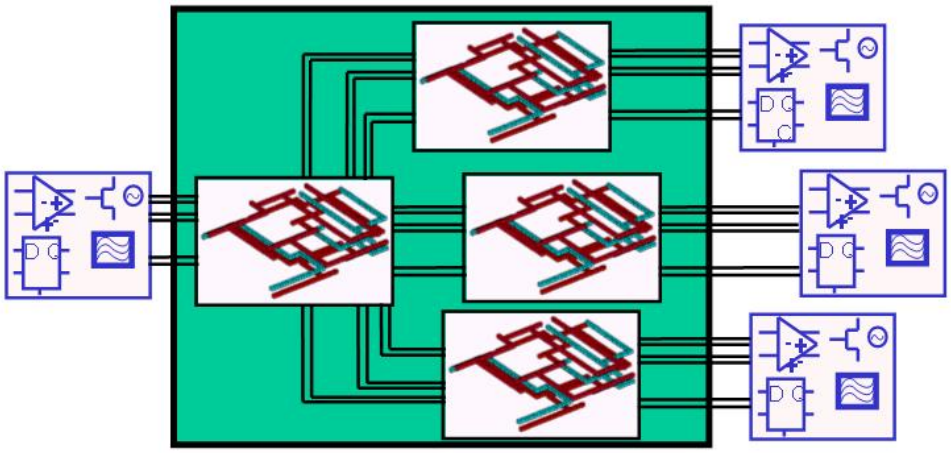

Figure 9.1: *Many interconnect reduced order models are typically connected among them and to circuit blocks to simulate large circuits. Preserving the passivity of the reduced models is crucial. While the arbitrary interconnection of passive models is passive (and hence also stable), the arbitrary interconnection of stable (but not passive) models is not necessarily even stable.*

products in X, the standard inner product

$$\langle u,y\rangle = \int_{-\infty}^{\infty} y(t)^T u(t)dt, \tag{9.2}$$

and a product which acts on truncated signals

$$\langle u,y\rangle_\tau = \langle u_\tau,y\rangle = \langle u,y_\tau\rangle = \int_{-\infty}^{\tau} y(t)^T u(t)dt, \tag{9.3}$$

where $u_\tau(t) \equiv \{u(t) \text{ if } t \le \tau, 0 \text{ if } t > \tau\}$.
If u and y are port current/voltage pairs, $y(t)^T u(t)$ has the physical interpretation of *power*, $\langle u,y\rangle_\tau$ is the total *energy* passed by the system up to time τ. We will generally work in the space of signals $x \in X = L_2$ that have finite norm $||x||$ for any τ, where $||x||^2 = \langle x,x\rangle_\tau$.
A *passive* system is a system that cannot produce energy. For the systems of interest here we may define:

Definition 3 (Passivity) *A system $H : X \to X$ is passive if*

$$\langle u, H\,u\rangle_\tau \ge 0,\ \forall\ \tau \in \mathbf{R}^+,\ \forall\ u \in X,\ u : \mathbf{R}^+ \to \mathbf{R}^p. \tag{9.4}$$

In practice, almost all systems of interest for model reduction are non-ideal and contain some loss. That is, they internally consume energy. If a system consumes energy, it is said to be *strictly passive*.

Definition 4 (Strict Passivity) *A system H is strictly passive if there is a $\delta \in \mathbf{R}^+$ s.t.*

$$\langle u, H\,u\rangle_\tau \ge \delta||u_\tau||^2,\ \forall\ \tau \in \mathbf{R}^+,\ \forall\ u : \mathbf{R}^+ \to \mathbf{R}^p. \tag{9.5}$$

For many electrical systems of interest, passivity is implied by positive-realness of the transfer function $H(s)$.

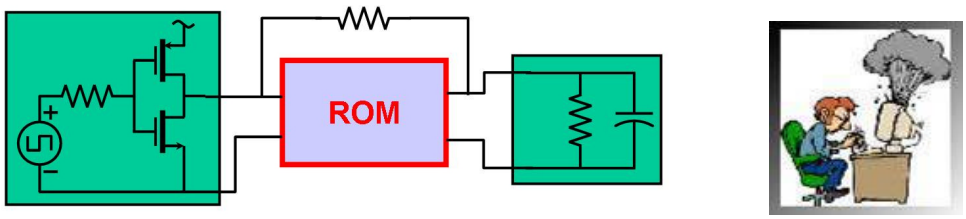

Figure 9.2: *In mixed-signal and analog circuits interconnect models may be included in feedback loops. Only preserving the passivity of the model we are guaranteed that the feedback loop does not cause numerical instability in a time domain simulator.*

Definition 5 (Positive Realness) *Let $H(s) : \mathbf{C} \rightarrow \mathbf{C}^{n\times n}$ be a matrix-valued function of complex variable. Then $H(s)$ is positive-real [4] if*

$$\overline{H(\overline{s})} = H(s), \tag{9.6}$$

$$H(s) \text{ is analytic in } Re(s) > 0, \tag{9.7}$$

$$\Pi_H(s) \equiv H(s) + H(s)^* \geq 0 \text{ in } Re(s) > 0. \tag{9.8}$$

where the overline bar indicates complex conjugate, while the asterix indicates complex conjugate and transposed.

Definition 6 (Strict Positive Realness) *A matrix valued function $H(s)$ is strictly-positive-real [145] if there exists an $\varepsilon \in \mathbf{R}^+$ s.t. $H(s-\varepsilon)$ is positive-real.*

Intuitively, the first condition requires that the time domain impulse response is real, the second condition requires that the system is stable, finally the third condition requires that the symmetric and real part (or loosely speaking the resistive part) of the immittance is a matrix positive semi-definite in the entire right half plane.

Definition 7 (Positive Semi-Definiteness) *A square matrix $E \in \mathbf{R}^{n\times n}$ is positive semi-definite if*

$$x^T E x \geq 0, \quad \forall x \in \mathbf{R}^{n\times 1} \tag{9.9}$$

Positive realness is of interest because of its relation to passivity for lumped networks:

Theorem 3 *A system H with rational system transfer function $H(s)$ is passive and stable if and only if $H(s)$ is positive-real [4].*

In the context of model reduction, the implication for state-space systems is that if a reduction algorithm for lumped RLC networks produces models with positive-real transfer functions $H(s)$, then it generates guaranteed passive models.

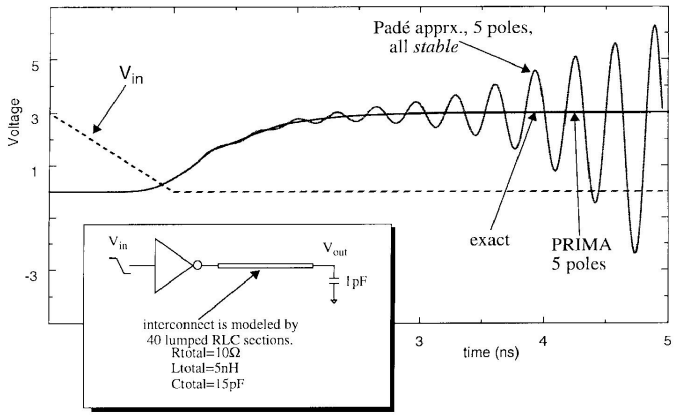

Figure 9.3: *Numerical instability and simulation explosions usually manifest themselves as growing oscillations in time domain waveforms, as in this example where a stable but not passive model of a lossy transmission line has been connected to a driver and a load and simulated in a time domain circuit simulator. [Picture from [97] by A. Odabasioglu, M. Celik, L. T. Pileggi].*

9.1.1 Congruence transformations

In the remainder of this Chapter we will make extensive use of the concept of congruence transformations and their properties related to passivity. Hence we briefly recall them here.

Definition 8 (Congruence Transformation) *Given a square matrix $E \in \mathbf{R}^{n\times n}$ and a rectangular matrix $U \in \mathbf{R}^{n\times q}$, with $q \leq n$, a congruence transformation is a matrix $\hat{E} \in \mathbf{R}^{q\times q}$ defined as*

$$\hat{E} = U^T E U. \tag{9.10}$$

Lemma 2 (Congruence transformations preserve positive semi-definiteness) *Given a positive semi-definite matrix E, any congruence transformation $U^T E U$ is also positive semi-definite.*

Proof. This can be derived by observing that congruence transformations preserve the field of values, i.e.

$$\{x^T U^T E U x, \quad \forall x \in \mathbf{R}^n\} \subset \{x^T E x, \quad \forall x \in \mathbf{R}^n\}. \tag{9.11}$$

Lemma 3 (Congruence transformations preserve positive realness) *Given a positive real matrix value function $Z(s)$, any congruence transformation $U^T Z(s) U$ is positive real.*

Proof. Conditions (9.6) and (9.7) are easily verified. Condition (9.8) can be derived from Lemma 2.

9.1.2 Tools for assessing passivity

It is generally necessary to be able to easily assess the passivity of a generated model. It is not practical to check the conditions (9.6), (9.7), and in particular (9.8), via explicit evaluation since an infinite number of values $\{s, \ Re(s) > 0\}$ should be checked.

Checking positivity only on the imaginary axis

We can observe that, thanks to the analyticity of $H(s)$ in the right half plane, the positivity condition (9.8) simply needs to be verified on the contour of the right half plane, i.e. the imaginary axis [4]:

Theorem 4 *A rational $H(s)$ is positive-real if and only if (9.6) and (9.7) hold, and*

$$\Pi_H(j\omega) \equiv H(j\omega) + H(j\omega)^* \geq 0, \ \forall\, \omega \in \mathbf{R} \tag{9.12}$$

except for simple poles $i\omega_0$ of $H(s)$, where the residue matrix must be nonnegative definite [4]. $H(s)$ is strictly positive real if the inequality is strict [4, 145].

However even using this result, we would still need to check (9.12) for an infinite number of frequencies $j\omega$ on the imaginary axis, which is still not practical.

A necessary but not sufficient condition for passivity

A common misconception when checking for passivity is to simply verify that all poles and zeros are in the left half plane. The following theorem is in part responsible for such misconception.

Theorem 5 *If a rational matrix valued function $H(s)$ is positive-real then $H^{-1}(s)$ is positive-real.*

Based on this theorem we observe that a *necessary* condition for passivity is that, not only all poles of the transfer functions are in the left half plane (stability), but also that all zeros are in the left half plane. However we point out that this condition is *not sufficient*. Hence checking for location of poles and zeros can only be used to prove that a given model is *not* passive when some right half plane poles or zeros are found. Nothing instead can be concluded about passivity of the system when all poles and zeros are found in the left half plane.

A sufficient but not necessary condition for passivity

Theorem 6 *Given a dynamical linear system in the general form*

$$sEx = Ax + Bu, \quad y = Cx \tag{9.13}$$

IF

$$E = E^T \tag{9.14}$$
$$E \geq 0, \quad E \text{ is positive semi-definite} \tag{9.15}$$
$$-A \geq 0, \quad -A \text{ is positive semi-definite} \tag{9.16}$$
$$C = B^T \tag{9.17}$$

THEN *the system is passive.*

Proof. In order to prove that the system in passive we simply need to show that its transfer function $H(s) = C(sE - A)^{-1}B$ is positive real. From the first three conditions (9.14)-(9.16), we can easily conclude that the function $sE - A$ is positive real. From Theorem 5 $Z(S) = (sE - A)^{-1}$ is positive real. Finally, if $C = B^T$ then $H(s) = B^T\ Z(s)\ B$ is a congruence transformation which preserves positive semi-definiteness from lemma 3. This theorem gives a nice way to prove that a system is passive when observing that matrices E and $-A$ are positive semi-definite and $C = B^T$. We care to correct here a second common misconception: such properties are *not necessary* for passiveness. In other words, there are plenty of passive systems with indefinite matrices. As a matter of fact, it usually requires a particular care to describe a passive system, such as a collection of interconnect, with positive semi-definite matrices. That can be achieved for instance when only RLC elements are modeled, and Modified Nodal Analysis (MNA) is used as in [97]. However, if sign conventions in the KCLs are not used consistently across all circuit nodes indefinite matrices can easily be produced.

Example 1 *Let's assume for example that a transmission line has been described using a dynamical linear system as in Fig. 7.2 constructed using Modified Nodal Analysis (MNA). If things are done properly it is*

possible in this particular case to obtain system matrices that verify the sufficient conditions for passivity in Theorem 6, in particular $L = E$ and $R = -A$ are both positive semi-definite, and $C = B^T$. For this particular example we can further observe that matrix E is diagonal and all entries are positive. Now change the sign of one of the equations in the dynamical linear system. Algebraically this corresponds to pre-multiplying by matrix

$$Q = \begin{bmatrix} 1 & 0 & & & & & & \\ 0 & \dots & 0 & & & & & \\ & 0 & 1 & 0 & & & & \\ & & 0 & -1 & 0 & & & \\ & & & 0 & 1 & 0 & & \\ & & & & 0 & \dots & 0 & \\ & & & & & 0 & 1 & \end{bmatrix} \tag{9.18}$$

We obtain the system

$$sQEx = QAx + QBu, \quad y = B^T x. \tag{9.19}$$

We can observe that for instance matrix QE is still diagonal, with all entries positive except for one negative entry. QE is therefore indefinite. Although the conditions in Theorem 6 are not satisfied, the transfer function is exactly the same

$$\begin{aligned} H_Q(s) &= B^T(sQE - QA)^{-1}QB = & (9.20)\\ &= B^T(sE - A)^{-1}Q^{-1}QB = & (9.21)\\ &= H(s), & (9.22) \end{aligned}$$

hence still positive real or in other words the system is still passive.

Example 2 *Another particularly interesting example is the following. Consider again the same passive system described by positive semi-definite matrices E and $-A$ with $C = B^T$ as in Theorem 6. Consider the transformation assumed in all the projection framework algorithms presented in Chapter 8,*

$$sA^{-1}Ex = x + A^{-1}Bu, \quad y = B^T x \tag{9.23}$$

Such new system has the same positive real transfer function of the original system, hence it is still passive, however once again the matrix $A^{-1}E$ may not be in general positive semi-definite.

9.1.3 A necessary and sufficient condition for passivity

All the passive conditions presented so far are only sufficient or only necessary or not practical. Fortunately another mean is available [4] to certify the passivity of a system with a practical efficient algorithm.

Lemma 4 (Positive-Real Lemma, Version 1) *Let $H(s) = D + C(s\mathbf{I} - A)^{-1}B$ be a matrix-valued function, (A, B, C, D) minimal, with poles either in the left half-plane or on the imaginary axis, in which case they are simple. $H(s)$ is positive-real if and only if there exist matrices $X_c = X_c^T, J_c, K_c$ such that the Lur'e equations:*

$$AX_c + X_cA^T = -K_cK_c^T \tag{9.24}$$

$$X_cC^T - B = -K_cJ_c^T, \tag{9.25}$$

$$J_cJ_c^T = D + D^T \tag{9.26}$$

are satisfied, and $X_c \geq 0$ (X_c is positive semi-definite).

X_c is analogous to the controllability Grammian. In fact, it is the controllability Grammian for a system with the input-to-state mapping given by the matrix K_c. It should not be surprising that there are a dual set of Lur'e equations for $X_o = X_o^T > 0, J_o, K_o$ that are obtained from Eqns. (9.24)-(9.26) by the substitutions $A \to A^T, B \to C^T, C^T \to B$.

Lemma 5 (Positive-Real Lemma, Version 2) *Let $H(s) = D + C(s\mathbf{I} - A)^{-1}B$ be a matrix-valued function, (A,B,C,D) minimal, with poles either in the left half-plane or on the imaginary axis, in which case they are simple. $H(s)$ is positive-real if and only if there exist matrices $X_o = X_o^T, J_o, K_o$ such that the dual Lur'e equations:*

$$A^T X_o + X_o A = -K_o^T K_o \tag{9.27}$$
$$X_o B - C^T = -K_o^T J_o, \tag{9.28}$$
$$J_o^T J_o = D + D^T. \tag{9.29}$$

are satisfied, and $X_o \geq 0$ (X_o is positive semi-definite).

The dual equations have a corresponding observability quantity $X_o \geq 0$ for a positive-real $H(s)$. It is easy to verify that X_c, X_o transform under similarity transformation just as W_c, W_o (Eqn. 7.15 in Section 7.4), that their eigenvalues are invariant, and in fact in most respects they behave as the Grammians W_c, W_o. Lemmas 4 or 5 can be used to check the passivity of the produced systems in form:

$$sx = Ax + Bu, \quad y = Cx + Du. \tag{9.30}$$

Computational procedures may be found in [5]. Also, [9] gives a computational procedure that involves only standard matrix computation, such as computing the eigenvalues of a matrix or a matrix pencil. Extensions of the positive-real lemma are available for transfer functions in the descriptor form $H(s) = D + C(sE - A)^{-1}B$. Such extensions can be used to check the passivity of the systems in form:

$$sEx = Ax + Bu, \quad y = Cx + Du, \tag{9.31}$$

where E is singular such that the transfer function cannot be put into the above form [61]. Computational procedures can be found in [109].

9.2 Passivity for systems modeling scattering parameters

In some PCB, some package, and some microwave applications we may encounter interconnect models where the system inputs, u, represent incoming waves of voltage (or current, or electromagnetic field), and that the outputs y represent outgoing waves of voltage (or current, or electromagnetic field). In this case the Laplace-domain representation of the system transfer function H is then a "scattering parameter" matrix function $H(s)$. In this case we can define the two following inner products in X,

$$\langle u,y\rangle = \int_{-\infty}^{\infty} u(t)^T u(t)dt - \int_{-\infty}^{\infty} y(t)^T y(t)dt, \tag{9.32}$$

and a product which acts on truncated signals

$$\langle u,y\rangle_\tau = \langle u_\tau, y\rangle = \langle u, y_\tau\rangle = \int_{-\infty}^{\tau} u(t)^T u(t)dt - \int_{-\infty}^{\tau} y(t)^T y(t)dt \tag{9.33}$$

where

$$u_\tau(t) \equiv \begin{cases} u(t) & \text{if } t \leq \tau, \\ 0 & \text{if } t > \tau. \end{cases} \tag{9.34}$$

$u(t)^T u(t)$ and $y(t)^T y(t)$ have the physical interpretation of *energy* of the incoming and outgoing waves respectively. $\langle u,y\rangle_\tau$ is the difference between the two, hence it is the total *energy* passed by the system up to time τ. To represent a passive system in this case it is necessary that $H(s)$ be bounded-real [4].

Definition 9 (Bounded Realness) *A matrix valued function $H(s)$ is bounded-real if*

$$\overline{H(\overline{s})} = H(s), \tag{9.35}$$
$$H(s) \text{ is analytic in } Re(s) > 0, \tag{9.36}$$
$$I - H(s)^* H(s) \geq 0 \text{ in } Re(s) > 0. \tag{9.37}$$

The term "bounded" arises as Eqn. (9.37) is equivalent to stating that $||H(s)||_2 \leq 1$ in the open right-half plane. Intuitively this corresponds to roughly requiring that the amplitude of all reflection coefficients is less than one.

9.2.1 Bounded-Real conditions

In order to check if the transfer function of a system is bounded real one can use the following necessary and sufficient conditions.

Lemma 6 (Bounded-Real Lemma, Version 1) *Let $H(s) = D + C(s\mathbf{I} - A)^{-1}B$ be a matrix-valued function, (A,B,C,D) minimal, with poles either in the left half-plane or on the imaginary axis, in which case they are simple. $H(s)$ is bounded-real if and only if there exist matrices $Y_c = Y_c^T, J_c, K_c$ such that the Lur'e equations:*

$$AY_c + Y_cA^T = -BB^T - K_cK_c^T \tag{9.38}$$

$$Y_cC^T + BD = -K_c^T J_c \tag{9.39}$$

$$J_cJ_c^T = I - D^T D \tag{9.40}$$

are satisfied, and $Y_c \geq 0$ (Y_c is positive semi-definite).

A dual condition can also be given.

Lemma 7 (Bounded-Real Lemma, Version 2) *Let $H(s) = D + C(s\mathbf{I} - A)^{-1}B$ be a matrix-valued function, (A,B,C,D) minimal, with poles either in the left half-plane or on the imaginary axis, in which case they are simple. $H(s)$ is bounded-real if and only if there exist matrices $Y_o = Y_o^T, J_o, K_o$ such that the Lur'e equations:*

$$A^TY_o + Y_oA = -C^TC - K_o^TK_o \tag{9.41}$$

$$Y_oB + C^TD = -K_oJ_o^T, \tag{9.42}$$

$$J_o^TJ_o = I - D^TD \tag{9.43}$$

are satisfied, and $Y_o \geq 0$ (Y_o is positive semi-definite).

9.3 Causality

A *causal* system is a system whose output depends only on past inputs, not future inputs.

Definition 10 (Causality) *A system H is causal if and only if $Hu(\tau) = Hu_\tau(\tau)$, $\forall\, \tau \in \mathbf{R}^+$, $\forall\, u : \mathbf{R}^+ \to \mathbf{R}^p$.*

All physical systems are causal. Hence, causality is a necessary property of all models intended to be used in any simulator that has a concept of time. However, it is often neglected, specially when modeling distributed systems. When constructing model reduction algorithms for distributed systems, we must keep in mind that the condition in Equation (9.12) is not sufficient by itself to insure that the model is physical and well-behaved when used in a time domain simulator.

There are systems that satisfy the passivity conditions without being causal. Those systems both cannot represent any physical interconnect, and cannot be represented by dynamical models to be used in causal time-domain simulators.

Example 3 *Let's consider from a practical point of view a one port ($p = 1$) network function $Z_{skin}(j\omega) = R_0 + R_{ac}\sqrt{|\omega|}$ that is commonly used as a model for the "resistance" of interconnect in the skin-effect regime. This function satisfies all the passivity conditions including $\Pi_Z(j\omega) > 0$, $\forall\, \omega \in \mathbf{R}$. However, it is* not *a representation of any passive system, because it is not a causal function. In fact, it can be shown that any physical, passive network function that is purely real must be constant with respect to the frequency*

ω. *In Section 12.4.3 we further illustrate the non-causality of this model. Practically speaking, although the function is passive no physical collection of interconnect can have such function as a transfer function. Furthermore no causal dynamical system model for a time-domain simulator can be constructed to represent it.*

Algorithms that generate successively better rational approximations of non-causal systems (for example, $Z_{\text{skin}}(j\omega)$) must in some limit fail to be passive, for example by generating unstable approximants. Therefore we will require that all the systems representing interconnect we are supposed to reduce be not only passive but also causal.

9.4 Existing model reduction methods preserving passivity (PRIMA)

Because of the need to obtain accurate high-order models at reasonable computational cost, the Krylov-subspace model reduction methods [46, 73, 13, 53, 74, 99, 43, 130, 97, 128, 12, 16] have occupied the forefront of research over the past five years. The importance of producing *passive* reduced models has been realized, and several algorithms that preserve passivity of RLC circuits in specialized cases have appeared [13, 95, 74, 11, 10, 42, 100, 99, 47, 43, 97, 87, 48, 102, 14, 98, 16, 28, 27]. In Chapters 11, 12 and 13 we will present the algorithms that we have developed to preserve passivity in cases not yet covered in literature [36, 33, 108, 109]. In this section we describe instead PRIMA [100, 99, 97], a crucial modification of the Krylov subspace projection framework via Arnoldi presented in Section 8.2.2. Consider a dynamical linear system in the form

$$sEx = Ax + Bu, \quad y = Cx \tag{9.44}$$

that not only is passive but also the much stronger sufficient conditions in Theorem 6 in Section 9.1.2 are all satisfied.

1. As in Section 8.2.2 consider the equivalent system

$$sA^{-1}Ex = x + A^{-1}Bu, \quad y = Cx. \tag{9.45}$$

2. As in Section 8.2.2, calculate the change of basis U_q matrix using the Arnoldi process in Fig. 8.4 whose columns span the Krylov subspace $K_q(A^{-1}E, A^{-1}B)$.

3. As in Section 8.2.2 choose $V_q = U_q$.

4. In Section 8.2.2 the projection framework was applied to the system (9.45), obtaining the reduced system

$$sU_q^T A^{-1} E U_q x = x + U_q^T A^{-1} Bu, \quad y = CU_q x. \tag{9.46}$$

   In PRIMA instead the projection framework is applied to the original system (9.44), obtaining the reduced system

$$sU_q^T E U_q x = U_q^T A U_q x + U_q^T Bu, \quad y = B^T U_q x. \tag{9.47}$$

Theorem 7 *The reduced system produced by PRIMA is passive.*

Proof. This can be seen observing that the projection framework, when choosing $V_q = U_q$ as in this case, results in congruence transformations for matrices E and A. From Lemma 2, since the original matrices were positive and negative semi-definite respectively, also the reduced matrices are positive and negative semi-definite respectively. We farther observe that the projection framework in this special case preserves the input/output symmetry condition, i.e. if $C = B^T$ then $CU_q = U_q^T B$. In conclusion, when the original system is passive and satisfies all the strong sufficient conditions in Theorem 6 then the reduced by PRIMA also satisfies to the same conditions and hence is guaranteed passive.

Examining example 2 one can instead realize that the the same result cannot be achieved by the simple reduction via Arnoldi in Section 8.2.2. In that case although the original system is passive, matrix $A^{-1}E$

is not necessarily positive semi-definite and therefore the reduction via congruence transformation does not produce necessarily positive semi-definite matrices.

Finally, besides preserving passivity, PRIMA has the same matching properties and numerical robustness of the reduction via Arnoldi in Section 8.2.2

Theorem 8 *The transfer function $\hat{H}(s)$ of the reduced system produced by PRIMA matches the first q derivatives (or moments, or Taylor series coefficients) of the transfer function $H(s)$ of the original system*

$$H(0) = \hat{H}(0) \tag{9.48}$$

$$\frac{d^k H}{ds^k}(0) = \frac{d^k \hat{H}}{ds^k}(0) \quad \text{for} \quad k = 1, 2, \ldots, q-1 \tag{9.49}$$

and the procedure is numerically robust (i.e. high orders of derivatives can be matched even in finite precision arithmetic)

Proof. The numerical robustness derives as usual from the Arnoldi orthonormalization process. In order to show the moment matching properties we can expand in Taylor series the original model and the reduced model

$$H(s) = \sum_{k=0}^{\infty} m_k s^k = \sum_{k=0}^{\infty} \left[B^T (A^{-1}E)^k A^{-1} B \right] s^k \tag{9.50}$$

$$\hat{H}(s) = \sum_{k=0}^{\infty} \hat{m}_k s^k = \sum_{k=0}^{\infty} \left[(U_q^T B)^T ((U_q^T A U_q)^{-1} (U_q^T E U_q))^k (U_q^T A U_q)^{-1} (U_q^T B) \right] s^k \tag{9.51}$$

$$\tag{9.52}$$

For each of the first q moments we can show that

$$\hat{m}_k = B^T U_q (U_q^T A U_q)^{-1} U_q^T E U_q \ldots (U_q^T A U_q)^{-1} U_q^T E U_q (U_q^T A U_q)^{-1} U_q^T B \tag{9.53}$$

$$= B^T U_q (U_q^T A U_q)^{-1} U_q^T E U_q \ldots (U_q^T A U_q)^{-1} U_q^T E U_q U_q^T A^{-1} B \tag{9.54}$$

$$= B^T U_q (U_q^T A U_q)^{-1} U_q^T E U_q \ldots (U_q^T A U_q)^{-1} U_q^T E A^{-1} B \tag{9.55}$$

$$= B^T U_q (U_q^T A U_q)^{-1} U_q^T E U_q \ldots U_q^T A^{-1} E A^{-1} B \tag{9.56}$$

$$= B^T (A^{-1}E) \ldots (A^{-1}E) A^{-1} B \tag{9.57}$$

$$= B^T (A^{-1}E)^k A^{-1} B \tag{9.58}$$

$$= m_k \tag{9.59}$$

Note that $U_q^T U_q = I$ because of the Arnoldi orthonormalization process used to construct U_q. In general instead $U_q U_q^T$ is not the identity matrix. However, in the previous derivation we have used Lemma 8 and 9. Note that such Lemmas can be applied only to the first q moments since the columns of U_q span the Krylov subspace $K_q(A^{-1}E, A^{-1}B)$ of order q.

Lemma 8 **If** *U_q is an orthonormal matrix $U_q \in \mathbf{C}^{n \times q}$, $U_q^T U_q = I \in \mathbf{R}^{q \times q}$, and v is any vector in the column span of the matrix U_q, $v \in$ columnspan(U_q)*
then $U_q U_q^T v = v$.

Proof. If $v \in$ columnspan(U_q) then there exists a vector g such that $v = U_q g$. Substituting $U_q U_q^T v = U_q U_q^T U_q g = U_q g = b$.

Lemma 9 **If** *U_q is an orthonormal matrix $U_q \in \mathbf{C}^{n \times q}$, $U_q^T U_q = I \in \mathbf{R}^{q \times q}$, and v is any vector such that $A^{-1}v \in$ columnspan(U_q),*
then $(U_q^T A U_q)^{-1} U_q^T v = U_q^T A^{-1} v$.

Proof. If $A^{-1}v \in \text{columnspan}(U_q)$ then there exists a vector g such that $A^{-1}v = U_q g$. Substituting

$$\begin{aligned}
(U_q^T A U_q)^{-1} U_q^T v &= (U_q^T A U_q)^{-1} U_q^T A A^{-1} v && (9.60)\\
&= (U_q^T A U_q)^{-1} (U_q^T A U_q) g && (9.61)\\
&= g && (9.62)\\
&= U_q^T U_q g && (9.63)\\
&= U_q^T A^{-1} b && (9.64)
\end{aligned}$$

Finally we observe that PRIMA can be formulated to include the same type of multi-point moment matching capabilities following the procedure illustrated in Section 8.2.4.

Chapter 10

Background: comparing existing model order reduction methods

As seen in the previous in this introductory chapters, there exist many model order reduction procedures. When selecting a procedure for a particular application one should consider four main characteristics:

- the **computational cost** required to build a model of a given accuracy (or order) from an originally huge and dense dynamical linear system. This characteristic is crucial when *producing* the reduced order model. Typically one can afford only a complexity linear in the size of the original model.

- the **accuracy** achieved by the reduced order model for a given order. This characteristic is important when *using* the reduced order model. Smaller models for a given accuracy can result in faster runtimes when using the model in a circuit simulator.

- the **numerical robustness** of the reduction procedure. This is important when trying to increase the size of the reduced model to *increase the accuracy*. Reduction procedures that are not numerically robust can only produce models of small accuracy regardless of the size of the produced model.

- the ability to **preserve passivity** of the original model. This is an essential property when *using* the reduced model in a time domain simulator. Failing to preserve passivity can easily result in numerical instability in the simulator.

We summarize in Table 10 the properties of the most important model order reduction algorithms presented in this Chapter.

Table 10.1: Comparison of some Model Order Reduction methods.

	Cost for reducing from order n to q	Accuracy for given order q	Numerical robustness	Preserving passivity
Eigenmodes (7.3)	$O(n^3)$	poor	yes	no
TBR (7.4)	$O(n^3)$	almost optimal	yes	no
Point match (7.5)	$O(q\ n\ log(n))$	match q points	no	no
Pade-AWE (7.6)	$O(q\ n\ log(n))$	match $2q$ moments	no	no
Arnoldi (8.2.2)	$O(q\ n\ log(n))$	match q moments	yes	no
PVL (8.2.3)	$O(q\ n\ log(n))$	match $2q$ moments	yes	no
PRIMA (9.4)	$O(q\ \ n\ log(n))$	match q moments	yes	yes

10.1 The "two steps procedure"

We can observe from table 10 that the only algorithms that can be used to handle the large and dense dynamical linear systems produced by typical interconnect structures on modern electronic circuits are the Krylov subspace projection framework methods: the reduction via Arnoldi in Section 8.2.2, PRIMA in Section 9.4 and PVL in Section 8.2.3. The Truncated Balance Realization (TBR) method presented in Section 7.4 would be quite more effective in terms of accuracy for a given order of the produced model. However its cubic complexity makes it useful only for original models with order not larger than few hundreds.

A common approach in practical applications is then to use a *"two steps procedure"*.

1. Typically one would apply a first reduction using a Krylov subspace method (e.g. PRIMA) and reduce the original system of size around 500,000 to an intermediate system of size as large as a TBR can handle.

2. The one would complete the reduction with TBR which is more efficient in terms of final size for a given order.

An alternative approach is to directly solve the large Lyapunov equations via a Krylov subspace method [81, 115, 63, 64, 116] in order to reduce the TBR cubic complexity.

10.2 The main contributions of this thesis in model order reduction

The most important observation when looking at Table 10 is that preservation of passivity is still an critical issue in the field of model order reduction. The problem has been partially address by the algorithm PRIMA. However PRIMA requires the passive system to be a very specific form in order to preserve passivity. It has been shown how to setup the original system in such special form only for problems including conductors. In Chapter 11 we will develop a method to produce dynamical systems that satisfy the passivity conditions for model order reduction using PRIMA ***for structures including dielectrics*** [36, 34].

Furthermore, PRIMA is only applicable to dynamical linear systems with constant descriptor matrices E and A. In many modern applications we need to be able to handle ***"distributed" systems, that are described by frequency dependent matrices*** $E(s)$ ***and*** $A(s)$**.** No reduction technique is available for such systems capable of preserving passivity. In Chapter 12 we will develop such a needed reduction procedure [33].

Finally, "the second step" of the previously mentioned "two steps procedure" involves using an algorithm that although accurate, in general may not preserve passivity. This problem is currently addressed in practice by checking if the model generated by TBR is passive and if it is not passive a model of higher order is generated until a passive model is "hopefully" generated. In Chapter 13 we develop instead ***a technique similar to TBR that preserves*** passivity [108, 109]. Our new technique has the same optimal properties of TBR in terms of accuracy for a given order, Furthermore, differently from PRIMA, our algorithm does not require the the original passive system to be in any special form.

Chapter 11

Preserving passivity when including dielectrics

The work in this chapter has been done in collaboration with Prof. Jacob White, Massachusetts Institute of Technology, and it has first appeared in [36, 34].

Dielectric materials are present in almost all modern electronic circuits: from Printed Circuit Boards (PCBs), to packages, Multi-Chips Modules (MCMs), and Integrated Circuits. Dielectrics can significantly affect both the performance and the functionality of electronic circuits. For instance, they can change interconnect delays, as well as the positions of frequency response resonances. Ignoring dielectrics can therefore potentially lead to very inaccurate results both in timing analysis tools and in signal integrity tools.

Integral equation methods have proved to be very effective tools for analyzing on-chip and off-chip interconnect structures, and there are several approaches for including dielectric interfaces in integral formulations. For problems which can be viewed as flat interfaces of infinite extent, such as multilayer printed circuit boards, the dielectric interface conditions can be satisfied by an appropriate choice of Green's function [26, 3, 90, 150, 15]. For general shape or finite-size dielectric bodies, it is possible to "replace" the dielectrics with equivalent fictitious electric and/or magnetic surface currents [50, 135]. General dielectric shapes can also be handled by a Volume Integral Equation (VIE) approach, in which case the polarization currents are introduced in the volume of the dielectrics, and charges are introduced on their surfaces [122, 125]. Several comparisons of the Volume Integral Equation method against the Surface Integral Equation (SIE) method [126, 124], against the Finite Difference Time Domain (FDTD) method [29], and against the Finite Element Method (FEM) [76] have proven extensively its accuracy and viability. Common conclusions of these comparisons is that in general the Integral Equation Methods (Green Functions, VIE and SIE) are preferred to FDTD and FEM, for systems *not* located inside metal shielding enclosures. For such systems, the Green Function and the SIE method introduce a smaller number of unknowns than the VIE method. In this chapter, however, we show how, combining a VIE approach with a full mesh analysis formulation, both for the conductors and for the dielectrics, one can obtain a well conditioned system. Therefore, fast iterative solver convergence rates are possible. Furthermore, dielectrics in PCBs, packages and MCMs systems appear typically in the form of one or more thin parallelepiped layers. When performing Signal Integrity (SI) or Electromagnetic Interference (EMI) analysis on such applications, the VIE approach might be a viable approach, since one could use an FFT based "fast method", such as Conjugate Gradient FFT (CGFFT) [124] or Precorrected-FFT [110]. The Precorrected-FFT grid can be chosen to coincide with a regular volume discretization grid used in the dielectric parallelepiped layer. In this way, one can avoid significant extra precorrection computations.

As the last decade has made clear, detailed electromagnetic analysis is a vastly more effective tool if it can be used to automatically generate small and accurate circuit-level models of the interconnect via Model Order Reduction (MOR) techniques [46, 73, 13, 53, 74, 99, 43, 130, 97, 128, 12, 16]. For instance, the power and ground distribution system of a package or of an integrated circuit can be pre-analyzed using a MOR

technique independently from the rest of the non-linear circuitry. The reduced order model resulting from the analysis, can then be re-coupled with the rest of the circuitry in a non-linear time domain circuit simulator. However, numerical stability problems can arise in the time domain simulator when non-passive models are generated from originally passive interconnect structures.

Some MOR algorithms have been recently developed to address such critical issue [13, 53, 74, 99, 43, 97, 16] under some conditions on the original large linear system. Such conditions are easily verified by many existing formulations used to analyze "conductors-only" interconnect structures. However, when dielectrics are included such as in [94], matrices are generated that do not satisfy to the passivity conditions. To our knowledge, no formulation is yet available to guarantee passivity for interconnect structures that *include dielectrics*. In this chapter we show that a VIE method combined with a full mesh-based formulation both for conductors and dielectrics leads to, at least in the low frequency regime, a linear dynamical system with positive semi-definite matrices [36]. This positive-definite result is important because it makes possible the straight-forward application of the Krylov-subspace based guaranteed passive model-order (MOR) [97].

11.1 Handling dielectrics with a Volume Integral Equation method

One way to include dielectrics with a Volume Mixed Potential Integral Equation is to write Maxwell equations as

$$\frac{\mathbf{J_c}(\mathbf{r_c})}{\sigma_c} + j\omega\frac{\mu}{4\pi}\left[\int_{V_c} K(\mathbf{r_c},\mathbf{r_c}')\,\mathbf{J_c}(\mathbf{r_c}')\,d\mathbf{r_c}' + \int_{V_d} K(\mathbf{r_c},\mathbf{r_d}')\,\mathbf{J_d}(\mathbf{r_d}')\,d\mathbf{r_d}'\right] = -\nabla\phi_c \qquad (11.1)$$

$$\frac{\mathbf{J_d}(\mathbf{r_d})}{j\omega(\varepsilon-\varepsilon_0)} + j\omega\frac{\mu}{4\pi}\left[\int_{V_c} K(\mathbf{r_d},\mathbf{r_c}')\,\mathbf{J_c}(\mathbf{r_c}')\,d\mathbf{r_c}' + \int_{V_d} K(\mathbf{r_d},\mathbf{r_d}')\,\mathbf{J_d}(\mathbf{r_d}')\,d\mathbf{r_d}'\right] = -\nabla\phi_d \qquad (11.2)$$

$$\frac{1}{4\pi\varepsilon_0}\left[\int_{S_c} K(\mathbf{r_{cs}},\mathbf{r'_{cs}})\,\rho_c(\mathbf{r'_{cs}})\,d\mathbf{r'_{cs}} + \int_{S_d} K(\mathbf{r_{cs}},\mathbf{r'_{ds}})\,\rho_d(\mathbf{r'_{ds}})\,d\mathbf{r'_{ds}}\right] = \phi_c(\mathbf{r_{cs}}) \qquad (11.3)$$

$$\frac{1}{4\pi\varepsilon_0}\left[\int_{S_c} K(\mathbf{r_{ds}},\mathbf{r'_{cs}})\,\rho_c(\mathbf{r'_{cs}})\,d\mathbf{r'_{cs}} + \int_{S_d} K(\mathbf{r_{ds}},\mathbf{r'_{ds}})\,\rho_d(\mathbf{r'_{ds}})\,d\mathbf{r'_{ds}}\right] = \phi_d(\mathbf{r_{ds}}) \qquad (11.4)$$

where V_c and V_d are the union of the conductor and dielectric volumes respectively, $\mathbf{r_c}$ and $\mathbf{r_d}$ are vectors indicating points in V_c and V_d respectively. μ is the magnetic permeability, ε_0 is the permittivity, ε_r is the dielectric relative permittivity, σ_c is the conductivity of the metal, and ω is the angular frequency of the conductor excitation. $\mathbf{J_c}$ is the current density in the conductors. $\mathbf{J_d} = j\omega(\varepsilon-\varepsilon_0)\mathbf{E}$ is the polarization current density in the interior of the dielectrics (as shown in Fig. 11.1), and $\mathbf{E}$ is the electric field.

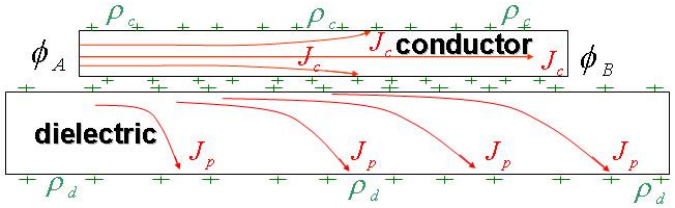

Figure 11.1: *Volume Mixed Potential Integral Equation where dielectrics are accounted for using polarization currents J_d.*

The kernel $K(\cdot,\cdot)$ for a full-wave formulation is a frequency dependent function

$$K(\mathbf{r_1},\mathbf{r_2}) = \frac{e^{j\omega\sqrt{\varepsilon_0\mu}|\mathbf{r_1}-\mathbf{r_2}|}}{|\mathbf{r_1}-\mathbf{r_2}|}. \qquad (11.5)$$

When the relevant length scales are much smaller than a wavelength, the above kernel can be approximated with the frequency independent function

$$K(\mathbf{r_1},\mathbf{r_2}) = \frac{1}{|\mathbf{r_1}-\mathbf{r_2}|}. \tag{11.6}$$

The scalar potentials ϕ_c and ϕ_d, can be related to the surface charge ρ_c and ρ_d, on *both the conductor and dielectric surfaces* as shown in (11.3)-(11.4), where S_c is the union of the conductor surfaces, S_d is the union of the dielectric surfaces, $\mathbf{r_{cs}}$ is a vector indicating a point in S_c, and $\mathbf{r_{cs}}$ is a vector indicating a point in S_d. Within each conductor, and within each homogeneous block of dielectric,

$$\nabla \cdot \mathbf{J_c}(\mathbf{r_c}) = 0 \tag{11.7}$$
$$\nabla \cdot \mathbf{J_d}(\mathbf{r_d}) = 0 \tag{11.8}$$

for all points $\mathbf{r_c}$ and $\mathbf{r_d}$ in the *interior* of V_c and V_d respectively. In addition, the current normal to the conductor and dielectric surfaces is responsible for the accumulation of surface charge,

$$\hat{\mathbf{n}} \cdot \mathbf{J_c}(\mathbf{r_{cs}}) = j\omega\rho_c(\mathbf{r_{cs}}) \tag{11.9}$$
$$\hat{\mathbf{n}} \cdot \mathbf{J_d}(\mathbf{r_{ds}}) = j\omega\rho_d(\mathbf{r_{ds}}) \tag{11.10}$$

where $\hat{\mathbf{n}}$ is the unit normal to S_c and S_d at the points $\mathbf{r_{cs}}$ and $\mathbf{r_{cs}}$ respectively.

The main unknowns, $\mathbf{J_c}$, $\mathbf{J_d}$, ρ_c, and ρ_d can be approximated by a weighted sum of a finite set of basis functions. One classical choice for the basis functions is to cover the surface of each conductor and of each dielectric with *panels*, each of which hold a constant charge density. To model current flow, the interiors of all conductors and dielectrics are divided into a 3-D grid of *filaments*. Fig. 11.6 shows an example of 3D volume discretization of a dielectric parallelepiped. Each filament carries a constant current. Other basis functions choices [35, 37, 39, 38] are possible for the interior of the conductors as shown in Chapters 4 and 5.

A Galerkin method [54] can be used to transform the Mixed Potentials Integral Equations (11.1)-(11.4) into an algebraic form

$$\begin{bmatrix} R+sL+\frac{1}{s}\begin{bmatrix} 0 & 0 \\ 0 & Pol \end{bmatrix} & \begin{bmatrix} 0 & 0 \\ 0 & 0 \end{bmatrix} \\ \begin{bmatrix} 0 & 0 \\ 0 & 0 \end{bmatrix} & P \end{bmatrix} \begin{bmatrix} I_c \\ I_d \\ q_c \\ q_d \end{bmatrix} = \begin{bmatrix} V_c \\ V_d \\ \phi_c \\ \phi_d \end{bmatrix} \tag{11.11}$$

where I_c, I_d, q_c and q_d are vectors of basis function weights for the conductor currents, dielectric polarization currents, conductor charges and dielectric charges respectively. V_c, V_d, ϕ_C and ϕ_d are the vectors generated by inner products of the basis functions with the potential gradient and with the potential itself. The resistance matrix R, the inductance matrix L and the coefficients of potential matrix P are all derived directly from the Galerkin condition [54], and their physical interpretation is illustrated in Fig. 11.2,

$$R = \begin{bmatrix} R_c & 0 \\ 0 & 0 \end{bmatrix}, \tag{11.12}$$
$$L = \begin{bmatrix} L_{cc} & L_{cd} \\ L_{dc} & L_{dd} \end{bmatrix}, \tag{11.13}$$
$$P = \begin{bmatrix} P_{cc} & P_{cd} \\ P_{dc} & P_{dd} \end{bmatrix}. \tag{11.14}$$

L and P are frequency dependent when using a full-wave kernel as in (11.5), and frequency independent when using a quasi-static kernel as in (11.6). Matrix Pol in (11.11) is a diagonal matrix carrying the polarization coefficients

$$Pol_{i,i} = \frac{l_i}{A_i(\varepsilon - \varepsilon_0)} \tag{11.15}$$

where l_i and A_i are the length and the cross-sectional area of dielectric filament i respectively.

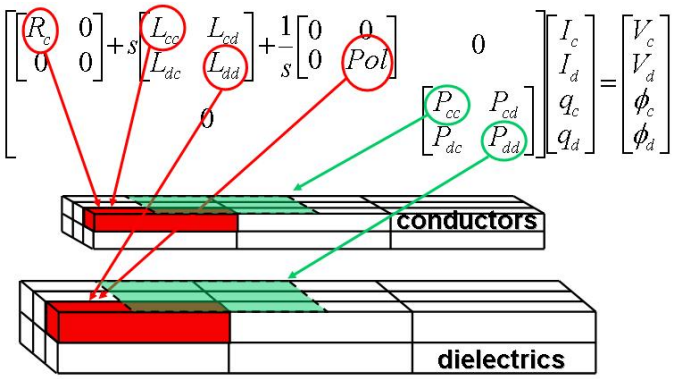

Figure 11.2: *Physical meaning of the discretization matrices in the Volume Mixed Potential Integral Equation method.*

11.2 Comparing an enforced-potentials with a mesh formulation

When considering equations (11.1)-(11.10), several alternative approaches are possible to treat interconnect structures including dielectrics. As noted in [66] and elsewhere, boundary artifacts make it impossible to simultaneously satisfy equations (11.1)-(11.4), $\nabla^2\phi = 0$ and $\nabla \cdot \mathbf{J} = 0$. Typical formulations either enforce (11.1)-(11.4) together with $\nabla^2\phi = 0$, or they enforce (11.1)-(11.4) and $\nabla \cdot \mathbf{J} = 0$. In this chapter, we will refer to first formulation as "enforced-potentials formulation". Imposing the latter formulation *on surface and on interior of both conductors and dielectrics* (11.7)-(11.10), makes it possible to use a mesh analysis approach, hence in this chapter we will refer to the latter formulation as "current-conservation mesh formulation".

As a summary, a complete mesh formulation for structures including both conductors and dielectrics, after the Galerkin transformation can be written simply as:

$$M Z_{cd} M^T I_m = V_{m_s} \tag{11.16}$$

where I_m are the unknown mesh currents, V_{m_s} is the vector of known mesh voltage sources, non zero only on the rows associated with the external circuit terminals. Z_{cd} is the Galerkin impedance matrix

$$Z_{cd} = \begin{bmatrix} R + sL + \frac{1}{s}\begin{bmatrix} 0 & 0 \\ 0 & Pol \end{bmatrix} & 0 \\ 0 & \frac{1}{s}P \end{bmatrix} \tag{11.17}$$

M is a very sparse mesh analysis matrix,

$$M = [M_{fc} M_{fd} M_{pc} M_{pd}], \tag{11.18}$$

where submatrices M_{fc} and M_{pc} are the KVL's mesh matrices for the conductors filaments and panels as described in [66]. In a very similar way to [66], we can construct also M_{fd} and M_{pd}, the KVL's mesh matrices for the dielectric filaments and panels. In fact, as for the conductors, dielectric panel charges can be treated as displacement currents flowing on circuit branches to the node at infinity. A set of independent meshes for the three dimensional discretization of the block of dielectric can be found using a minimum spanning tree. Fig. 11.3 shows some of of the conductor and dielectric KVL meshes.

11.2.1 Comparing condition numbers

We compare here the enforced potentials and the current conservation mesh formulations on a simple example. Two wires are considered in a typical PCB transmission line configuration as shown in Fig. 11.6.

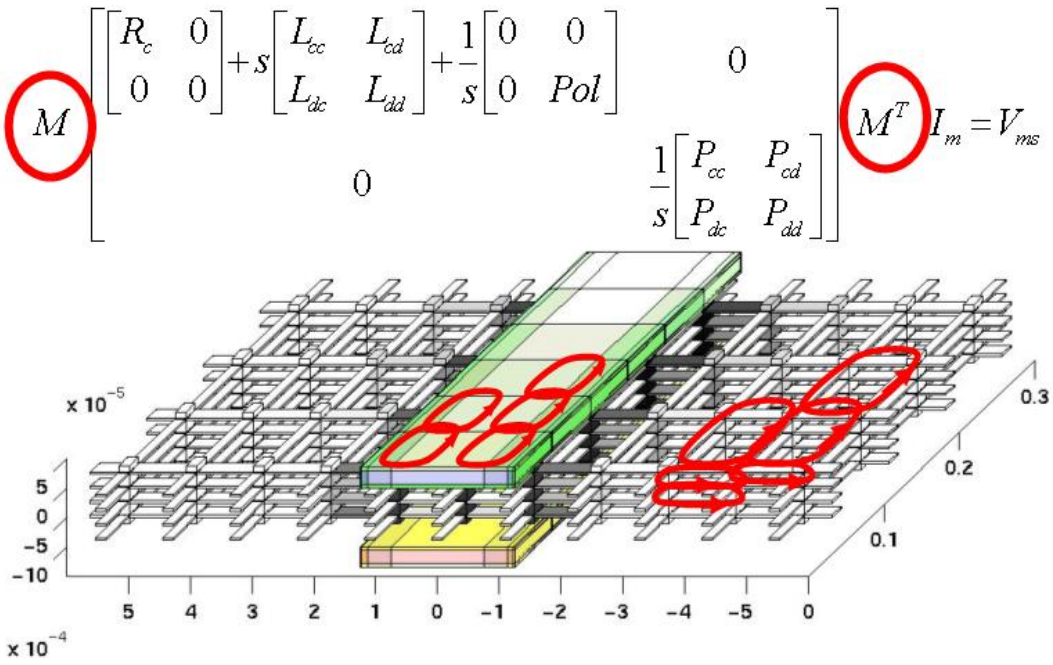

Figure 11.3: *In this picture we show a two conductors transmission line with a dielectric layer between the conductors. Both conductor and dielectric volumes are discretize. For visualization purposes the dielectric filaments are shown with cross-sections thinner than their actual values. Red circles indicate some of the KVL meshes uses to set up the linear system of equations shown above. Matrix M is a sparse matrix. Each raws represents one of such meshes.*

The two wires are shorted at one end, and driven at the other end. A dielectric layer with relative permittivity $\varepsilon_r = 4$ is present between the two wires, as shown in Fig. 11.6.

In Fig. 11.4 we show the frequency response of the line, with and without the dielectric layer. Incidently, in this picture one can immediately observe the importance of including dielectrics for correct resonance positions. For the case with the dielectric layer, we compare in the same Fig. 11.4 the solutions obtained by an enforced-potentials implementation and by a current-conservation mesh implementation. Similar results can be observed from the two approaches. The small difference can be mostly explained by calculating the condition numbers of the two implementations.

Fig 11.5 shows the condition number for the two implementations. The enforced-potentials implementation is poorly conditioned, and it appears very difficult to be preconditioned. A simple and very effective preconditioner, $[M\,\mathrm{diag}(Z_{cd})\,M^T]^{-1}$, can instead be given [66] for the current-conservation mesh formulation. The mesh approach is therefore more accurate, and presents faster convergence rates when used in an iterative solution algorithm.

11.3 Passive model order reduction for structures including dielectrics

In this Section, we will limit ourself to the usage of the quasi-static kernel in (11.6) which produces frequency independent L and P matrices in (11.13) and (11.14). The technique to handle dielectrics in [94] uses a similar quasi-static assumption, and seems more advantageous requiring fewer unknowns. However, not only magnetic coupling between conductive and polarization currents are neglected by that formulation, but also the matrices used in that formulation are not in the form required for Krylov-subspace based passive model-reduction schemes [97]. In this Section, we show instead an easy way to cast our mesh analysis

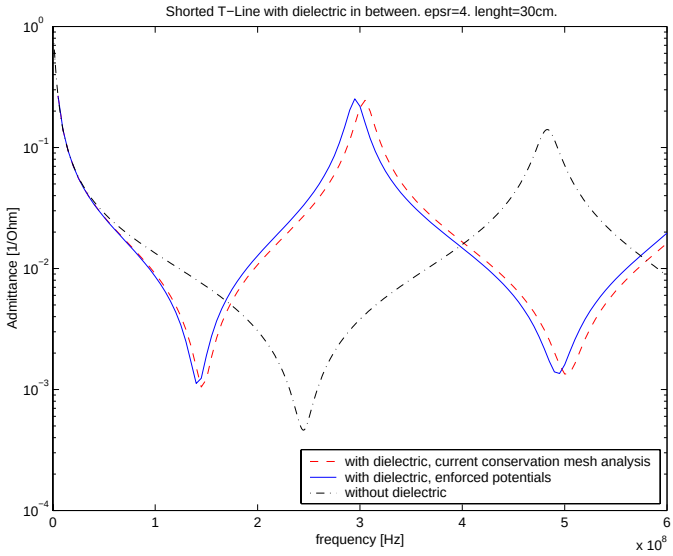

Figure 11.4: *Frequency response for the transmission line in Fig. 11.6. The enforced-potentials and the current-conservation mesh-analysis approaches give similar results even if not identical. The enforced-potentials method is less accurate because of its large condition number. Incidently, this figure also shows how the presence of dielectrics can significantly change resonances' positions.*

approach into the form in Theorem 6 in Section 9.1.2 suitable for passive reduced order modeling using algorithm PRIMA in Section 9.4.

Choose as state vector for a linear system representation:

$$x = \begin{bmatrix} I_m \\ Q_{cs} \\ Q_{ds} \\ Q_{dv} \end{bmatrix} \tag{11.20}$$

In view of this choice, we can rewrite (11.16) as shown in (11.19), where

$$\begin{bmatrix} Q_{cs} \\ Q_{ds} \\ Q_{dv} \end{bmatrix} = \begin{bmatrix} M_{pc}^T \\ M_{pd}^T \\ M_{fd}^T \end{bmatrix} \frac{I_m}{s}. \tag{11.21}$$

Or finally in linear system terms:

$$\hat{L}\frac{dx}{dt} = -\hat{R}x(t) + Bu(t) \tag{11.22}$$

$$y(t) = Cx(t) \tag{11.23}$$

where matrices $\hat{L}$ and $\hat{R}$ are defined as

$$\hat{L} = \begin{bmatrix} [M_{fc}M_{fd}]\,L\,[M_{fc}M_{fd}]^T & 0 & 0 \\ 0 & P^T & 0 \\ 0 & 0 & [Pol]^T \end{bmatrix} \tag{11.24}$$

$$\hat{R} = \begin{bmatrix} [M_{fc}M_{fd}]\,R\,[M_{fc}M_{fd}]^T & [M_{pc}M_{pd}]P & M_{fd}[Pol] \\ -P^T[M_{pc}M_{pd}]^T & 0 & 0 \\ -[Pol]^T M_{fd}^T & 0 & 0 \end{bmatrix} \tag{11.25}$$

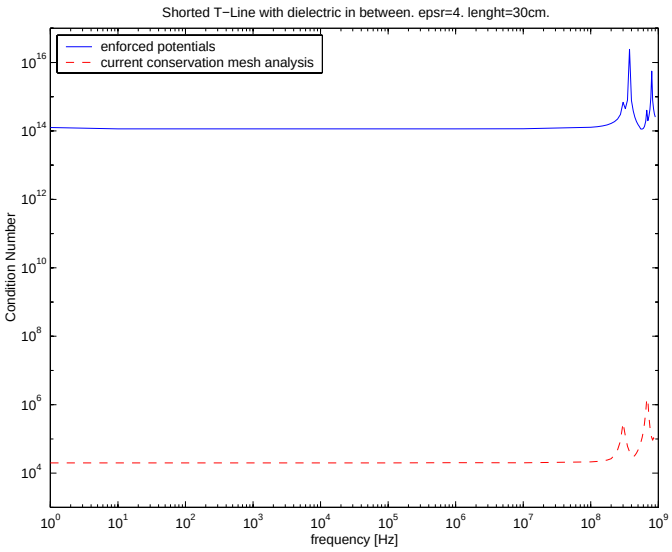

Figure 11.5: *The enforced-potentials approach generates a system with a very large condition number (continuous curve), and a good preconditioner is hard to derive. Very good preconditioners are easy to find instead for the current-conservation mesh approach. For instance the preconditioner* $(M\,\mathrm{diag}(Z_{cd})M^T)^{-1}$ *gives a very low condition number in the bottom of this figure (curve: - - -).*

$$[M_{fc}\,M_{fd}]\,[R+sL]\,[M_{fc}\,M_{fd}]^T\,I_m \;+\; [M_{pc}\,M_{pd}]\,P\,\begin{bmatrix} Q_{cs} \\ Q_{ds} \end{bmatrix} \;+\; M_{fd}\,[Pol]\,Q_{dv} = V_{m_s} \tag{11.19}$$

Vector $u(t)$ contains the excitation voltage sources, $Bu(t) = V_{ms}$. Vector $y(t)$ contains the observed output currents, derived through matrix C from the mesh currents I_m in the state vector $x(t)$. Note that for instance the second equation the system (11.22) can be easily derived from eq. (11.21) pre-multiplying it by matrix P^T.

Definition 11 *A matrix A is positive semi-definite if for any vector x,*

$$x^* Ax \geq 0. \tag{11.26}$$

Theorem 9 *Matrices* $\hat{L}+\hat{L}^*$ *and* $\hat{R}+\hat{R}^*$ *in (11.24) and (11.25) are positive semi-definite.*

Proof. The polarization matrix $[Pol]$ is diagonal with positive coefficients, hence it is positive semi-definite. When using a Galerkin technique [54], the coefficient of potential matrix P in (11.14) and the inductance matrix L in (11.13), are both positive semi-definite. The matrix $[M_{fc}\,M_{fd}]\,L\,[M_{fc}\,M_{fd}]^T$ is then also positive semi-definite. Since all the three blocks of the block-diagonal matrix $\hat{L}$ in (11.24) are positive semi-definite, $\hat{L}$ is positive semi-definite and so is $\hat{L}+\hat{L}^*$. This concludes the first part of the proof.

To prove that $\hat{R}+\hat{R}^*$ in (11.25) is positive semi-definite calculate:

$$\hat{R}+\hat{R^T} = \begin{bmatrix} 2\,[M_{fc}\,M_{fd}]\,R\,[M_{fc}\,M_{fd}]^T & 0 & 0 \\ 0 & 0 & 0 \\ 0 & 0 & 0 \end{bmatrix} \tag{11.27}$$

The resistance matrix R is positive semi-definite, hence the submatrix $2\,[M_{fc}\,M_{fd}]R[M_{fc}\,M_{fd}]^T$ is positive semi-definite and so is $\hat{R}+\hat{R}^*$.

Observation 1 *When modeling the input impedances and the transfer functions of a 3D structure, we apply input voltages at some ports, and we measure the resulting currents on the same set of ports, hence we are choosing* $C = B^T$ *in eq (11.22) and (11.23).*

Observation 2 *The matrix* $\hat{L}$ *is symmetric since L and P are symmetric when using a Galerkin discretization scheme (Section 3.3, Pol is diagonal.*

Observation 3 *From Theorem 9 and from Observations 1-2, one can conclude that the formulation in (11.22)-(11.25) satisfies to the conditions in Theorem 6 Section 9.1.2 for guaranteed passive Krylov subspace based model reduction PRIMA in Section 9.4*

11.4 Numerical implementation considerations

The most expensive operation in the model reduction algorithm with multipoint expansions is the computation of the quantity $[\hat{R} + s_0\hat{L}]^{-1}\hat{L}\,v$, where v is some known vector, and s_0 is any of the chosen frequency expansion points. A first observation is that one does not need to form explicitly matrices $\hat{L}$, or $\hat{R}$, nor it is necessary to explicitly invert matrix $[\hat{R} + s_0\hat{L}]$. In fact, one can evaluate the matrix-vector product $w = \hat{L}v$ using "fast-algorithms" for the subproducts within $\hat{L}v$ that involve the coefficients of potentials submatrix P [94, 110] and the inductance submatrix L [68]. Then, one can solve the system $[\hat{R} + s_0\hat{L}]z = w$ using Krylov subspace iterative methods, combined once again with fast-algorithms for the subproducts involving matrices P and L. A preconditioner for the matrix $[\hat{R} + s_0\hat{L}]$ can be found observing that

$$[\hat{R} + s_0\hat{L}] = \hat{P}^T \left[\hat{R}_k + s_0\hat{L}\right] \hat{P} \tag{11.28}$$

where

$$\hat{P} = \begin{bmatrix} I & 0 & 0 \\ 0 & P & 0 \\ 0 & 0 & [Pol] \end{bmatrix} \tag{11.29}$$

and

$$\hat{R}_k = \begin{bmatrix} [M_{fc}M_{fd}]\,R\,[M_{fc}M_{fd}]^T & M_{pc} & M_{pd} & M_{fd} \\ -M_{pc}^T & 0 & 0 & 0 \\ -M_{pd}^T & 0 & 0 & 0 \\ -M_{fd}^T & 0 & 0 & 0 \end{bmatrix} \tag{11.30}$$

Hence, for instance, one could use the following preconditioner where matrices $\hat{R}_k$, M_{fc}, and M_{fd} are all extremely sparse

$$[\mathrm{diag}(\hat{P}^T)]^{-1} \left(\hat{R}_k + s_0 \begin{bmatrix} [M_{fc}M_{fd}]\,\mathrm{diag}(L)\,[M_{fc}M_{fd}]^T & 0 & 0 \\ 0 & \mathrm{diag}(P^T) & 0 \\ 0 & 0 & \mathrm{diag}([Pol]^T) \end{bmatrix} \right)^{-1} [\mathrm{diag}(\hat{P})]^{-1} \tag{11.31}$$

As a second observation, one notices that a non-singular $\hat{R}$ would be necessary in order to be able to include also the point $s_0 = 0$ among the other expansion points. The matrix $\hat{R}$ in (11.25) can be written as

$$\hat{R} = \hat{P}^T \hat{R}_k \hat{P} \tag{11.32}$$

It can been shown [65] that $\hat{R}_k$ is non-singular (and therefore also $\hat{R}$ is non-singular) under the condition that there are no cut-sets of only capacitors. Unfortunately, each node in our dielectric discretization is such a cut-set when dielectric losses are negligible. Therefore, the point $s_0 = 0$ cannot be included in the multipoint expansion algorithm, and a non-zero low frequency expansion point is used instead. In the next section, we show that for the examples considered, this expansion point restriction is not interfering with accuracy.

11.5 Summary of our procedure

We summarize here briefly for the convenience of the reader the entire simulation procedure in its final form:

1. First, we discretize both the volumes and the surfaces of the conductors and dielectrics. An example is shown in Fig. 11.13.

2. We use a standard Galerkin technique [54] to construct matrices R, L, P, Pol in eq.(11.12) to (11.15).

3. A mesh analysis approach is used to construct the sparse KVL's matrices M_{fc}, M_{fd}, M_{pc}, and M_{pd} in (11.18). More details on how to handle conductors are in [66]. For the dielectrics, we use a minimum spanning tree to find a set of independent meshes.

4. A Krylov subspace based model reduction algorithm such as [97] is then used to produce reduced order linear system models. At each step of the algorithm the quantity $[\hat{R} + s_0\hat{L}]^{-1}\hat{L}v$, could be computed using fast matrix vector products and Krylov subspace iterative methods.

5. The reduced order model is then used to obtain a plot of the frequency response, or to produce an equivalent SPICE circuit for a time domain simulation including the non-linear circuitry.

The overall complexity of this procedure is $O(N_m\, nlog(n))$, where N_m is the total number of moments matched by the model reduction algorithm at all frequency expansion points. n is the size of the original full linear system model in (11.22)-(11.23), or about the number of basis functions used in the volume and surface discretization.

11.6 Examples

11.6.1 A transmission line example

Two PCB wires are considered in this example in a transmission line configuration. Wires are located on opposite sides of a dielectric substrate, and shorted at one end.

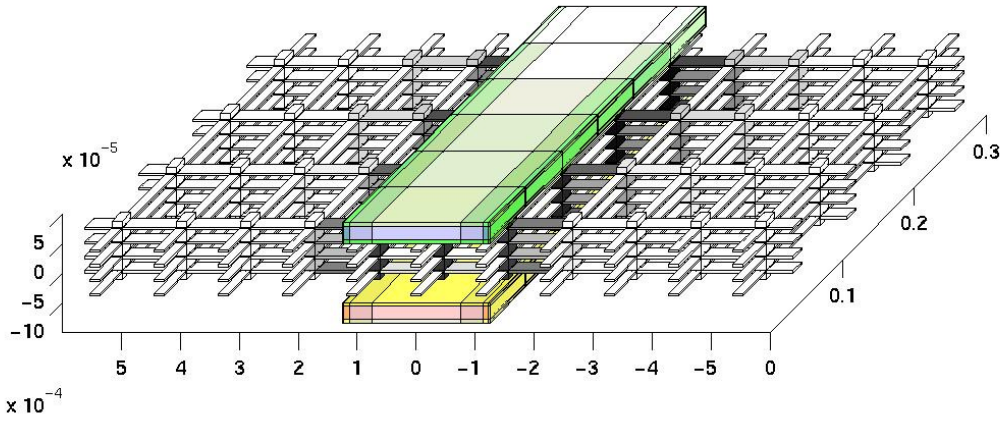

Figure 11.6: *Two PCB wires (250μm x 35μm x 30cm). A 100μm thick dielectric layer ($\varepsilon_r = 4$) is present between the two wires. This figure also shows the dielectric volume discretization. The intensity of the shadings is associated with current densities near the first quarter wavelength resonance.*

Fig 11.7 shows the frequency response of such transmission line structure. In Fig 11.7 we also show the response of the calculated reduced order model. When building the reduced order model, we used multi-point expansions matching four moments around each of the following frequencies: $s_1 = j2\pi 5\text{KHz}$, $s_2 = j2\pi 250\text{MHz}$, and $s_3 = j2\pi 500\text{MHz}$. The low frequency expansion point $s_1 = j2\pi 5\text{KHz}$ captures correctly the DC behavior as shown in the "zoomed" picture at very low frequencies in Fig. 11.8.

At the frequencies where the frequency independent kernel in (11.6) yields accurate results, it may also be reasonable to neglect magnetic coupling between conductors and dielectric polarization currents. However there are cases where even with a non-fullwave kernel one might observe some effects of the magnetic coupling between dielectric polarization currents and conductors. One of such cases is illustrated in Fig. 11.10. A via is located in proximity of the shorted PCB transmission line.

The line is then excited at a frequency close to the first quarter-wavelength resonance. In this situation most of the current closes its path through the dielectric layer in the form of polarization currents. If a nearby via corresponds to a quiet victim line, some coupling can be observed between the vertical polarization currents and the via.

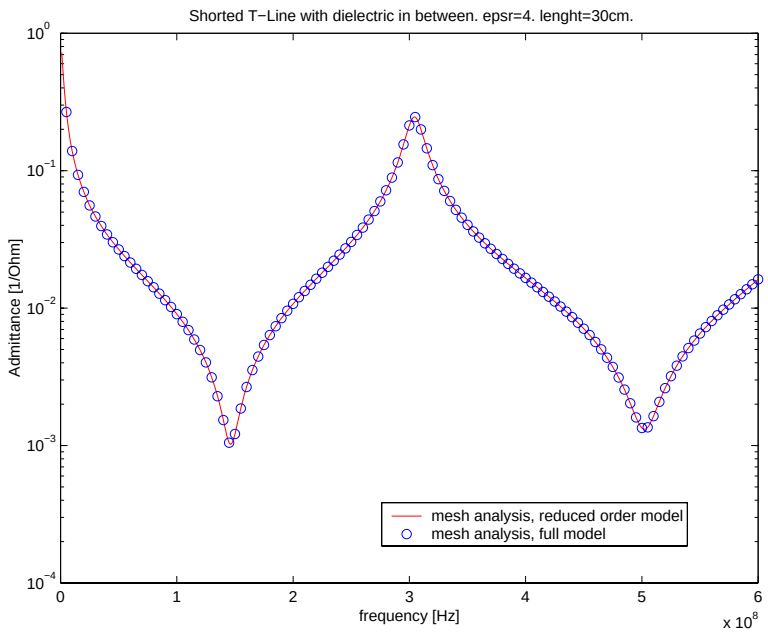

Figure 11.7: *Reduce order modeling of a shorted PCB transmission line. Wires' dimensions are 250µm x 35µm x 30cm. A* 100*µm thick dielectric layer* ($\varepsilon_r = 4$) *is present between the two wires. The continuous line is the admittance vs. frequency of the calculated reduced model. The circles are the response of the original system.*

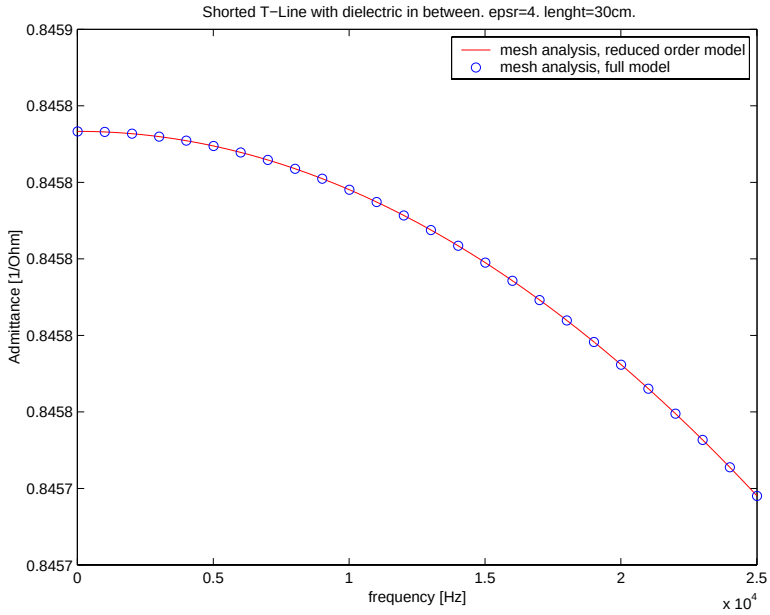

Figure 11.8: *"Zoom" on the DC frequency response in Fig. 11.7 to verify that the reduced model (continuous line) captures correctly the DC behavior of the original system (circles).*

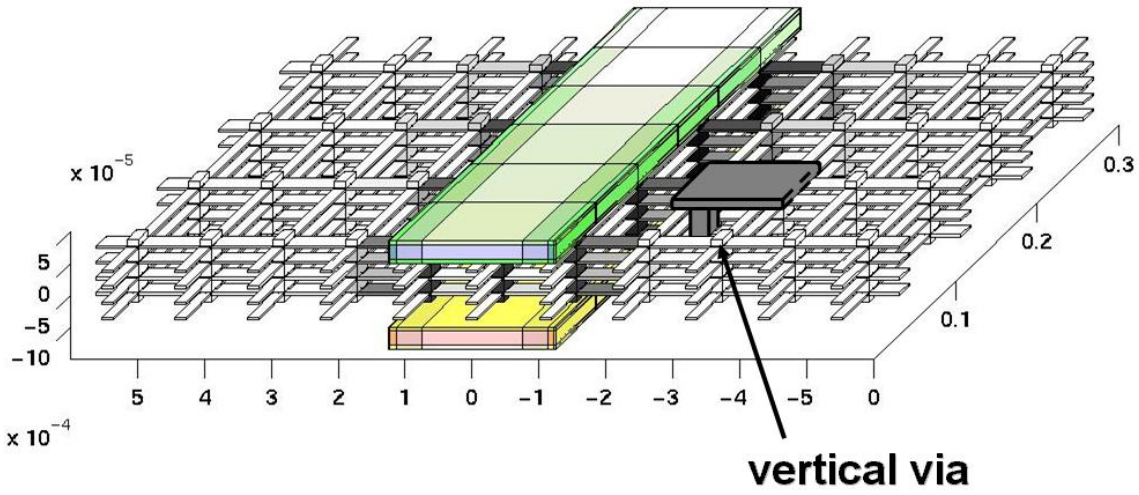

Figure 11.9: *A via is located in proximity of the shorted PCB transmission line.*

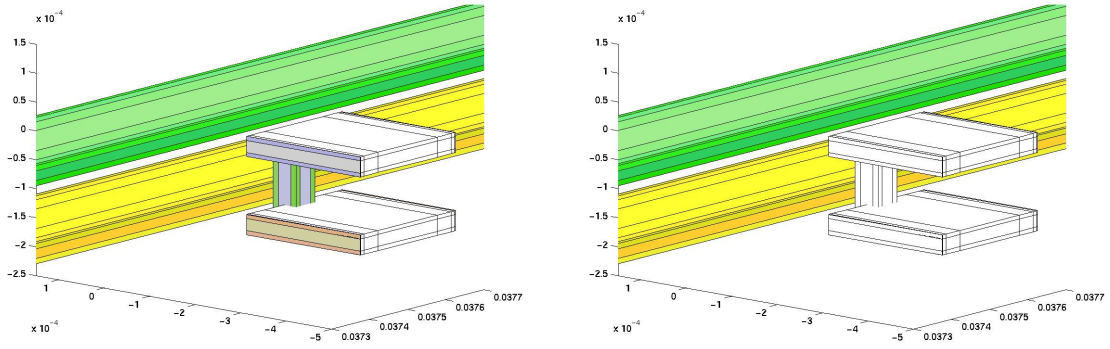

Figure 11.10: *Via located near a PCB transmission line. In this picture we do not show the dielectric layer which is located between the two dark PCB transmission line wires. Shadings correspond to current density amplitudes. On the left we show the current densities corresponding to the case where magnetic coupling between polarization currents and conductors is accounted for. On the right we show the same example but setting* $L_{dc} = 0$ *and* $L_{dd} = 0$ *in (11.13) which corresponds to neglecting magnetic coupling between polarization currents and conductors.*

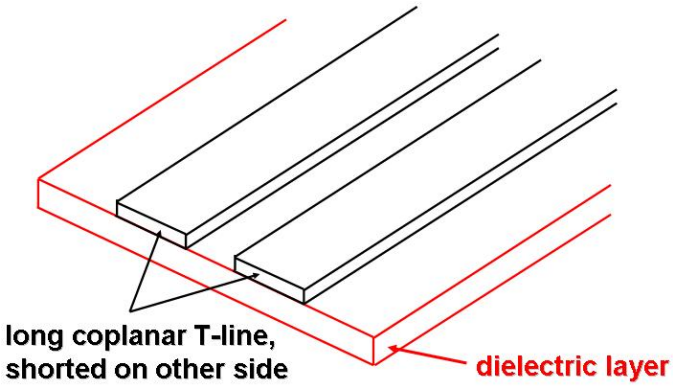

Figure 11.11: *Two wire coplanar transmission line. Wires are 250μm wide, 35μm thick, and 30cm long. The two wires are shorted at one end. A dielectric layer with relative permittivity $\varepsilon_r = 4$ is present below the two wires. Some of the dielectric volume discretization is also shown. A complete 3D grid is used with filaments in all directions, but in this picture we only show the dielectric filaments parallel to the conductor wires.*

11.6.2 A second example: coplanar transmission line

In a second example we analyze another typical scenario in todays electronic circuits. A two-conductors coplanar transmission line is shown in Fig 11.11. Wires have the same dimensions as in the previous example. Their separation is 150μm. The same dielectric layer of the previous example is this time underneath the two wires. Fig 11.12 shows the frequency response of the reduced order model compared to the response of the original system.

11.6.3 MCM interconnect example

In a third example, we have applied our technique to analyzing two wires of an interconnect bus on an Multi-Chip Module (MCM), as shown in Fig. 11.13.

A dielectric layer ($\varepsilon_r = 4$) is present underneath the wires and the chips. In Fig. 11.14 we show the frequency response of the two interconnects when shorted on one side and driven on the other. We show the frequency response with and without the dielectric substrate. A significant difference in the resonance position can be observed. Fig. 11.13 shows the polarization volume currents at the first resonance $f = 3$GHz. In Fig. 11.14 we compare the reduced order model to the full model for the case when the dielectric substrate is present. The reduced order model has been built matching four moments around each of the following expansion points: $s_1 = j2\pi 100$KHz, $s_2 = j2\pi 3$GHz, and $s_3 = j2\pi 6$GHz. In order to include also the point $s_0 = 0$ among the other expansion points a non-singular $\hat{R}$ in (11.25) would be necessary. The matrix $\hat{R}$ in (11.25) can be written as

$$\hat{R} = \hat{P}^T \hat{R}_k \hat{P} \tag{11.33}$$

It can been shown [65] that a matrix of the form such as in (11.25) is non-singular under the condition that there are no cut-sets of only capacitors. Unfortunately, each node in our dielectric discretization is such a cut-set when dielectric losses are negligible. Therefore, for lossless dielectrics the point $s_0 = 0$ cannot be included in the multipoint expansion algorithm, and a non-zero low frequency expansion point is used instead. From our experiments, we have observed that this expansion point restriction is not interfering with accuracy. For instance in this particular example, the zero frequency behavior of the structure has been accurately captured as shown in Fig. 11.15, which is a magnified view of the low frequency part of the plot in Fig. 11.14,

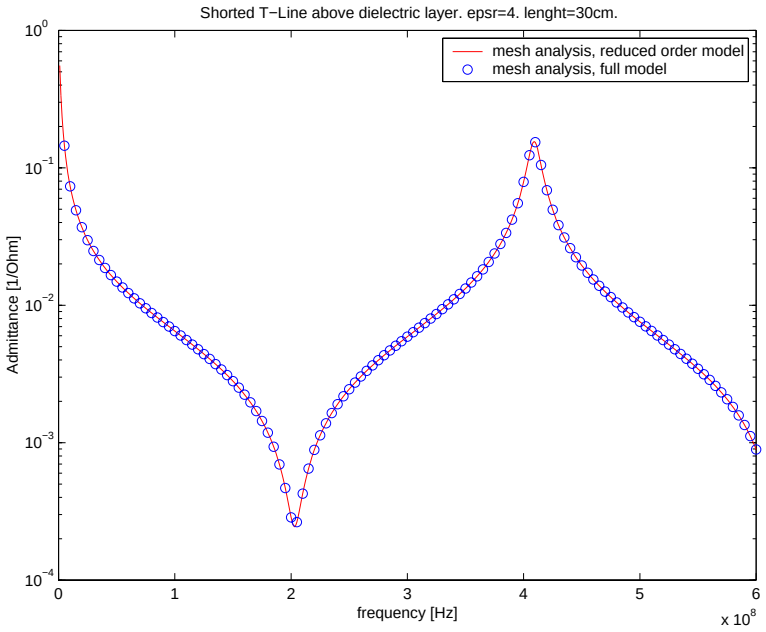

Figure 11.12: *Frequency response of the coplanar transmission line over a dielectric layer shown in Fig. 11.11. The continuous line is the response of the reduced model which compares quite nicely with the response of the original system shown by the small dots.*

11.7 Conclusions on passive model order reduction including dielectrics

In this Chapter we described applying the mesh analysis approach to solving for the discretized currents and charges in a VIE formulation for structures including dielectrics. We showed that the approach leads to a system with provably positive semi-definite matrices, making for easy application of Krylov-subspace based model-reduction PRIMA (Section 9.4) to generate accurate guaranteed passive reduced-order models. Several printed circuit board examples demonstrated the effectiveness of the strategy.

Arguably, it is tempting to assume that the VIE approach is a step backward, as it involves discretizing volumes instead of surfaces. However, volume integral equation methods are used for magnetic analysis of conductor problems, because conductors occupy a vanishingly small region of the problem domain. The same vanishingly small occupancy argument can be made for dielectrics as well. In addition, since polarization currents are not "outputs", it might be possible to align them with a regular grid. Such an alignment might improve the performance of fast solvers, such as the Conjugate Gradient FFT (CGFFT) [124] or Precorrected-FFT [110] methods, an important consideration as such solvers are required when using any integral formulation on models with complicated geometries.

A more efficient way to model dielectrics is to use special Green functions or to use Surface Integral Equation (SIE) methods. Both such approaches generate dynamical linear systems with frequency dependent matrix descriptors $[E(s), A(s)]$ (distributed systems). In the next Chapter 12 we develop an algorithm for guaranteed passive reduction of such systems.

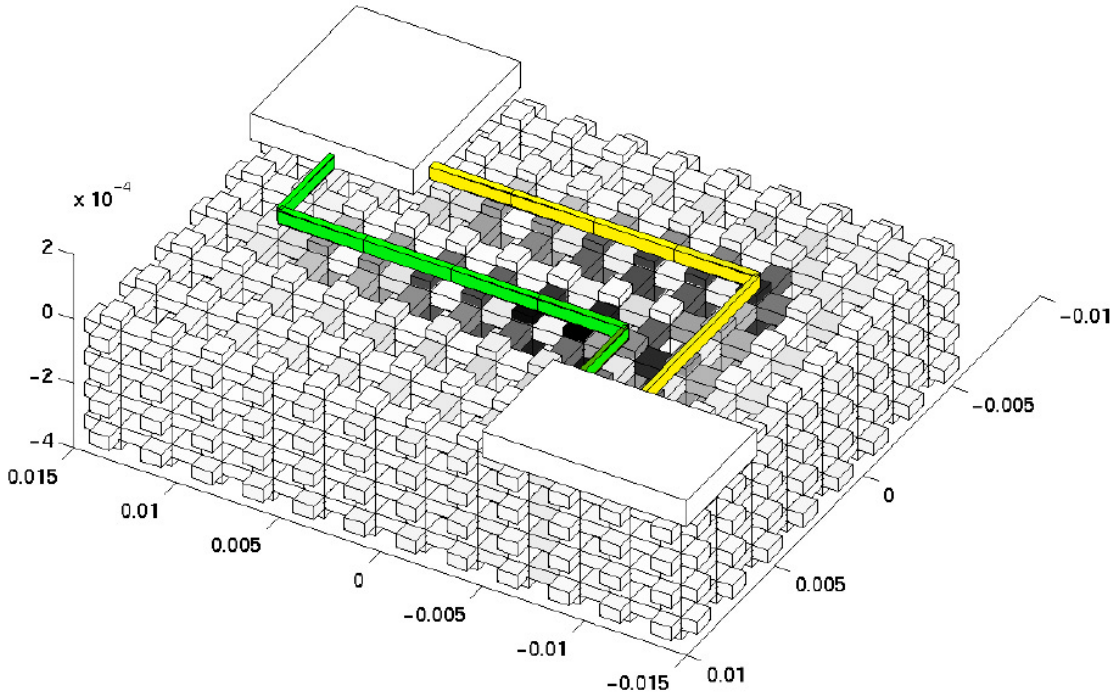

Figure 11.13: *Two wires part of an MCM interconnect system (figure above). A dielectric layer* $\varepsilon_r = 4$ *is present underneath the wires and the chips. The figure below shows the volume polarization currents inside the dielectric layer at the 3GHz resonance. For visualization purposes, the axes in this picture are not "to-scale". Wires are 2cm long, 4mm far apart, 250µm wide and 40µm thick.*

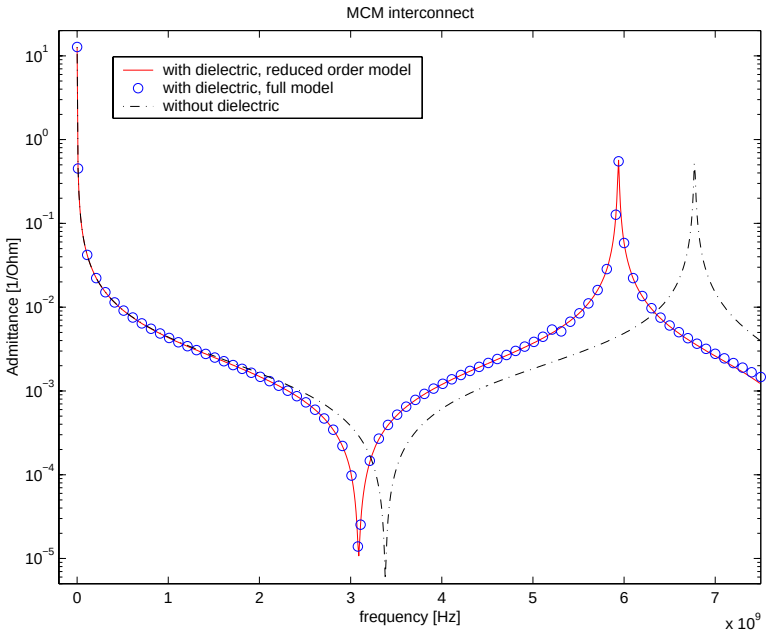

Figure 11.14: *Admittance vs. frequency for the two wires in Fig. 11.13.*

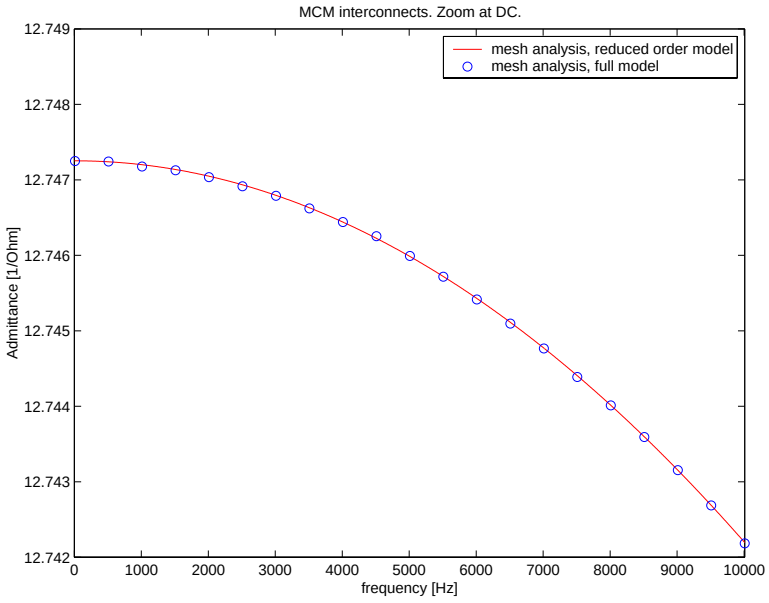

Figure 11.15: *Magnified view of the low frequency part of the plot in Fig. 11.14, to verify that the reduced model (continuous line) captures correctly the DC behavior of the original system (circles).*

Chapter 12

Preserving passivity when reducing distributed systems

The work in this Chapter has been done in collaboration with Dr. Joel Phillips during an internship at Cadence Berkeley Labs, Berkeley, CA and it has first appeared in [33].

"Lumped" RLC circuits, can be typically represented by matrices that are independent of frequency. For such lumped systems, positive-realness preserving procedures such as those based on congruence transforms [97] and presented in Section 9.4 are sufficient to guarantee that the reduced models of passive full systems are passive as well. *However, when accounting for high frequency effects, "distributed" systems represented by frequency dependent matrices are typically encountered.* For example, frequency dependent matrices are generated by integral-equation based field solvers that employ full-wave kernels, special Green functions for lossy dielectrics/substrates, or frequency dependent basis functions [37].

There are several approaches to distributed model reduction that essentially convert the model reduction problem to an interpolation or data-fitting problem [25, 28] (and Section 7.5), where it is irrelevant whether the original systems is distributed or lumped. In our experience all of the data-fitting like approaches are limited in some aspect, and to the best of our knowledge, there is no approach that can simultaneously guarantee good model accuracy, numerically stable and computationally practical generation of models of arbitrary order, generation of models that are "well-behaved" when embedded into a simulation tool with models of other physical elements. Krylov-based model reduction schemes for lumped systems [97] (and in Section 9.4), on the other hand, routinely satisfy all these conditions, so we desire to extend their capabilities to distributed systems.

As input, our algorithm takes a time-invariant state-space-like frequency-domain model whose matrix descriptors may be a function of frequency. As output, it produces a time-invariant state-space model with frequency independent matrix descriptors and whose transfer function is a rational approximant of the original (infinite-order, possibly irrational) transfer function. The algorithm requires only matrix-implicit operations such as matrix-vector products, hence it is suitable for incorporation into modern fast integral equation solvers.

12.1 Distributed systems in descriptor form

Assume the original distributed system (e.g. an interconnect network) has been described, for instance by the discretization step of an integral equation method, in terms of a frequency dependent matrix $Z(s)$. $Z(s)$ describes the couplings between all the discretization basis functions and may be very large in the applications of interest. Many integral equation methods, when applied to distributed systems, produce $Z(s)$ as a linear combination of matrices. One example is $Z(s) = R(s) + sL(s)$, where $R(s)$ and $L(s)$ can still be in general frequency dependent. Incidentally this particular form for $Z(s)$ may be advantageous for our

approach, although in general not necessary. We assume input and output information is of interest at some "ports" of the network for which the model is to be generated. The frequency-domain description of the system can be written as

$$[R(s) + sL(s)]i_m(s) = Bv_p(s), \quad i_p(s) = B^T i_m(s), \tag{12.1}$$

where $v_p(s) \in \mathbf{C}^p$ and $i_p(s) \in \mathbf{C}^p$ are Laplace-domain representations of voltages and currents at the p defined ports of interest, $i_m(s) \in \mathbf{C}^n$ are the internal currents, and $B \in \mathbf{R}^{n\times p}$ is a matrix relating ports to internal currents. In this case $u = v_p$ represents the system inputs (voltages), $y = i_p$ the system outputs (currents), and $x = i_m$ the internal states (also in this case currents). The transfer function from inputs to outputs is $H(s) = B^T[R(s) + sL(s)]^{-1}B, \quad i_p(s) = H(s)v_p(s)$, and one view of model reduction is that it seeks an approximation to the transfer function $H(s)$. For instance, they could represent the resistance and partial inductance matrices of a set of piece-wise constant basis functions (see Section 3.3.1 used to discretize conductor volumes in a Mixed Potential Integral Equation approach (MPIE) with a frequency dependent kernel. Such a case is found for instance using the full-wave kernel in the Partial Element Equivalent Circuits (PEEC) approach [121]. They could represent the matrices generated in method-of-moments integral equation codes when using Green function approaches to handle dielectrics or lossy substrates [24], in either a full-wave or quasi-static setting. The matrices $R(s)$ and $L(s)$ could also represent the resistance and partial inductance matrices of frequency dependent NON-piecewise constant basis functions used to discretize the MPIE formulation. The conduction modes basis functions presented in Chapter 4 are such an example.

In the form of Equation (7.2) the analogies to lumped systems are obvious : lumped systems can always be put into the form (7.2) in a way such that $R(s)$ and $L(s)$ are constant independent of s.

12.2 The optimal global interpolation approach

To illustrate some of the problems encountered in model reduction for distributed systems, consider the algorithm presented in [107]. The central approach of the algorithm is a Taylor expansion of the system matrix descriptor $Z(s) \approx \sum_{k=0}^{N} Z_k s^k$, using polynomials as interpolants. A standard Krylov method is then applied to a system constructed from the Taylor expansion. This approach does not generate well-behaved models because the Taylor approximation is not *globally* well-behaved. In fact, all polynomials diverge in the $s \to \infty$ limit. Hence, although good accuracy can be achieve in a given frequency band of interest, *global* properties such as positive-realness cannot be guaranteed. Empirically, the resulting reduced models are often found to have unstable poles, the models are not passive, and thus the algorithm is of little practical value.

In our approach, we will seek to combine approximation of the $Z(s)$ internal matrix descriptors with a Krylov method as in [107]. However, our method differs in the following fundamental aspect.

12.2.1 The key idea

Almost all systems for which one would wish to extract reduced models are non-ideal (non-ideality is why they must be modeled in detail) and so contain a small amount of loss. These systems are strictly passive and can typically be described by strictly positive real system matrices.
The key idea of our algorithm is based on the observation that **if a system descriptor is strictly positive-real to begin with, a *globally* and *uniformly* convergent interpolant will eventually (for a large enough order of the interpolant) be positive-real as well.** (This will be seen in the proof of Theorem 10.) Furthermore, a well-chosen global interpolant will be positive-real for low enough orders to be practical. Local approximations based on Taylor and Padé typically do not have these properties.

There is one more point, subtle yet of great importance, that we wish to underline before proceeding with the main algorithm. In our algorithm, as in others [97], we require that, not only the transfer function $H(s)$ of the given large system be strictly positive-real, but also that its internal system matrix descriptor $Z(s)$ be strictly positive real (i.e. that the state-space description be internally positive-real). However, as discussed in Section 9.3 in a physical system, $H(s)$ must also be causal. Hence, as for the the positive realness property, we shall require that not only the transfer function $H(s)$ of the given large system be strictly positive-real *and*

causal but also that its internal system matrix descriptor $Z(s)$ be strictly positive real *and causal* (i.e. that the state-space description be internally positive-real *and causal*). In this case we can restrict our search for approximations of $Z(s)$ to the set of stable, positive-real interpolants. For non-causal $Z(s)$, either accuracy or stability/passivity would have to be eventually sacrificed.

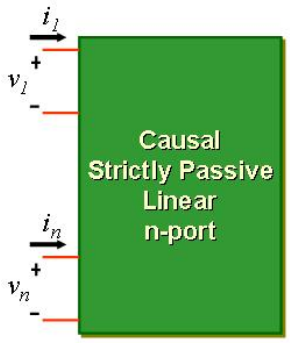

Figure 12.1: *Assumptions.*

12.2.2 Proposed algorithm

We propose an eight step procedure, which we term **G**lobal **R**ational **I**nterpolation, **P**assive (GRIP):

1. Obtain/estimate/given a set of q points at which the transfer function at the network ports $H(s) \in \mathbf{C}^{p\times p}$ is to be matched,
2. Compute the basis $U_q \in \mathbf{C}^{n\times q}$ for the projection operation (see Section 8.1).
3. Project the internal system matrices $R(s), L(s) \in \mathbf{C}^{n\times n}$ to obtain smaller $\hat{R}(s), \hat{L}(s) \in \mathbf{C}^{q\times q}$ as in Fig. 8.2). Note that this is a conceptual operation; the reduced matrices are still frequency-dependent, so the system is still of potentially infinite order.
4. Perform a *global* and *uniform* interpolation of the (projected) internal system matrices $\hat{R}(s), \hat{L}(s)$ (see Section 12.3).
5. Check the passivity (see [5]), and accuracy of the matrix interpolants. If not passive, or if matrix interpolants are not accurate, go to Step 4 and increase the order N of the global interpolant.
6. Check the accuracy of the reduced model transfer function $\hat{H}(s)$. If not accurate, go to Step 1 and add additional matching points q.
7. Realize as state-space system.
8. Perform a second-stage guaranteed-passive optimal reduction step, if desired [108].

Steps 1,2,3, and 6 are standard in lumped-system model reduction. Various approaches are possible, and many are described in the literature. As they are not the main focus here, they will not be discussed further. Step 5 can be performed solving the Lur'e equation in the Positive-Real Lemma [5], for which computational procedures are available in the literature [5]. Step 7 is dependent on how Step 4 is performed, but is always possible if Steps 4-6 are feasible.

It can be noticed that our algorithm is posed in such a way that if it terminates, accuracy, stability, and passivity are guaranteed. However, we have not yet shown that it is possible to construct specific instantiations that *will* terminate. Such task is equivalent to finding for the key Step 4 a suitable interpolant that is guaranteed to converge globally and uniformly. To this purpose, in the next Section, one possible choice will be described.

	Matrix sizes	System order
Start from original system described by causal, strictly positive-real matrices	~ 500,000	infinite
1) Projection (squash matrix sizes with congruence transformation which preserves positive-realness)	~ 20	infinite
2) Interpolation (capture matrix frequency dependency with uniformly convergent basis functions)	~ 20	~ 100
3) Realization of a dynamical linear system	~ 100	~ 100
4) Further reduction (e.g. see passive truncated balance)	~ 10	~ 10

Figure 12.2: *The "Grip".*

12.3 A Laguerre-basis implementation

12.3.1 Choosing the global uniform interpolant

Several approaches are possible to the global interpolation problem. One possibility is to use algorithms developed for general-purpose interpolation or data-fitting [28] that guarantee passivity by construction. These algorithms are very computationally demanding. For many applications of interest, a simpler alternative is available. First, it is advantageous (although not necessary) to find some decomposition of matrix $Z(s)$ into for instance some matrices $R(s)$ and $L(s)$ for which the individual matrix entries do not have sharply discontinuous behavior in the frequency parameter s. Many integral-equation-based electromagnetic field solvers for distributed systems already produce such a decomposition. In order to use our method, particular attention will need to be dedicated to making sure that such solvers generate strictly positive-real and causal system matrices.

Second, the frequency dependency of projected matrices $\hat{R}(s)$ and $\hat{L}(s)$ in Fig.8.2 can then be captured for instance using the set of basis functions [149], $E_k(s) = \left(\frac{\lambda - s}{\lambda + s}\right)^k$, where λ is a positive real number. In this way we can write:

$$\hat{R}(s) = \sum_{k=0}^{\infty} \hat{R}_k E_k(s), \qquad \hat{L}(s) = \sum_{k=0}^{\infty} \hat{L}_k E_k(s). \tag{12.2}$$

The basis created by the functions $E_k(s)$, sometimes called the Laguerre basis, is a member of a larger family [96] of basis, all of which consist of sets of stable rational functions orthonormal over the imaginary axis $s = j\omega$. An interesting contrast with the Taylor series approach is that the $E_k(s)$ are, in a sense, band-limited. For $|\omega| > \lambda$, the $E_k(s)$ have monotonic magnitude, and for $|\omega| < \lambda$, they are nearly equi-ripple, much like Chebyshev polynomials. This implies that with suitable choice of λ, the approximations to $R(s), L(s)$ will be well behaved outside the approximation interval, and convergence will be fast within it.

The Laguerre basis is particularly interesting because, under the bilinear transformation, $s = \lambda(1-z)/(1+z)$, the series expansion in terms of the basis functions $E_k(s)$ is mapped to a Fourier series of complex exponentials, since $E_k(s) = z^k$, where $z = e^{i\phi}, \phi \in [0, 2\pi)$. The problem of rationally approximating the matrix functions $\hat{R}(s), \hat{L}(s)$ is reduced to the problem of approximating a function on the circle via a Fourier series, or equivalently computing a Discrete Fourier Transform (DFT), as the entries of $\hat{R}(s), \hat{L}(s)$ may be approximated term-wise.

12.3.2 Global uniform convergence

If the entries of $\hat{R}(s), \hat{L}(s)$ are smooth when mapped to the circle, then the partial sums

$$\hat{R}^{(N)}(s) = \frac{1}{N}\sum_{k=0}^{N-1} \hat{R}_k z^k, \qquad \hat{L}^{(N)}(s) = \frac{1}{N}\sum_{k=0}^{N-1} \hat{L}_k z^k. \tag{12.3}$$

converge uniformly to $\hat{R}(s), \hat{L}(s)$. If $\hat{R}(s), \hat{L}(s)$ are not smooth, but are continuous, it is still possible to obtain uniformly convergent approximates by summing the Fourier series in the sense of Cesaro [7]. Practically speaking, this means replacing the summations (12.3) by

$$\tilde{R}^{(N,C)}(s) = \frac{1}{N}\sum_{k=0}^{N-1} \hat{R}_k \left[1 - \frac{k}{N}\right] z^k, \qquad \tilde{L}^{(N,C)}(s) = \frac{1}{N}\sum_{k=0}^{N-1} \hat{L}_k \left[1 - \frac{k}{N}\right] z^k. \tag{12.4}$$

Equivalently, we may say that as successive approximates, we take the arithmetic means of the partial sums $\hat{R}^{(N)}(s), \hat{L}^{(N)}(s)$, rather than the partial sums themselves. Summation in this manner has the property of suppressing the Gibbs effect, and also ensuring uniform convergence on a broader class of functions.

Lemma 10 *If the entries of $\hat{R}^{(N)}(s), \hat{L}^{(N)}(s)$ are continuous when mapped to the circle, $\tilde{R}^{(N,C)}(s), \tilde{L}^{(N,C)}(s)$ converge uniformly to $\hat{R}^{(N)}(s), \hat{L}^{(N)}(s)$ as $N \to \infty$ [7].*

Shortly we will need the following definitions:

Definition 12 (Strong-η condition) $\Pi_{\hat{Z}}$ *is Strongly-η if $\Pi_{\hat{Z}}(s) - \eta I \geq 0$ for any $\eta > 0$.*

where $\Pi_{\hat{Z}}(s) \equiv \hat{Z}(s) + \hat{Z}^*(s)$ was defined by eq. (9.8) in Section 9.1.

Definition 13 (Weak-η condition) $\Pi_{\hat{Z}}$ *is Weakly-η if for any $\varepsilon \geq 0$, there is an $\eta > 0, \eta < \varepsilon$ s.t. $\Pi_{\hat{Z}}(s) + \eta I > 0$.*

From Lemma 10 we obtain a major result of this chapter:

Theorem 10 *Given a system description $\hat{Z}(s) = \hat{R}(s) + s\hat{L}(s)$ where matrices $\hat{R}(s)$ and $\hat{L}(s)$ are causal, strictly positive real, and continuous on the imaginary axis, there exists an integer N and coefficients $\tilde{R}_k^{(N,C)}, \tilde{L}_k^{(N,C)}$ for the partial sums in (12.4) such that the matrix rational function $\tilde{Z}(s) = \tilde{R}^{(N,C)}(s) + s\tilde{L}^{(N,C)}(s)$ is a positive-real rational interpolant of $\hat{Z}(s)$ whose error can be bounded from above by any chosen positive constant.*

Proof. Using Definition 5 in Section 9.1, property (9.6) follows by construction as the E_k satisfy (9.6). Property (9.7) also follows by construction, since by inspection the E_k have poles only in the left half-plane. Thanks to Theorem 4, in order to complete this proof it is now sufficient to show condition (9.12).
Case 1: Π_Z is Strongly-η. From Lemma 10, if $\hat{R}(s)$ and $\hat{L}(s)$ are continuous when mapped to the circle, $\tilde{R}^{(N,C)}(s), \tilde{L}^{(N,C)}(s)$ converge uniformly and so does $\tilde{Z}(s) = \tilde{R}^{(N,C)}(s) + s\tilde{L}^{(N,C)}(s)$. Thus $\forall \eta > 0$, $\exists N$ s.t. $||\tilde{Z}(j\omega) - \hat{Z}(j\omega)||_2 < \eta/4$, $\forall \omega \in \mathbf{R}$. Hence

$$||\Pi_{\tilde{Z}}(j\omega) - \Pi_{\hat{Z}}(j\omega)||_2 \leq 2||\tilde{Z}(j\omega) - \hat{Z}(j\omega)||_2 \leq \eta/2, \ \forall \omega \in \mathbf{R}. \tag{12.5}$$

since

$$\Pi_{\tilde{Z}}(j\omega) > \Pi_{\hat{Z}}(j\omega) - ||\Pi_{\tilde{Z}}(j\omega) - \Pi_{\hat{Z}}(j\omega)||_2 > \eta - \eta/2, \tag{12.6}$$

then[1] $\Pi_{\tilde{Z}} > \eta/2$ and $\Pi_{\tilde{Z}}$ is Strongly-η, which implies (9.12) (see [145]). Thus $\tilde{Z}$ is strictly positive-real.
Case 2: $\Pi_{\hat{Z}}$ is [strictly] positive-real but not Strongly-η. Choose any $\eta > 0$ and Map $\hat{Z} \to \hat{Z} + \eta I$. $\hat{Z}$ is now Strongly-η. Go to Case 1. [2]

[1] In this we needed to use the result that perturbations of a Hermitian matrix ($\Pi_{\hat{Z}}$) result in perturbations of the eigenvalues bounded by the 2-norm of the perturbation.

[2] The upshot of all this is that the Strongly-η condition is slightly stronger than strict positive-realness and may not be satisfied for all strictly passive systems. However, by introducing an additional error of $O(\eta)$ (i.e., roughly doubling the

Theorem 10 proves that an order of interpolation N large enough *does exist* and therefore that the algorithm in Section (12.2.2) terminates. A practical algorithm would require a small N. The order of the interpolant is related to the smoothness of the function being approximated. Hence, although we could use this algorithm to approximate $H(s)$ or $Z(s)$ directly, that would require evaluation of an awful lot of matching points around resonances, and most likely a very large order of the interpolant. A small N is instead needed when the algorithm is used on some internal decomposed matrices $R(s)$ and $L(s)$ which are almost always continuous within a given band of interest. Out-of-band non-smoothness (for example, for delay functions, which create essential singularities at ∞) can be insured by filtering operations which must be designed to preserve passivity and causality of the original matrices.

12.3.3 Computing the DFT coefficients

The DFT coefficients in the sums (12.3) can be efficiently calculated for instance using a Fast Fourier Transform (FFT) algorithm. Hence the steps for one possible global approximation procedure are

1. For a desired interpolation order N, choose the size M of the FFT as some power of two: $M = 2^n > N$.
2. Calculate the frequency points s_k on the imaginary axis corresponding to the M equally spaced FFT points
   $z_k = exp(j2\pi k/M)$, $k = 1,\ldots,M$ on the unit circle using the bilinear transform: $s_k = \lambda(1-z_k)(1+z_k)$, where $\lambda = 2\pi f_0$ is a parameter to be chosen around the center of the frequency band of interest for the system response.
3. Use the projection in Fig.8.2 to evaluate each individual projected matrix $\hat{R}(s_k)$ and $\hat{L}(s_k)$ at the selected frequency points s_k, $k = 1,\ldots,M$.
4. Use an FFT algorithm to calculate the M coefficients $\hat{R}_k$ and $\hat{L}_k$ in (12.3) from the sequences $\hat{R}(s_k)$ and $\hat{L}(s_k)$, $k = 1,\ldots,M$.
5. Apply to each of the M FFT coefficients the Cesaro's transformation in (12.4) and obtain the coefficients $\tilde{R}_k$ and $\tilde{L}_k$.

Note that, since the $R(s)$ and $L(s)$ matrices usually satisfy conjugate symmetry relations, $R(s), L(s)$ need to be evaluated at only half the points on the circle. Also, once the M Cesaro's FFT coefficients are available one can construct at no additional cost several interpolants of increasing order $N < M/2$ simply truncating the sums in (12.4) to the first N coefficients.

12.3.4 Realization

In this section we describe how to perform Step 7 in the general algorithm 12.2.2, realization as a state-space model. Having performed the global rational approximation on the projected matrix functions $\hat{R}(s)$ and $\hat{L}(s)$, the system (7.2) is now:

$$\left[\frac{1}{M}\sum_{k=0}^{N-1}\tilde{R}_k z^k + \lambda\left(\frac{1-z}{1+z}\right)\frac{1}{M}\sum_{k=0}^{N-1}\tilde{L}_k z^k\right]\hat{i}_m = \hat{B}\mathbf{v}_p \tag{12.7}$$

where $\tilde{R}_k$ and $\tilde{L}_k$ contain already the Cesaro's correction (12.4). Collecting the terms corresponding to the same powers of z we obtain

$$\sum_{k=0}^{N} F_k z^k \mathbf{i}_m - (1+z)\hat{B}\mathbf{v}_p = 0, \tag{12.8}$$

interpolation error bound) through the η-shifting procedure we may guarantee strict positive-realness of the final model. An alternative is to not perform the η-shifting, in which case we may prove that $\tilde{Z}$ is Weakly-η, which allows $\tilde{Z}$ to have an excess energy gain of $O(\eta)$. Since we may drive $\eta \to 0$, neither deviation is of practical consequence in systems with loss modeled over a finite bandwidth.

where

$$F_k = \begin{cases} \frac{1}{M}\left[\tilde{R}_0 + \lambda\tilde{L}_0\right] & k = 0 \\ \frac{1}{M}\left[\tilde{R}_k + \tilde{R}_{k-1} + \lambda\tilde{L}_k - \lambda\tilde{L}_{k-1}\right] & 1 \le k \le N-1 \\ \frac{1}{M}\left[\tilde{R}_{N-1} - \lambda\tilde{L}_{N-1}\right] & k = N \end{cases} \tag{12.9}$$

define an augment state Define an augmented state

$$x = \left[\ z^{N-1}\mathbf{i}_m^T \quad z^{N-2}\mathbf{i}_m^T \quad \ldots \quad z^2\mathbf{i}_m^T \quad z\mathbf{i}_m^T \quad \mathbf{i}_m^T\ \right]^T. \tag{12.10}$$

and produce a finite dimension discrete linear system, Eq. (12.8) becomes

$$zE_d x - A_d x - (1+z)\hat{B}\mathbf{v}_p = 0. \tag{12.11}$$

where one trivial choice for E_d and A_d is

$$E_d = \begin{bmatrix} 0 & I & \ldots & 0 & 0 \\ 0 & 0 & \ldots & 0 & 0 \\ \ldots & \ldots & \ldots & \ldots & \ldots \\ 0 & 0 & \ldots & 0 & I \\ F_N & F_{N-1} & \ldots & F_2 & F_1 \end{bmatrix}$$

$$A_d = -\begin{bmatrix} -I & 0 & \ldots & 0 & 0 \\ 0 & -I & \ldots & 0 & 0 \\ \ldots & \ldots & \ldots & \ldots & \ldots \\ 0 & 0 & \ldots & -I & 0 \\ 0 & 0 & \ldots & 0 & F_0 \end{bmatrix}$$

One can observe that some of the coefficients of L_d and R_d are not uniquely determined and many choices are possible. A choice that will provide a block bi-diagonal A_c matrix in the final linear system realization is

$$E_d = \begin{bmatrix} 0 & I & \ldots & 0 & 0 \\ 0 & 0 & \ldots & 0 & 0 \\ \ldots & \ldots & \ldots & \ldots & \ldots \\ 0 & 0 & \ldots & 0 & I \\ F_N & F_N + F_{N-1} & \ldots & F_N + \ldots + F_2 & F_N + \ldots + F_1 \end{bmatrix}$$

$$A_d = -\begin{bmatrix} -I & 0 & \ldots & 0 & 0 \\ 0 & -I & \ldots & 0 & 0 \\ \ldots & \ldots & \ldots & 0 & \ldots \\ 0 & 0 & \ldots & -I & 0 \\ -F_N & -(F_N + F_{N-1}) & \ldots & -(F_N + \ldots F_2) & F_0 \end{bmatrix}$$

Substituting $z = (\lambda - s)/(\lambda + s)$ we obtain the continuous and final system realization

$$\begin{aligned} sE_c x_c &= A_c x_c + B_c \mathbf{v}_p \\ \mathbf{i}_p &= C_c x_c \end{aligned} \tag{12.12}$$

where

$$
\begin{aligned}
E_c &= E_d + A_d = \\
E_c &= \begin{bmatrix} I & I & \dots & 0 & 0 \\ 0 & I & \dots & 0 & 0 \\ \dots & \dots & \dots & \dots & \dots \\ 0 & 0 & \dots & I & I \\ 2\mathbf{F}_N & 2(\mathbf{F}_N+\mathbf{F}_{N-1}) & \dots & 2(\mathbf{F}_N+\dots+\mathbf{F}_2) & \mathbf{F}_N+\dots+\mathbf{F}_1-\mathbf{F}_0 \end{bmatrix} \\
A_c &= \lambda(E_d - A_d) = \\
A_c &= \lambda \begin{bmatrix} I & -I & \dots & 0 & 0 \\ 0 & I & \dots & 0 & 0 \\ \dots & \dots & \dots & \dots & \dots \\ 0 & 0 & \dots & I & -I \\ 0 & 0 & \dots & 0 & -(\mathbf{F}_N+\dots+\mathbf{F}_1+\mathbf{F}_0) \end{bmatrix}, \\
B_c &= -2\lambda \begin{bmatrix} 0 & 0 & 0 & 0 & \dots & 0 & \hat{B} \end{bmatrix}^T, \\
C_c &= \hat{B}^* \begin{bmatrix} 0 & 0 & 0 & 0 & \dots & 0 & I \end{bmatrix},
\end{aligned}
$$

and

$$
\mathbf{F}_k = \begin{cases} \frac{1}{M}\left[\tilde{R}_0 + \lambda\tilde{L}_0\right] & k = 0, \\ \frac{1}{M}\left[\tilde{R}_k + \tilde{R}_{k-1} + \lambda\tilde{L}_k - \lambda\tilde{L}_{k-1}\right] & 1 \le k \le N-1, \\ \frac{1}{M}\left[\tilde{R}_{N-1} - \lambda\tilde{L}_{N-1}\right] & k = N. \end{cases} \tag{12.13}
$$

The same matrices in terms of the DFT coefficients are

$$
\begin{aligned}
E_c &= \begin{bmatrix} I & I & \dots & 0 \\ 0 & I & \dots & 0 \\ \dots & \dots & \dots & \dots \\ 0 & 0 & \dots & I \\ \frac{1}{M}[\tilde{R}_{N-1} - \lambda\tilde{L}_{N-1}] & \frac{1}{M}[2\tilde{R}_{N-1} + \tilde{R}_{N-2} - \lambda\tilde{L}_{N-2}] & \dots & \frac{1}{M}[2\tilde{R}_{N-1} + \dots + 2\tilde{R}_1 - 2\lambda\tilde{L}_0] \end{bmatrix} \\
A_c &= -\lambda \begin{bmatrix} I & -I & \dots & 0 & 0 \\ 0 & I & \dots & 0 & 0 \\ \dots & \dots & \dots & \dots & \dots \\ 0 & 0 & \dots & I & -I \\ 0 & 0 & \dots & 0 & -\frac{2}{M}[\tilde{R}_{N-1} + \dots + \tilde{R}_0] \end{bmatrix} \\
B_c &= -2\lambda \begin{bmatrix} 0 & 0 & 0 & 0 & \dots & 0 & \hat{B} \end{bmatrix}^T \\
C_c &= \hat{B}^* \begin{bmatrix} 0 & 0 & 0 & 0 & \dots & 0 & I \end{bmatrix}
\end{aligned}
$$

The reduced models generated by the above approach may be larger than desired for final simulation. In this case it is desirable to perform a "second-stage" model reduction step using an optimal or near-optimal reduction approach, such as a truncated balanced realization that guarantees passivity by construction presented in Chapter 13 and in [108].

12.4 Examples

12.4.1 Effect of lossy substrate on line impedance

The geometry in this example consists of two wires over a lossy substrate. The two wire volumes are discretized into short and thin filaments using a set of piece-wise constant basis functions. A standard Galerkin

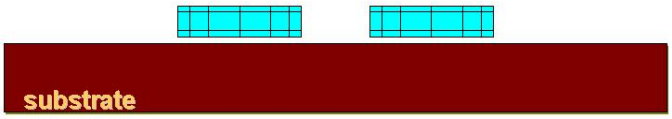

Figure 12.3: *2d lines setup*

technique is used to calculate the resistance and partial inductance matrices $R(s)$ and $L(s)$. *A frequency dependent Green function is used in the kernel of the Galerkin integration to account for the effects of the lossy substrate. Hence, the resulting matrices are frequency dependent.* The system, before model reduction, appears as in (7.2). The descriptor matrices have been projected to a reduced space of size $q = 4$ obtained by solving the original full system at frequencies $f = 0,\ 0.4GHz,\ 1GHz,\ 2.4GHz.$ which correspond to the points on the unit circle: $z = 1, exp(-j\pi/4), -j,\ exp(-j3\pi/4)$. As center frequency for our band of interest we have chosen $\lambda = 2\pi 10^9$. In this example we have chosen $M = 64$ points for the FFT size. Fig. 12.13.b shows the real part of the DFT coefficients for the inductance matrices. Coefficients $32,\ldots,63$ are very small indicating the original system matrix is causal. We have then truncated the DFT series to N=6 coefficients,

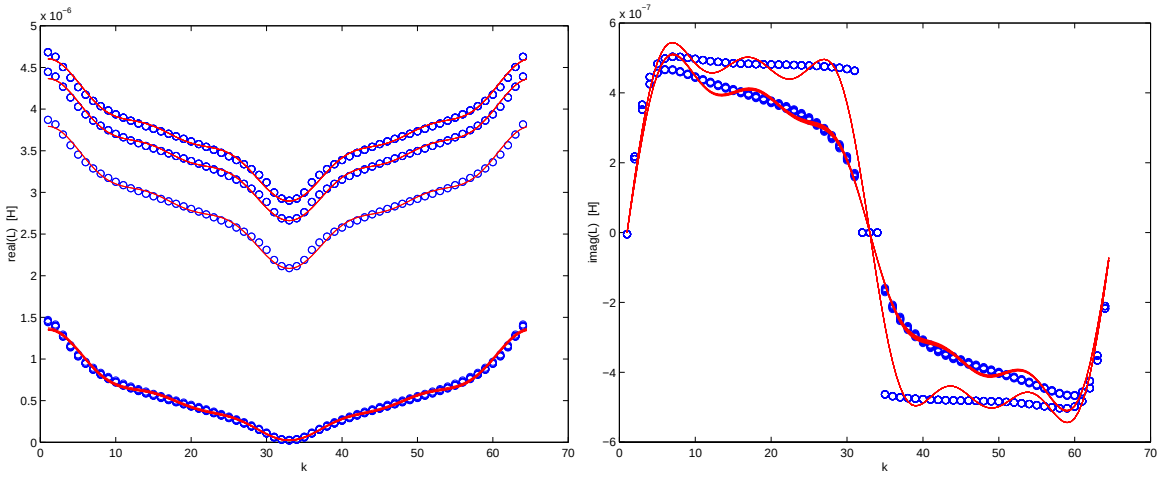

Figure 12.4: *Real and imaginary part of the original inductance matrix (circles) evaluated on the unit circle and compared to its DFT series (continuous lines) truncated at N=6 coefficients out of M=64 total.*

producing a final model of order 28. Fig. 12.4 compares the real and imaginary part of the original inductance with their truncated DFT series representations. Fig. 12.5 compares the frequency response of the original full system with the frequency response of the final realized linear state space model. Fig. 12.6 shows that all the poles of the realized model are in the half-plane $Re(s) < 0$, hence stable. In order to check the performance of our reduction procedure in terms of passivity preservation, we show in Fig. 12.7 the minimum eigenvalue of the internal matrix $Z_{em_r} + Z^*_{em_r}$ vs. frequency at different stages of the algorithm

$$Z_{em_r}(s) = \tilde{R}(s) + s\tilde{L}(s) \tag{12.14}$$

The truncation process introduces some positive and negative error with respect to the minimum eigenvalue of the system. The projection process instead can only increase the minimum eigenvalue, hence preserving the degree of passivity in the system. Using the Positive-Real Lemma [5], we confirmed that the generated system is passive.

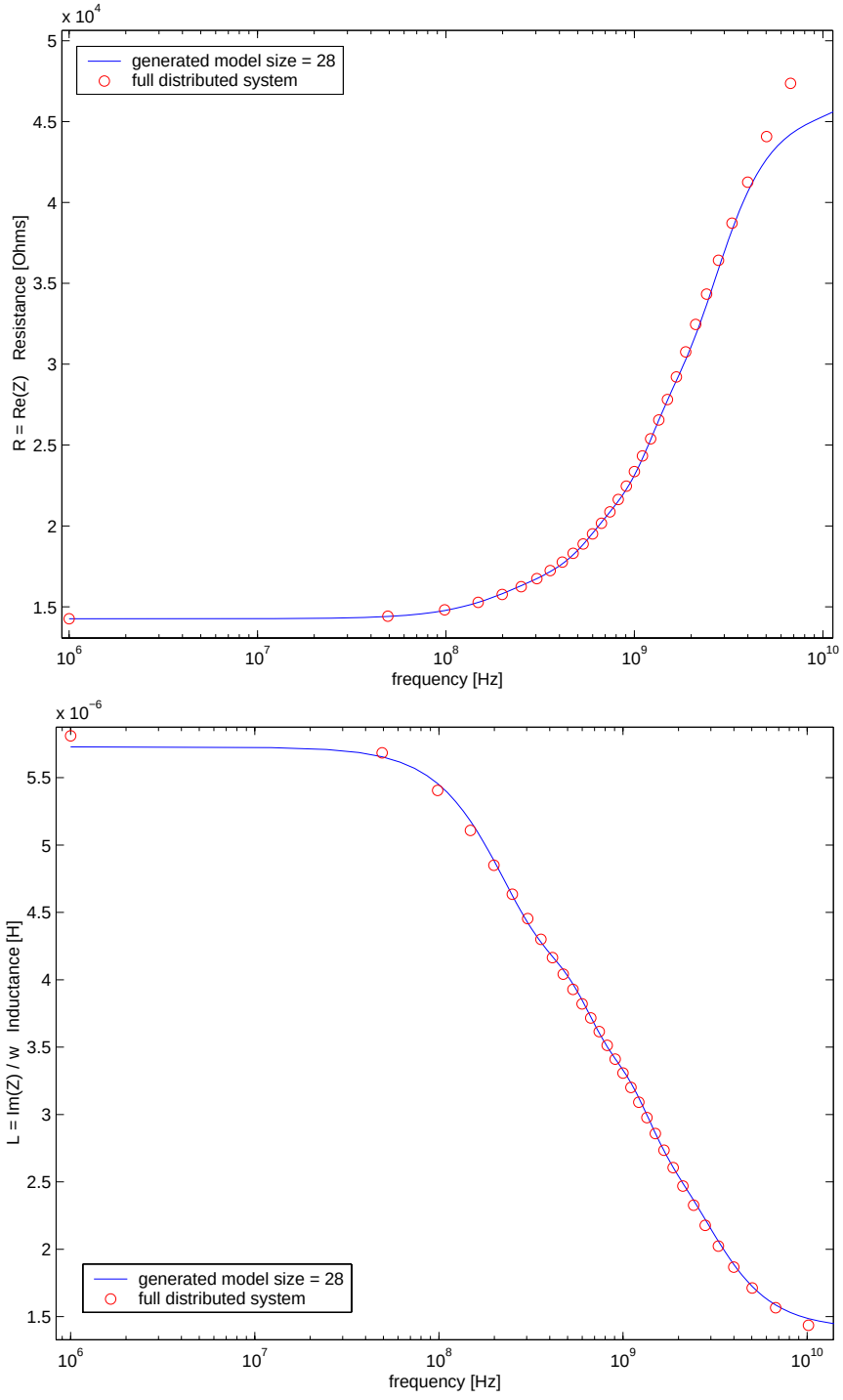

Figure 12.5: *Real part and imaginary part divided by ω of the frequency response for the lossy substrate example.*

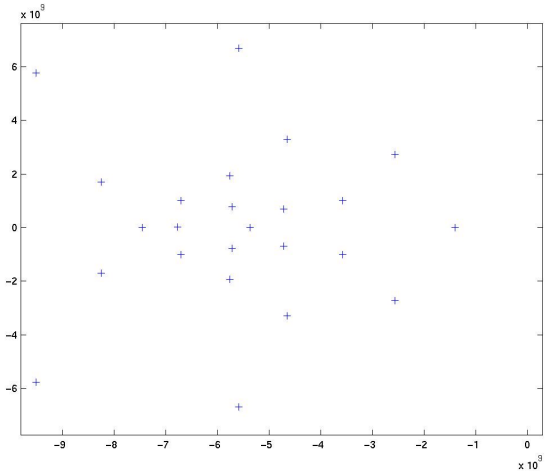

Figure 12.6: *All the poles of the frequency response of the realized model are in the half-plane* $Re(s) < 0$*, hence stable.*

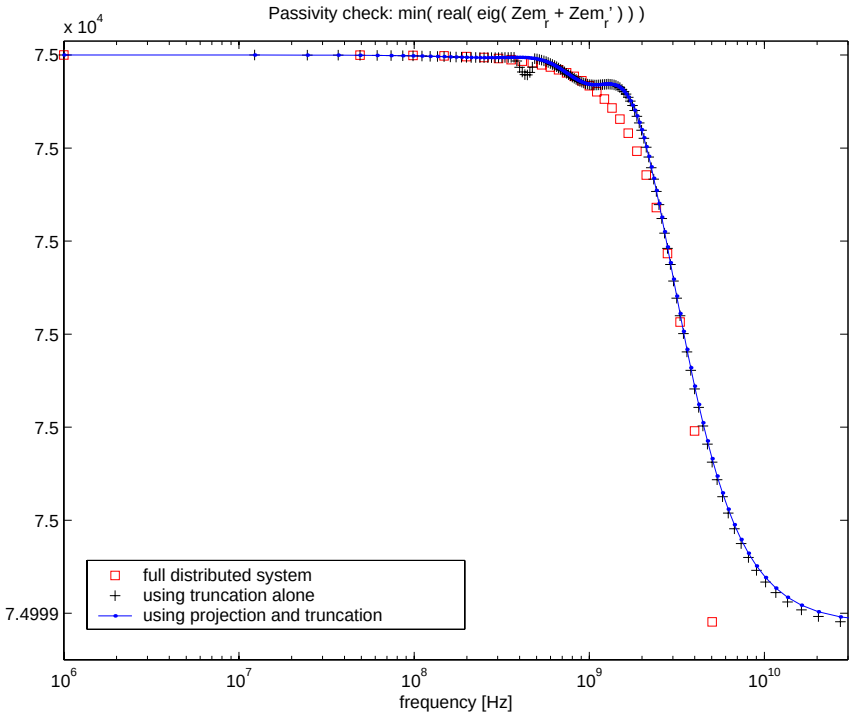

Figure 12.7: *Minimum eigenvalue of* $Z_{em_r} + Z^*_{em_r}$*. The system is passive if the minimum eigenvalue is positive. The minimum eigenvalue after the projection is larger or equal to the minimum eigenvalue before the projection, hence the projection has preserved the degree of passivity.*

12.4.2 Full-Wave PEEC kernel

In this example we consider two parallel wires 4um wide, 1um thick and 750 um long. The two wires are separated by 3cm. The wire volumes are discretized into short and thin filaments using a set of piecewise constant basis functions. A Galerkin technique is used to calculate the resistance and partial inductance matrices $R(s)$ and $L(s)$. *Since the separation between the two wires is not small compared to the minimum wavelength of interest, a frequency dependent full-wave Green Function needs to be employed in the kernel of the Galerkin integration. Hence, the resistance and inductance matrices are frequency dependent.* The system, before model reduction, appears as in (7.2). The descriptor matrices have been projected to a reduced space of size $q = 4$ obtained by solving the full system at frequencies $f = 0,\ 1.3GHz,\ 3.3GHz,\ 8GHz$. which correspond to the points on the unit circle: $z = 1,\ exp(-j\pi/4),\ -j,\ exp(-j3\pi/4)$. As center frequency we have chosen $\lambda = 2\pi \times 3.3GHz$. Fig. 12.8 shows the DFT coefficients for both the resistance and the inductance matrices. In this example we have chosen $M = 128$ points for the FFT size. We have then truncated the DFT series to N=23 coefficients, producing a final model of order 96. Fig. 12.9, compare the real part of the original inductance with its truncated DFT series representations. Fig. 12.10 compares the frequency response of the original full system with the frequency response of the final realized linear state space model. Fig. 12.11 shows that all the poles of the realized model are in the half-plane $Re(s) < 0$, hence the system is stable. In order to check the performance of our reduction procedure in terms of passivity preservation, we show in Fig. 12.12 the minimum eigenvalue of the internal matrix $Z_{em_r} + Z^*_{em_r}$ vs. frequency at different stages of the algorithm. Once again $Z_{em_r}(s) = \tilde{R}(s) + s\tilde{L}(s)$. The truncation process introduces some positive and negative error with respect to the minimum eigenvalue of the system. The projection process instead can only increase the minimum eigenvalue, hence preserving the degree of passivity in the system. Using the Positive-Real Lemma [4], we confirmed that the generated system is passive.

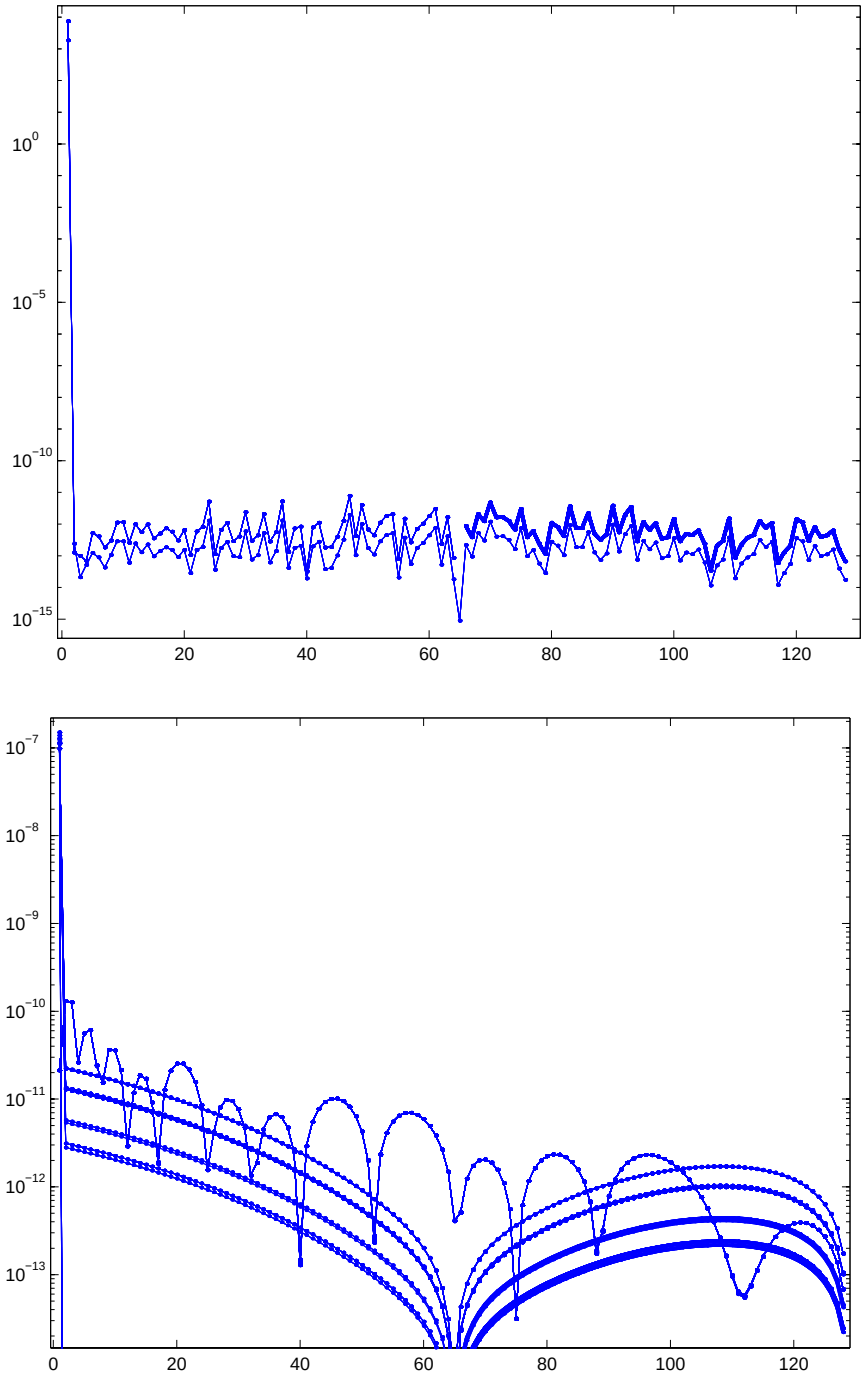

Figure 12.8: *DFT coefficients of the resistance and inductance matrix for the fullwave example.*

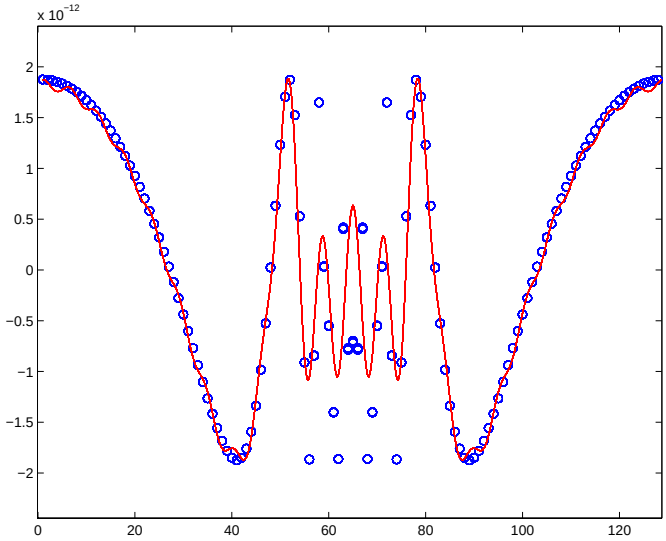

Figure 12.9: *Real part of the original inductance matrix (circles) evaluated on the unit circle and compared to its DFT series (continuous lines) truncated at N=23 coefficients out of M=128 total.*

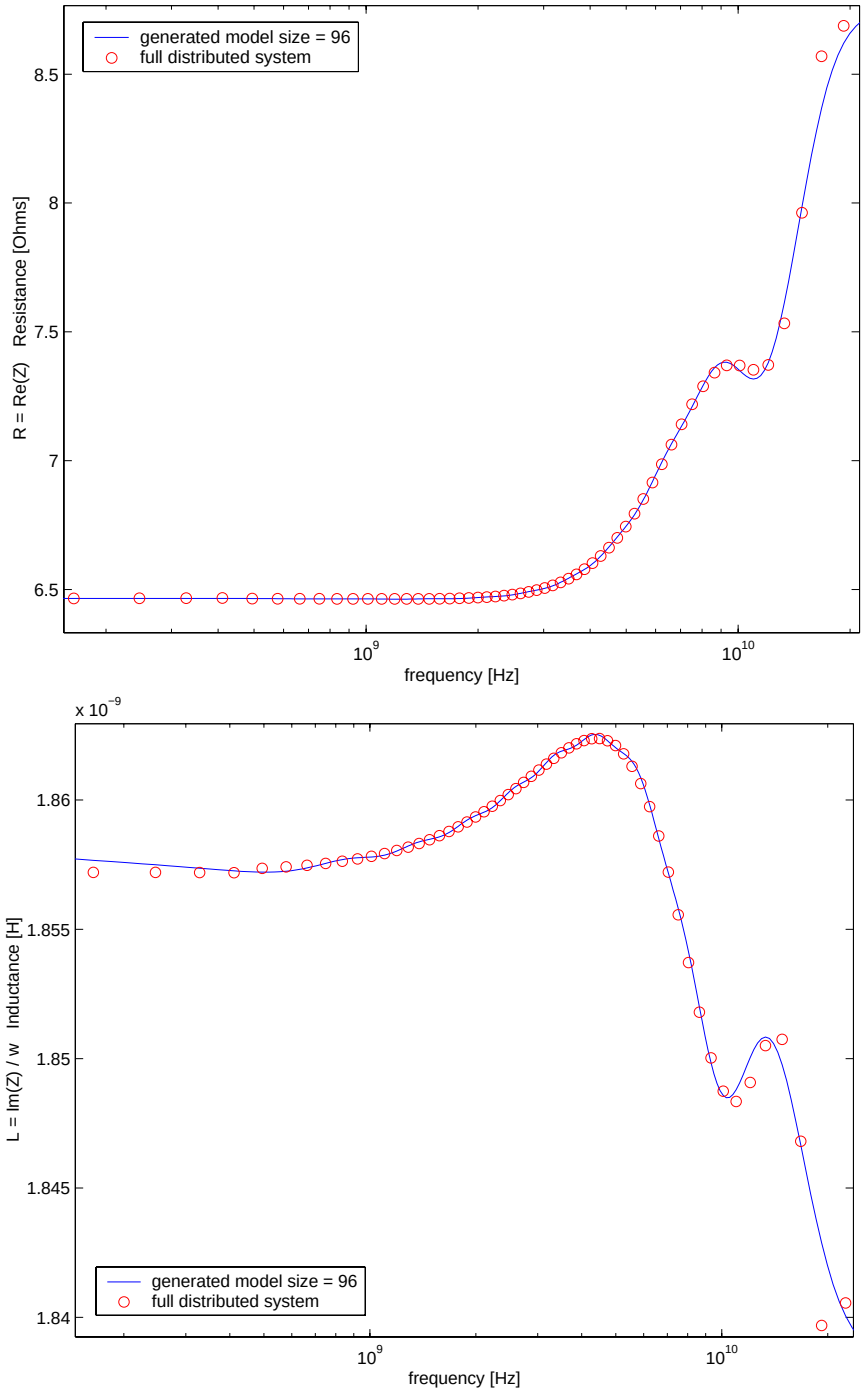

Figure 12.10: *Real part and imaginary part divided by ω of the frequency response for the full-wave example.*

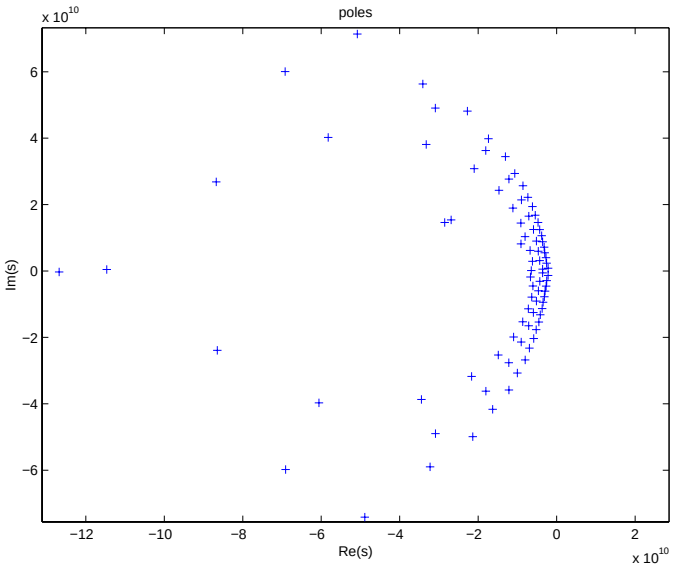

Figure 12.11: *All poles of the reduced fullwave model are stable.*

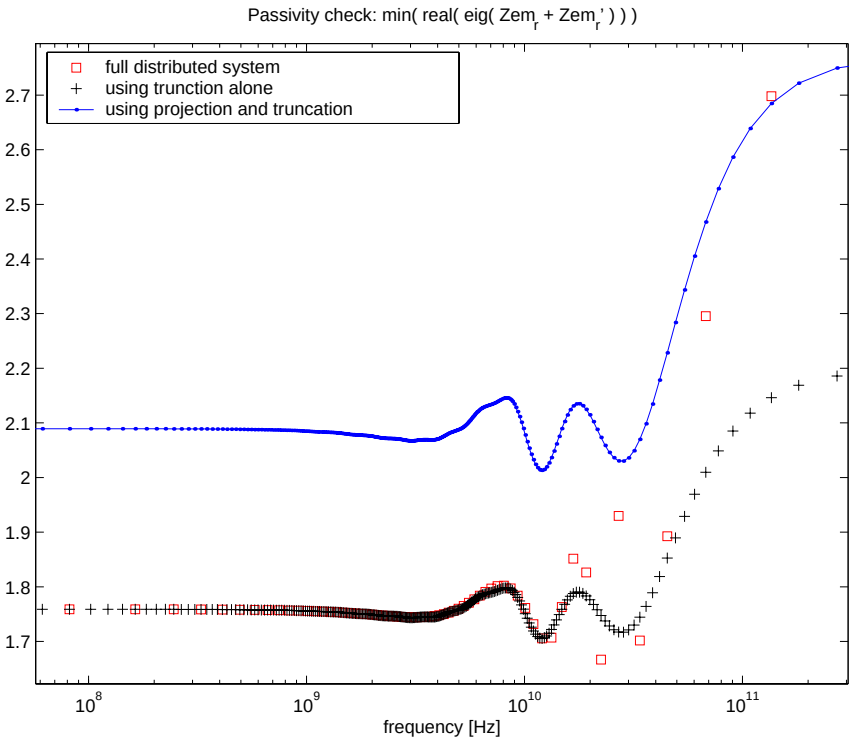

Figure 12.12: *Minimum eigenvalue of* $Z_{em_r} + Z^*_{em_r}$. *The system is passive if the minimum eigenvalue is positive. The minimum eigenvalue after the projection is larger or equal to the minimum eigenvalue before the projection, hence the projection has preserved the degree of passivity.*

12.4.3 A non-causal example

Since $R(s)$ and $L(s)$ are frequency domain representations, when we calculate their FFT interpolants we obtain something related to their time domain impulse response (actually the impulse response of a discrete-time system obtained by sampling the continuous-time system at rate λ). Since the FFT produces M coefficients that repeat periodically, the $k = M/2, \ldots, M-1$ coefficients are related to negative-time part of the time domain impulse response of $R(s)$ and $L(s)$. In Fig. 12.13.a we show the FFT coefficients of a common *non-causal* example mentioned in Section 9.3: $Z_{\text{skin}}(i\omega) = R_0 + R_{ac}\sqrt{|\omega|}$ used as a model for the "resistance" of interconnect in the skin-effect regime. We can easily notice in such Figure that the coefficients $k = M/2, \ldots, M-1$ related to non-causal coefficients of the time domain response are non-zero. If a model order reduction is attempted on such an originally non-causal system, one will obtain non-stable models. Alternatively one could deliberately ignore the non-causal coefficients and set them to zero before beginning the reduction. However in this case stable but highly inaccurate models will be produced.

In our approach we require therefore that the original system descriptor matrices $R(s)$ and $L(s)$ be causal. This means checking that the non-causal $k = M/2, \ldots, M-1$ coefficients of the FFT be zero except for some aliasing phenomena. Fig. 12.13.b shows the real part of the DFT coefficients for the $L(s)$ in example 12.4.1. One can easily verify that such original system matrix descriptor is actually a causal one.

12.5 Conclusions on passive model order reduction for distributed systems

In this Chapter we have presented a class of algorithms for guaranteed passive model order reduction of strictly passive and causal linear systems with frequency dependent matrices (distributed systems). Our approach is based on the key idea that if a system is strictly positive-real to begin with, a *globally* and *uniformly* convergent interpolant will eventually (for a large enough order of the interpolant) be positive-real as well. Laguerre basis are a set of well-behaved uniformly convergent interpolation functions whose coefficients can be conveniently calculated using the FFT algorithm. An implementation using a Laguerre basis as interpolant is given and examples are presented. While the Laguerre basis reduces the infinite order of the original distributed system to a finite order, a standard Krylov subspace congruence transformation can still be employed to reduce the size of the matrices. The algorithm is also perfectly compatible with fast matrix-vector product algorithms.

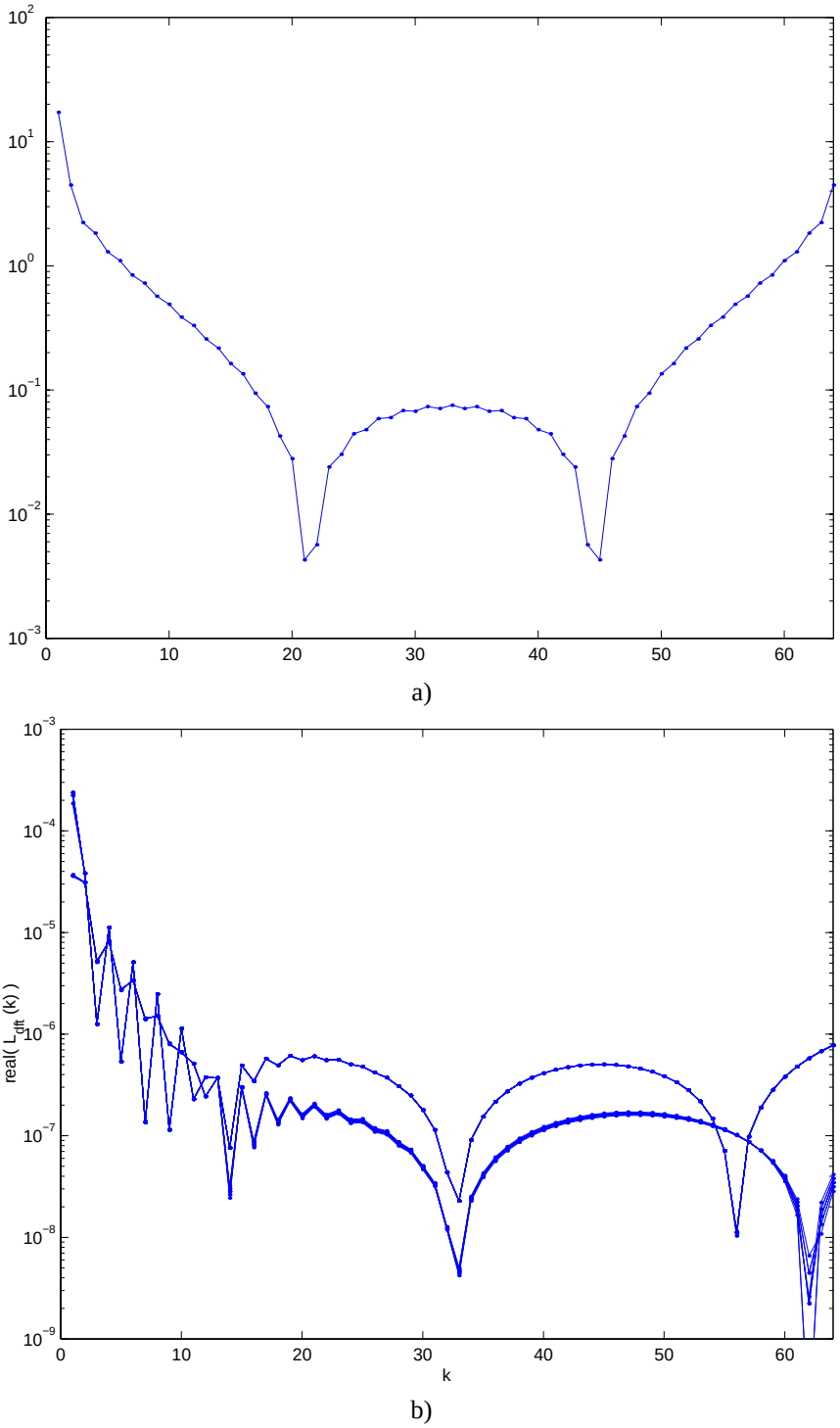

Figure 12.13: *a) FFT coefficients for the non-causal example* $Z_{skin}(i\omega) = R_0 + R_{ac}\sqrt{|\omega|}$ *used as a model for the skin-effect "resistance". b) FFT coefficients of the inductance matrix for the lossy substrate example. Note that non-causal coefficients* $32-63$ *are in a) very large and in b) very small.*

Chapter 13

Preserving passivity in Truncated Balance Realizations

The work in this Chapter has been done in collaboration with Dr. Joel Phillips (Cadence Berkeley Labs) and with Prof. L. Miguel Silveira (Cadence Euro Labs and Technical University of Lisbon, Portugal) during an internship at Cadence Berkeley Labs, Berkeley, CA and subsequent collaboration. This work has first been published in [108, 109].

The model order reduction techniques based on the Krylov subspace projection framework and presented in Chapter 8 are very suitable for analysis of large-scale systems, since they only require matrix-vector operations, and therefore can exploit almost linear complexity fastsolvers [94, 68, 152]. For the same final accuracy, more compact optimal norm approximants are generated by the Truncated balanced realization algorithms (TBR) [93] (Section 7.4) and Hankel model order reduction algorithms [51]. However the computations required by TBR and Hankel reduction techniques have $O(n^3)$ complexity when performed directly (n is the order of the system to be reduced). Therefore the TBR methods are of more interest when combined with iterative Krylov-subspace procedures. One formulation of this method is to directly solve the large Lyapunov equations via a Krylov subspace method [81, 115, 63, 64, 116]. The reduced models are obtained directly from the reduced Lyapunov equation. Another strategy is to use the two steps procedure [69, 88] as illustrated in Section 10.1. One first uses the less efficient but computationally feasible Krylov-subspace technique to reduce the system to a few hundreds and then one can employ the more computationally demanding TBR to obtain a final very compact model.

None of the above literature however addresses the issue of preserving passivity when using TBR type methods. A passivity-preserving initial reduction is used in [69, 132], but then a standard TBR method follows the initial reduction. The second TBR step may destroy the passivity of the initial model.

A second issue is that passivity preserving Krylov reductions such as PRIMA ([97] Section 9.4), can handle only systems such as RLC circuits, that can generate positive semidefinite internal descriptor matrices. That is because such methods rely on congruence transformations to preserve positive-semi-definiteness of such internal descriptors. However, whether or not a state-space model represents a passive system is a property of the input-output transfer function, not a property of the internal representation. Some passive systems may have descriptor matrices that are not non-positive semi-definite. Some examples include the systems that come from rational approximation of tabular data[27], the magnetic charge formulation of the inductance problem[89], and general linear circuits, in particular those with gyrators, formulated in the sparse tableau form. This issue even appears in RLC circuits: the positive-definiteness of the matrices in the MNA formulation depends on the choices of signs (the circuit response is of course invariant to this choice). Finally, in many cases positive positive realness of the input output transfer function may not even be the correct property characterizing the passivity of the system. For instance, if the state-space model represents scattering (S) parameters of a passive system, the system is passive if the norm of the S-parameter matrix is bounded by unity. Such systems cannot be reduced by congruence with any passivity guarantees.

***Algorithm* 2 Positive-Real TBR (PR-TBR)**

1. *Solve Eqns. (9.24)-(9.26) in Section 9.1.3 for X_c and Eqns. (9.27)-(9.29) for X_o.*
2. *Proceed with steps 3-8 in Algorithm 1 in Section 7.4, substituting X_c for W_c and X_o for W_o.*

In the systems and control literature one can find many results (e.g. [146, 147, 4]) and reduction algorithms (e.g., [52]) with properties potentially relevant to passivity preserving model reduction. Such techniques so far were not well known in the circuit simulation and design automation communities. By collecting all of those control system techniques, and by applying, and extending them in the context of large-scale integrated circuit analysis and modeling, we hope to provide a first step in their wide adoption by the circuit and design automation community.

In this chapter we discuss TBR-like model reduction algorithms that can preserve system passivity, have computable error bounds, and, unlike other algorithms such as PRIMA, pose no constraints on the internal structure of the state-space model. We describe variants that preserve both positive-realness (useful for systems that represent Y or Z parameters) and bounded-realness (useful for systems that represent S parameters). These algorithms can be applied directly to a given state-space description [129], or can be used as the second stage of a Krylov-subspace based procedure [81, 63, 69].

13.1 Guaranteed passive balanced truncations

We will show in Section 13.5 that the TBR procedure in Algorithm 1 in Section 7.4 does not necessarily produce passive models. In making assessments about passivity, we require a tool that can assess the positive-realness of a state-space model in a global manner. One such tool for systems representing immittance matrices is the positive-real lemma [4] presented in Section 9.1.3.

A passivity-preserving reduction procedure follows by noting that the Lur'e equations can be solved for the quantities X_c, X_o which may then be used as the basis for a TBR procedure. We may find a coordinate system in which $\hat{X}_c = \hat{X}_o = \Sigma$, with Σ again diagonal. In this coordinate system, the matrices $\hat{A}, \hat{B}, \hat{C}$ may be partitioned and truncated, just as for the standard TBR procedure, to give the reduced model defined by $(\tilde{A}, \tilde{B}, \tilde{C}, D)$. We present this as Algorithm 2 and call it PR-TBR, as it preserves positive-realness of the transfer function. Several approaches that turn out to give essentially similar results have appeared previously in different contexts [52, 101, 23].

Theorem 11 *Algorithm 2 applied to systems with positive-real transfer functions produces reduced models with positive-real transfer functions.*

Proof. From the form of the partitioning, (7.16) and (7.17), likewise partitioning either $\hat{K}_c$ or $\hat{K}_o$, it is clear that the reduced system, in the PR-balanced coordinates, satisfies

$$\hat{A}_{11}\Sigma_1 + \Sigma_1\hat{A}_{11}^T = -\hat{K}_1\hat{K}_1^T \tag{13.1}$$

$$\Sigma_1\hat{C}_1^T - \hat{B}_1 = -\hat{K}_1\hat{J}_c^T, \tag{13.2}$$

$$\hat{J}_c\hat{J}_c^T = \hat{D} + \hat{D}^T. \tag{13.3}$$

Therefore the reduced system satisfies the Lur'e equations with positive semi-definite Σ_1 ($\Sigma_1 \geq 0$ as $\Sigma \geq 0$). By the positive-real lemma, the reduced system is positive-real. We emphasize that Theorem 11 holds regardless of the internal form of the state-space system. Again, this is not true for congruence based procedures.

To obtain equivalent TBR procedures that guarantee a final transfer function that is bounded-real, useful when working with transfer functions representing S-parameters, we can use the bounded real equations

***Algorithm* 3 Bounded-Real TBR (BR-TBR)**

1. *Solve Eqns. (9.38)-(9.40) in Section 9.2.1 for Y_c and Eqns. (9.41)-(9.43) for Y_o.*
2. *Proceed with steps 3-8 in Algorithm 1 in Section 7.4, substituting Y_c for W_c and Y_o for W_o.*

***Algorithm* 4 Hybrid TBR**

1. *Perform Algorithm 1 in Section 7.4*
2. *Using the reduced model matrices $\tilde{A},\tilde{B},\tilde{C}$, solve Eqns. (9.24)-(9.26) for $\tilde{X}_c$ (or Eqns. (9.38)-(9.40)).*
3. **if** *Eqns. (9.24)-(9.26) (or Eqns. (9.38)-(9.40)) are solvable and $X_c \geq 0$, then terminate and return $\tilde{A},\tilde{B},\tilde{C}$.*
   else *discard TBR-reduced model and proceed with Algorithm 2 (or 3).*

in Section 9.2.1. The Algorithm 3 can then be introduced to perform truncated balanced realization while guaranteeing the boundedness of the reduced transfer function [1].

13.2 A hybrid approach

In many cases, while not guaranteed by construction, it is often the case that the TBR approximants produced by Algorithm 1 in Section 7.4 turn out to be positive-real. Therefore we propose Algorithm 4, which performs the TBR procedure, solves the positive-real (or bounded-real) equations on the reduced model to check its passivity, and if it turns out not to be passive, discard it and proceeds to Algorithm 2 (or Algorithm 3). There is an advantage in this procedure as often the TBR approximates are more accurate for a given order than PR-TBR. Because of the cubic scaling of cost, it is relatively cheap, compared to the cost of the TBR reduction, to check a reduced model for passivity since the reduced system is presumably of lower order. As often the TBR models are passive, the net effect of the composite algorithm is to approximately double the cost in the worst case, versus usually getting better models at smaller cost (PR-TBR "costs" more than TBR) in the more-common average case.

Algorithm 4, which appropriately combines all of the previously presented algorithms, can be used as generic flow for generating accurate guaranteed passive reduced-order models of systems with arbitrary structure.

13.3 Physical interpretation of the PR/BR-TBR procedures

In Section 7.4.1 we discussed how the TBR procedure, and eigenvalues of associated Grammians, could be interpreted in terms of the relative importance of system modes to the system input and output norms. It turns out that the PR/BR-TBR techniques have a similar interpretation, but one that is more closely tied to a circuit-theoretic notion of energy. To make this connection, we draw upon concepts from the theory of passive dynamical systems, discussion of which can be found in [101, 146, 147].

In order to provide a physical interpretation for the PR/BR-TBR algorithm let us introduce the concept of a supply function $s[u(t),y(t)]$. A supply function describes the rate at which power is supplied by the environment into the system, and typically is defined such that $s[u(t),y(t)] > 0$ implies a positive amount

[1] The bound does not have to be unity; it can be any positive constant.

of energy input, while $s[u(t),y(t)] < 0$ means energy is extracted from the system back to the environment. When the system inputs and outputs are currents or voltages, i.e. when the system transfer function represents impedance or admittance matrices, we may use the supply function $s[u(t),y(t)] = u(t)^T y(t)$. When the system transfer function represents scattering parameters, we may use the supply function $s[u(t),y(t)] = u(t)^T u(t) - y(t)^T y(t)$. Regardless of the particular form of supply function we can further define the following two quantities:

$$V_{av}(x_0) = \sup\left\{-\int_0^\infty s[u(t),y(t)]dt, \qquad x(0)=x_0\right\} \tag{13.4}$$

$$V_{req}(x_0) = \inf\left\{\int_{-\infty}^0 s[u(t),y(t)]dt, \qquad u(t) \text{ controlling to } x(0)=x_0\right\}, \tag{13.5}$$

where $V_{av}(x_0)$ is the *available storage energy*, or maximum energy that can be extracted from the system over any possible trajectory of the state from an initial state x_0 at time 0. $V_{req}(x_0)$ can be interpreted as the *required supply*, or the minimum amount of energy that must be provided by the environment to the system in order to control the system to state x_0 at time 0 over any possible trajectory. It can be shown ([146, 147]) that for passive and controllable systems, $V_{av}(x_0)$ is always a positive number not larger than $V_{req}(x_0)$

$$0 \le V_{av}(x_0) \le V_{req}(x_0). \tag{13.6}$$

Furthermore, it can be shown ([146, 147]) that the solutions X_o and X_c to the positive real Lur'e equations (9.27)-(9.29) and their dual (9.24)-(9.26) respectively, obtained from the procedure in Section 13.4 have a physical interpretation for passive immittance systems in terms of the energy quantities $V_{av}(x_0)$ and $V_{req}(x_0)$,

$$x_0^T X_o x_0 = V_{av}(x_0) \tag{13.7}$$

$$x_0^T X_c^{-1} x_0 = V_{req}(x_0). \tag{13.8}$$

Using a similar argument to the classical TBR interpretation, small eigenvalues of X_o are associated with modes for which the maximum energy we can extract, $V_{av}(x_0)$, is small. They are therefore not likely to be important "energy-wise" for the system response. Small eigenvalues of X_c are associated with modes for which the minimum amount of energy $V_{req}(x_0)$ we have to supply in order to reach them is large. Hence it is relatively difficult to drive the system into those states and they are not likely to be important "energy-wise" for the system response.

As in the classical TBR, it can be noticed that some modes, although energy-wise hardly accessible, are energy-wise important and we can extract back from them large amounts of energy. Vice-versa, there can be some modes for which, although we cannot extract large amounts of energy, they require a small amount of energy to reach. Thus, in a similar way as classical TBR, PR-TBR balances the importance of past energy inputs and future energy outputs by transforming to a coordinate system in which X_o and X_c are equal and diagonal, and in which the invariant quantities that are the eigenvalues of the product of X_o and X_c are easily calculated. The algorithm will keep in the final reduced model only modes that are

- **"energy-wise"** easily "controllable", that is they do not need much energy input to be reached
- and **"energy-wise"** easily "observable", that is, it is possible to extract a lot of energy from them.

It is also interesting to note ([52, 101, 146]) that the solutions X_o and X_c of the positive real Lur'e equations (9.27)-(9.29) and their dual (9.24)-(9.26), are related and not unique. Specifically, there exists a minimal solution $X_{o,min}$ and a maximal solution $X_{o,max}$ for (9.27)-(9.29), a minimal solution $X_{c,min}$ and a maximal solution $X_{c,max}$ for (9.24)-(9.26), such that

$$0 \le X_{o,min} = X_{c,max}^{-1} \le X_o = X_c^{-1} \le X_{o,max} = X_{c,min}^{-1} \tag{13.9}$$

A procedure is given in [109] that produces the minimal solutions used in (13.7)-(13.8) respectively

$$X_o = X_{o,min} = X_{c,max}^{-1}, \tag{13.10}$$

$$X_c = X_{c,min} = X_{o,max}^{-1}, \tag{13.11}$$

$$\tag{13.12}$$

The same physical interpretation presented above for positive real systems representing impedance or admittance can be given to bounded real systems representing scattering parameters by defining as in [101]

$$x_0^T\, Y_o\, x_0 = V_{av}(x_0) \tag{13.13}$$

$$x_0^T\, Y_c^{-1}\, x_0 = V_{req}(x_0). \tag{13.14}$$

where Y_o and Y_c are the minimal solutions of the bounded real Lur'e equations (9.41)-(9.43) and their dual (9.38)-(9.40), respectively. A procedure is given in [109] to calculate such minimal solutions.

13.4 Computational considerations

The complexity of the algorithms presented for passivity-preserving balancing transformation is cubic in the number of state variables, due to the use of direct, dense linear algebra for eigenvector computations and matrix-matrix products. Thus, standard TBR and the passive-TBR variants cannot be directly applied to extremely large systems such as large collections of interconnect because of the high cubic computational complexity. However, this cost is acceptable if the algorithms are being applied to systems that are moderate in size, as is usually the case with systems that result from a prior reduction step (see Section 10.1). Therefore we wish to re-iterate that in the case of large systems, one would use the TBR algorithms as a *"second step"* of a "two-step" reduction procedure. During the first step one would use the less computationally demanding (but less efficient) Krylov subspace guaranteed passive reduction techniques such as PRIMA to reduce the originally very large system to order around few hundred. At such point one can easily use without much computational effort passive-TBR to reduce the system to order around 10 to 20. This "two-step" procedure produces a much better compression (i.e. better accuracy for the same final order) than using PRIMA to reduce in one single step the original very large system to the final order around 10 to 20.

13.5 Results

13.5.1 An RLC line

For our first example we use a 40-segment uniform RLC line that is L-dominated. The values of the line were chosen to be $R = 25$, $C = L = 0.39894$. For the purpose of comparison we computed $25^{\,th}$ order models using both TBR and PR-TBR. Figure 13.1-a) shows the low-frequency behavior of the exact line impedance as well as that obtained using the two models. For this particular case it turns out that PR-TBR performs much better than regular TBR in terms of the model error. More important, however is the result shown in Figure 13.1-b) where we plot the minimal eigenvalue of the symmetric part of the transfer function as a function of frequency. As can be seen from the plot, the minimal eigenvalue for the TBR model can go below zero at some frequencies which implies that the model is non-passive and may produce non-physical responses when used in time-domain simulations. In fact, on this example, *almost none* of the models produced by TBR were passive. Only very high order models exhibiting an almost exact match to the transfer function over the entire frequency axis were passive. In contrast, all the models produced by the PR-TBR method were found to be passive, as expected.

13.5.2 A bounded-real example from rational function fitting

In the next example we consider the bounded-real variant of the TBR procedure (BR-TBR). First, a rational fitting method was used to fit a high-order model to tabulated 2-port S-parameter data originating

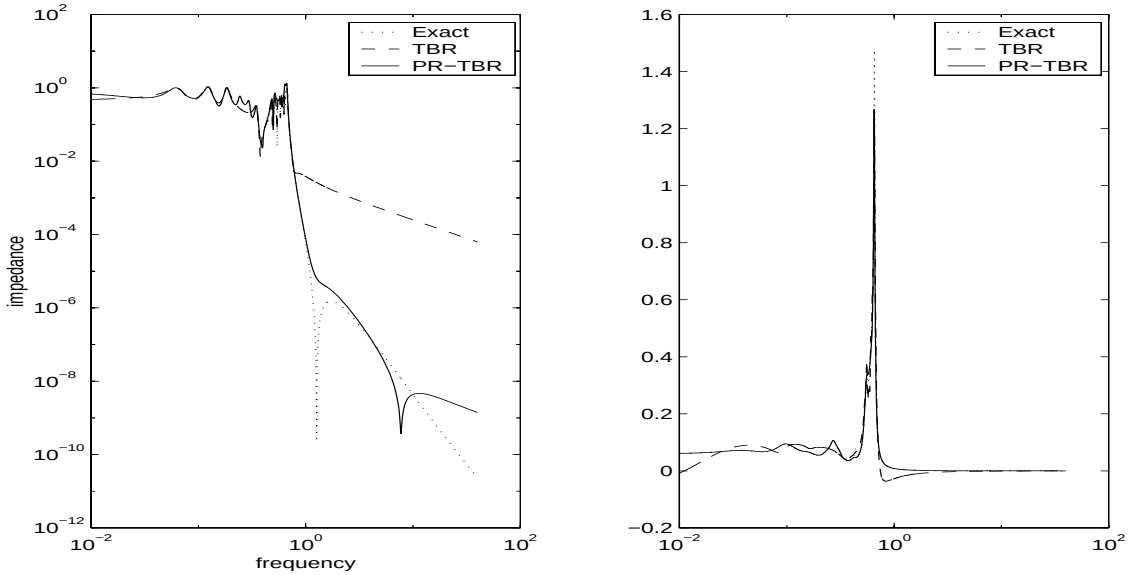

Figure 13.1: *Left: Magnitude of Y_{12} for LC line. Right: Minimum eigenvalue of symmetric part of reduced model transfer function. Note that the minimum eigenvalue the TBR model drops below zero for some frequencies, indicating non-passivity. [Figure by Joel Phillips.*

from a full-wave EM field solver. The fitting algorithm, which has provision for automatic estimation of model order, was tuned to a conservative setting, and generated an order-42 initial model that was nearly an exact fit to the data in the given frequency range. The resulting 42-state model was much larger than desired for final simulation, so the BR-TBR procedure was used to reduce the model to six states. The results are shown in Figure 13.2. The reduced model had norm bounded by unity, indicating that it represented a passive element. Several models of orders six to eight were also generated by both TBR and congruence transform strategies, but all had H_∞ norms ranging from 1.05 to 1.9, i.e. they were not passive. Such techniques are therefore unusable for this type of systems.

13.6 Conclusion on passive truncated balance realizations

In this Chapter we presented a family of algorithms that can be used to compute guaranteed passive, reduced-order models of controllable accuracy for state-space systems with arbitrary internal structure.

The algorithms presented are similar to the well-known truncated balanced realization (TBR) techniques and share some of their advantages, such as computable error bounds [109]. However, unlike standard TBR techniques, the algorithms presented have been shown to produce provably passive reduced-order models. In addition, unlike other techniques known to also produce passive reduction, the algorithms presented pose no constraints on the internal structure of the state-space. They are thus equally well applicable to systems that represent for instance Y or Z parameters as well as systems that represent S parameters. An hybrid algorithm was also presented where a TBR model is first computed, then checked for passivity and the passive-TBR algorithm is only used if that check fails. Our hybrid algorithm is more reliable than simply slightly changing the order of the produced model which can often produce passive systems, although not always. In addition we also examined a DC-accurate technique that can be used in conjunction with the algorithms presented in order to produce models that have accurate steady-state responses.

We have experimented with our techniques in a number of settings. They can be used as stand-alone pro-

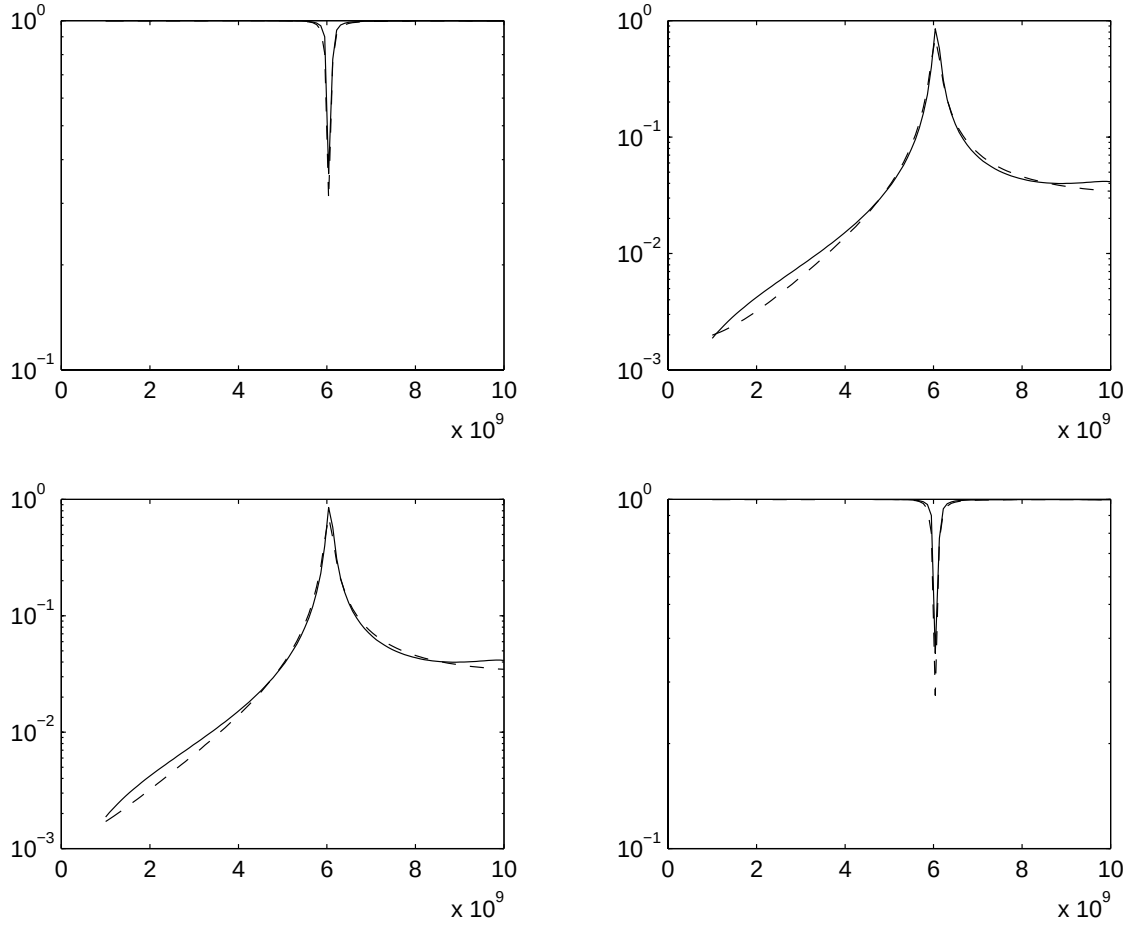

Figure 13.2: *Magnitude of rational function fit and reduced model for S-parameters tabulated by full-wave field solver. Solid line shows initial data and order-42 rational fit (complete overlap). Dashed line shows order-6 reduced model obtained via BR-TBR. [Figures by Luis Miguel Silveira and Joel Phillips]*

cedures or as part of second step reductions for systems with a large number of unknowns, perhaps replacing the usual TBR procedure. In our experiments with our technique all models were found to be accurate and passive. All previously known techniques failed to produce acceptable models in some of the examples used.

Part III

SYNTHESIS

Chapter 14

Background: existing tools for EMC-aware synthesis

Automatic layout tools accounting for crosstalk, substrate noise and parasitics have been developed for digital IC's and even for analog IC's [85] and RF/Microwave IC's [21]. Some routing tools accounting for *conducted* interferences at the Printed Circuit Board level exist [137]. In this Chapter, several *expert systems*, *rules checkers* and an *auto-router* are presented. A *rule checker* is a piece of software that reads component data-sheets and board layout informations from automated board layout tools, looking for violations of basic EMC design rules [58]. An *expert system* is an interactive computer-based tool that uses both facts and heuristics to solve difficult decision problems based on knowledge acquired from an expert [8]. An *auto-router* is a tool that routes automatically wires on a PCB based on given constraints.

HardSys. "HardSys", one of the first expert systems, has been proposed in [83] and evaluated in [84]. HardSys treats entire systems: electronics, shielding, etc. It deals with radiation coupling to electronics. Fields are considered scalar, as a worst case analysis. Frequency domain representation is used in the database for the storage of field magnitude. Ambient fields, path shielding effectiveness and component susceptibility are classified *qualitatively*. The underlying assumption is that certain radiation levels could potentially give problems but no quantification is attempted.

A tool for EMC of power supplies. This tool is described in [148] and it is meant for switching power supply design providing EMC prediction. It incorporates a layout editor, an auto-router, a component library builder, and an EMI simulator which creates models for SPICE.

ATHENA. ATHENA is a layout assistant tool developed within the environment of MENTOR GRAPHICS layout editor. ATHENA is presented in [92]. It has been developed in France by SEXTANT. It accounts for transmission line effects and crosstalk, but not for radiation. It can give simulated waveforms for selected wires.

EMIcheck. "EMIcheck" is a rule checker presented by Hubing in [59]. EMIcheck has been developed at University of Missouri-Rolla and by Quad Design Technologies. Recently, EMIcheck assumed an expert system structure [58]. EMIcheck evaluates a given PCB layout providing to the user a list of violated rules. Mostly, it is a design tool for users not familiar with electro-magnetic compatibility problems. First, a classification of each net and of each pin of the components is performed. Then, informations are obtained from data sheet files of the components and from the PCB layout file generated by other tools. The classification is still qualitative and it considers: radiation potentials, susceptibility potentials, power bus voltage, and if a signal is balanced and if it goes out of the board. EMC rules are checked. It incorporates a good set of rules.

However they are are not based on calculated/simulated/measured radiation levels or on noise effects on the circuit. Rules include: long nets (radiation and susceptibility potential), crosstalk, placement of components over the appropriate power plane, no unbalanced signal crossing gaps in their returning plane, no planes with thin necks. In parallel to the work of the rule checker, critical circuit geometries are individuated. Numerical simulation tools are then used to estimate radiated fields.

HERO. HERO is a Hierarchical auto-router developed at University of Paderborn in Germany by Lengauer and others [137]. Siemens has also collaborated to the project. This is a PCB router considering also *conducted* EMC constraints. The tool assumes a complete placement of the components is given. It considers only reflection (due to impedance mismatch between transmission lines and loads) and crosstalk. The routing is divided in two phases: first a "hierarchical" global routing is performed using linear programming techniques. In this phase reflection is taken into account controlling the maximum length of the nets. Then, a "sequential" detailed routing is performed considering also crosstalk. Blocks and nets are ordered. The routing proceeds net by net with a modified maze-running. In [127] a new layer-assignment and net-ordering phase is introduced after the global routing and before the detailed routing. A 50 percent performance improvement is achieved in this way. Completion rate is only 93 percent in the example presented. Only two EMC rules are implemented, but they are based on previous intensive simulations and measurements. This seems a very good approach applicable in the future also to radiation phenomena.

Chapter 15

Geometrically parameterized model order reduction

The work in this Chapter has been done in collaboration with Prof. Jacob White, Massachusetts Institute of Technology, and it has first appeared in [32, 31].

Developers of routing tools for mixed signal applications could make productive use of more accurate performance models for interconnect, but the cost of extracting even a modestly accurate model for a candidate route is far beyond the computational budget of the inner loop of a router. If it were possible to extract geometrically parameterized, but inexpensive to evaluate, models for the interconnect performance, then such models could be used for detailed interconnect synthesis in performance critical digital or analog applications.

The idea of generating parameterized reduced-order interconnect models is not new, recent approaches have been developed that focus on statistical performance evaluation [82, 55] and clock skew minimization [114]. However, our target application, interconnect synthesis, requires parameterized models valid over a wide geometric range. Generating such parameterized models is made difficult by the fact that even though the electrical behavior of interconnect can be modeled by a linear time-invariant dynamical system, that system typically depends nonlinearly on geometric parameters.

One recently developed technique for generating geometrically parameterized models of physical systems assumed a linear dependence on the parameter, and was applied to reducing a discretized linear partial differential equation [113]. The approach used closely paralleled the techniques used for dynamical system model reduction, an unsurprising fact given that if the parameter dependence is linear, the generated parameterized system of equations is structurally identical to a Laplace transform description of a linear time-invariant dynamical system, though the frequency variable is in the place of the geometric parameter.

The observation that geometric parameters and frequency variables are interchangeable, at least when the geometric variation is linear, suggests that the parameterized reduction problem could be formulated so as to make use of extensions to the projection-subspace based moment matching methods that have proved so effective in interconnect modeling [49, 46, 73, 53, 43, 97, 128, 12, 16]. In this Chapter we develop approaches for generating parameterized interconnect models exploiting just such a connection. In Section 15.1 we present a general problem formulation for an arbitrary number of parameters, and in Section 15.2 we present an extension to the multiple parameter moment-matching model reduction work in [144]. In Sections 15.3 we demonstrate the effectiveness of the method on a wire-spacing parameterized multi-line bus example, and consider both delay and cross-talk effects. In Section 15.4 we use the generalized multi-parameter model reduction approach to re-examine the multi-line bus example, but now allow both wire width and wire spacing to be parameters. Finally, conclusions are given in Section 15.6.

15.1 A general problem formulation

When modeling long interconnect wires, the long wires are usually modeled using a distribution of resistors and capacitors, and sometimes even inductors. Even if there is only one geometric parameter of interest, such interconnect examples still generate a multiparameter reduction problem, with frequency being the second parameter.

In order to derive an approach for the multiparameter problem, consider the following parameterized state space system model:

$$E(s_1,\ldots,s_\mu)x = Bu \quad (15.1)$$

$$y = Cx \quad (15.2)$$

where s_1,...,s_μ are μ parameters, x is the state of the system, $E(s_1,\ldots,s_\mu) \in \mathbf{C}^{n\times n}$ is the system descriptor matrix, B is a matrix relating the inputs u to the state x, and C is a matrix relating the state to the outputs y.

In general the descriptor matrix $E(s_1,\ldots,s_\mu)$ could have a complicated and non-linear dependency on the parameters s_1,...,s_μ. As a first step of our approach we capture such dependency by means of a power series in the parameters s_1,...,s_μ:

$$E(s_1,\ldots,s_\mu) = E_0 + \sum_i s_i E_i + \sum_{h,k} s_h s_k E_{h,k} + \sum_{h,k,j} s_h s_k s_j E_{h,k,j} + \ldots \quad (15.3)$$

One of the easiest ways to produce such a power series representation is to truncate a μ-variables Taylor series expansion:

$$E(s_1,\ldots,s_\mu) = E(\bar{s_1},\ldots,\bar{s_\mu}) + \sum_i \left(\frac{\Delta s_i}{\bar{s_i}}\right)\left[\bar{s_i}\frac{\partial E}{\partial s_i}(\bar{s_1},\ldots,\bar{s_\mu})\right] + \sum_{h,k}\left(\frac{\Delta s_h}{\bar{s_h}}\right)\left(\frac{\Delta s_k}{\bar{s_k}}\right)\left[\bar{s_h}\bar{s_k}\frac{\partial^2 E}{\partial s_h \partial s_k}(\bar{s_1},\ldots,\bar{s_\mu})\right] + \ldots \quad (15.4)$$

where $\bar{s_1},\ldots,\bar{s_\mu}$ are the expansion points. In a practical implementation, one could for instance choose the expansion points to coincide with the "nominal values" for each of the parameters. Also, in practical implementations one could be more interested in working explicitly with variables that represent relative variations $\Delta s_i/\bar{s_i}$ of the actual parameters around the expansion points, rather then working with absolute variations Δs_i. Finally, as an alternative to using a μ-variables Taylor series expansion, it is also possible to generate the power series representation using instead polynomial interpolation to a set of data points.

Given the power series representation in (15.3), a reduced order model can then be generated by using a congruence transformation on the power series representation

$$\left[V^*E_0V + \sum_i s_i V^*E_iV + \sum_{h,k} s_h s_k V^*E_{h,k}V + \sum_{h,k,j} s_h s_k s_j V^*E_{h,k,j}V + \ldots\right] x = V^*Bu \quad (15.5)$$

$$y = CVx \quad (15.6)$$

where $V \in \mathbf{C}^{n\times q}$, and the size q of the reduced order system matrices is typically much smaller than the size n of the original system matrices.

In order to calculate the column span of the projection matrix V, it is convenient to use the power series (15.3) to re-write system (15.1) as

$$\left[I - (\sum_i s_i(-E_0^{-1})E_i + \sum_{h,k} s_h s_k(-E_0^{-1})E_{h,k} + \sum_{h,k,j} s_h s_k s_j(-E_0^{-1})E_{h,k,j} + \ldots)\right] x = E_0^{-1}Bu \quad (15.7)$$

so that

$$\begin{aligned} x &= \left[I - \left(\sum_i s_i(-E_0^{-1})E_i + \sum_{h,k} s_h s_k(-E_0^{-1})E_{h,k} + \sum_{h,k,j} s_h s_k s_j(-E_0^{-1})E_{h,k,j} + \ldots\right)\right]^{-1} E_0^{-1}Bu \\ &= \sum_{m=0}^{\inf}\left[\sum_i s_i(-E_0^{-1})E_i + \sum_{h,k} s_h s_k(-E_0^{-1})E_{h,k} + \sum_{h,k,j} s_h s_k s_j(-E_0^{-1})E_{h,k,j} + \ldots\right]^m E_0^{-1}Bu \end{aligned}$$

15.2 P Parameter Model Order Reduction

One simple way to construct the columns of the projection matrix V for the reduced order model in (15.5) is to identify a new set parameters $\tilde{s}_i$ and matrices $\tilde{A}$, $\tilde{E}_i$

$$\begin{aligned}
\tilde{A} &= -E_0 \\
\tilde{E}_i &= \begin{cases} E_i & i = 1,\ldots,\mu \\ E_{h,k} & h = 1,\ldots,\mu;\ k = 1,\ldots,\mu \\ E_{h,k,j} & h = 1,\ldots,\mu;\ k = 1,\ldots,\mu\ j = 1,\ldots,\mu \\ \cdots \end{cases} \\
\tilde{s}_i &= \begin{cases} s_i & i = 1,\ldots,\mu \\ s_h s_k & h = 1,\ldots,\mu;\ k = 1,\ldots,\mu \\ s_h s_k s_j & h = 1,\ldots,\mu;\ k = 1,\ldots,\mu\ j = 1,\ldots,\mu \\ \cdots \end{cases}
\end{aligned}$$

so that one can re-write the parameterized system in (15.1) as a linearly parameterized model

$$[\tilde{s}_1\tilde{E}_1 + \cdots + \tilde{s}_p\tilde{E}_p - \tilde{A}]x = Bu \tag{15.8}$$

$$y = Cx \tag{15.9}$$

In the special case where the power series is constructed using a Taylor series expansion

$$\tilde{A} = -E(\bar{s_1},\ldots,\bar{s_p}) \tag{15.10}$$

$$\tilde{E}_i = \begin{cases} \left[\bar{s_i}\frac{\partial E}{\partial s_i}(\bar{s_1},\ldots,\bar{s_p})\right] & i = 1,\ldots,\mu \\ \left[\bar{s_h}\bar{s_k}\frac{\partial^2 E}{\partial s_h \partial s_k}(\bar{s_1},\ldots,\bar{s_p})\right] & h = 1,\ldots,\mu;\ k = 1,\ldots,\mu \\ \cdots \end{cases} \tag{15.11}$$

$$\tilde{s}_i = \begin{cases} \left(\frac{\Delta s_i}{s_i}\right) & i = 1,\ldots,\mu \\ \left(\frac{\Delta s_h}{s_h}\right)\left(\frac{\Delta s_k}{s_k}\right) & h = 1,\ldots,\mu;\ k = 1,\ldots,\mu \\ \cdots \end{cases} \tag{15.12}$$

In this simplified setting the reduced model is now

$$[\tilde{s}_1 V^*\tilde{E}_1 V + \cdots + \tilde{s}_p V^*\tilde{E}_p V - V^*\tilde{A}V]\hat{x} = V^*Bu \tag{15.13}$$

$$y = CV\hat{x} \tag{15.14}$$

and once again, in order to calculate the column span of the projection matrix V it is convenient to write the system (15.8) as

$$\begin{aligned}
[I - (\tilde{s}_1 M_1 + \cdots + \tilde{s}_p M_p)]x &= B_M u \\
y &= Cx
\end{aligned}$$

where

$$\begin{aligned}
M_i &= \tilde{A}^{-1}\tilde{E}_i \quad \text{for} \quad i = 1,2,\ldots,p \\
B_M &= -\tilde{A}^{-1}B
\end{aligned}$$

and finally

$$\begin{aligned}
x &= [I - (\tilde{s}_1 M_1 + \cdots + \tilde{s}_p M_p)]^{-1} B_M\, u \\
&= \sum_{m=0}^{\infty} [\tilde{s}_1 M_1 + \cdots + \tilde{s}_p M_p]^m B_M\, u \\
&= \sum_{m=0}^{\infty} \sum_{k_2=0}^{m-(k_3+\cdots+k_p)} \cdots \sum_{k_{p-1}=0}^{m-k_p} \sum_{k_p=0}^{m} [F^m_{k_2,\ldots,k_p}(M_1,\ldots,M_p)B_M\, u]\ \tilde{s}_1^{m-(k_2+\cdots+k_p)}\tilde{s}_2^{k_2}\ldots\tilde{s}_p^{k_p}
\end{aligned}$$

Lemma 11 *The coefficients of the series $F^m_{k_2,\ldots,k_p}(M_1,\ldots,M_p)$ can be calculated using:*

$$F^m_{k_2,\ldots,k_p}(M_1,\ldots,M_p) = \begin{cases} 0 & \text{if } k_i \notin \{0,1,\ldots,m\} \quad i=2,\ldots,p \\ 0 & \text{if } k_2+\cdots+k_p \notin \{0,1,\ldots,m\} \\ I & \text{if } m=0 \end{cases} \tag{15.15}$$

and for all other cases

$$\begin{aligned} F^m_{k_2,\ldots,k_p}(M_1,\ldots,M_p) &= M_1 F^{m-1}_{k_2,\ldots,k_p}(M_1,\ldots,M_p) + \\ &\quad + M_2 F^{m-1}_{k_2-1,\ldots,k_p}(M_1,\ldots,M_p) + \ldots \\ &\quad + M_p F^{m-1}_{k_2,\ldots,k_p-1}(M_1,\ldots,M_p) \end{aligned} \tag{15.16}$$

Proof. This can be shown by induction on m. For $m=0$ we can easily verify that

$$[\tilde{s}_1 M_1 + \cdots + \tilde{s}_p M_p]^0 = I. \tag{15.17}$$

Now assume for $m-1$ that

$$[\tilde{s}_1 M_1 + \cdots + \tilde{s}_p M_p]^{m-1} = \sum_{k_2=0}^{(m-1)-(k_3+\cdots+k_p)} \cdots \sum_{k_{p-1}=0}^{(m-1)-k_p} \sum_{k_p=0}^{m-1} [F^{m-1}_{k_2,\ldots,k_p}(M_1,\ldots,M_p)]\ \tilde{s}_1^{(m-1)-(k_2+\cdots+k_p)} \tilde{s}_2^{k_2} \ldots \tilde{s}_p^{k_p}, \tag{15.18}$$

in order to show that the property holds for m we can then simply observe that

$$\begin{aligned} &[\tilde{s}_1 M_1 + \cdots + \tilde{s}_p M_p]^m = \\ &[\tilde{s}_1 M_1 + \cdots + \tilde{s}_p M_p] \sum_{k_2=0}^{(m-1)-(k_3+\cdots+k_p)} \cdots \sum_{k_{p-1}=0}^{(m-1)-k_p} \sum_{k_p=0}^{m-1} [F^{m-1}_{k_2,\ldots,k_p}(M_1,\ldots,M_p)]\ \tilde{s}_1^{(m-1)-(k_2+\cdots+k_p)} \tilde{s}_2^{k_2} \ldots \tilde{s}_p^{k_p} = \end{aligned}$$

Multiplying and collecting the terms with the same powers of $\tilde{s}_1, \ldots \tilde{s}_p$

$$\begin{aligned} &= \sum_{k_2=0}^{(m-1)-(k_3+\cdots+k_p)} \cdots \sum_{k_{p-1}=0}^{(m-1)-k_p} \sum_{k_p=0}^{m-1} \Big[\tilde{s}_1 M_1 F^{m-1}_{k_2,\ldots,k_p}\ \tilde{s}_1^{(m-1)-(k_2+\cdots+k_p)} \tilde{s}_2^{k_2} \ldots \tilde{s}_p^{k_p} + \cdots + \\ &\quad + \cdots + \tilde{s}_p M_p F^{m-1}_{k_2,\ldots,k_p-1}\ \tilde{s}_1^{(m-1)-(k_2+\cdots+k_p)} \tilde{s}_2^{k_2} \ldots \tilde{s}_p^{k_p-1} \Big] = \\ &= \sum_{k_2=0}^{(m-1)-(k_3+\cdots+k_p)} \cdots \sum_{k_{p-1}=0}^{(m-1)-k_p} \sum_{k_p=0}^{m-1} \Big[M_1 F^{m-1}_{k_2,\ldots,k_p} + \cdots + M_p F^{m-1}_{k_2,\ldots,k_p-1} \Big]\ \tilde{s}_1^{m-(k_2+\cdots+k_p)} \tilde{s}_2^{k_2} \ldots \tilde{s}_p^{k_p}. \end{aligned}$$

which proves that the statement holds for m.
For a single input system ($B_M = b_M = -\tilde{A}^{-1} b \in \mathbf{C}^{n\times 1}$) The columns of V can be constructed to span the Krylov subspace

$$\begin{aligned} \text{colspan}(V) &= \text{span}\{b_M, M_1 b_M, M_2 b_M, \ldots, M_p b_M, M_1^2 b_M, (M_1 M_2 + M_2 M_1) b_M, \ldots, \\ &\quad \ldots, (M_1 M_p + M_p M_1) b_M, M_2^2 b_M, (M_2 M_3 + M_2 M_3) b_M, \ldots\}, \end{aligned}$$

or equivalently

$$\text{colspan}(V) = \text{span} \left\{ \bigcup_{m=0}^{m_q} \bigcup_{k_2=0}^{m-(k_p+\cdots+k_3)} \cdots \bigcup_{k_{p-1}=0}^{m-k_p} \bigcup_{k_p=0}^{m} F^m_{k_2,\ldots,k_p}(M_1,\ldots,M_p) b_M \right\}. \tag{15.19}$$

The following lemmas are useful to proof the main moment matching theorem for parameterized model order reduction.

Lemma 12

$$\hat{F}^m_{k_2,\ldots,k_p}\left[(V^*\tilde{A}V)^{-1}V^*\tilde{E}_1V,\ldots,(V^*\tilde{A}V)^{-1}V^*\tilde{E}_pV\right](V^*\tilde{A}V)^{-1}V^*b = V^*F^m_{k_2,\ldots,k_p}[\tilde{A}^{-1}\tilde{E}_1,\ldots,\tilde{A}^{-1}\tilde{E}_p]\tilde{A}^{-1}b. \quad (15.20)$$

Proof. A proof is given in this Chapter by induction on the order m of the coefficient. First let us prove the statement for $m=0$. $\hat{F}^0_{k_2,\ldots,k_p}\left[(V^*\tilde{A}V)^{-1}V^*\tilde{E}_1V,\ldots,(V^*\tilde{A}V)^{-1}V^*\tilde{E}_pV\right](V^*\tilde{A}V)^{-1}V^*b = I(V^*\tilde{A}V)^{-1}V^*b$. Since $\tilde{A}^{-1}b \in \text{colspan}(V)$, from Lemma 9 we have

$$(V^*\tilde{A}V)^{-1}V^*b = V^*\tilde{A}^{-1}b = V^*F^0_{k_2,\ldots,k_p}[\tilde{A}^{-1}\tilde{E}_1,\ldots,\tilde{A}^{-1}\tilde{E}_p]\tilde{A}^{-1}b.$$

This concludes the proof for m=0. Now assume that the statement is correct for order $m-1$ and let us show that this implies it is correct for order m. From the recursive definition formula (15.16),

$$\begin{aligned}
&\hat{F}^m_{k_2,\ldots,k_p}\left[(V^*\tilde{A}V)^{-1}V^*\tilde{E}_1V,\ldots,(V^*\tilde{A}V)^{-1}V^*\tilde{E}_pV\right](V^*\tilde{A}V)^{-1}V^*b = \\
&= [\,(V^*\tilde{A}V)^{-1}V^*\tilde{E}_1V\hat{F}^{m-1}_{k_2,\ldots,k_p}((V^*\tilde{A}V)^{-1}V^*\tilde{E}_1V,\ldots,(V^*\tilde{A}V)^{-1}V^*\tilde{E}_pV) + \ldots \\
&\cdots + (V^*\tilde{A}V)^{-1}V^*\tilde{E}_pV\hat{F}^{m-1}_{k_2,\ldots,k_p-1}((V^*\tilde{A}V)^{-1}V^*\tilde{E}_1V,\ldots,(V^*\tilde{A}V)^{-1}V^*\tilde{E}_pV)\,] \quad (V^*\tilde{A}V)^{-1}V^*b =
\end{aligned}$$

using the inductive hypothesis on order $m-1$ for each of the terms in the summation we have

$$= [(V^*\tilde{A}V)^{-1}V^*\tilde{E}_1VV^*F^{m-1}_{k_2,\ldots,k_p}(\tilde{A}^{-1}\tilde{E}_1,\ldots,\tilde{A}^{-1}\tilde{E}_p)+\cdots+(V^*\tilde{A}V)^{-1}V^*\tilde{E}_pVV^*F^{m-1}_{k_2,\ldots,k_p-1}(\tilde{A}^{-1}\tilde{E}_1,\ldots,\tilde{A}^{-1}\tilde{E}_p)]\;\tilde{A}^{-1}b =$$

using Lemma 8 on each of the terms of the summation,

$$\begin{aligned}
&= [(V^*\tilde{A}V)^{-1}V^*\tilde{E}_1F^{m-1}_{k_2,\ldots,k_p}(\tilde{A}^{-1}\tilde{E}_1,\ldots,\tilde{A}^{-1}\tilde{E}_p)+\ldots\cdots+(V^*\tilde{A}V)^{-1}V^*\tilde{E}_pF^{m-1}_{k_2,\ldots,k_p-1}(\tilde{A}^{-1}\tilde{E}_1,\ldots,\tilde{A}^{-1}\tilde{E}_p)]\;\tilde{A}^{-1}b = \\
&= (V^*\tilde{A}V)^{-1}V^*\left[\tilde{E}_1F^{m-1}_{k_2,\ldots,k_p}(\tilde{A}^{-1}\tilde{E}_1,\ldots,\tilde{A}^{-1}\tilde{E}_p)+\ldots\cdots+\tilde{E}_pF^{m-1}_{k_2,\ldots,k_p-1}(\tilde{A}^{-1}\tilde{E}_1,\ldots,\tilde{A}^{-1}\tilde{E}_p)\right]\tilde{A}^{-1}b =
\end{aligned}$$

since

$$\begin{aligned}
\tilde{A}^{-1}\left[\tilde{E}_1F^{m-1}_{k_2,\ldots,k_p}(\tilde{A}^{-1}\tilde{E}_1,\ldots,\tilde{A}^{-1}\tilde{E}_p)+\ldots\cdots+\tilde{E}_pF^{m-1}_{k_2,\ldots,k_p-1}(\tilde{A}^{-1}\tilde{E}_1,\ldots,\tilde{A}^{-1}\tilde{E}_p)\right]\tilde{A}^{-1}b = \\
= F^m_{k_2,\ldots,k_p}[\tilde{A}^{-1}\tilde{E}_1,\ldots,\tilde{A}^{-1}\tilde{E}_p]\tilde{A}^{-1}b \in \text{colspan}(V)
\end{aligned}$$

we can use Lemma 9 and obtain

$$\begin{aligned}
(V^*\tilde{A}V)^{-1}V^*\left[\tilde{E}_1F^{m-1}_{k_2,\ldots,k_p}(\tilde{A}^{-1}\tilde{E}_1,\ldots,\tilde{A}^{-1}\tilde{E}_p)+\ldots\cdots+\tilde{E}_pF^{m-1}_{k_2,\ldots,k_p-1}(\tilde{A}^{-1}\tilde{E}_1,\ldots,\tilde{A}^{-1}\tilde{E}_p)\right]\tilde{A}^{-1}b = \\
= V^*F^m_{k_2,\ldots,k_p}[\tilde{A}^{-1}\tilde{E}_1,\ldots,\tilde{A}^{-1}\tilde{E}_p]\tilde{A}^{-1}b.
\end{aligned}$$

This concludes the proof of Lemma 12.

Theorem 12 ***[Moment Matching Theorem] The first moments up to order*** m_q ***of the transfer function for the reduced order model (15.13) constructed using the*** q ***columns projection matrix*** $V \in \mathbf{C}^{n\times q}$ ***in (15.19) match the first moments up to order*** m_q ***of the transfer function of the original system (15.8).***

Proof. The transfer function of the system in (15.8) for a single input case ($B = b \in \mathbf{C}^{n\times 1}$) is given by

$$\begin{aligned}
H &= C\,[I-(\tilde{s}_1M_1+\cdots+\tilde{s}_pM_p)]^{-1}\tilde{A}^{-1}b \\
&= C\sum_{m=0}^{\infty}\sum_{k_2=0}^{m-(k_3+\cdots+k_p)}\cdots\sum_{k_{p-1}=0}^{m-k_p}\sum_{k_p=0}^{m}[F^m_{k_2,\ldots,k_p}(M_1,\ldots,M_p)\tilde{A}^{-1}b]\;\tilde{s}_1^{m-(k_2+\cdots+k_p)}\tilde{s}_2^{k_2}\ldots\tilde{s}_p^{k_p}
\end{aligned}$$

Similarly the transfer function of the system in (15.13) is given by

$$\begin{aligned}
\hat{H} &= CV\left[I-(\tilde{s}_1(V^*\tilde{A}V)^{-1}V^*\tilde{E}_1V+\cdots+\tilde{s}_p(V^*\tilde{A}V)^{-1}V^*\tilde{E}_pV)\right]^{-1}(-V^*\tilde{A}V)V^*b \\
&= CV\sum_{m=0}^{\infty}\sum_{k_2=0}^{m-(k_3+\cdots+k_p)}\cdots\sum_{k_{p-1}=0}^{m-k_p}\sum_{k_p=0}^{m}\Big[\hat{F}^m_{k_2,\ldots,k_p}((V^*\tilde{A}V)^{-1}V^*\tilde{E}_1V,\ldots, \\
&\qquad \ldots,(V^*\tilde{A}V)^{-1}V^*\tilde{E}_pV)(V^*\tilde{A}V)^{-1}V^*b\Big]\;\tilde{s}_1^{m-(k_2+\cdots+k_p)}\tilde{s}_2^{k_2}\ldots\tilde{s}_p^{k_p}
\end{aligned}$$

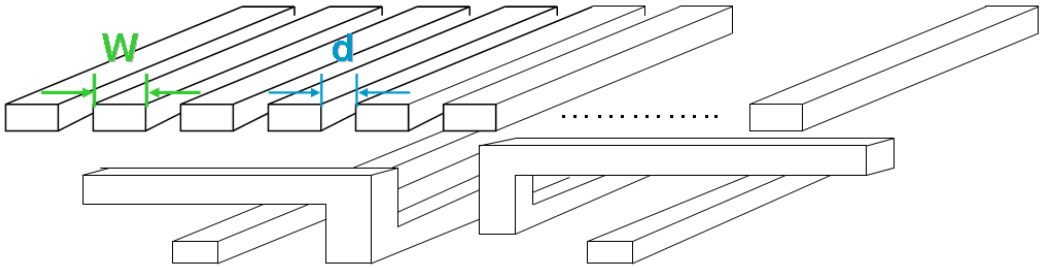

Figure 15.1: *Sketch of the modeled 16 parallel wires interconnect bus.*

Using first Lemma 12, and then Lemma 8, each moment of the reduced model transfer function is

$$\begin{aligned} C\hat{F}^m_{k_2,\ldots,k_p}[(V^*\tilde{A}V)^{-1}V^*\tilde{E}_1V,\ldots,(V^*\tilde{A}V)^{-1}V^*\tilde{E}_pV] \quad (V^*\tilde{A}V)^{-1}V^*b &= CVV^*F^m_{k_2,\ldots,k_p}(\tilde{A}^{-1}\tilde{E}_1,\ldots,\tilde{A}^{-1}\tilde{E}_p)\tilde{A}^{-1}b \\ &= CF^m_{k_2,\ldots,k_p}(\tilde{A}^{-1}\tilde{E}_1,\ldots,\tilde{A}^{-1}\tilde{E}_p)\tilde{A}^{-1}b. \end{aligned}$$

For a multi-input system the columns of V can then be constructed to span the Krylov subspaces produced by all the columns $[b_M]_j$ of B_M:

$$\begin{aligned} &\text{colspan}(V) = \\ &= \text{span}\left\{ \bigcup_{m=0}^{m_q} \bigcup_{k_2=0}^{m-(k_p+\ldots k_3)} \ldots \bigcup_{k_p=0}^{m} F^m_{k_2,\ldots,k_p}[b_M]_1, \ldots, \bigcup_{m=0}^{m_q} \bigcup_{k_2=0}^{m-(k_p+\ldots k_3)} \ldots \bigcup_{k_p=0}^{m} F^m_{k_2,\ldots,k_p}[b_M]_j \right\} \end{aligned}$$

15.3 Example: a bus model parameterized in the wires' spacing

One design consideration for interconnect busses is the trade-off between:

- wider spacing to reduce propagation delays and crosstalk
- narrower spacing to reduce area and therefore cost.

In this example we have used a multi-parameter model order reduction approach to construct a low-order model of an interconnect bus, parameterized by the wire spacing. The model can be efficiently constructed "on the fly" during the design and can account for the topology of the surrounding interconnect already present in the design. Once produced, the model can be simply evaluated for different values of the main parameter, the wire spacing, in order to determine propagation delay, crosstalk or even detailed step responses.

Our example problem is the bus in Fig. 15.1 which consists of $N = 16$ parallel wires, with thickness $h = 1.2\mu$m, and width $w = 1\mu$m. The total length of each wire is $l = 1$mm. Above and below our bus we assumed a random collection of interconnect at several layout levels ranging from a distance of 1μm to 5μm. We have subdivided each wire into 20 equal sections delimited by $n = 21$ nodes. Each section has been modeled with a resistor. Each node has a "grounded capacitor" representing the interaction with upper and lower interconnect levels. In addition, each node has two coupling capacitors to the adjacent wires on the bus as shown in Fig. 15.2. The value of the capacitors was determined using simple parallel plate formulas. Standard frequency domain nodal analysis leads to a system of equations of the form

$$s\left(C_g + \frac{C_s}{d}\right)v + Gv = Bv_{in} \tag{15.21}$$

$$v_{out} = Cv, \tag{15.22}$$

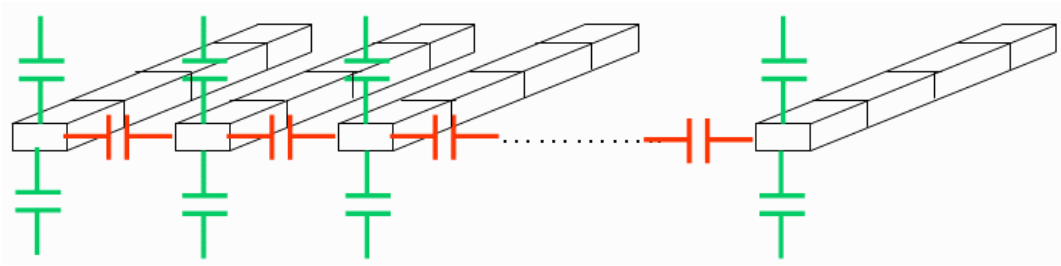

Figure 15.2: *Discretization of the bus wires and coupling capacitors included in the model.*

where s is the Laplace Transform variable, d is the spacing between wires, G is the $n \times n$ nodal conductance matrix, The $n \times n$ matrix C_g is the diagonal nodal matrix associated with the grounded capacitors, and C_s is the sparse nodal matrix associated with the adjacent coupling capacitors. B is the $n \times t$ matrix relating t input voltages v_{in} to the n internal node potentials v, C is a $t \times n$ matrix relating node potentials v to the t output voltages v_{out}. We would like to underline that our model is limited to capturing the behavior of the interconnect, which is linear for almost all practical applications. Our models can then be used in conjunction with any device model, from the most simple linear device model to the most sophisticated spice device model. It is not the purpose of this Chapter to discuss model for devices, however, just in order to "simulate" our interconnect model, for simplicity we will drive our wires with ideal linear devices having impedance $r_d = 1/g_d$. In general when g_d is small compared to the wire conductance, all the capacitors in the different sections of each wire appear as lumped, and the detailed model presented here is not necessary. A more interesting case is observed when instead g_d is large. In such case the wires charge up slowly from the input side of the bus and continue to charge up along the length of the bus. In order to observe this more interesting effect we chose $g_d = g$ where g is the conductance of each of the 20 sections in each wire. All the wires are left open on the other side.

15.3.1 Crosstalk from one input to all outputs

When determining the crosstalk generated on all the outputs by a transition on a single input, the input matrix becomes a vector,

$$B = b = [0 \ldots 0\, g_d\, 0 \ldots 0]^*, \tag{15.23}$$

and the output matrix is

$$C = \begin{bmatrix} \ldots 010 \ldots & & & \\ & \ldots 010 \ldots & & \\ & & \ddots & \\ & & & \ldots 01 \end{bmatrix} \tag{15.24}$$

The system in (15.21) has the following parameterized descriptor matrix

$$E\left(s, \frac{1}{d}\right) = sC_g + s\frac{1}{d}C_s + G; \tag{15.25}$$

where we choose to work with parameter $1/d$ instead of parameter d. For frequency s we choose as expansion point $\bar{s_1} = \bar{s} = 0$. For the separation we choose $\bar{s_2} = 1/d_0 = 1/1\mu$m.

$$E\left(s, \frac{1}{d}\right) = G + s\left[C_g + \frac{1}{d_0}C_s\right] + s\left(\frac{\Delta\left(\frac{1}{d}\right)}{\frac{1}{d_0}}\right)\left[\frac{1}{d_0}C_s\right] \tag{15.26}$$

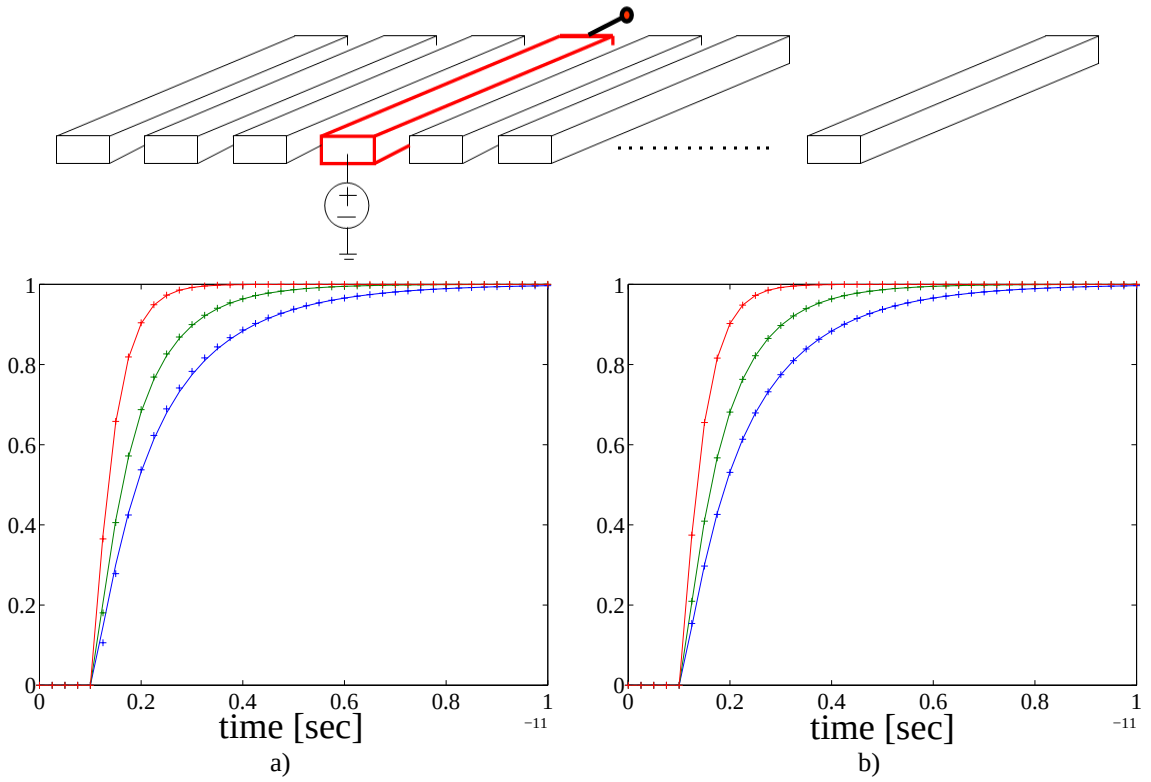

Figure 15.3: *Responses at the end of wire 4 when a step is applied at the beginning of the same wire. Continuous lines are the response of the original system (order 336). Small crosses are the response of the reduced model, order 3 on the left, and order 6 on the right. The model was constructed using a nominal wire spacing $d_0 = 1um$ and responses are shown here evaluating it at spacings (from the lowest curves to the highest) $d = d_0 + \Delta d = 0.5\mu m, 1\mu m, 10\mu m$.*

Either by identifying terms directly on eq. (15.26) or by using the formulas in (15.10)-(15.12), one can recognize a system as in (15.8) defining

$$\begin{aligned}
\tilde{A} &= -G \\
\tilde{E}_1 &= C_g + \frac{1}{d_0} C_s \\
\tilde{E}_2 &= \frac{1}{d_0} C_s \\
\tilde{s}_1 &= s \\
\tilde{s}_2 &= s \left(\frac{\Delta\left(\frac{1}{d}\right)}{\frac{1}{d_0}} \right)
\end{aligned}$$

The original system for this example has order 336 (16 wires $\times$ 21 nodes each). We performed a model order reduction procedure as described in Section 15.2 and obtained a small model capturing the transfer functions from one input to all outputs.

$$[\tilde{s}_1 \hat{\tilde{E}}_1 + \tilde{s}_2 \hat{\tilde{E}}_2 - \hat{\tilde{A}}]\hat{x} = \hat{b}u \quad (15.27)$$

$$y = \hat{C}\hat{x} \quad (15.28)$$

where

$$\begin{aligned}
\hat{\tilde{A}} &= V^* \tilde{A} V = -V^* G V \\
\hat{\tilde{E}}_1 &= V^* \tilde{E}_1 V = V^* \left[C_g + \frac{1}{d_0} C_s \right] V \\
\hat{\tilde{E}}_2 &= V^* \tilde{E}_2 V = V^* \left[\frac{1}{d_0} C_s \right] V \\
\hat{b} &= V^* b \\
\hat{C} &= CV.
\end{aligned}$$

The projection matrix V can be constructed such that

$$\text{colspan}(V) = \text{span}\{b_M,\, M_1 b_M,\, M_2 b_M,\, M_1^2 b_M,\, (M_1 M_2 + M_2 M_1) b_M,\, M_2^2 b_M,\, \dots\},$$

where

$$\begin{aligned}
b_M &= -\tilde{A}^{-1} b = G^{-1} b \\
M_1 &= \tilde{A}^{-1} \tilde{E}_1 = -G^{-1} \left[C_g + \frac{1}{d_0} C_s \right] \\
M_2 &= \tilde{A}^{-1} \tilde{E}_2 = -G^{-1} \left[\frac{1}{d_0} C_s \right]
\end{aligned}$$

The Arnoldi algorithm [53] can be used to orthonormalize the columns of V during the matrix construction.

The step response at the end of the wire excited in Fig 15.3 is shown in Fig 15.3.a comparing the step responses of the original system (continuous lines) and a reduced model of order three (small crosses) when the spacing distance assumes the values $d = d_0 + \Delta d = 0.5\mu m, 1\mu m, 10\mu$m. The model was constructed using a nominal spacing $d_0 = 1\mu$m, hence the error is smaller near $d \approx d_0 = 1\mu$m. Fig. 15.3.b shows the same comparison with a reduced model of order six. One can notice that the reduced model can be easily and accurately used to evaluate the step response and propagation delay for any value of parameter d around d_0 plugging into the reduced model (15.27). From the reduced model (15.27) we have readily available not only step responses on the same wire, but also crosstalk step responses from one wire to all the other wires. Fig. 15.4.a shows for instance step responses from the input of wire 4 to the output of wires 4, 5, 6 and 7. In this figure we compare again the response of the original system order 336 (continues curves) with the response of a reduced model order 10 (small crosses) constructed at nominal spacing $d_0 = 1\mu$m, but evaluated in this particular figure at spacing $d = 0.5\mu$m. Note that the model produced by our procedure is parameterized in the wire spacing, hence *any* of such crosstalk responses can be evaluated at *any* spacing. For instance we show in Fig. 15.4.b the response at the output of wire 5 when a step waveform is applied at the input of wire 4 for different spacing values, $d = d_0 + \Delta d = 0.5\mu m, 1\mu m, 10\mu m$.

15.3.2 Exploiting the adjoint method for crosstalk from all inputs to one output

It is possible to construct with the same amount of calculation a model that provides the susceptibility of one output to all inputs. In order to do this we can use an adjoint method and start from an original system which swaps positions of C and B and transposes all system matrices. Note that since we are considering a single output $C \in \mathbf{C}^{1\times n}$ and $C^T \in \mathbf{C}^{n\times 1}$ is a vector.

$$\begin{aligned}
\left[I - (\tilde{s}_1 M_1^T + \tilde{s}_2 M_2^T) \right] v' &= C^T v'_{in} \qquad (15.29) \\
v'_{out} &= B_M^T v', \qquad (15.30)
\end{aligned}$$

In this case the columns of the projection operator V will span the Krylov subspace

$$\begin{aligned}
\text{colspan}(V') = \text{span}\{ & C^T,\, M_1^T C^T,\, M_2^T C^T,\, M_1^T M_1^T C^T, \\
& (M_1^T M_2^T + M_2^T M_1^T) C^T,\, M_2^T M_2^T C^T,\, \dots\}
\end{aligned}$$

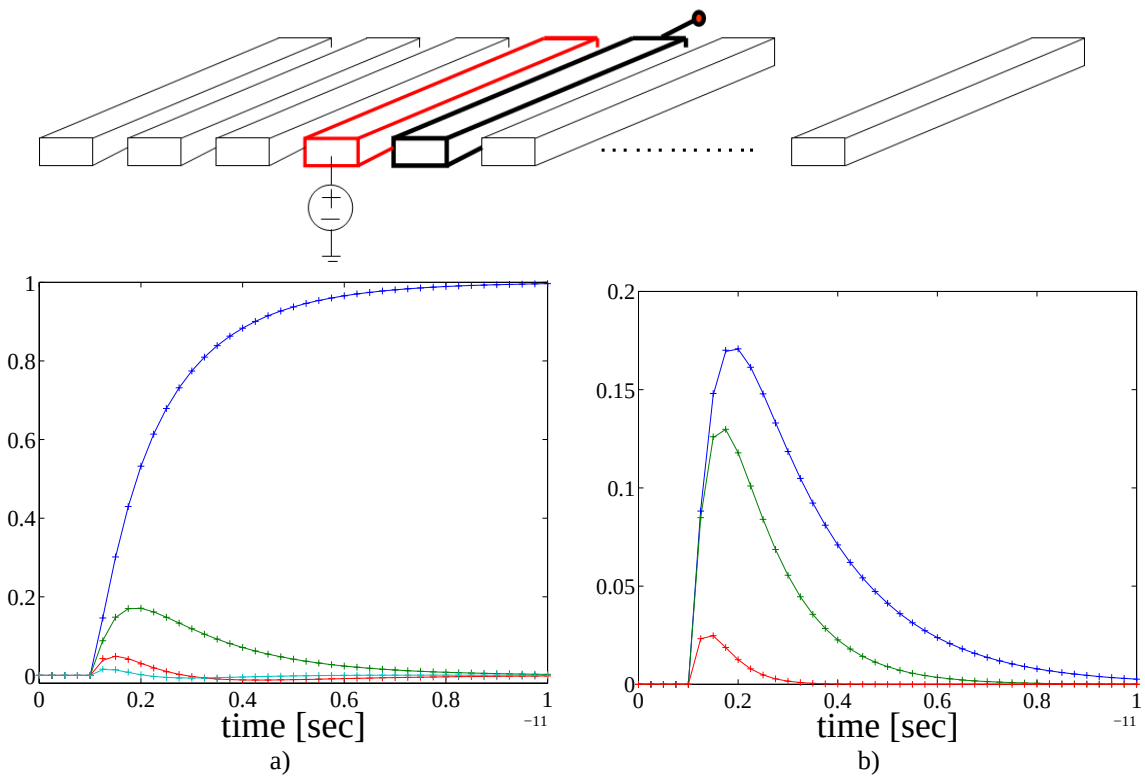

Figure 15.4: *On the left: responses at the end of wires (from highest to lowest curve) 4, 5, 6 and 7 when a step is applied at the beginning of wire 4. Continuous lines are the response of the original system (order 336). Small crosses are the response of the reduced model (order 10). The model was constructed using a nominal wire spacing* $d_0 = 1um$ *and responses are shown here evaluating it at spacing* $d = 0.5\mu m$*. On the right: crosstalk responses at the end of wire 5 when a step is applied at the beginning of wire 4, for different values of spacing (from highest to lowest curve)* $d = d_0 + \Delta d = 0.5\mu m, 1\mu m, 10\mu m$*.*

or in general

$$\text{colspan}(V') = \text{span}\left\{ \bigcup_{m=0}^{m_q} \left(\bigcup_{k=0}^{m} F_k^m(M_1^T, M_2^T) C^T \right) \right\}. \tag{15.31}$$

In Fig. 15.5 we show the responses at the end of wire 4 when a step is applied at the beginning of wires 4, 5, 6 and 7. The model was constructed using a nominal wire spacing $d_0 = 1um$. Responses in Fig. 15.5.a are for $d = 0.25\mu m$. Responses in Fig. 15.5.b are for $d = 2\mu m$.

15.4 Example: bus model parameterized in both wire width and separation

Often when designing an interconnect bus, one would like to quickly evaluate design trade-offs originating not only from different wire spacings, but also for different wire widths. Wider wires have lower resistances but use more area and have higher capacitance. The higher capacitance to ground however helps improving crosstalk immunity. We show here a procedure that produces small models that can be easily evaluated with respect to propagation delays and crosstalk performance for different values of the two parameters: wire

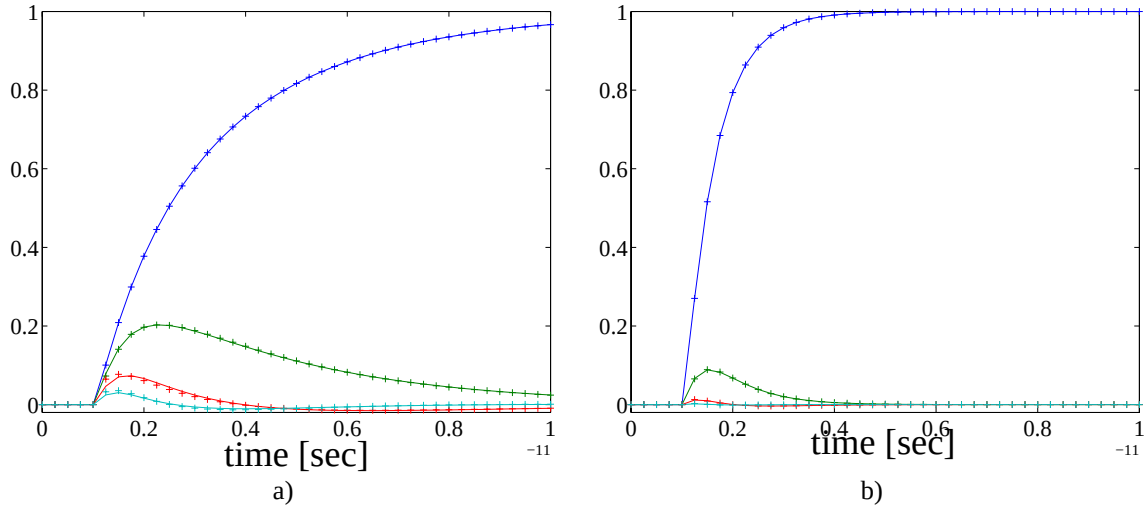

Figure 15.5: *Responses at the end of wire 4 when a step is applied at the beginning of wires 4, 5, 6 and 7 (from highest to lowest curve). Continuous lines are the response of the original system (order 336). Small crosses are the response of the reduced model (order 10). The model was constructed using* $d_0 = 1um$. *Responses on the left are for* $d = 0.25\mu m$, *and on the right for* $d = 2\mu m$.

spacing d, and wire width W. As in the case of wire spacing, we constructed models for a given nominal wire width W_0, and then we parameterized in terms of perturbations ΔW. Considering the same bus example with N parallel wires described in Section 15.3, we can write the equations for the original large parameterized linear system

$$\begin{aligned} s\left(WC_g' + \frac{C_s}{d}\right)v + WG'v &= Bv_{in} \\ v_{out} &= Cv \end{aligned}$$

The system has the following parameterized descriptor matrix

$$E\left(s, \frac{1}{d}, W\right) = sWC_g' + s\frac{1}{d}C_s + WG'; \tag{15.32}$$

where $C_g' = C_g/W$, $G' = G/W$, and C_g and G are as described in Section 15.3. With respect to the expansion points $\bar{s_1} = \bar{s_0} = 0$, $\bar{s_2} = 1/d_0$, $\bar{s_3} = W_0$,

$$E\left(s, \frac{1}{d}\right) = W_0G' + s\left[W_0C_g' + \frac{1}{d_0}C_s\right] + \left(\frac{\Delta W}{W_0}\right)[W_0G'] + s\left(\frac{\Delta W}{W_0}\right)[W_0C_g'] + s\left(\frac{\Delta\left(\frac{1}{d}\right)}{\frac{1}{d_0}}\right)\left[\frac{1}{d_0}C_s\right] \tag{15.33}$$

Either by identifying terms directly on eq. (15.33) or by using the formulas in (15.10)-(15.12), one can recognize a system as in (15.8) defining

$$\begin{aligned}
\tilde{A} &= -W_0 G' \\
\tilde{E}_1 &= W_0 C_g' + \frac{1}{d_0} C_s \\
\tilde{E}_2 &= W_0 G' \\
\tilde{E}_3 &= W_0 C_g' \\
\tilde{E}_4 &= \frac{1}{d_0} C_s \\
\tilde{s}_1 &= s \\
\tilde{s}_2 &= \frac{\Delta W}{W_0} \\
\tilde{s}_2 &= s\left(\frac{\Delta W}{W_0}\right) \\
\tilde{s}_2 &= s\left(\frac{\Delta\left(\frac{1}{d}\right)}{\frac{1}{d_0}}\right)
\end{aligned}$$

Following the procedure in Section 15.2 the produced reduced order model is

$$[\tilde{s}_1\hat{\tilde{E}}_1 + \tilde{s}_2\hat{\tilde{E}}_2 + \tilde{s}_3\hat{\tilde{E}}_3 + \tilde{s}_4\hat{\tilde{E}}_4 - \hat{\tilde{A}}]\hat{x} = \hat{B}u \tag{15.34}$$

$$y = \hat{C}\hat{x} \tag{15.35}$$

where

$$\begin{aligned}
\hat{\tilde{A}} &= V^* \tilde{A} V = -V^* W_0 G' V \\
\hat{\tilde{E}}_1 &= V^* \tilde{E}_1 V = V^* \left[W_0 C_g' + \frac{1}{d_0} C_s\right] V \\
\hat{\tilde{E}}_2 &= V^* \tilde{E}_2 V = V^* \left[W_0 G'\right] V \\
\hat{\tilde{E}}_3 &= V^* \tilde{E}_3 V = V^* \left[W_0 C_g'\right] V \\
\hat{\tilde{E}}_4 &= V^* \tilde{E}_4 V = V^* \left[\frac{1}{d_0} C_s\right] V \\
\hat{B} &= V^* B \\
\hat{C} &= CV.
\end{aligned}$$

The projection matrix V can be constructed for instance for a single input case ($B = b \in \mathbf{C}^{n\times 1}$) as shown in (15.19) where

$$\begin{aligned}
b_M &= -\tilde{A}^{-1} b = (W_0 G')^{-1} b \\
M_1 &= \tilde{A}^{-1}\tilde{E}_1 = -(W_0 G')^{-1}\left[W_0 C_g' + \frac{1}{d_0} C_s\right] \\
M_2 &= \tilde{A}^{-1}\tilde{E}_2 = -(W_0 G')^{-1}\left[W_0 G'\right] \\
M_3 &= \tilde{A}^{-1}\tilde{E}_3 = -(W_0 G')^{-1}\left[W_0 C_g'\right] \\
M_4 &= \tilde{A}^{-1}\tilde{E}_4 = -(W_0 G')^{-1}\left[\frac{1}{d_0} C_s\right]
\end{aligned}$$

The Arnoldi algorithm [53] can be used to orthonormalize the columns of V during the matrix construction.

In Fig. 15.6 we compare the step and crosstalk responses of the original system to the reduced and parameterized model obtained using a Krylov subspace of order $q = 5$. This corresponds to choosing $m_q = 1$ in (15.19), or in other words it corresponds to constructing a reduced model that matches the original model up to one moment (or derivative) for each parameter. The model was constructed using a nominal spacing $1/d_0 = 1/1\mu$m and nominal wire width $W_0 = 1\mu$m. The key point is that this parameterized model can be rapidly evaluated for any value of spacing and wire width, for instance for a fast and accurate trade-off design optimization procedure.

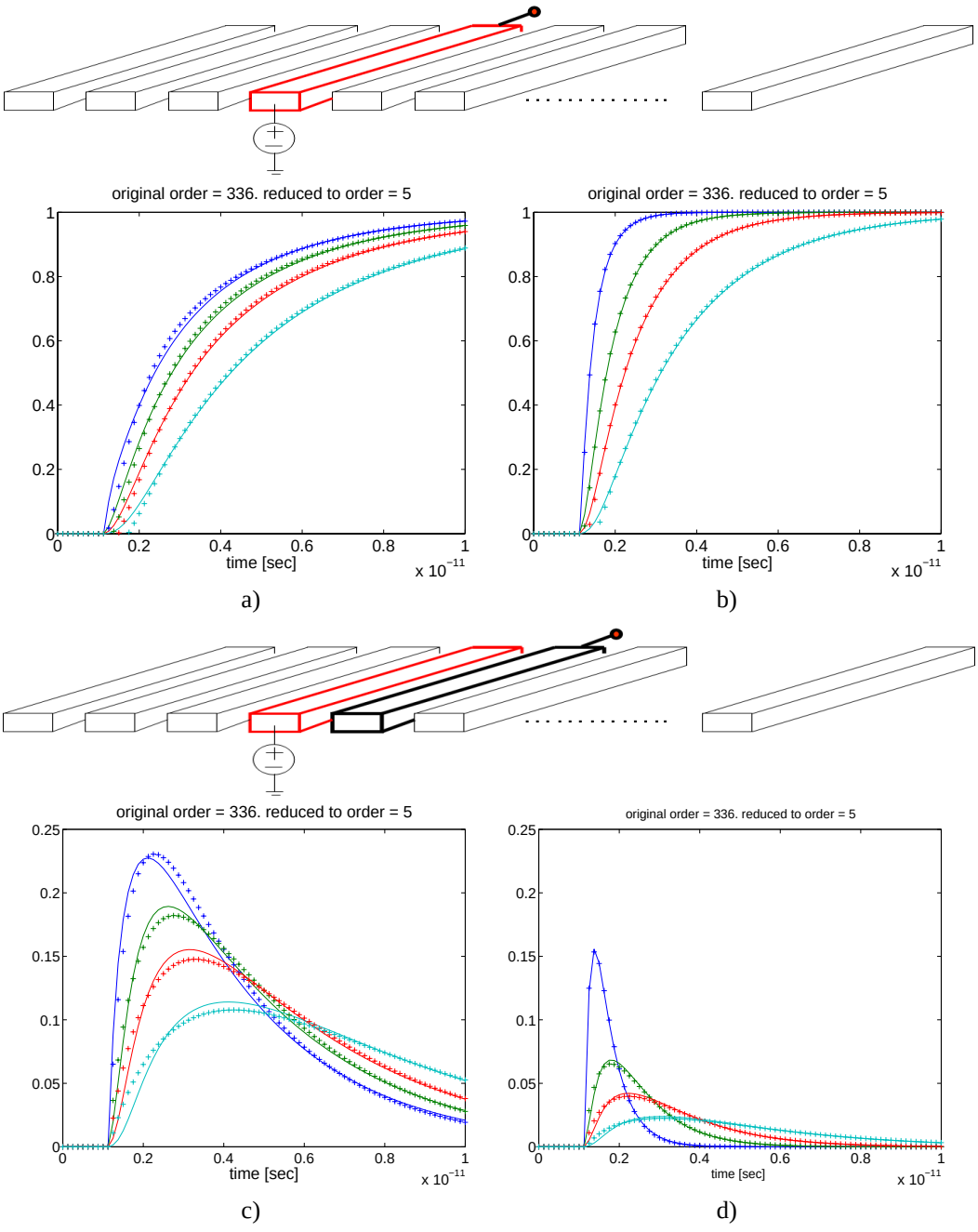

Figure 15.6: *Original system (continuous curves) versus* 5^{th} *order reduced model (small crosses) using both spacing and width parameters. The nominal wire spacing was* $d_0 = 1\mu m$ *and the nominal wire width was* $W = 1\mu m$*. Responses at the end of wire 4 due to a step at the beginning of the same wire are show in a) for different widths (from highest to lowest curve)* $W = .25\mu m, 2\mu m, 4\mu m, 8\mu m$ *and for spacing* $d = .25\mu m$*. In b) we show the same responses but for spacing* $d = 2\mu m$*. In c) we show the crosstalk response at the end of wire 5 due to a step at the beginning of wire 4. Curves correspond to widths (from highest curve to lowest)* $W = .25\mu m, 2\mu m, 4\mu m, 8\mu m$ *and spacing is* $d = .25\mu m$*. In d) we show the same crosstalk responses but for spacing* $d = 2\mu m$*.*

15.5 Computational complexity

Lemma 13 *If p is the total number of parameters and m_q is the largest order of derivative that will be matched with respect to any parameter, then the order q of the parameterized reduced system is*

$$q = O\left(\frac{p^{m_q}}{m_q^{m_q-\frac{1}{2}}}\right) \tag{15.36}$$

Proof. The number $f_{m,p}$ of coefficients of order m, for a system with p parameters, can be obtained by induction

$$f_{m,p} = \begin{cases} 1 & \text{if } m = 0, \\ \sum_{k=1}^{p} f_{m-1,k} & \text{if } m > 0 \end{cases} \tag{15.37}$$

or equivalently,

$$f_{m,p} = f_{p-1,m+1} = \begin{pmatrix} m+p-1 \\ m \end{pmatrix} = \begin{pmatrix} m+p-1 \\ p-1 \end{pmatrix} = \frac{(m+p-1)!}{m!(p-1)!} \tag{15.38}$$

Using then the asymptotic approximation [2] for the Gamma Function $\Gamma(z) = (z-1)!$, one obtains

$$f_{m,p} = \frac{\Gamma(m+p)}{\Gamma(m+1)\Gamma(p)} \approx \frac{e}{\sqrt{2\pi}} \frac{(m+p)^{m+p-\frac{1}{2}}}{m^{m+\frac{1}{2}} p^{p-\frac{1}{2}}}. \tag{15.39}$$

Observing that for most practical problems $m << p$, we have

$$f_{m,p} = O\left(\frac{p^m}{m^{m+\frac{1}{2}}}\right). \tag{15.40}$$

The order q of the produced parameterized reduced system is then

$$q = \sum_{m=0}^{m_q} f_{m,p} = O(m_q f_{m,q}) = O\left(\frac{p^{m_q}}{m_q^{m_q-\frac{1}{2}}}\right). \tag{15.41}$$

One way to improve accuracy is to increase m_q. Unfortunately, with large m_q the order of the produced model might quickly become impractical. When $m_q = 1$, the order of the produced model scales linearly with the number of parameters and a large number of parameters can be handled. In some applications the accuracy given by matching a single derivative per parameter can be good enough. In particular, we recall that many of the examples presented in this Chapter are obtained using $m_q = 1$ and show good accuracy. Using $m_q = 2$ improves the accuracy but generates a larger system. For example, with $m_q = 2$ the order of the produced parameterized model is

$$q = f_{0,p} + f_{1,p} + f_{2,p} = 1 + p + \frac{p(p+1)}{2} = \frac{p^2+3p+2}{2} \tag{15.42}$$

which implies that a 66^{th} order model will be generated from a problem with $p = 10$ parameters. For larger values of m_q, impractically large models will be generated even for a small number of parameters p.

In terms of computational cost, it is important to make a distinction between the cost of "constructing" the model and the cost of "evaluating" the model. The models constructed by our procedure are extremely small compared to the original systems, therefore their evaluation cost is also small compared to the construction cost. In particular, when constructing the model, most of the cost is in constructing each of the q columns of matrix V. In particular, generating vectors $F^m b_M$ in eq. (15.19), is the most expensive operation, given that it involves one linear system solve and several matrix-vector multiplications. In order to make the cost of model computation practical one can use Krylov subspace iterative methods combined with "fast-methods" [94, 68, 110, 136, 71] for the required matrix-vector products. Exploiting such well developed techniques we need to perform $O(n)$ operations for each column of V. Hence the total construction cost is $O(qn)$, where q is typically not larger than few hundreds, and n can be as large as hundreds of thousands. When evaluating the model one needs only solve a small matrix of size q, therefore the evaluation cost is very low.

15.6 Conclusions on parameterized model order reduction

In this Chapter we described an approach for generating geometrically - parameterized integrated-circuit interconnect models that are efficient enough for use in interconnect synthesis. The model generation approach presented is automatic, and is based on series expansion of the parameter dependence followed by multi-parameter model-reduction. The effectiveness of the techniques described were tested using a multi-line bus example. Multiparameter model reduction was used to generate, from a formula based capacitance and resistance extraction algorithm, high order models for the dependence of delay and cross-talk on line separation and conductor width. The experimental results clearly demonstrated the reduction strategies generated models that were accurate over a wide range of geometric variation.

It should be noted, however, that there are closed-form analytical models which relate geometric parameters to self and coupling capacitances, and the model reduction approaches presented herein are unlikely to be as efficient. However, the methods presented here are potentially more accurate, and certainly more automatic and more flexible.

Chapter 16

Future work in synthesis

16.1 Further development of parameterized model order reduction algorithms

There are many potential issues that can lead to new contributions in the field of parameterized model order reduction described in the previous Chapter 15. The multi-parameter method was tested using only resistor-capacitor interconnect models, and accuracy issues may arise when inductance is included. We also did not investigate using multi-point moment-matching, which could be a better choice given the range of the parameters is often known a-priori. In addition, the multi-parameter reduction method can become quite expensive when a large accuracy is required and the model has a large number of parameters, so the method would not generate a very efficient model if each wire pair spacing in a 16 wire bus was treated individually. Finally, there are some interesting error bounds in [113], and these results could be applied to automatically select the reduction order.

16.2 Sizing of on-package and on-chip decoupling capacitors

We now address EMI emissions due to the switching activity of digital chips in Systems-on-PCB, or EMI due to the switching activity of digital IP blocks in Systems-on-Chip. As described in Section 1.4, our methodology propagates EMC constraints down along the branches of the system hierarchy until leaves are encountered. In this case, a leaf can be represented by the insertion of one or more decoupling capacitors around some digital switching blocks. According to our top-down synthesis with bottom-up verification scheme, we need:

- a way to estimate the size of such capacitors for the bottom-up phase. To address this task we present here:
  - a technique to build a small but effective circuit model for the switching block,
  - and a technique to build a small but effective circuit model for the global Vdd and Gnd system.

  Given the two models, sizing the capacitors is just a matter of solving a few circuit equations.
- We also need a way to verify the effectiveness of the chosen capacitors for the bottom-up phase. For this task we can simply use our simulation tool described in Part I.

16.2.1 Model of the internal switching activity of the blocks.

In order to model the switching blocks, we need

- to estimate the current spikes produced on the global Vdd/Gnd system by the switching events.
- We also need to estimate the amount of capacitance between Vdd and Gnd already present inside the switching block.

The final goal is a very simple model as shown in Fig. 16.1

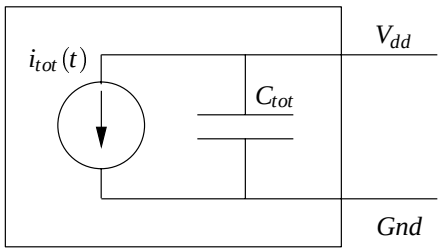

Figure 16.1: *Simple model of a switching digital circuit block. The current source models the spikes of currents, and it is characterized by the spectrum of such conducted emissions. The capacitors models the amount of decoupling capacitance already present inside the block.*

Estimation of the current sources

Simulating with Spice the entire chip would not be feasible because of the millions of gates on a die. In order to get the current on the Vdd and ground pins, one could for example realize that a power estimation tool calculating the "instant power consumption" $p_{tot}(t)$ of a circuit, provides the desired current waveform result $i_{tot}(t)$ in the assumption that the supply voltage V_{dd} is almost constant

$$i_{tot}(t) = \frac{p_{tot}(t)}{V_{dd}}. \tag{16.1}$$

We propose here an alternative, and probably more accurate simulation technique. We are implementing a method which was originally designed and presented in [91, 22] to model substrate noise on integrated circuits.

1. Spice simulations are first used to pre-characterize the current spikes on the supply system for each type and for each size of gates present in the chip. Note that there are no more than hundreds of types and sizes of gates on a chip. Hence this operation is reasonably fast, and it gives a table with all the current waveforms $i(t)$ produced by each type and size of gate.

2. The digital circuit is then simulated by an *event driven simulator*. Such a simulator works at the gate level, not at the transistor level such as for example Spice. This is a common method for digital circuit timing verification.

   - Each gate is pre-characterized by its propagation delay d_i.
   - A queue of events is initialized at the clock signal. Each element in a queue will contain a gate and the time when that gate is supposed to begin its switching action.
   - Every time a gate j is extracted from the queue, new events corresponding to the gate fun-outs are inserted in the queue at a new time position t_{new}:

     $$t_{new} = t_{present} + d_j \tag{16.2}$$

     where $t_{present}$ is the present simulation time

The output of the event driven simulator, for our purposes, is the queue itself, indicating what gate is switching and at what exact time it switches during the clock period. The event simulation does not need to solve any circuit equation, hence it is extremely fast. For example, even millions of gates can be simulated for many clock cycles in no time.

3. The final current waveform on the Vdd and ground system can be calculated simply adding all the contributions from all the switching gates, according to the information in the event queue. This is basically a convolution operation:

$$i_{tot}(t) = \sum_j i_j(t - \tau_j) \tag{16.3}$$

where τ_j is the time gate j begins switching, and $i_j(t)$ is the current waveform on the supply obtained from the table for the type and size of gate in consideration.

The result of this procedure is the high frequency current waveform present on the supply system. In order to have a significant information on the typical chip operation mode, we need to run the event driven simulator for hundreds or thousands of clock cycles, varying the inputs of the circuit. Such operation, as mentioned above is still very fast, having about linear computational complexity both in the size of the circuit and in the number of simulated clock cycles. Finally, we can apply a Fast Fourier Transform on the time domain current waveform to obtain the desired spectrum.

Further developments

The technique just described has the disadvantage of calculating the current for a very specific evolution of the input vectors. It would be of utmost importance to develop instead a technique to calculate an *upper bound* for the current spectrum at each clock harmonic for all possible input vector evolutions.

Estimation of the internal capacitance

Capacitance between Vdd and ground can substantially reduce the conducted emissions we are considering in this section. Some capacitance is already present inside the chip as parasitics of the transistors. Consider for example the simple CMOS inverter in Fig. 16.2. During the clock periods in which such gate is

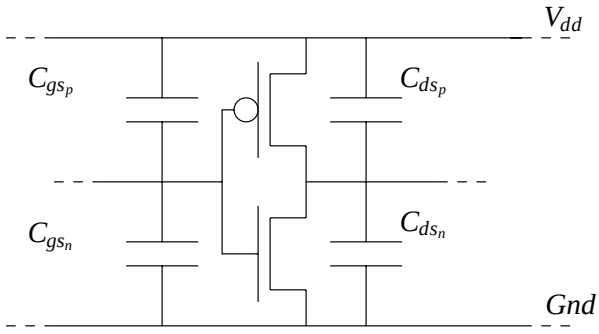

Figure 16.2: *Simple CMOS inverter showing parasitic capacitances that can supply charge to adjacent gates when the inverter is not switching.*

not switching, Gate-to-Source capacitances C_{gs}, and Drain-to-Source parasitic capacitances C_{ds} can provide some charge storage capability from Vdd to ground. Hence, nearby switching gates can use such charge, reducing the high frequency currents on the global Vdd and ground system. Some discussion with signal integrity experts during a brief experience in the HP Research Labs in California, together with some preliminary simulations, show that the effect of such capacitance on large chips with reduced switching activity can be considerable.

One simple way to estimate this "parasitic" decoupling capacitance is as follows:

- Use a layout parasitic extractor to calculate the capacitance C_j for each type and each size of the gates present on the chip.
- Use the results of the event driven simulation in the previous section to estimate the switching activity α_j of each gate in the circuit.
- Estimate the average capacitance available using

$$C_{tot} = \sum_j (1 - \alpha_j) C_j \tag{16.4}$$

16.2.2 Model of the Vdd and ground system

The entire Vdd and ground system needs to be included in this model. In particular we want to capture any resonance the Vdd and ground system might have. Hence, we apply to all interconnects in the Vdd and ground system the same full wave PEEC-type discretization we used in Chapter 3 for our EMI simulator. We obtain a huge equivalent circuit network of type shown in Fig. 3.6. This circuit network can be expressed as a huge passive linear system. We apply to such system the *Multipoint Expansion Reduced Order Modeling* technique described in Part II, obtaining a much smaller linear system with the same poles and resonances of the original one. This passive linear system can be expressed as a simple circuit which can be connected to the model developed before for the excitation sources (Fig. 16.1) giving the final simple circuit model in Fig. 16.3. Building the Vdd and ground reduced order model takes as much time as a system simulation. But

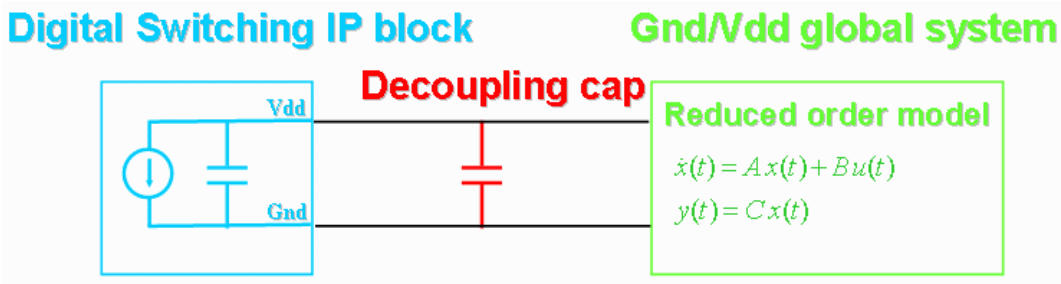

Figure 16.3: *Simple circuit models for sizing of decoupling capacitors. On the left we capture the current spectrum and internal capacitance of a digital switching block. On the right, we capture frequency dependent impedance and resonances of the Vdd and ground network with a reduce order model containing the dominant poles of the network.*

we can observe that once the model is built, it can be used for the sizing of all decoupling capacitors on the board (or on the chip).

16.2.3 An alternative approach: exploiting parameterized model order reduction

As an alternative one can think of using the parameterized model produced by the algorithms in Chapter 15 in conjunction with a function optimizer in order to size decoupling capacitors.

Part IV

Conclusions

The pervasive development of Systems-on-Package and Systems-on-Chip in future high frequency electronic system scenario will require design styles based on the assembling of components "encapsulated" and pre-characterized with respect to all levels of abstraction, from the functional to the physical. In this thesis we have addressed the physical problem, considering all sorts of electromagnetic interference phenomena, from the quasi-static electric field cross-talk, or magnetic inductive coupling, all to way to the full-wave propagating electromagnetic fields. Specifically, we have developed techniques for enabling analysis, modeling and synthesis of high frequency interconnect:

- ***Analysis*** tools should be able to handle extremely large collection of interconnect. Fast solvers exist with an affordable computational complexity $O(n\,log(n))$, where n is the number of discretization basis functions for the Mixed Potential Integral Equation (MPIE). However, when using the standard piecewise constant basis functions to discretize wires into short and thin filaments, the thousands of closely interacting thin filaments m in each wire cross-section cannot exploit the fast solver acceleration, and need to be resolved directly resulting in a deleterious computational complexity $O(m^2)$. In order to overcome such problem, in this thesis we have developed two new sets of higher order basis functions. Our basis functions are constructed using the same Helmholtz equation that the current is supposed to satisfy inside each conductor. The *conduction modes basis functions* are obtained by solving *analytically* such equation in rectangular of circular cross-sections. The *proximity template basis functions* are obtained by solving instead *numerically* the same equation for any shape of wire cross-section. In both our sets, our implementation results show that twenty times fewer basis functions are needed to produce the same solution accuracy obtained with the piecewise constant basis. Hence our basis functions reduce runtime and memory requirements by factors of 400.

- ***Modeling*** tools should be able to produce models of very large collections of interconnect that are both as accurate as an electromagnetic field solver, and at the same time small enough to be used effectively in a higher level circuit simulator in conjunction with other models. When used in a time domain circuit simulator, it is very important that such interconnect models are numerically well-behaved. Specifically, we need to guarantee that the produced interconnect models are passive, otherwise energy can be generated from nothing, and the simulation may easily become numerically unstable. A recently established procedure to produce small interconnect models is to use a field solver to generate a large dynamical system description, then reduce such system to an intermediate size system using not-optimal but computationally efficient Krylov-subspace projection framework methods. Finally one can use an optimal but computationally demanding Truncated Balance technique to squeeze the intermediate model to the final small model. Algorithms to guarantee passivity of the reduced model are available only for the first step, and only for the case on a collection of conductors in a quasi-static assumption. In this thesis we have developed algorithms to *guarantee passivity* at the first reduction step for structures that include also *dielectrics*. Furthermore, we have developed algorithms to guarantee passivity at the first reduction step for *distributed systems*, i.e. systems with frequency dependent matrix descriptors $E(s), A(s)$. Such systems are typically encountered when integrated circuit substrate are present and are treated using special Green functions, or when system dimensions are not small compared to wavelength and are treated with full-wave analysis, or finally when higher order basis functions are used for the discretization of the MPIE as our "conduction modes". We have also developed a model order reduction technique for the "second reduction step". Our algorithm has the same optimal compression properties of *Truncated Balance* but in addition our procedure can *guarantee the passivity* of the reduced interconnect models.

- ***Synthesis*** tools for interconnect could be enabled by the availability of parameterized models that can describe with the accuracy of an electromagnetic field solver performance changes as a function of geometrical parameter changes (such as wire widths and separations), and in addition are small enough to be used within an optimization loop. In this thesis we have developed such a *geometrically parameterized model reduction technique.* The model generation approach presented is automatic, and is based on series expansion of the parameter dependence followed by multi-parameter model-reduction. The effectiveness of the techniques described were tested using a multi-line bus example.

The experimental results clearly demonstrated the reduction strategies generated models that were accurate over a wide range of geometric variation.

Bibliography

[1] . *V.S.I. Virtual Socket Interface Alliance, Interface Standards for Design Re-use of Virtual Components*. http://www.vsi.org/ , .

[2] M. Abramowitz and I. A. Stegun. *Handbook of mathematical functions with formulas, graphs, and mathematical tables*. Washington: U.S. Govt. Print. Off., 1972.

[3] M. I. Aksun and R. Mittra. Derivation of closed-form green's functions for a general microstrip geometry. *IEEE Trans. on Microwave Theory and Techniques*, 40(11):2055–62, November 1992.

[4] B. D. Anderson and S. Vongpanitlerd. *Network Analysis and Synthesis*. Prentice-Hall, Englewood Cliffs, New Jersey, 1973.

[5] W. F. Arnold and A. J. Laub. Generalized eigenproblem algorithms and software for algebraic Riccati equations. *Proc. IEEE*, 72:1746–1754, 1984.

[6] Rao SM. Wilton DR. Glisson AW. Rao sm. wilton dr. glisson aw. *IEEE Trans. on Antennas and Propagation*, AP-30(3):409–18, May 1982.

[7] G. Bachmann, L. Narici, and E. Beckenstein. *Fourier and wavelet analysis*. Springer-Verlag, 2000.

[8] Adedeji B. Badiru. *Expert Systems Applications in Engineering and Manufacturing*. Prentice-Hall, Englewood Cliffs, NJ, 1992.

[9] Z. Bai and R. W. Freund. Eigenvalue-based characterization and test for positive realness of scalar transfer functions. *IEEE Trans. Computer-Aided Design*, 45(12):2396–402, December 2000.

[10] Zhaojun Bai, Peter Feldmann, and Roland W. Freund. How to make theoretically passive reduced-order models passive in practice. Technical Report Numerical Analysis Manuscript No.97-3-10, Bell Laboratories, Lucent Technologies, Murray Hill, New Jersey, October 1997.

[11] Zhaojun Bai, Peter Feldmann, and Roland W. Freund. Stable and passive reduced order models based on partial pade approximation via the lanczos process. Technical Report Numerical Analysis Manuscript No.97-3-10, Bell Laboratories, Lucent Technologies, Murray Hill, New Jersey, October 1997.

[12] J. E. Bracken, D. K. Sun, and Z. Cendes. Characterization of electromagnetic devices via reduced-order models. *Computer Methods in Applied Mechanics and Engineering*, 169(3-4):311–330, February 1999.

[13] J. Eric Bracken. Algorithms for passive modeling of linear interconnect networks. Technical report, ECE, CMU, 1996.

[14] A. C. Cangellaris and M. Celik. Order reduction of high-speed interconnect electrical models: The issue of passivity. In *Proceedings of the 1998 IEEE Symposium on IC/Package Design Integration*, pages 132–137, 1998.

[15] A. C. Cangellaris and V. Okhmatovsky. New closed-form electromagnetic green's functions in layered media. In *IEEE MTT-S International Microwave Symposium*, pages 1065–8, June 2000.

[16] A. C. Cangellaris and L. Zhao. Passive reduced-order modeling of electromagnetic systems. *Computer Methods in Applied Mechanics and Engineering*, 169(3-4):345–358, February 1999.

[17] L. P. Carloni, K. L. McMillan, A. Saldanha, and A. L. Sangiovanni-Vincentelli. A methodology for correct-by-costruction latency insensitive design. In *International Conference on Computer Aided-Design*, November 1999.

[18] M. Celik and A. C. Cangellaris. Efficient transient simulation of lossy packaging interconnects using moment-matching techniques. *IEEE Transactions on Components, Packaging, and Manufacturing Technology*, 19(1):64–73, February 1996.

[19] M. Celik and A. C. Cangellaris. Simulation of multiconductor transmission lines using krylov subspace order-reduction techniques. *IEEE Trans. Computer-Aided Design*, 16(5):485–496, May 1997.

[20] H. Chang, E. Charbon, E. Malavasi, A. Sangiovanni-Vincentelli, and alt. *A top-down constrain-driven design methodology for analog integrated circuits*. Kluwer academic publ., Boston/London/Dordrecht, 1997.

[21] E. Charbon, G. Holmlund, B. Bonecker, and A. Sanviovanni-Vincentelli. A performance-driven router for RF and microwave analog circuit design. In *IEEE 1995 Custom Integrated Circuits Conference*, 1995.

[22] E. Charbon, P. Miliozzi, L. P. Carloni, A. Ferrari, and A. L. Sangiovanni-Vincentelli. Modeling modeling digital substrate noise injection in mixed-signal ICs. *IEEE Trans. on Computer-Aided Design of Integrated Circuits and Systems*, 18, March 1999.

[23] X. Chen and J. T. Wen. Positive realness preserving model reduction with h_∞ norm error bounds. *IEEE Transactions on Circuits and Systems I: Fundamental Theory and Applications*, 42(1):23–29, January 1995.

[24] W. C. Chew. *Waves and fields in inhomogeneous media*. IEEE Press, New York, 1995.

[25] Eli Chiprout and Michael S. Nakhla. Analysis of interconnect networks using complex frequency hopping (CFH). *IEEE Trans. Computer-Aided Design*, 14(2):186–200, February 1995.

[26] Y. L. Chow, J. J. Yang, D. G. Fang, and G. E. Howard. A closed-form spatial green's function for the thick microstrip substrate. *IEEE Trans. on Microwave Theory and Techniques*, 39(3):588–592, March 1991.

[27] C. Coelho, J. R. Phillips, and L. M. Silveira. On generating compact, passive models of frequency-described systems. In *Symposium on Integrated Circuits and Systems*, Porto Alegre, RS, Brazil, September 2002.

[28] Carlos P. Coelho, Joel R. Phillips, and L. Miguel Silveira. A convex programming approach to positive real rational approximation. In *Proc. of IEEE/ACM International Conference on Computer Aided-Design*, pages 245–251, San Jose, CA, November 2001.

[29] J. S. Colburn, M. A. Jensen, and Y. Rahmat-Samii. Comparison of MOM and FDTD for radiation and scattering involving dielectric objects. In *Proc. of the IEEE Antennas and Propagation Society International Symposium*, pages 1802–5, 1994.

[30] K. M. Coperich, A. E. Ruehli, and A. Cangellaris. Enhanced skin effect for partial-element equivalent-circuit (PEEC) models. *IEEE Trans. on Microwave Theory and Techniques*, 48(9):1435–42, September 2000.

[31] L. Daniel, C. S. Ong, S. C. Low, K. H. Lee, and J. K. White. A multiparameter moment matching model reduction approach for generating geometrically parameterized interconnect performance models. *IEEE Trans. on Computer-Aided Design of Integrated Circuits and Systems*. Accepted for publication.

[32] L. Daniel, C. S. Ong, S. C. Low, K. H. Lee, and J. K. White. Geometrically parameterized interconnect performance models for interconnect synthesis. In *International Symposium in Physical Design*, pages 202–207, San Diego, CA, USA, April 2002.

[33] L. Daniel and J. R. Phillips. Model order reduction for strictly passive and causal distributed systems. In *Proc. of the IEEE/ACM Design Automation Conference*, New Orleans, LA, June 2002.

[34] L. Daniel, A. Sangiovanni-Vincentelli, and J. K. White. Techniques for including dielectrics when extracting passive low-order models of high speed interconnect. *IEEE Trans. on Computer-Aided Design of Integrated Circuits and Systems*. in process of being submitted for publication.

[35] L. Daniel, A. Sangiovanni-Vincentelli, and J. K. White. Interconnect electromagnetic modeling using conduction modes as global basis functions. In *IEEE Topical Meeting on Electrical Performance of Electronic Packaging*, pages 203–206, Phoenix, AZ, October 2000.

[36] L. Daniel, A. Sangiovanni-Vincentelli, and J. K. White. Techniques for including dielectrics when extracting passive low-order models of high speed interconnect. In *Proc. of the IEEE/ACM International Conference on Computer-Aided Design*, San Jose, CA, November 2001.

[37] L. Daniel, A. Sangiovanni-Vincentelli, and J. K. White. Using conduction modes basis functions for efficient electromagnetic analysis of on-chip and off-chip interconnect. In *Proc. of the IEEE/ACM Design Automation Conference*, Las Vegas, June 2001.

[38] L. Daniel, A. Sangiovanni-Vincentelli, and J. K. White. Proximity templates for modeling of skin and proximity effects on packages and high frequency interconnect. In *Proc. of the IEEE/ACM International Conference on Computer-Aided Design*, San Jose, CA, November 2002.

[39] L. Daniel, J. K. White, and Alberto Sangiovanni-Vincentelli. Conduction mode basis functions for capturing skin and proximity effects in an integral equation electromagnetic field solver. *IEEE Trans. on Computer-Aided Design of Integrated Circuits and Systems*. submitted for publication in 2001.

[40] E. M. Deeley. Surface impedance near edges and corners in three-dimensional media. *IEEE Trans. on Magnetics*, 2:712–714, 1990.

[41] James W. Demmel. *Applied Numerical Linear Algebra*. SIAM Society for Industrial and Applied Mathematics, Philadelphia, 1997.

[42] I. M. Elfadel and David D. Ling. Zeros and passivity of Arnoldi-reduced-order models for interconnect networks. In 34^{th} *ACM/IEEE Design Automation Conference*, pages 28–33, Anaheim, California, June 1997.

[43] I. M. Elfadel and David. L. Ling. A block rational arnoldi algorithm for multipoint passive model-order reduction of multiport RLC networks. In *Proc. of IEEE/ACM International Conference on Computer Aided-Design*, pages 66–71, San Jose, California, November 1997.

[44] D. Fairbairn and D. Anderson. The vsi alliance: the journey from vision to production. electronic design. *Penton Publishing*, 46:86–92, January 1998.

[45] P. Feldmann and R. W. Freund. Efficient linear circuit analysis by Padé approximation via the Lanczos process. *IEEE Transactions on Computer-Aided Design of Integrated Circuits and Systems*, 14:639–649, 1995.

[46] Peter Feldmann and Roland W. Freund. Reduced-order modeling of large linear subcircuits via a block Lanczos algorithm. In 32^{nd} *ACM/IEEE Design Automation Conference*, pages 474–479, San Francisco, CA, June 1995.

[47] R. W. Freund and P. Feldmann. Reduced-order modeling of large linear passive multi-terminal circuits using matrix-pade approximation. In *Proc. of IEEE/ACM International Conference on Computer Aided-Design*, pages 456–460, San Jose, CA, 1997.

[48] Roland W. Freund and Peter Feldmann. Reduced-order modeling of large linear passive multi-terminal circuits using matrix-padé approximation. In *DATE'98 - Design, Automation and Test in Europe, Exhibition and Conference*, pages 530–537, Paris, France, February 1998.

[49] K. Gallivan, E. Grimme, and P. Van Dooren. Asymptotic Waveform Evaluation via a Lanczos Method. *Applied Mathematics Letters*, 7(5):75–80, 1994.

[50] A. W. Glisson. An integral equation for electromagnetic scattering from homogeneous dielectric bodies. *IEEE Trans. on Antennas and Propagation*, AP-32(2):173–175, February 1984.

[51] Keith Glover. All optimal Hankel-norm approximations of linear multivariable systems and their L^∞-error bounds. *International Journal on Control*, 39(6):1115–1193, June 1984.

[52] M. Green. Balanced stochastic realizations. *Linear Algebra Apps.*, 98:211–247, 1988.

[53] Eric Grimme. *Krylov Projection Methods for Model Reduction*. PhD thesis, Coordinated-Science Laboratory, University of Illinois at Urbana-Champaign, Urbana-Champaign, IL, 1997.

[54] R. F. Harrington. *Field Computation by Moment Methods*. MacMillan, New York, 1968.

[55] P. Heydari and M. Pedram. Model reduction of variable-geometry interconnects using variational spectrally-weighted balanced truncation. In *Proc. of IEEE/ACM International Conference on Computer Aided-Design*, San Jose, CA, November 2001.

[56] Chung-Wen Ho, Albert E. Ruehli, and Pierce A. Brennan. The modified nodal approach to network analysis. *IEEE Transactions on Circuits and Systems*, 22(6):504–509, June 1975.

[57] Roger A. Horn and Charles R. Johnson. *Topics in Matrix Analysis*. Cambridge University Press, Cambridge, 1991.

[58] T. Hubing, J. Drewniak, T. Van Doren, and N. Kashyap. An expert system approach to EMC modeling. In *In the Proc. of the IEEE International Symposium in Electromagnetic Compatibility*, 1996.

[59] T. Hubing, P. Grover, T. Van Doren, J. Drewniak, and L. Hill. An algorithm for automated printed circuit board layout and routing evaluation. In *In the Proc. of the IEEE International Symposium in Electromagnetic Compatibility*, 1993.

[60] M. Hunt and J. A. Rowson. Blocking in a system on a chip. *IEEE Spectrum*, 33:35–41, November 1996.

[61] V. Ionescu, C. Oara, and M. Weiss. General matrix-pencil techniques for the solution of algebraic Riccati equations: a unified approach. *IEEE Transactions on Automatic Control*, 42:1085–1097, 1997.

[62] J. D. Jackson. *Classical Electrodynamics*. John Wiley, New York, 1975.

[63] I. M. Jaimoukha and E. M. Kasenally. Krylov subspsace methods for solving large Lyapunov equations. *SIAM Journal on Numerical Analysis*, 31:227–251, 1994.

[64] I. M. Jaimoukha and E. M. Kasenally. Oblique projection methods for large scale model reduction. *SIAM J. Matrix Anal. Appl.*, 16:602–627, 1995.

[65] M. Kamon. *Fast parasitic extraction and simulation of three-dimensional interconnect via quasistatic analysis*. PhD Thesis, Massachusetts Institute of Technology, Cambridge, MA, 1998.

[66] M. Kamon, N. Marques, L. M. Silveira, and J. K. White. Automatic generation of accurate circuit models. *IEEE Trans. on Components, Packaging, and Manufact. Tech.*, August 1998.

[67] M. Kamon, N. Marques, and J. K. White. FastPep: a fast parasitic extraction program for complex three-dimensional geometries. In *Proc. of the IEEE/ACM International Conference on Computer-Aided Design*, pages 456–460, San Jose, CA, November 1997.

[68] M. Kamon, M. J. Tsuk, and J. K. White. FASTHENRY: A multipole-accelerated 3-D inductance extraction program. *IEEE Trans. on Microwave Theory and Techniques*, 42(9):1750–8, September 1994.

[69] Mattan Kamon, Frank Wang, and Jacob K. White. Generating nearly optimally compact models from Krylov-subspace based reduced-order models. *IEEE Transactions on Circuits and Systems II: Analog and Digital Signal Processing*, 47(4):239–248, April 2000.

[70] W.H. Kao, Zhang Qian-Ling, Tang Ting-Ao, and Yu Huihua. A new block-based design methodology and cad toolset for mixed signal ASIC design. In *2nd International Conference on ASIC Proceedings*, 1996.

[71] S. Kapur and D. Long. Large scale capacitance calculations. In *Proc. of the IEEE/ACM Design Automation Conference*, pages 744–9, Los Angeles, June 2000.

[72] A. E. Kennelly, F. A. Laws, and P. H. Pierce. Experimental researches on skin effect in conductors. *Trans. A.I.E.E.*, 34-II:1749–85, September 1915.

[73] K. J. Kerns, I. L. Wemple, and A. T. Yang. Stable and efficient reduction of substrate model networks using congruence transforms. In *Proc. of IEEE/ACM International Conference on Computer Aided-Design*, pages 207 – 214, San Jose, CA, November 1995.

[74] K. J. Kerns, I. L. Wemple, and A. T. Yang. Preservation of passivity during RLC network reduction via split congruence transformations. In 34^{th} *ACM/IEEE Design Automation Conference*, pages 34–39, Anaheim, California, June 1997.

[75] D. Kirkpatrick and A. L. Sangiovanni-Vincentelli. Techniques for crosstalk avoidance in the design of high-performance digital systems. In *Proc. of the IEEE/ACM International Conference on Computer-Aided Design*, San Jose, CA, November 1994.

[76] B. M. Kolundzija and V. V. Petrovic. Comparison of MoM/SIE, MoM/VIE and FEM based on topological analysis of two canonical problems. In *Proc. of the IEEE Antennas and Propagation Society International Symposium*, pages 274–7, 1998.

[77] E. S. Kuh and R. A. Rohrer. *Theory of Linear Active Networks*. Holden-Day, San Francisco, 1967.

[78] A. J. Laub, M. T. Heath, C. C. Paige, and R. C. Ward. Computation of system balancing transformations and other applications of simultaneous diagonalization algorithms. *IEEE Transactions on Automatic Control*, 32:115–122, 1987.

[79] Jing-Rebecca Li. *Model Reduction of Large Linear Systems via Low Rank System Gramians*. PhD thesis, Massachusetts Institute of Technology, Cambridge, MA, September 2000.

[80] Jing-Rebecca Li, F. Wang, and J. K. White. An efficient lyapunov equation-based approach for generating reduced-order models of interconnect. In 36^{th} *ACM/IEEE Design Automation Conference*, pages 1–6, New Orleans, Louisiana, June 1999.

[81] Jing-Rebecca Li, F. Wang, and J. K. White. Efficient model reduction of interconnect via approximate system grammians. In *Proc. of IEEE/ACM International Conference on Computer Aided-Design*, pages 380–383, SAN JOSE, CA, November 1999.

[82] Y Liu, Lawrence T. Pileggi, and Andrzej J. Strojwas. Model order-reduction of RCL interconnect including variational analysis. In *Proc. of the ACM/IEEE Design Automation Conference*, pages 201–206, New Orleans, Louisiana, June 1999.

[83] J. LoVetri, S. Abu-Hakima, A. Podgorski, and G. Costache. Hardsys: Applying expert system techniques to electromagnetic hardening. In *In the Proc. of the IEEE International Symposium in Electromagnetic Compatibility*, pages 23–25, May 1989.

[84] J. LoVetri and A. Podgorski. Evaluation of hardsys: a simple emi expert system. In *In the Proc. of the IEEE International Symposium in Electromagnetic Compatibility*, 1990.

[85] E. Malavasi, E. Charbon, and A. Sangiovanni-Vincentelli. Automation of ic layout with analog constrains. *IEEE Trans. on Computer-Aided Design of Integrated Circuits and Systems*, 1996.

[86] N. Marques, M. Kamon, J. K. White, and L. M. Silveira. A mixed nodal-mesh formulation for efficient extraction and passive reduced-order modeling of 3D interconnects. In *Proc. of the IEEE/ACM Design Automation Conference*, pages 297–302, San Francisco, CA, June 1998.

[87] Nuno Marques, Mattan Kamon, Jacob K. White, and L. Miguel Silveira. An efficient algorithm for fast parasitic extraction and passive order reduction of 3d interconnect models. In *DATE'98 - Design, Automation and Test in Europe, Exhibition and Conference*, pages 538–548, Paris, France, February 1998.

[88] Nuno Marques, Mattan Kamon, Jacob K. White, and L. Miguel Silveira. A mixed nodal-mesh formulation for efficient extraction and passive reduced-order modeling of 3d interconnects. In 35^{th} *ACM/IEEE Design Automation Conference*, pages 297–302, San Francisco, CA, USA, June 1998.

[89] Y. Massoud and J. K. White. Improving the generality of the fictitious magnetic charge approach to computing inductances in the presence of permeable materials. In *Proceedings of the 2002 Design Automation Conference*, pages 552–555, June 2002.

[90] K. A. Michalski and J. R. Mosig. Multilayered media green's functions in integral equation formulations. *IEEE Trans. on Antennas and Propagation*, 45(3):508–519, March 1997.

[91] P. Miliozzi, L. Carloni, E. Charbon, and A. Sangiovanni-Vincentelli. SubWave: a methodology for modeling digital substrate noise injection in mixed-signal ICs. In *Custom Integrated Circuit Conference*, pages 385–388, 1996.

[92] H. Mission, S. Charruau, J. C. Moulondo, and A. Touboul. Designing emc-free multilayered substrates within the mentor graphics cad system. In *1993 International Symposium in Microelectronics*, pages 597–604, 1993.

[93] Bruce Moore. Principal Component Analysis in Linear Systems: Controllability, Observability, and Model Reduction. *IEEE Transactions on Automatic Control*, AC-26(1):17–32, February 1981.

[94] K. Nabors and J. K. White. FastCap: a multipole accelerated 3-d capacitance extraction program. *IEEE Trans. on Computer-Aided Design of Integrated Circuits and Systems*, 10(11):1447–59, November 1991.

[95] Tuyen V. Nguyen, Jing Li, and Zhaojun Bai. Dispersive coupled transmission line simulation using an adaptive block lanczos algorithm. In *Proc. of the International Custom Integrated Circuits Conference*, pages 457–460, 1996.

[96] B. Ninness and F. Gustafsson. A unifying construction of orthonormal bases for system identification. *IEEE Transactions on Automatic Control*, 42:515–521, 1997.

[97] A. Odabasioglu, M. Celik, and L. T. Pileggi. PRIMA: passive reduced-order interconnect macromodeling algorithm. *IEEE Trans. Computer-Aided Design*, 17(8):645–654, August 1998.

[98] A. Odabasioglu, M. Celik, and L. T Pileggi. Practical considerations for passive reduction of RLC circuits. In *Proc. of IEEE/ACM International Conference on Computer Aided-Design*, pages 214–219, San Jose, CA, November 1999.

[99] Altan Odabasioglu, Mustafa Celik, and Lawrence Pileggi. Prima: Passive reduced-order interconnect macromodeling algorithm. In *Proc. of IEEE/ACM International Conference on Computer Aided-Design*, pages 58–65, San Jose, California, November 1997.

[100] Altan Odabasioglu, Mustafa Celik, and Lawrence Pileggi. Prima: Passive reduced-order interconnect macromodeling algorithm. Technical report, Carnegie-Mellon University, Pittsburgh, PA, 1997.

[101] P. C. Opdenacker and E. A. Jonckheere. A contraction mapping preserving balanced reduction scheme and its infinity norm error bounds. *IEEE Transaction on Circuits and Systems*, 35(2):184–189, February 1988.

[102] S. Pasha, A. C. Cangellaris, J. L. Prince, and M. Celik. Passive model order reduction of multiconductor interconnects. In *IEEE 7th Topical Meeting on Electrical Performance of Electronic Packaging*, pages 291–294, 1998.

[103] C. Paul. *Introduction to electromagnetic compatibility*. Wiley, New York, 1992.

[104] J. R. Phillips. Model reduction of time-varying linear systems using approximate multipoint krylov-subspace projectors. In *Proc. of IEEE/ACM International Conference on Computer Aided-Design*, pages 96–102, Santa Clara, California, November 1998.

[105] J. R. Phillips. Automated extraction of nonlinear circuit macromodels. In *Proceedings of the Custom Integrated Circuit Conference*, pages 451–454, Orlando, FL, May 2000.

[106] J. R. Phillips. Projection frameworks for model reduction of weakly nonlinear systems. In 37^{th} *ACM/IEEE Design Automation Conference*, pages 184–189, 2000.

[107] J. R. Phillips, E. Chiprout, and D. D. Ling. Efficient full-wave electromagnetic analysis via model-order reduction of fast integral transforms. In 33^{rd} *ACM/IEEE Design Automation Conference*, pages 377–382, Las Vegas, Nevada, June 1996.

[108] J. R. Phillips, L. Daniel, and M. Silveira. Guaranteed passive balancing transformations for model order reduction. In *Proc. of the IEEE/ACM Design Automation Conference*, New Orleans, LA, June 2002.

[109] J. R. Phillips, L. Daniel, and M. Silveira. Guaranteed passive balancing transformations for model order reduction. *IEEE Trans. on Computer-Aided Design of Integrated Circuits and Systems*, 2003. Accepted for publication.

[110] J. R. Phillips and J. K. White. A Precorrected-FFT method for electrostatic analysis of complicated 3-D structures. *IEEE Trans. on Computer-Aided Design of Integrated Circuits and Systems*, 16(10):1059–1072, October 1997.

[111] Lawrence T. Pillage and Ronald A. Rohrer. Asymptotic Waveform Evaluation for Timing Analysis. *IEEE Transactions on Computer-Aided Design*, 9(4):352–366, April 1990.

[112] Lawrence T. Pillage and Ronald A. Rohrer. Asymptotic Waveform Evaluation for Timing Analysis. *IEEE Trans. Computer-Aided Design*, 9(4):352–366, April 1990.

[113] C. Prud'homme, D. Rovas, K. Veroy, Y. Maday, A.T. Patera, and G. Turinici. Reliable real-time solution of parametrized partial differential equations: Reduced-basis output bounds methods. *Journal of Fluids Engineering*, 2002.

[114] S. Pullela, N. Menezes, and L.T. Pileggi. Moment-sensitivity-based wire sizing for skew reduction in on-chip clock nets. *IEEE Trans. Computer-Aided Design*, 16(2):210–215, February 1997.

[115] P. Rabiei and M. Pedram. Model order reduction of large circuits using balanced truncation. In *Asia and South Pacific Design Automation Conference*, pages 237–240, Hong Kong, Hong Kong, January 1999.

[116] P. Rabiei and M. Pedram. Model reduction of variable-geometry interconnects using variational spectrally-weighted balanced truncation. In *Proc. of IEEE/ACM International Conference on Computer Aided-Design*, pages 586–591, San Jose, CA, USA, November 2001.

[117] O. M. Ramahi and B. Archambeault. Adaptive absorbing boundary conditions in finite-difference time domain applications for emc simulations. *IEEE Trans. on Electromagnetic Compatibility*, 37(4):580–3, November 1995.

[118] S. Ramo, J. R. Whinnery, and T. Van Duzer. *Fields and Waves in communication electronics*. Wiley, 1994.

[119] M. Rewienski and J. K. White. A trajectory piecewise-linear approach to model order reduction and fast simulation of nonlinear circuits and micromachined devices. In *Proc. of IEEE/ACM International Conference on Computer Aided-Design*, pages 252–7, San Jose, CA, USA, November 2001.

[120] J. Roychowdhury. Reduced order modeling of linear time-varying systems. In *Proc. of IEEE/ACM International Conference on Computer Aided-Design*, pages 92–96, Santa Clara, California, November 1998.

[121] A. E. Ruehli. Equivalent circuit models for three dimensional multiconductor systems. *IEEE Trans. on Microwave Theory and Techniques*, 22:216–221, March 1974.

[122] A. E. Ruehli and H. Heeb. Circuit models for three-dimensional geometries including dielectrics. *IEEE Trans. on Microwave Theory and Techniques*, 40:1507–1516, July 1992.

[123] M. G. Safonov and R. Y. Chiang. A Schur method for balanced truncation model reduction. *IEEE Transactions on Automatic Control*, 34:729–733, 1989.

[124] B. G. Salman and A. McCowen. A comparative study of the computation of near-field scattering from resonant dielectric/pec scatterers. *IEEE Trans. on Magnetics*, 32(3):866–9, May 1996.

[125] T. K. Sarkar and E. Arvas. An integral equation approach to the analysis of finite microstrip antennas: Volume/surface formulation. *IEEE Trans. on Antennas and Propagation*, 38(3):305–312, March 1990.

[126] T. K. Sarkar, S. M. Rao, and A. R. Djordjevic. Electromagnetic scattering and radiation from finite microstrip structures. *IEEE Trans. on Microwave Theory and Techniques*, 38(11):1568–75, November 1990.

[127] H. Schmidt, D. Theune, R. Thiele, and T. Lengauer. EMC-Driven midway routing on PCBs. In *In the Proc. of the IEEE International Symposium in Electromagnetic Compatibility*, 1995.

[128] L. M. Silveira, M. Kamon, I. Elfadel, and J. K. White. Coordinate-transformed arnoldi algorithm for generating guarantee stable reduced-order models of RLC. *Computer Methods in Applied Mechanics and Engineering*, 169(3-4):377–89, February 1999.

[129] L. Miguel Silveira, Ibrahim M. Elfadel, Jacob K. White, Monirama Chilukura, and Kenneth S. Kundert. Efficient Frequency-Domain Modeling and Circuit Simulation of Transmission Lines. *IEEE Transactions on Components, Packaging, and Manufacturing Technology – Part B: Advanced Packaging*, 17(4):505–513, November 1994.

[130] L. Miguel Silveira, Mattan Kamon, and Jacob K. White. Algorithms for Coupled Transient Simulation of Circuits and Complicated 3-D Packaging. *IEEE Transactions on Components, Packaging, and Manufacturing Technology, Part B: Advanced Packaging*, 18(1):92–98, February 1995.

[131] L. Miguel Silveira, Mattan Kamon, and Jacob K. White. Efficent reduced-order modeling of frequency-dependent coupling inductances associated with 3-d interconnect structures. In *Proceedings of the European Design and Test Conference*, Paris, France, March 1995.

[132] L. Miguel Silveira, Nuno Marques, Mattan Kamon, and Jacob K. White. Improving the efficiency of parasitic extraction and simulation of 3d interconnect models. In *ICECS'99 - IEEE International Conference on Electronics, Circuits and Systems*, pages 1729–1736, Pafos, Cyprus, September 1999.

[133] P. Silvester. Modal network theory of skin effect in flat conductors. *Proc. IEEE*, 54(9):1147–1151, September 1966.

[134] Michel F. Sultan and Andreas C. Cangellaris. System level approach for automotive electromagnetic compatibility. In *In the Proc. of the IEEE International Symposium in Electromagnetic Compatibility*, 1987.

[135] D. R. Swatek and Ioan R. Ciric. Single source integral equation for wave scattering by multiply-connected dielectric cylinders. *IEEE Trans. on Magnetics*, 32(3):878–881, May 1996.

[136] J. Tausch and J. K. White. A multiscale method for fast capacitance extraction. In *Proc. of the IEEE/ACM Design Automation Conference*, pages 537–42, New Orleans, LA, June 1999.

[137] D. Theune, R. Thiele, W. John, and T. Lengauer. Robust methods for EMC-Driven routing. *IEEE Trans. on Electromagnetic Compatibility*, 1994.

[138] M. J. Tsuk and J. A. Kong. A hybrid method for the calculation of the resistance and inductance of transmission lines with arbitrary cross section. *IEEE Trans. on Microwave Theory and Techniques*, 39(8):1338–1347, August 1991.

[139] E. Tuncer, B. T. Lee, M. S. Islam, , and D. P. Neikirk. Quasi-static conductor loss calculations in transmission lines using a new conformal mapping technique. *IEEE Trans. on Microwave Theory and Techniques*, 42:1807–1815, September 1994.

[140] E. Tuncer, B. T. Lee, and D. P. Neikirk. Interconnect series impedance determination using a surface ribbon method. *IEEE Topical Meeting on Electrical Performance of Electronic Packaging*, pages 249–252, November 1994.

[141] E. Tuncer and D. P. Neikirk. Efficient calculation of surface impedance for rectangular conductors. *Electronic Letters*, 29(24):2127–2128, November 1993.

[142] J. Wang, J. Tausch, and J. K. White. A wide frequency range surface integral formulation for 3-D RLC extraction. In *Proc. of the IEEE/ACM International Conference on Computer-Aided Design*, pages 453–7, San Jose, CA, 1999.

[143] W. T. Weeks, L. L. Wu, M. F. McAllister, and A. Singh. Resistive and inductive skin effect in rectangular conductors. *IBM J. Res. Develop.*, 23(6):652–660, November 1979.

[144] D. S. Weile, E. Michielssen, Eric Grimme, and K. Gallivan. A method for generating rational interpolant reduced order models of two-parameter linear systems. *Applied Mathematics Letters*, 12:93–102, 1999.

[145] J. T. Wen. Time domain and frequency domain conditions for strict positive realness. *IEEE Transactions on Automatic Control*, 33:988–992, 1988.

[146] J. C. Willems. Least squares stationary optimal control and the algebraic riccati equation. *IEEE Transaction on Automatic Control*, 16(6):621–634, 1971.

[147] J. C. Willems. Dissipative dynamical systems. *Arch. Rational Mechanics and Analysis*, 45:321–393, 1972.

[148] M. Wu, C. Tse, and P. Chang. An integrated CAD tool for switching power supply design with electromagnetic interference prediction. In *11th Annual Applied Power Electronics Conf. end Expo.*, pages 340–46, 1996.

[149] N. E. Wu and G. Gu. Discrete Fourier transform and h_∞ approximation. *IEEE Transactions on Automatic Control*, 35(9):1044–1046, September 1990.

[150] J. Zhao, W. W. M. Dai, S. Kapur, and D. E. Long. Efficient three-dimensional extraction based on static and full-wave layered green's functions. In *Proc. of the IEEE/ACM Design Automation Conference*, pages 224–229, 1998.

[151] Z. Zhu, J. Huang, B. Song, and J. K. White. Improving the robustness of a surface integral formulation for wideband impedance extraction of 3d structures. In *Proc. of the IEEE/ACM International Conference on Computer-Aided Design*, pages 592–7, San Jose, CA, 2001.

[152] Z. Zhu, J. Huang, B. Song, and J. K. White. Algorithms in fastimp: a fast and wideband impedance extraction program for complicated 3-d geometries. In *Proc. of the IEEE/ACM Design Automation Conference*, Los Angeles, CA, June 2003.